Multiscale Transport and Dynamics in Ion-Dense Organic Electrolytes and Copolymer Micelles

Bryce E. Kidd

Dissertation submitted to the faculty of the Virginia Polytechnic Institute and State University in partial fulfillment of the requirements for the degree of

Doctor of Philosophy

In

Chemistry

Louis A. Madsen, Chair

John R. Morris

Harry W. Gibson

Diego Troya

September 2, 2016

Blacksburg, Virginia

Keywords: organic ionic plastic crystal, polymer-gel electrolyte, ion-conducting membrane, copolymer micelle, NMR, self-diffusion, T_1/T_2 relaxation, Stokes-Einstein relation.

Multiscale Transport and Dynamics in Ion-Dense Organic Electrolytes and Copolymer Micelles

Bryce E. Kidd

Abstract

Understanding molecular and ion dynamics in soft materials used for fuel cell, battery, and drug delivery vehicle applications on multiple time and length scales provides critical information for the development of next generation materials. In this dissertation, new insights into transport and kinetic processes such as diffusion coefficients, translational activation energies (E_a), and rate constants for molecular exchange, as well as how these processes depend on material chemistry and morphology are shown. This dissertation also aims to serve as a guide for material scientists wanting to expand their research capabilities via nuclear magnetic resonance (NMR) techniques. By employing variable temperature pulsed-field-gradient (PFG) NMR diffusometry, which can probe molecular transport over nm – μm length scales, I first explore transport and morphology on a series of ion-conducting materials: an organic ionic plastic crystal, a proton-exchange membrane, and a polymer-gel electrolyte. These studies show the dependencies of small molecule and ion transport on modulations to material parameters, including thermal or magnetic treatment, water content, and/or crosslink density. I discuss the fundamental significance of the length scale over which translational E_a reports on these systems (~ 1 nm) and the resulting implications for using the Arrhenius equation parameters to understand and rationally design new ion-conductors. Next, I describe how NMR spectroscopy can be utilized to investigate the effect of loading a small molecule into the core of a spherical block copolymer micelle (to mimic, *e.g.*, drug loading) on the hydrodynamic radius (r_H) and polymer chain dynamics. In particular, I present spin-lattice relaxation (T_1) results that directly measure single chain exchange rate k_{exch} between micelles and diffusion results that inform on

the unimer exchange mechanism. These convenient NMR methods thus offer an economical alternative (or complement) to time-resolved small angle neutron scattering (TR-SANS).

Multiscale Transport and Dynamics in Ion-Dense Organic Electrolytes and Copolymer Micelles

Bryce E. Kidd

General Audience Abstract

Lithium ion batteries, fuel cells, and drug-delivery vehicles each depend on a fundamental understanding of the interface between materials science and molecular dynamics. Optimization of such materials usually requires routine analysis through common polymer characterization techniques. The present dissertation highlights the usage of an uncommon analytical tool to the polymer science community, nuclear magnetic resonance (NMR); and how it gives unprecedented access in gauging material performance when subjected to judicious multiscale analysis. Chemical specificity, non-destructiveness, and the ability to study dynamics on multi-time and length scales are only a few of the many advantages of NMR offers over other polymer characterization techniques. Chapters 3, 4, 5, 6, and 7 investigate different classes of materials for their respective applications to better understand the aforementioned interface. These studies are intended to spark interest in new research areas while supplementing existing ones.

Acknowledgements

First, and foremost, I would like to thank Dr. Louis A. Madsen for the many years of continued support. You have provided me with a valuable skill set that will allow me to further mature as a person and scientist. A research group is only as strong as it's leader. You exemplify such a role and have fostered a very strong research group. Thank you for giving me, and others, the opportunity to do some awesome science in your lab.

To my committee members, Dr. John R. Morris, Dr. Harry W. Gibson, and Dr. Diego Troya, you each have also aided in my maturation as a person and scientist. I am more wholesome from your continued support, thank you.

To my fellow group members, past and present, Dr. Kyle Wilmsmeyer, Dr. Jianbo Hou, Dr. Zhiyang Zhang, Dr. Ying Chen, Dr. Cocoa Wang, Dr. Mark Lingwood, Dr. Mithun Goswami, Kacey McCreary, Jim Wahmhoff, Yongzheng Huang, Rachele Christina, Ying Wang, Drew Korovich, Xiuli Li, Curt Zanelotti, Rui Zhang, and Lam Thieu, I will always cherish the great times we had together. Thank you for giving me your support and guidance as well as allowing me to give you my support and guidance. I would also like to thank visiting students Friedrich Steuber and Katherine Miller for giving me inspiration in mentoring you through your short studies with me.

To my fellow cohort, Spencer Kidd, Dr. Eugene Camerino, Dr. Benjamin Sundell, and Dr. Jarrett Rowlett, you each have been with me through my ups and downs. I thank you for the great times we all had together on this crazy roller coaster.

To my family, Brent, Brenda, and Schyler Kidd, thank you so much for supporting me during my studies. You have helped me mature as person and have shown me how to appreciate

the simpler things in life. Ray and Laurie Ahrenholtz, thank you for supporting Spencer and I during our time here.

Finally, to my amazing wife, Spencer, thank you. I do not know how to thank you enough for everything you have done for me. I look forward to our future as we take on the world!

Table of Contents

Abstract

General Audience Abstract

Acknowledgements ..... **v**

Table of Contents ..... **vii**

Attributions ..... **x**

Chapter 1. From Batteries to Drug-Delivery Vehicles: How Polymer Morphology Influences Transport and Dynamics in Soft Materials **1**

1.1 General Motivations and Project Goals 1

1.2 Introduction to Ion-Dense Materials and Properties That Influence Performance 3

1.2.1 Organic Ionic Plastic Crystals 4

1.2.2 Polymer Electrolyte Membranes 8

1.2.3 Polymer-Gel Electrolytes 12

1.3 Introduction to Block Copolymer Micelles as Drug-Delivery Vehicles 14

1.4 Introduction to Molecular Diffusion and Restricted Diffusion 17

1.4.1 Diffusion Within Polycrystalline Materials 19

1.4.2 Diffusion Within Soft Materials 21

1.4.3 Restricted Diffusion 22

1.5 Physical Meaning of Diffusive Activation Energy in Materials 25

1.6 Concluding Remarks 30

1.7 References 31

Chapter 2. Nuclear Magnetic Resonance as a Versatile Tool to Study Soft Materials: Theory and Methods **35**

2.1 Basic Nuclear Magnetic Resonance Theory 35

2.2 Pulsed-Field-Gradient NMR Diffusometry 40

2.3 Multi-Component Relaxation and Diffusometry to Probe Material Morphology 46

2.3.1 Multi-Component Spin-Spin Relaxation 46

2.3.2 Multi-Component Diffusometry 50

2.4 General Remarks on Solid-State NMR 53

2.4.1 Quadrupolar NMR Theory 53

2.5 References 56

Chapter 3. Cation and Anion Transport in a Dicationic Imidazolium-Based Plastic Crystal Ion Conductor **59**

3.1 Introduction 60

3.2 Experimental 65

3.2.1 Sample Preparation 65

3.2.2 Variable Temperature Solid-State NMR 65

3.2.3 Variable Temperature Pulsed-Field-Gradient NMR 66

3.3 Results and Discussion 67

3.3.1 Temperature-Dependent ^{2}H NMR Studies 68

3.3.2 Temperature-Dependent ^{19}F and ^{1}H NMR 73
3.3.3 Thermal and Magnetic Treatment....79
3.3.4 Diffusion Coefficient vs. Temperature 80
3.3.5 Domain Boundary Restricted Diffusion 85
3.4 Conclusions....88
3.5 Acknowledgements....89
3.6 References....89
Chapter 4. Probing Ion-Conducting Channel Geometry in a Perfluorosulfonate Ionomer.92
4.1 Introduction....92
4.2 Experimental....95
4.2.1 ^{7}Li and ^{23}Na Quadrupolar NMR Spectroscopy....95
4.3 Results and Discussion 96
4.3.1 ^{7}Li and ^{23}Na Quadrupolar NMR Spectroscopy....96
4.4 Conclusions....104
4.5 References....105
Chapter 5. Multiscale Lithium and Counterion Transport in an Electrospun Polymer-Gel Electrolyte....107
5.1 Introduction....108
5.2 Experimental....111
5.2.1 Synthesis of Crosslinked PEO Fiber-Mats 111
5.2.2 Ionic Conductivity 112
5.2.3 NMR Analyses: Spin-Spin Relaxation, PFG Diffusion, and ^{17}O Spectroscopy....113
5.3 Results and Discussion 115
5.3.1 Probing the Morphology and Ion Transport of Polymer-Gel Electrolytes 115
5.3.2 Understanding Material Factors That Influence Ion Transport 128
5.4 Conclusions....138
5.5 Acknowledgments....139
5.6 References....139
Chapter 6. Tuning Self-Assembly and Diffusion of Block Copolymer Micelles Via Co-Solvent Addition....142
6.1 Introduction....143
6.2 Experimental....145
6.2.1 Diblock Copolymer Synthesis and Characterization 145
6.2.2 Pulsed-Field-Gradient NMR Diffusometry 147
6.3 Results and Discussion 148
6.3.1 Probing the Effect of Small Molecule Additives on Micelle and Unimer Dynamics 148
6.4 Conclusions....165
6.5 Acknowledgments....165
6.6 References....166

Chapter 7. Unimer Exchange Dynamics in Block Copolymer Micelles Using Time-Resolved NMR 168
7.1 Introduction 169
7.2 Experimental 172
7.2.1 Diblock Copolymer Synthesis and Characterization 172
7.2.2 Spin-Lattice Relaxation and NMR Diffusometry 172
7.3 Results and Discussion 173
7.4 Conclusions 184
7.5 Acknowledgments 185
7.6 References 185
Chapter 8. Summary and Future Work 187
8.1 Summary and General Material Design Guidelines 187
8.2 Future Work 192

Attributions

Throughout these research projects, multiple peers have helped guide my work. A brief description of their contributions has been added here.

Chapter 3: *Cation and Anion Transport in a Dicationic Imidazolium-Based Plastic Crystal Ion Conductor (DOI: 10.1021/jp4084629)*

Mark D. Lingwood, PhD (Dr. Louis Madsen's Lab, Department of Chemistry) is currently an assistant professor in chemistry at Saint Mary's College of California. Dr. Lingwood was a co-author on this paper and aided in data analysis and edits.

Minjae Lee, PhD (Dr. Harry Gibson's Lab, Department of Chemistry) is currently an assistant professor in chemistry at Kunsan University in South Korea. Dr. Lee was a co-author on this paper and synthesized the material used in this study and provided edits.

Harry W. Gibson, PhD (Faculty Member, Department of Chemistry) is currently a professor in chemistry at Virginia Tech. Dr. Gibson served as a committee member for this Thesis and committee chair for Dr. Lee. Dr. Gibson was a co-author on this paper and provided deep discussions on understanding the data.

Louis A. Madsen, PhD (Faculty Member, Department of Chemistry) is currently an associate professor in chemistry at Virginia Tech. Dr. Madsen served as the committee chair of this Thesis and provided deep discussions on understanding the data.

Chapter 4: *Probing Ion-Conducting Channel Geometry in a Perfluorosulfonate Ionomer*

Mithun Goswami, PhD (Dr. Louis Madsen's Lab, Department of Chemistry) is currently a research scientist at DSM. Dr. Goswami contributed to ^{23}Na data acquisition and analysis.

Louis A. Madsen, PhD (Faculty Member, Department of Chemistry) is currently an associate professor in chemistry at Virginia Tech. Dr. Madsen served as the committee chair of this Thesis and provided deep discussions on understanding the data.

Chapter 5: *Multiscale Lithium and Counterion Transport in an Electrospun Polymer-Gel Electrolyte (DOI: 10.1021/acs.macromol.5b00573)*

Scott J. Forbey, PhD (Dr. Robert Moore's Lab, Department of Chemistry) is currently working in the Morgan Center for Entrepreneurship at Purdue University. Dr. Forbey was a co-author on this paper and synthesized the material and conducted ionic conductivity measurements used in this study and provided edits.

Friedrich W. Steuber, MS (Department of Chemistry, RWTH Aachen University, Germany) is currently a PhD student at Trinity College Dublin. Mr. Steuber was a visiting student and aided in collection of data and provided edits.

Robert B. Moore, PhD (Faculty Member, Department of Chemistry) is currently a professor in chemistry at Virginia Tech. Dr. Moore served as the committee chair for Dr. Forbey. Dr. Moore was a co-author on this paper and provided deep discussions on understanding the data.

Louis A. Madsen, PhD (Faculty Member, Department of Chemistry) is currently an associate professor in chemistry at Virginia Tech. Dr. Madsen served as the committee chair of this Thesis and provided deep discussions on understanding the data.

Chapter 6: *Tuning Self-Assembly and Diffusion of Block Copolymer Micelles Via Co-Solvent Addition (to be submitted to Macromolecules)*

Tyler J. Cooksey, MS (Dr. Megan Robertson's Lab, Department of Chemistry, University of Houston) is currently a PhD student under Dr. Robertson. Mr. Cooksey synthesized the materials, conducted DLS experiments, analyzed SANS results, and provided edits.

Xiuli Li (Dr. Louis Madsen's Lab, Department of Chemistry) is currently a PhD Candidate under Dr. Madsen and helped collect NMR data. Ms. Li also provided discussion and edits.

Megan L. Robertson, PhD (Faculty Member, Department of Chemical and Biomolecular Engineering, University of Houston) is currently an assistant professor at University of Houston. Dr. Robertson was a co-author on this paper and provided deep discussions on understanding the data.

Louis A. Madsen, PhD (Faculty Member, Department of Chemistry) is currently an associate professor in chemistry at Virginia Tech. Dr. Madsen served as the committee chair of this Thesis and provided deep discussions on understanding the data.

Chapter 7: *Unimer Exchange Dynamics in Block Copolymer Micelles Using Time-Resolved NMR (to be submitted to the Journal of the American Chemical Society)*

Tyler J. Cooksey, MS (Dr. Megan Robertson's Lab, Department of Chemical and Biomolecular Engineering, University of Houston) is currently a PhD student under Dr. Robertson. Mr. Cooksey synthesized the materials and provided edits.

Xiuli Li (Dr. Louis Madsen's Lab, Department of Chemistry) is currently a PhD Candidate under Dr. Madsen and helped collect NMR diffusometry data. Ms. Li also provided discussion and edits.

Megan L. Robertson, PhD (Faculty Member, Department of Chemical and Biomolecular Engineering, University of Houston) is currently an assistant professor at University of Houston. Dr. Robertson was a co-author on this paper and provided deep discussions on understanding the data.

Katherine Miller (Department of Chemistry, Stockton University) is currently an undergraduate student that visited our lab and aided in data collection.

Louis A. Madsen, PhD (Faculty Member, Department of Chemistry) is currently an associate professor in chemistry at Virginia Tech. Dr. Madsen served as the committee chair of this Thesis and provided deep discussions on understanding the data.

Chapter 1

From Batteries to Drug-Delivery Vehicles: How Polymer Morphology Influences Transport and Dynamics in Soft Materials

1.1 General Motivations and Project Goals

The demand for new green technology grows each day, as evidenced by extensive research to produce more earth-friendly products, such as new solvent-free batteries, fuel cells, and molecularly self-assembled vehicles for targeted drug delivery or "nano-reactor" vessels for solvent-exhaustive reactions. While breakthrough developments of such technologies greatly benefit from advances in fundamental chemistry and materials understanding, Edisonian approaches can hinder progress. Powerful material characterization techniques, such as impedance spectroscopy (IS, ionic conductivity), differential scanning calorimetry (DSC, phase transitions), and X-ray/neutron scattering methods (domain size/structure and dynamics), substantially enrich overall understanding of fundamental properties that govern material performance. However, development of new techniques and methods to complement existing protocols will give material scientists new insights into material properties.

Nuclear magnetic resonance (NMR) can be used as a versatile and powerful tool to address many facets associated with material properties. Nuclear/chemical specificity and dynamics (e.g., diffusion coefficient, activation energy, exchange rates, etc.) on multiple time and length scales represent a fraction of possibilities that NMR offers. Thus, NMR theories and methods can allow materials scientists to acquire a deeper understanding of their materials and lead to more rational design strategies.

The purpose of this thesis is to investigate how multiscale morphological properties influence transport of ions and small molecules transport inside a range of ion-conducting materials, e.g., organic ionic plastic crystals (OIPCs),[1] polymer-gel electrolytes (PGEs),[2] and perfluorosulfonate ionomers.[3] This thesis will also cover the development of methods to better understand polymeric micelles, including unimer equilibrium and non-equilibrium properties. The remainder of Chapter 1 will briefly introduce and review OIPCs, PGEs, the perfluorosulfonate ionomer Nafion® 117, and block copolymer micelles, and discuss fundamental questions and concepts, such as:

- What are the sub-nm to μm-scale transport mechanisms and how does morphology influence such properties within the aforementioned ion-conducting materials?
- Can we use the Arrhenius equation to separate sub-nm-scale information from μm-scale measurements in ion-conducting membranes?
- Can we use NMR to characterize polymeric micelle properties, such as size, structure-property relationships, and unimer exchange kinetics, and thus provide new and/or complementary information to other analytical methods?

I aim to answer the above questions by presenting a series of studies throughout the following chapters. Chapter 2 will introduce a selection of NMR theory and methods that can be applied to study material properties. This is supported by work from our group, wherein we use NMR spectroscopy and diffusometry to probe the influence of nm - μm morphological properties on translational processes within a broad-range of materials.[1-10] Chapters 3, 4, and 5 present variable temperature and multinuclear (^{1}H, ^{19}F, ^{17}O, ^{2}H, ^{7}Li, and ^{23}Na) NMR analyses to study ion transport mechanisms within an imidazolium-based OIPC,[1] local geometry within the hydrophilic channels of Nafion® 117,[11] and how morphological modulations influence lithium

and counterion transport within a PEO-based PGE.[2] Chapters 6 and 7 present NMR analyses of a poly(ethylene oxide)-*b*-poly(caprolactone) (PEO-*b*-PCL) block copolymer micelle to determine micelle size, relative unimer and micelle fractions with varying solvent content, and unimer exchange kinetics and mechanism. Finally, Chapter 8 summarizes these results and offers future directions to further develop NMR methods as robust tools to bridge the gap between bulk material properties and fundamental molecular properties.

1.2 Introduction to Ion-Dense Materials and Properties That Influence Performance

While the battery and fuel cell date back to the 1800's,[12] advances in fundamental chemistry and material science have afforded gains in efficiency and stability through new materials. These technologies consist of an anode, cathode, and electrolyte separating the electrodes. For a fuel cell, a fuel source, such as H_2, is oxidized at the anode to generate H^+ ions and electrons. To conserve charge neutrality of the system, H^+ diffuses through the electrolyte to combine with O_2 (from ambient air) and electrons (from the external circuit) through reduction at the cathode to produce the product, H_2O. Thus chemical energy can be converted to electrical energy.

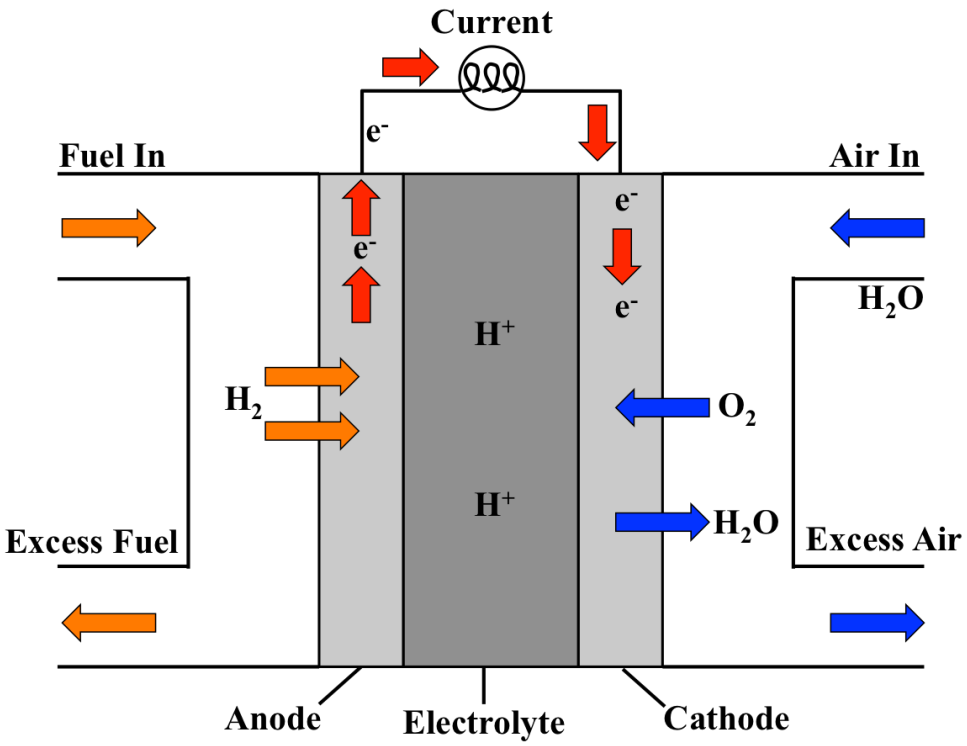

Figure 1.1. Illustration of an H^+ fuel cell wherein oxidation of H_2 at the anode produces electrons and H^+ diffuses through the electrolyte to combine with O_2 (from ambient air) and the electrons to produce H_2O in a reduction at the cathode.

One of the main issues in implementing a novel battery or fuel cell is finding an electrolyte that enables sufficient ion transport from anode to cathode. Conduction of small ions, such as H^+ and Li^+ generally allow the fastest transport and highest energy density. Thus, much research has gone into the development of mechanically stable solid-state electrolytes as next generation ion-conductors for battery and fuel cell applications that are non-flammable, thermally stable, and do not suffer from liquid electrolyte leakage.

1.2.1 Organic Ionic Plastic Crystals

One emerging class of solid-state electrolytes, OIPCs, resemble ionic liquids (IL) in the sense that they each consist of a cation and anion (Figure 1.2).[1,13-16] However, OIPCs are solids

while ILs are liquids at room temperature (25 °C). Unlike an ionic liquid, OIPCs exhibit efficient packing through long-range crystalline order of ions, and short-range disorder wherein isotropic states (i.e., isotropic rotational mobility of the cation and/or anion about one or more axes) can exist below the melting temperature.[1,13-15,17-30]

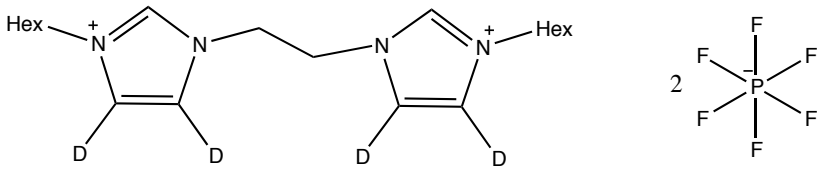

1,2-bis[*N*-(*N'*-hexylimidazolium-d_2(4,5))]C_2H_4 $2PF_6^-$

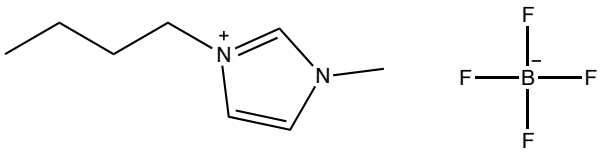

[bmim][BF_4]

Figure 1.2. Structure of an OIPC (top: 1,2-bis[*N*-(*N'*-hexylimidazolium-d_2(4,5))]C_2H_4 hexafluorophosphate)[1,14] and an IL (bottom: 1-butyl-3-methylimidazolium tetrafluoroborate).[16] Chemically similar to ILs, OIPCs are solid at room temperature (25 °C) while an IL is a liquid or molten salt.

During the 1960's, Timmermans showed that molecular compounds in the solid state, such as cyclohexane (which shows rotational mobility at -87 °C before melting at 6 °C), rotate freely because their shape is "quasi-spherical" upon rotation, with the centers of mass occupying fixed sites within the crystalline lattice.[17] The term "rotator phase" has been coined for the rotational motions in the crystalline lattice, which are reached through one or more highly enthalpic first-order solid-solid phase transitions.[13] Rotator phases of OIPCs contribute to the short-range disorder accompanied by low entropy of fusion; $\Delta S_f < 20$ J K^{-1} mol^{-1}, and this is commonly known as Timmermans' criterion.[13] For OIPCs, a volume expansion of the crystallites at a solid-

solid phase transition allows more degrees of freedom to become available, thus increasing entropy.

Pringle and MacFarlane *et al.* suggested that Timmermans' criterion may only be satisfied for systems that contain only one molecular species.[13] However, OIPCs contain more than one molecular species, which are ionically bound. If the material consists of cations and anions, the entropy of fusion may be higher due to only one of the molecular ions exhibiting internal degrees of freedom below T_m, hence a larger ΔS_f.[13] While Timmermans' criterion has been used extensively to sift through the many OIPCs studied thus far, it is also apparent that other fundamental properties need to be considered as well. Certain OIPCs have shown high conductivities upon entering a new solid phase, but molecular interactions, molecular reorientations, and ion transport within such phases are still not fully understood.[13]

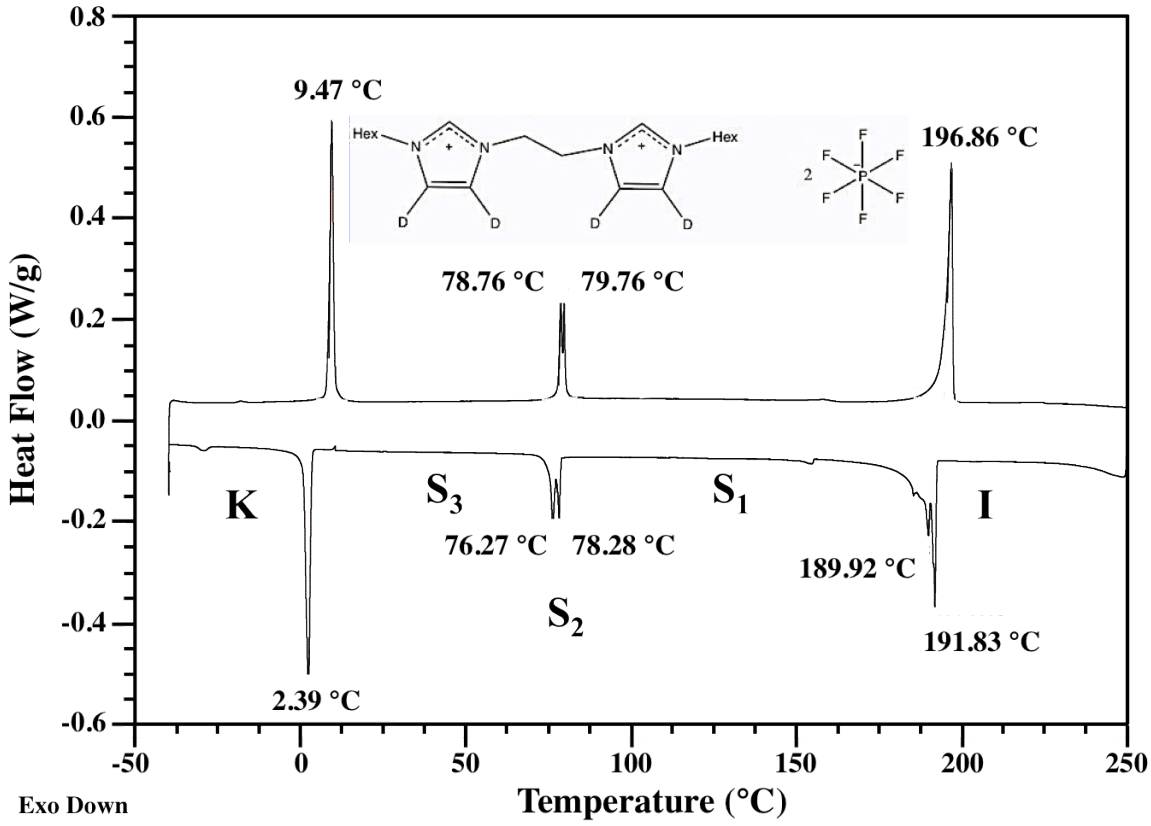

Figure 1.3. DSC thermogram for 1,2-bis[*N*-(*N'*-hexylimidazolium-d_2(4,5))]C_2H_4 $2PF_6^-$ displaying three solid-solid phase transitions below T_m (196 °C). Figure reproduced from Lee *et al.*[14,15]

OIPCs have been studied extensively through DSC, which has shown that many classes of OIPCs posses multiple first-order high enthalpy solid-solid phase transitions below T_m (Figure 1.3).[1,13-15,19] DSC measurements can be complemented with IS measurements to better understand ion conduction in the solid phases of OIPCs. By comparing DSC thermograms to IS measurements, it has also been shown that an increase in ion conductivity upon heating is observed at a solid-solid phase transition.[13] Conductivity values (represented as σ with units of S cm^{-1}) on the order of 10^{-3} S cm^{-1} [13,19,30] have been reported for OIPCs, naturally raising the question, why is there an increase in conductivity as a function of temperature? To increase

conductivity as a function of temperature, the diffusivity or concentration of the charge carrying species must increase as well,

$$\sigma = \frac{(D_+ c_+ + D_- c_-)q^2}{kT} \quad , \tag{1.1}$$

where $D_\pm$ is the diffusion coefficient of cation and anion, $c_\pm$ is the concentration of each charge carrying species, q is the electrical charge of a particle, and kT is the average thermal energy.[1,31]

Molecular diffusion within OIPCs is possible due to the nature of defects or dynamics present, such as rotator phases, lattice vacancies, and nm – μm size "domain boundaries" between crystallites. Generally for an OIPC, the higher the conductivity at ambient temperatures, the better the material will perform in applications. However, to be able to design a highly conductive material, one must deeply understand the fundamental interactions that influence translational motions that in turn give rise to conductivity. OIPCs have attracted increasing interest in the past two decades due to conductivity enhancements observed in one or more solid phases, but little knowledge has been gained on how cation and/or anion transport occurs. There are a large number of cation-anion combinations and currently it is impossible to predict which combination will show the best performance. Recent efforts utilize magnetic and thermal treatments to modulate the morphological properties of OIPCs. This gives NMR a unique opportunity to study how transport of ions is influenced by such changes and will be discussed in more detail in Chapter 3.

1.2.2 Polymer Electrolyte Membranes

Polymer electrolyte membranes (PEMs), such as Nafion® (Figure 1.4),[32] have garnered much interest as solid-state electrolytes in fuel cell and battery applications due to their highly desirable ion transport properties.[3,7,9,11,32]

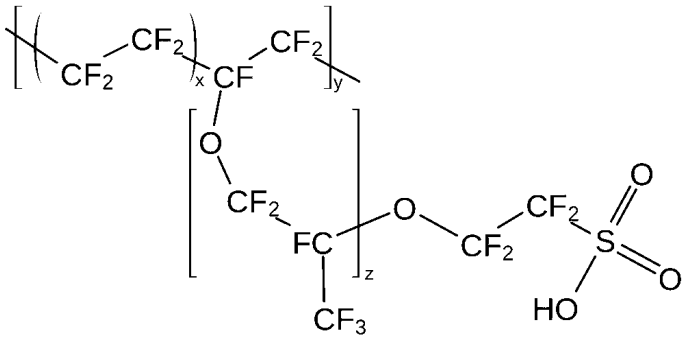

Figure 1.4. Chemical structure of Nafion®, where "x" is in the range of 6 – 7 for commercial membranes and "y" and is unknown due to the monomer being a random copolymer. "z" also shows monomer chain variation.

Nafion® is a tetrafluoroethylene copolymer functionalized with sulfonic acid terminated perfluorovinyl ether along the polymer backbone and is the benchmark PEM. The hydrophobic (yellow) and hydrophilic (blue) portions (Figure 1.5) undergo nanophase separation to produce a distinct morphology consisting of continuous ~ 1 – 2 nm ion-conducting channels lined with sulfonic acid groups that are embedded within a mechanically, thermally, and chemically stable polymer matrix.[32] Thus the transport of small ions, such as H^+, Li^+, and Na^+, and small charged molecules, such as ILs, is possible.[3,7]

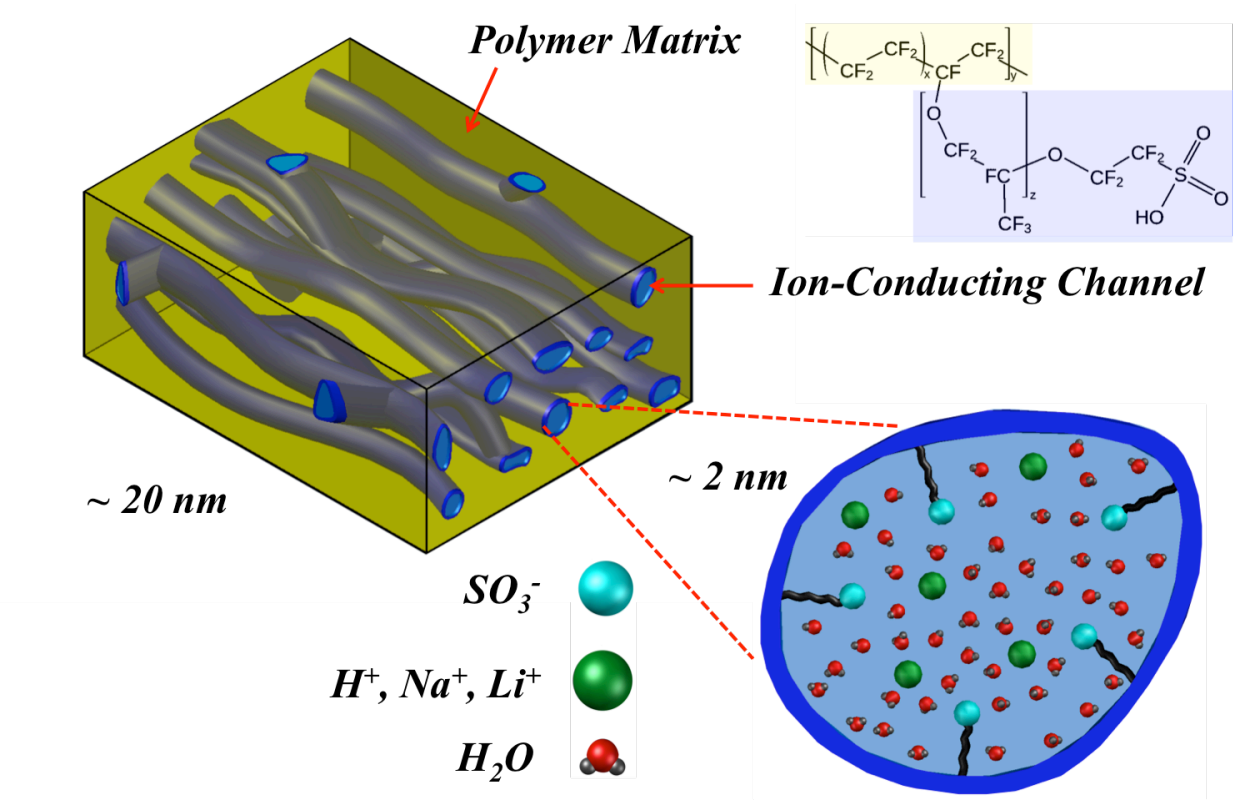

Figure 1.5. Illustration of the hydrophilic (blue) and hydrophobic (yellow) nanophase-separated morphology within Nafion®. The ~ 2 nm ion-conducting channels reside within a mechanically, chemically, and thermally stable polymer matrix.

One of the largest drawbacks to implementing Nafion® is the high cost of perfluorinated membranes (~$2500/kg).[4] Thus, extensive analysis to understand how the multi-scale morphology and transport are coupled can guide design of alternative PEMs that exhibit similar, or superior properties to Nafion®, but at a fraction of the cost. Neutron scattering and small/wide-angle X-ray scattering techniques represent some of the most widely used methods to study material morphology and dynamics.[3,11,32-34] The first X-ray study of hydrated Nafion® by Gierke *et al.* suggested that the nanophase-separated ion-conducting channels were interconnected inverted micelles supported by a polymeric matrix and provides a foundation for beginning to

understand the morphology of Nafion®.[33] Since the original Gierke study, the multi-scale morphology of Nafion® has been heavily debated. One issue that has still yet to be resolved is the local geometry of the hydrophilic ion-conducting channels. Schimdt-Rohr and Chen modeled the nano-morphology over a range of previously reported experimental SAXS patterns, including the original Gierke profile, concluding that parallel rod-like cylinders best represented the nano-morphology of Nafion®.[34] Schmidt-Rohr and Chen's conclusions highly depend on accurate assignment of water volume fractions, as the SAXS ionomer peak shifts with water content. Re-evaluation of Schmidt-Rohr and Chen's data by Kreuer *et al.* suggested a flaw in experimental conditions that caused Schmidt-Rohr and Chen to come to the parallel rod-like cylinder conclusion.[11] Alternatively, Kreuer *et al.* offered their own perspective and modeled their SAXS profiles as "flattened channels" to suggest that the nano-morphology of Nafion® is composed of nm-size "water films" that are flat in geometry.[11] That is, water acts like glue within the hydrophilic channels to aid in self-assembly of the nano-phase separated membrane. While these studies combined offer insights into understanding the geometric nature of the ion-conducting channel, experimental uncertainties associated with such techniques as well as limitations in modeling have raised many questions in defining the nano-morphology of Nafion®.

Application of liquid crystal (LC) theory to ion-conducting materials that exhibit some degree of ordering has yielded new advances in our understanding of how morphological properties influence transport.[3] Using D_2O as a small probe molecule that can be swollen into Nafion®, our group has shown the utility of combining LC theory and NMR spectroscopy to gain new insights into domain structure and ordering within Nafion®.[3,9] However, our group did not observe flattened hydrophilic channels due to the lengthscales (~ 1 – 0.5 μm) that the D_2O reports on, thus averaging out any non-cylindrical information that is obtainable from ^2H NMR

measurements. Alternatively, ^{7}Li and ^{23}Na have stronger interactions with the sulfonate groups and diffuse more slowly and over shorter lengthscales during the experimental timescale. Accessing subtle material features by tailoring the molecule/ion used to probe the PEM internal morphology will be discussed in more detail in Chapter 4.

1.2.3 Polymer-Gel Electrolytes

The use of PGEs has gained tremendous interest due to many attractive qualities, such as high ionic conductivity σ (2 – 15 mS cm^{-1}) over a useful temperature window (-20 to 50 °C) for lithium-ion battery applications.[2,35-40] Current PGEs utilize a polymer host matrix, such as poly(vinylidene fluoride) (PVdF), to act as a mechanical separator between battery electrodes.[38] Coupling the polymer matrix with a lithium salt (such as lithium trifluoromethanesulfonate (LiOTf)) solution composed of cyclic and/or linear polar solvents (such as such as ethylene carbonate (EC) and dimethyl carbonate (DMC)) can give a highly conductive electrolyte.[38]

The issue with using simple polymer and lithium salt solutions is that they lack mechanical stability. Typically a rigid support material is used to prevent an electrical short circuit due to contact of the anode and cathode. Taking advantage of the high ionic conductivity available in solution-based PEO electrolytes and imparting mechanical stability can give a new type of electrolyte that also acts as the separator between anode and cathode. One method to impart such mechanical stability is through electrospinning in conjunction with UV-crosslinking.[2,40] Typically, a polymer solution is forced through a syringe and spinneret (hollow needle) and a large voltage difference between the spinneret and counter electrode fiber collector promotes rapid fiber extrusion and then solvent evaporation to form a fiber mat composed completely of polymer.[2,40] This method offers fine control in creating mechanically stable

fibrous networks that can swell and retain large concentrations of liquid electrolyte for battery separators (Figure 1.6).[2]

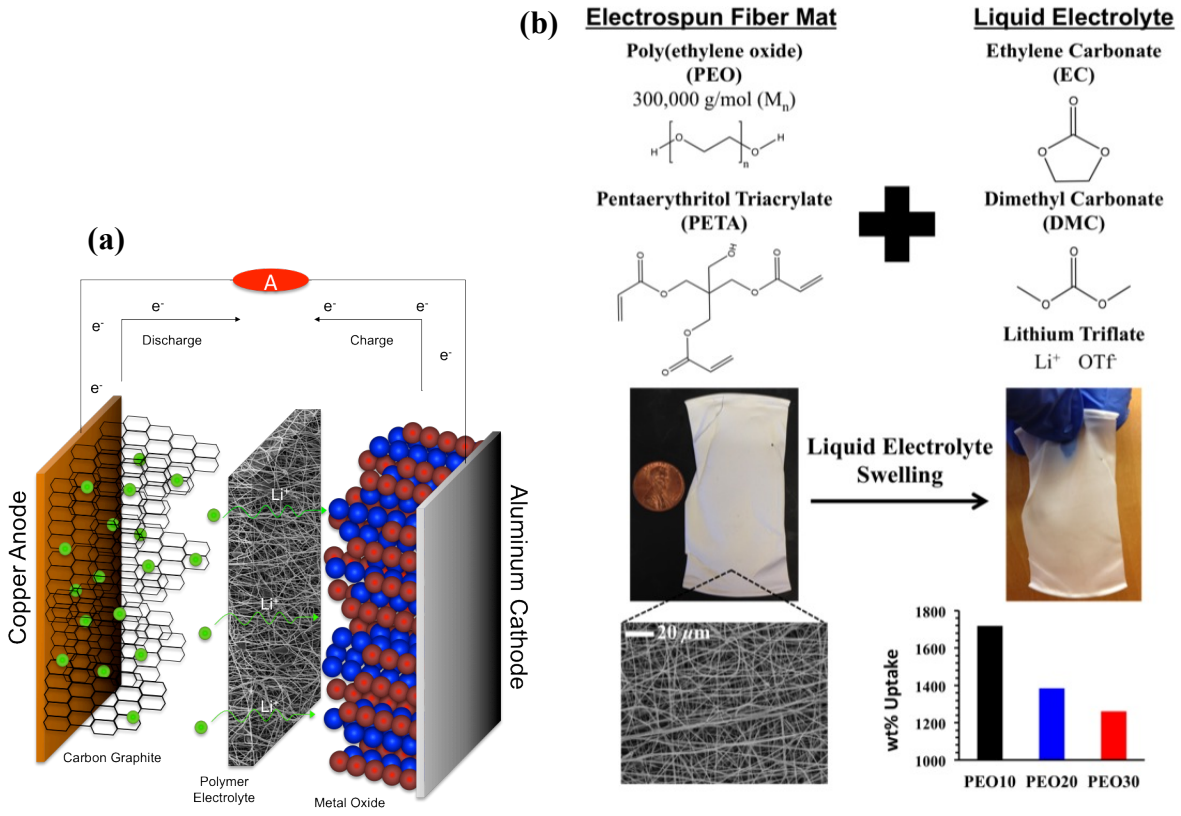

Figure 1.6. Illustration of the components within a lithium-ion battery (a) and a unique PEO-based polymer-gel electrolyte (b). Electrospinning in conjunction with UV-crosslinking can give a mechanically stable support matrix that swells and retains a large concentration (1,200 – 1,700 wt%) of lithium-based liquid electrolyte.[2]

Imparting mechanical stability through crosslinked fibers can create μm-length scale morphological features that can influence transport within such materials. NMR diffusometry measurements allow modulation of the diffusion time (ms – s); thus a range of length scales (250 nm – 3 μm) are accessible and offer a more in-depth analysis of such materials.[1,2,5,41-43] Moreover, NMR relaxation studies can determine the relative fractions of ions within chemically

distinct environments (within and between fibers) and how these fractions are influenced by modulation in morphology.[2] NMR methods to study PGEs will be discussed in more detail in Chapter 5.

1.3 Introduction to Block Copolymer Micelles as Drug-Delivery Vehicles

The largest problems facing the pharmaceutical industry are bioavailability of a given drug and site-specific toxicity.[44,45] Common drugs are bulky and hydrophobic, thus requiring an overdose for the human body to retain therapeutic levels. Much research has been devoted to designing block copolymer micelles as drug-delivery vehicles by loading the hydrophobic drug into the core of a micelle for targeted delivery through intravenous injection.[44,45] More recently, this class of micelles has been highlighted as candidates for "nanoreactors" to replace synthetic routes that use large quantities of harmful or expensive solvents.[46]

Different micellar morphologies, such as wormlike micelles, lamellae, spherical micelles, and vesicles are attainable through careful unimer and solvent system design.[47] Such morphologies are governed by polymer molecular weight, chain composition, concentration of polymer, and solvent-polymer intermolecular interactions.[48,49] Design of self-assembled copolymer micelles for drug-delivery applications begins with hydrophobic and hydrophilic blocks that form a core-shell nanostructure highly stable in H_2O (Figure 1.7).[44]

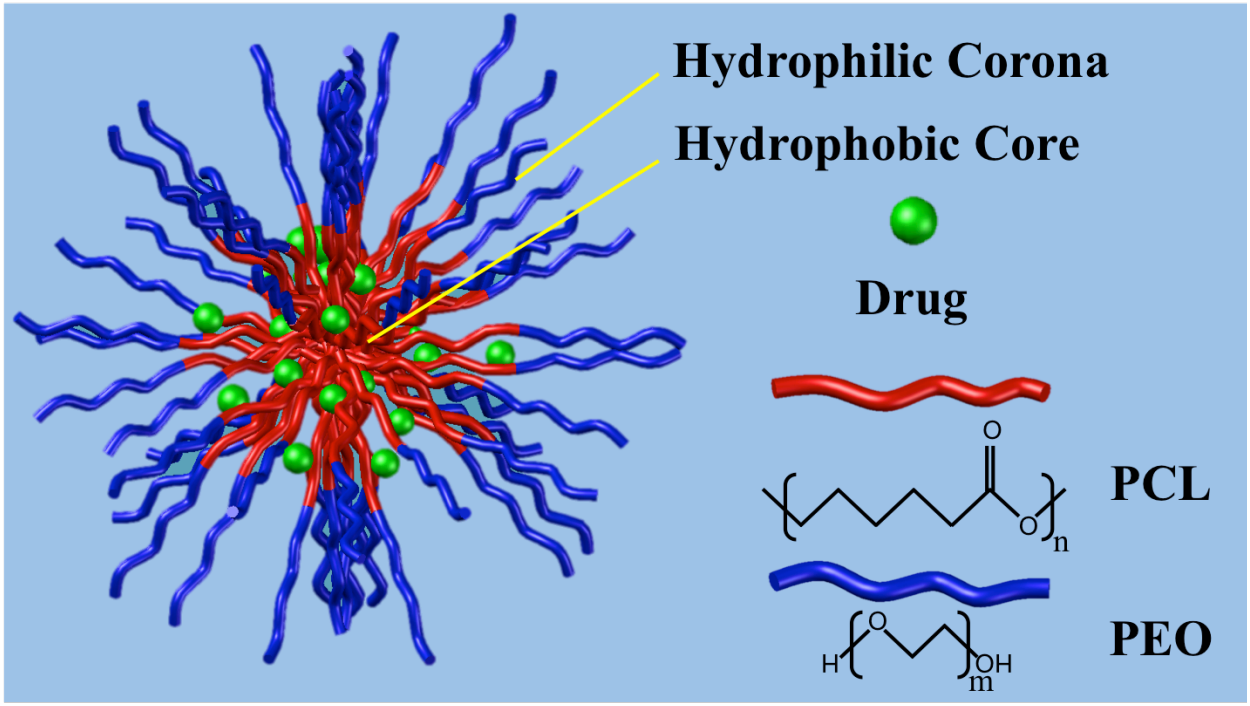

Figure 1.7. Illustration of a spherical block copolymer micelle. Careful tailoring of the poly(ethylene oxide) (PEO) and polycaprolactone (PCL) block lengths can give a surfactant that self-assembles into spherical micelles. Such morphologies are gaining interest as drug-delivery vehicles, wherein the hydrophobic core retains the drug for targeted delivery.

Maximizing the micelle core "micro-reservoir" drug-loading capacity is dependent on the core size and specific molecular interactions between drug and polymer within the core. A micelle size no larger than ~ 50 nm is necessary for penetration through the tumor wall as well as to survive microfiltration sterilization in cancer treatment applications.[44] It is imperative that the micelle retains structure upon introduction into the human body, as various degradation pathways (enzymatic and non-enzymatic) can eliminate the drug-carrying micelles. Thus, the ability to tune self-assembly and drug-loading capacity of micelles holds powerful potential in developing next generation drug delivery vehicles.[44] Understanding unimer and micelle

dynamics as well as drug cargo capacity and delivery properties will aid in design of block copolymer micelles.

For drug-delivery applications, triggered release (through pH, UV-Vis, etc.) of the drug from the hydrophobic core is desirable.[50] Thus, fundamental understanding of unimer and micelle dynamics is needed in order to optimize such systems. Unimer exchange phenomena (Figure 1.8), such as insertion/expulsion (part a) and fusion/fission (part b), depend strongly on block chemistry, solvent type, and other molecules in solution.[51,52] We seek to understand and quantify such properties via new NMR methods.

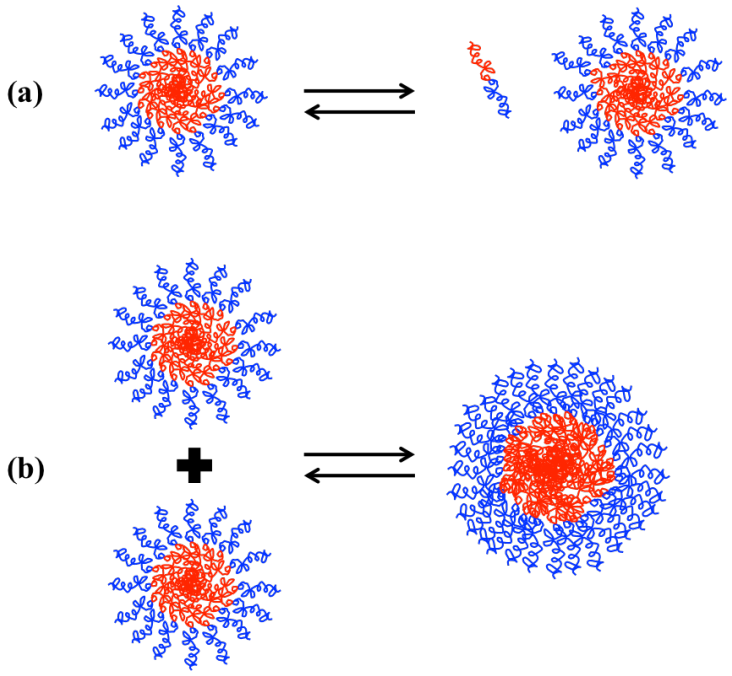

Figure 1.8. Insertion/expulsion (a) and fusion/fission (b) of unimers and micelles, respectively, are the two dominant unimer exchange mechanisms between polymeric micelles.

Dynamic light scattering (DLS) and small angle neutron scattering (SANS) are commonly used to characterize block copolymer micelles.[44,53,54] DLS can give information on micelle size and shape distributions, but lacks chemically specific information.[44] SANS can yield core and corona

sizes as well as unimer exchange kinetics through time-resolved contrast-matching experiments, but requires a ~ $1 billion instrument and provides very limited instrument time.[53-55] Thus, a technique that affords more accessible and robust characterization methods will accelerate development of design strategies for polymeric micelles. In Chapters 6 and 7, we present complementary NMR analysis of PEO-PCL spherical micelles, in which we probe equilibrium and non-equilibrium dynamics with chemical specificity across a range of time scales within these systems. These methods help to overcome the barriers raised by time- and resource-exhaustive analytical techniques, while also providing a larger breadth of information.

1.4 Introduction to Molecular Diffusion and Restricted Diffusion

The aforementioned systems highly depend on transport and dynamics across a wide range of time and length scales. One way to describe diffusion is through Fick's laws, whereby a negative concentration gradient drives particles from a high concentration to a low concentration region until equilibrium.[56] Holding true for non-equilibrium systems, Fick's laws are insufficient to describe the diffusion of a homogenous system in the absence of a concentration gradient, where the main driving force for diffusion is the average thermal kinetic energy, quantified by kT. During the diffusion process, a given particle receives "thermal kicks" from neighboring particles, thus resulting in a "random walk." The random walk of a particle is a well-known phenomenon that was discovered by Robert Brown and is fundamental to all chemistry. Commonly referred to as "Brownian motion," it describes the random translational mobility of any molecular species throughout a given environment.[56]

A simple illustration of Brownian motion is shown in Figure 1.9. Equation 1.2 describes the root mean square displacement $\langle r \rangle$ of a particle diffusing in a 3-D system (x, y, and z-coordinates), where D is the diffusion coefficient and t is the diffusion time.

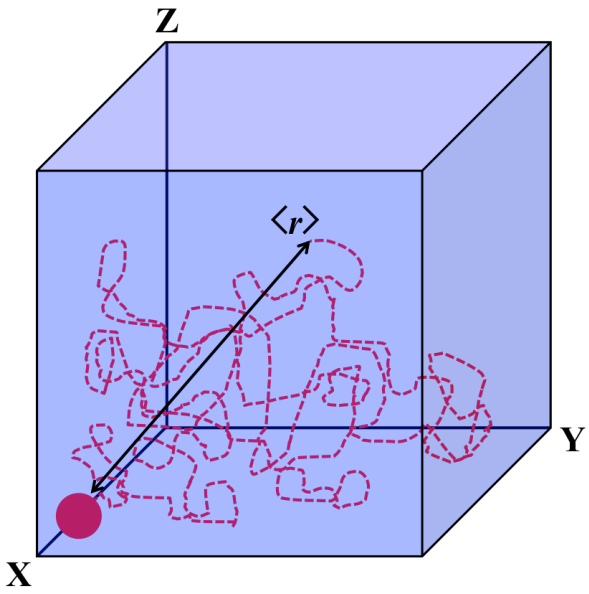

Figure 1.9. Illustration of the Brownian motion a particle (red) experiences due to the thermal "kicks" the particle receives from neighboring particles. The experimentally measured diffusion coefficient D depends on the average displacement of the particle as a function of time t.

$$\langle r \rangle = \sqrt{6Dt} \tag{1.2}$$

The diffusion of particles will depend not only on kT, but also on the local environment (the number of degrees of freedom and potential energy landscape) available to the diffusive species. We can think of the random walk, for a single particle, being governed by thermal kicks that particle receives from neighboring particles as it diffuses through the system (undergoing a random walk), which depends on the potential and kinetic energy of each individual particle in

the system. kT and diffusion are tightly correlated, and one cannot consider diffusion without considering kT.

In conjunction with Brown's observations, Einstein[57,58] proposed that the self-diffusion coefficient of a spherical particle in an infinitely dilute environment could be described by (Equation 1.3):[56,58]

$$D = \frac{kT}{f} \quad , \tag{1.3}$$

where f is referred to as the frictional coefficient. Stokes later proposed that the frictional coefficient for a spherical particle with radius r_H (commonly known as the hydrodynamic radius) in an environment with viscosity η could be described by (Equation 1.4):[56,58]

$$f = 6\pi\eta r_H \quad , \tag{1.4}$$

which led to the well-known Stokes-Einstein equation (Equation 1.5):[56,58]

$$D = \frac{kT}{6\pi\eta r_H} \quad . \tag{1.5}$$

Thus a fundamental approach to understand the relationship between the self-diffusion coefficient of a diffusing species and the intrinsic properties of the environment encompassing the diffusing species was formulated. We see that the diffusion coefficient is inversely proportional to the product of the viscosity η of the material and hydrodynamic radius r_H of the diffusing species.

1.4.1 Diffusion Within Polycrystalline Materials

With the ultimate goal of understanding the mechanism for ion transport in the aforementioned organic ion conducting materials, we start with how ion transport on the nm-length scale in a well-ordered material (ionic solid) occurs. For ion transport to occur within an

ionic solid, defects (in the form of lattice vacancies) must be present.[59] One type of lattice disorder that is commonly present in ionic solids is Schottky disorder,[59,60] as seen in Figure 1.10.[61]

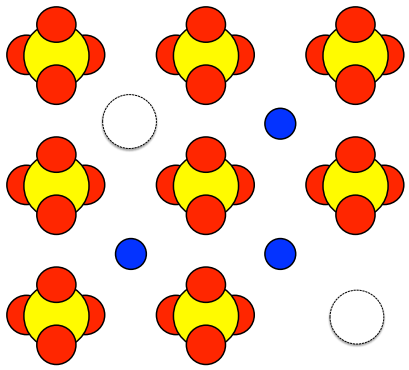

Figure 1.10. Illustration of Schottky disorder. Schottky disorder is defined as a cation-anion pair missing from the crystallite, thus conserving charge neutrality. Figure adapted from MacFarlane *et al.*[61]

Schottky disorder is classified as a cation and anion missing from the crystalline lattice and thus contributes to the overall short-range disorder present in an ionic material.[60] With each ion missing, the counterion will be missing as well to conserve charge neutrality of the crystallite.[60] Vacancies in an ionic solid can facilitate translational motion of ions, which can strongly impact ion conduction. Other relevant factors, such as vacancy size, critical volume (minimal volume needed to allow translational and/or rotational mobility of the ion),[62] and ion size also influence ion transport, which are all dependent on the cation-anion pair. In the presence of Schottky disorder, ion transport can occur through an "ion hopping" mechanism.

Extending our view from ion transport on the nm scale to ion transport on the μm scale in a polycrystalline material, another possible ion transport pathway is through grain boundaries

(sometimes referred to as domain boundaries).[1,60] The grain boundary naturally occurs for polycrystalline materials and originates from the mismatch of crystallites upon nucleation from the melt (Figures 1.11a,b, and c) and through the coalescence of vacancies upon heating.[60] In the literature, the grain boundary is sometimes referred to as an extended network of vacancies/defects.[28]

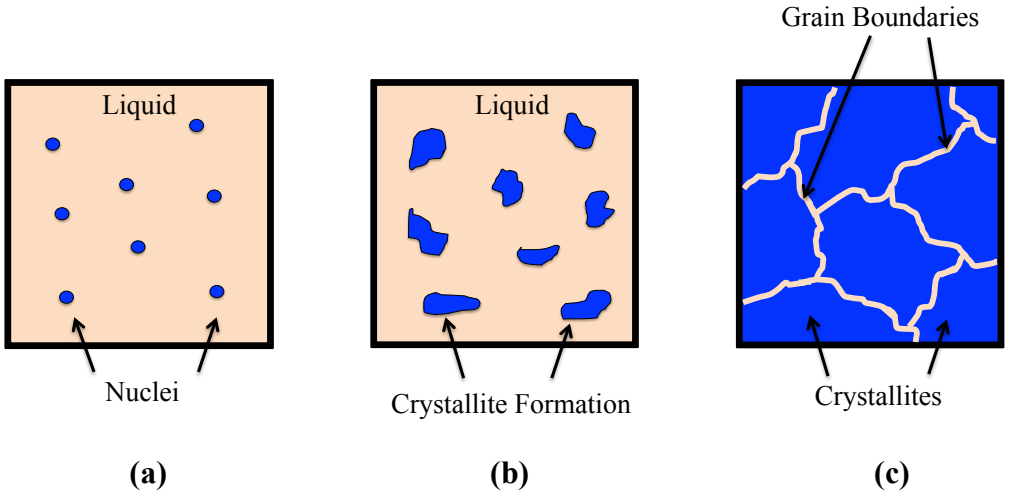

Figure 1.11. A polycrystalline material forms from nuclei in a liquid cooled below the crystallization temperature (a), which propagate to form larger crystallites (b). Finally, due to the mismatch of crystallite lattices, nanometer to micron-scale grain boundaries form (c).

1.4.2 Diffusion Within Soft Materials

Nanometer length scale diffusion within solvent-swollen polymeric materials is not as well-defined as for even a polycrystalline ionic solid. Unlike ionic polycrystalline materials, ion transport within nanophase-separated materials such as Nafion®, cannot be well-described by a lattice vacancy jump model, as such materials are not nearly as ordered on the nm-length scale. Different transport mechanisms can dominate ion conduction depending on the degree of hydration within the PEM Nafion®. For instance, at high hydration levels, rotational and

translational degrees of freedom of H_2O allow short time scale (~ 1 ps) exchange of H^+ between neighboring H_2O molecules, hydronium ions (H_3O^+), and the hydrophilic channel-lined SO_3^- groups. This type of transport mechanism is commonly known as Grotthuss hopping (Figure 1.12).[63] At lower hydration levels within a PEM, a "vehicular" mechanism dominates conduction.[64] That is, a reduction in the density of H_2O molecules disrupts the hydrogen-bonding network such that ions diffuse predominantly along with H_2O molecules.

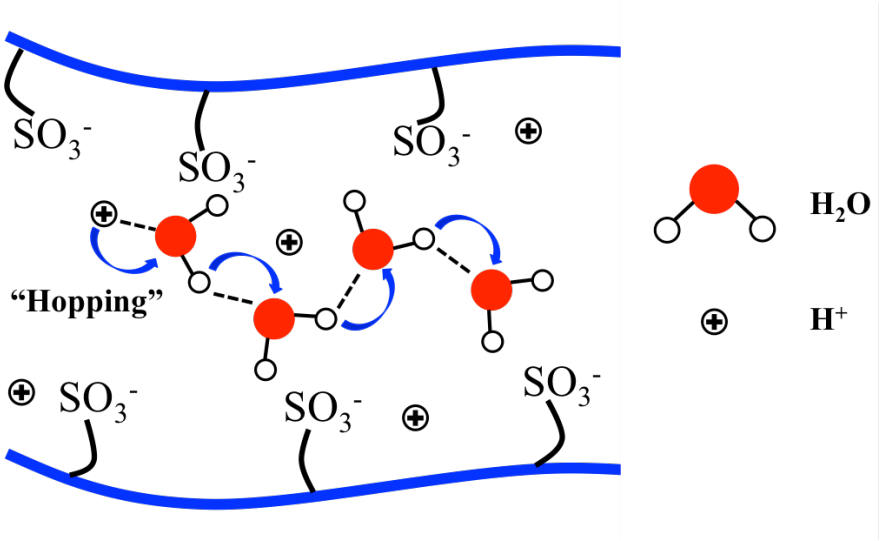

Figure 1.12. Grotthuss hopping mechanism. At high hydration levels within PEMs, ions conduct through the hydrophilic channels during short time scale (~ 1 ps) exchange between neighboring H_2O molecules, H_3O^+, and SO_3^-.

1.4.3 Restricted Diffusion

Application-specific performance of OIPCs, PGEs, and PEMs highly depends on bulk diffusion of ions or other small molecules across the plane of a membrane or film that is typically micrometers thick. Figure 1.11c shows 50 – 500 nm bulk domains (blue) wherein transport can take place between domains. When describing transport within heterogeneous materials, we need to consider how such morphological domains can influence the measured

diffusion coefficient. Equation 1.2 tells us that the diffusion coefficient of a particle will be independent of the diffusion time within unrestrictive environments (an isotropic liquid such as bulk H_2O). However, for a particle within a restrictive environment, the diffusion coefficient will be independent of the diffusion time until the particle diffuses far enough to sample the domain that restricts its motion, such that a reduction in the diffusion coefficient is seen at longer diffusion probing times.[1,2,5,41-43] This allows a restricted diffusion method to directly probe the size of such domains in which the particles exist by: 1) measuring the diffusion coefficient as a function of diffusion probing time (Δ, discussed in more detail in Chapter 2), 2) modulating the diffusion coefficient by changing the probe molecule size, and/or 3) modulating the diffusion coefficient by changing solvent uptake (if applicable). Figure 1.13 illustrates unrestricted and restricted diffusion of a particle.

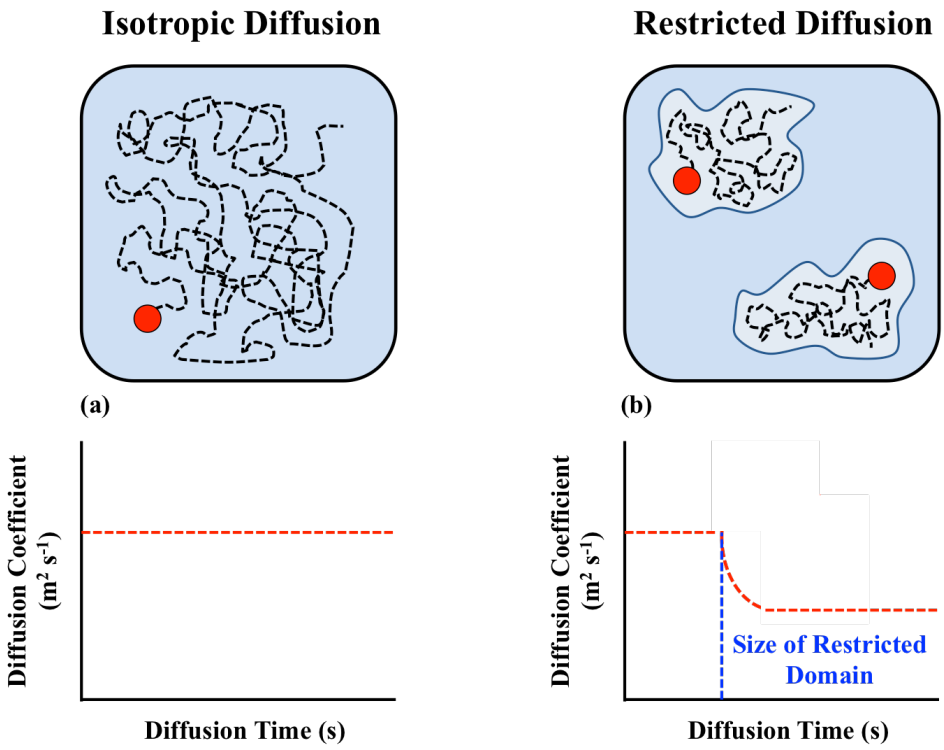

Figure 1.13. Illustration of unrestricted (a) and restricted diffusion (b) of a particle. The diffusion coefficient is independent of the diffusion time when a particle experiences free diffusion, such as in bulk liquid H_2O. For a particle within a restrictive environment, a reduction in diffusion coefficient can be seen once the particle begins to collide with the environmental boundaries.

Many researchers have shown that the diffusion coefficient is a very powerful tool with which to gauge the performance of a material.[1-5,7-10] While a given morphology can influence bulk transport and this can be probed using *variable diffusion time measurements*, sub-nm local molecular interactions also influence transport and this can help inform the design of new materials. The next section shows how *variable temperature* diffusion measurements allow extraction of the so-called translational activation energy and how we can use this quantity to dissect different contributions to the diffusion process within a given material.

1.5 Physical Meaning of Diffusive Activation Energy in Materials

The diffusion coefficient clearly contains rich information about the molecular environment surrounding the diffusing species. Measuring diffusion as a function of temperature allows one to extract the translational activation energy E_a for a given system, as described by the Arrhenius equation,

$$D(T) = D_0 e^{\frac{-E_a}{RT}}, \tag{1.6}$$

where $D(T)$ is the temperature-dependent diffusion coefficient, D_0 is the pre-exponential factor (diffusion coefficient at infinite temperature), and R is the gas constant.[1,2,10,65-68] Classically, E_a for a diffusing species is described as the minimum amount of energy needed for that species to jump from one lattice position to another ("ion hopping") through the crystalline lattice, providing there is a vacancy for the diffusing species to occupy. Figure 1.14 is an illustration of jump diffusion in an ionic solid in which the cations (blue) are representative of a small ion, such as Li^+, while the anions (red/yellow) are representative of a tetrahedral species, such as SO_4^{2-}.

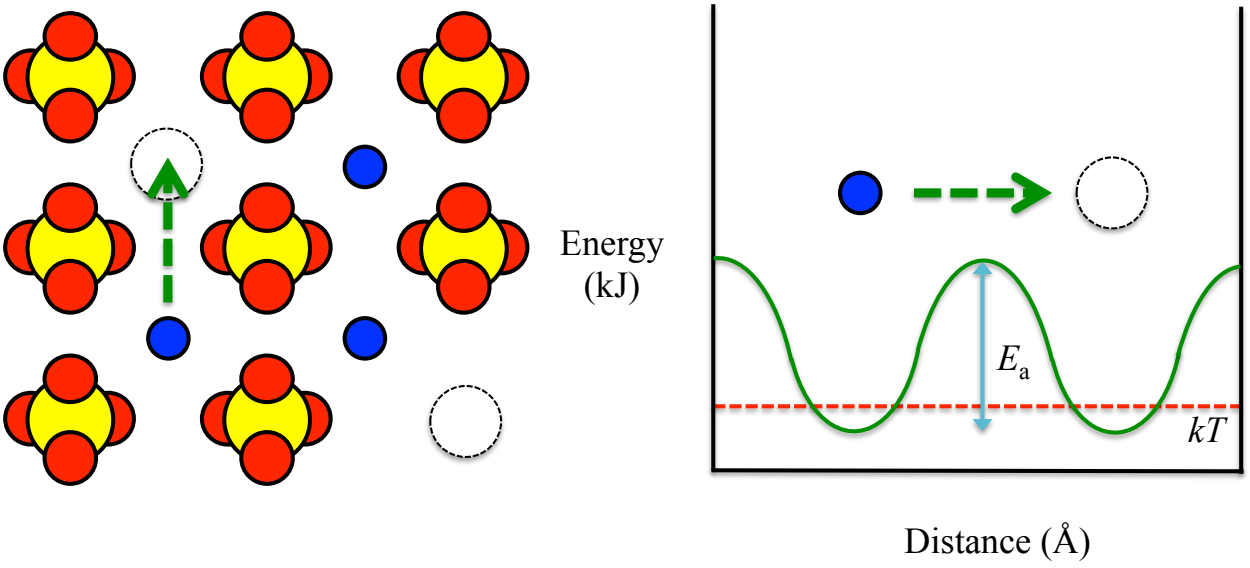

Figure 1.14. Extension of Figure 1.10 allows us to illustrate an ionic compound, such as Li_2SO_4, where the cation (blue) "jumps" from one lattice position to another past the anions (yellow/red) over some potential barrier that can be reflected in E_a.

Defining the length and time scale that the translational E_a reports on within a liquid or liquid-swollen material is not as easy as in crystallites. We can begin to understand translational E_a within such systems by describing translational motion of a particle "frozen" in place within a local energy minimum, as determined by local intermolecular interactions surrounding the particle. If the particle becomes "unfrozen," there is a finite transient "pre-diffusion" correlation time, t (or τ_c), that is proportional to the distance traversed $\langle r(t) \rangle_{pre\text{-}diffusion}$ by the particle (Figure 1.15).[1,2,10,69]

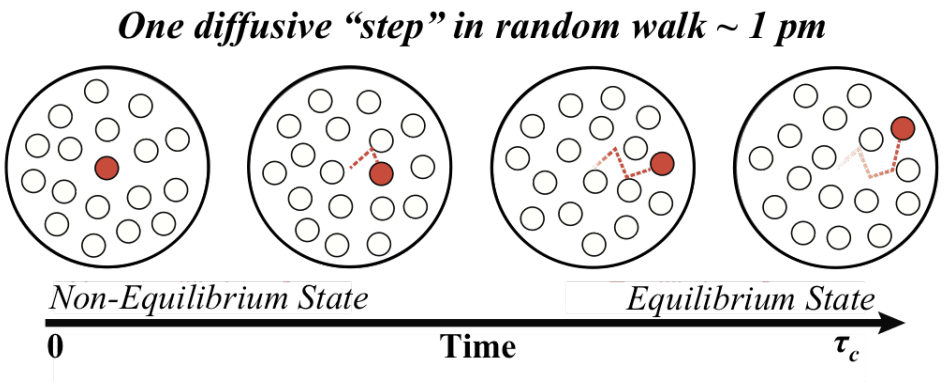

Figure 1.15. Illustration of a particle (red) that is initially (time = 0) "frozen" within an energy minimum, as determined by local intermolecular interactions. Upon "unfreezing" the particle (time > 0), the particle experiences random collisions and loses memory of its initial velocity at some correlation time (τ_c).[10]

At short pre-diffusion times, a slower region exists wherein the particle moves within its local energy minimum. At long pre-diffusion times, a faster region exists wherein the particle experiences short steps (~ 1 pm) due to random collisions with adjacent particles. Beyond the pre-diffusion time regime, the particle translates diffusively, as described above and illustrated in Figure 1.9. Hence, the pre-diffusion and diffusion time scales are commonly used to denote different regimes for which ions and/or molecules translate (Figure 1.16).

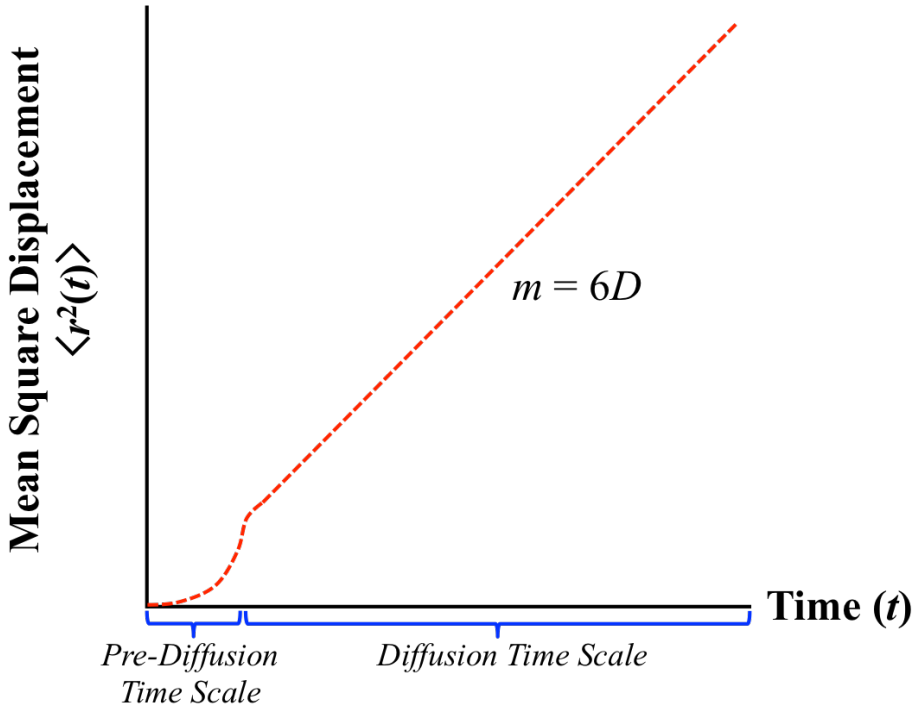

Figure 1.16. Illustration of the mean-square displacement $\langle r^2(t) \rangle$ as a function of time t. Two time regions are shown to separate the "pre-diffusion" and "diffusion" time scales, as discussed above. Note that the translated distance is linear with time (slope $m = 6D$) in the diffusive time regime.[69]

Experimentally, measuring translational motion on the pre-diffusion time scale (~ 1 ps) is currently out of range for conventional NMR diffusometry, which can currently only measure diffusion coefficients on ms – s time scales and over 100 nm – 10 μm length scales. However, our group has begun to utilize Arrhenius studies to infer what intermolecular interactions influence a given E_a value, thus giving insight into time and length scales associated with the extracted E_a value.[1,2,10]

As previously discussed, understanding what morphological and molecular features influence transport within ion-dense systems will give materials scientists new insights to

rationally design such systems. Recently, our group set out to understand what chemical features within the nm-size hydrophilic channel of Nafion® contribute to H_2O E_a as a function of hydration level (commonly referred to as λ, which in the case of Nafion® is the molar ratio H_2O:SO_3^-).[10] Arrhenius studies of H_2O within Nafion® show that at high hydration levels (λ = 8 to 15) the E_a value is nearly equivalent to E_a of H_2O in pure bulk H_2O (Figure 1.17). Moreover, H_2O E_a is independent of λ for λ > 8, implying that at high hydration H_2O within the channels is not influenced by the channel walls and experiences liquid-like local interactions.[10]

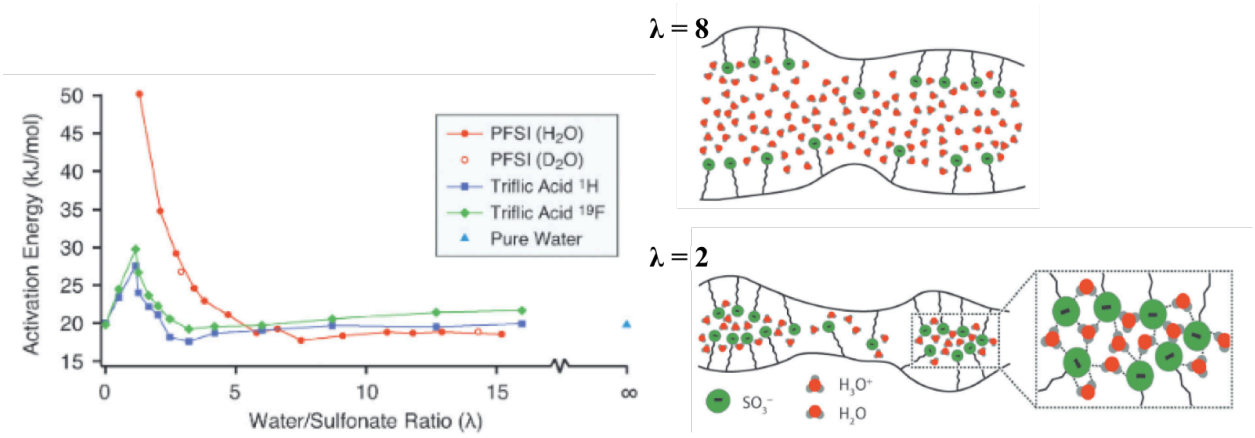

Figure 1.17. Activation energy (E_a) of H_2O within Nafion® and in triflic acid solutions as a function of hydration level (λ = molar ratio of H_2O:SO_3^-).[10] Reproduced from Ref 10 with permission of The Royal Society of Chemistry.

Decreasing the hydration level within Nafion® to below λ = 8 shows an exponential-like increase in E_a to a value of 50 kJ mol^{-1} at λ ≈ 2. To mimic the local interactions H_2O experiences within the SO_3^--lined channel, E_a measurements of H_2O in solutions of trifluoromethanesulfonic (triflic) acid show a striking resemblance to the dependence of H_2O E_a within Nafion®. Interestingly, while H_2O E_a within Nafion® and in solutions are nearly identical, the diffusion coefficients are quite different (Figure 1.18).[10]

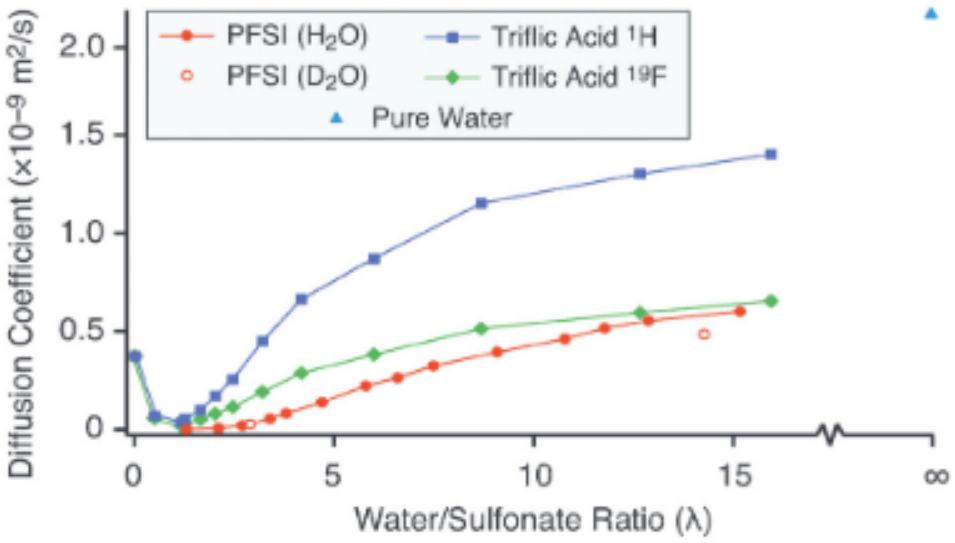

Figure 1.18. Diffusion coefficients of H_2O within Nafion® (PFSI) are 3× slower than in solution even though the measured E_a values are nearly identical (Figure 1.17).[10] Reproduced from Ref 10 with permission of The Royal Society of Chemistry.

Tightly correlated with D and E_a, D_0 is commonly termed the "pre-exponential factor" or "diffusion at infinite temperature" and traditionally gives insight into the local structure governing both D and E_a. However, the offset along the y-axis of an Arrhenius plot can give us deeper insight into how D_0 may contain new information about how material morphology, transport, and local interactions are connected and potentially separable.[2] Chapters 3 and 5 will describe how, in a material system with restrictions to diffusion on scales larger than > 1 nm, that a small D accompanied by a small E_a is possible due to the morphological properties of the surrounding system and how they influence the diffusing species.[1,2,10]

1.6 Concluding Remarks

Detailed understanding of multiscale transport and dynamics is necessary for future developments of novel materials for a range of applications. Chapter 2 will focus on theory and methods of NMR as applied to soft materials, as the following studies were conducted with an emphasis on novel NMR investigations. In conjunction with theory and current literature, Chapters 3, 4, 5, 6, and 7 present new and unique results across a range of soft materials systems as well as discuss how NMR can be used as a versatile and potent tool to understand such systems.

1.7 References

(1) Kidd, B. E.; Lingwood, M. D.; Lee, M.; Gibson, H. W.; Madsen, L. A. Cation and Anion Transport in a Dicationic Imidazolium-Based Plastic Crystal Ion Conductor. *J. Phys. Chem. B* **2014**, *118*, 2176.

(2) Kidd, B. E.; Forbey, S. J.; Steuber, F. W.; Moore, R. B.; Madsen, L. A. Multiscale Lithium and Counterion Transport in an Electrospun Polymer-Gel Electrolyte. *Macromolecules* **2015**, *48*, 4481.

(3) Li, J.; Park, J. K.; Moore, R. B.; Madsen, L. A. Linear coupling of alignment with transport in a polymer electrolyte membrane. *Nat. Mater.* **2011**, *10*, 507.

(4) Hou, J.; Li, J.; Madsen, L. A. Anisotropy and Transport in Poly(arylene ether sulfone) Hydrophilic−Hydrophobic Block Copolymers. *Macromolecules* **2010**, *43*, 347.

(5) Hou, J.; Li, J.; Mountz, D.; Hull, M.; Madsen, L. A. Correlating morphology, proton conductivity, and water transport in polyelectrolyte-fluoropolymer blend membranes. *J. Membr. Sci.* **2013**, *448*, 292.

(6) Hou, J.; Madsen, L. A. New insights for accurate chemically specific measurements of slow diffusing molecules. *J. Chem. Phys.* **2013**, *138*.

(7) Hou, J.; Zhang, Z.; Madsen, L. A. Cation/anion associations in ionic liquids modulated by hydration and ionic medium. *J. Phys. Chem. B* **2011**, *115*, 4576.

(8) Li, J.; Wilmsmeyer, K. G.; Hou, J.; Madsen, L. A. The role of water in transport of ionic liquids in polymeric artificial muscle actuators. *Soft Matter* **2009**, *5*, 2596.

(9) Li, J.; Wilmsmeyer, K. G.; Madsen, L. A. Anisotropic Diffusion and Morphology in Perfluorosulfonate Ionomers Investigated by NMR. *Macromolecules* **2009**, *42*, 255.

(10) Lingwood, M. D.; Zhang, Z.; Kidd, B. E.; McCreary, K. B.; Hou, J.; Madsen, L. A. Unraveling the local energetics of transport in a polymer ion conductor. *Chem. Commun.* **2013**, *49(39)*, 4283.

(11) Kreuer, K. D.; Portale, G. A Critical Revision of the Nano-Morphology of Proton Conducting Ionomers and Polyelectrolytes for Fuel Cell Applications. *Adv. Funct. Mater.* **2013**, *23*, 5390.

(12) Andújar, J. M.; Segura, F. Fuel cells: History and updating. A walk along two centuries. *Renew. Sust. Energ. Rev.* **2009**, *13*, 2309.
(13) Pringle, J. M.; Howlett, P. C.; MacFarlane, D. R.; Forsyth, M. Organic ionic plastic crystals: recent advances. *J. Mater. Chem.* **2010**, *20*, 2056.
(14) Lee, M.; Choi, U. H.; Wi, S.; Slebodnick, C.; Colby, R. H.; Gibson, H. W. 1,2-Bis[N-(N '-alkylimidazolium)]ethane salts: a new class of organic ionic plastic crystals. *J. Mater. Chem.* **2011**, *21*, 12280.
(15) Lee, M.; Niu, Z.; Slebodnick, C.; Gibson, H. W. Structure and Properties of N,N-Alkylene Bis(N '-Alkylimidazolium) Salts. *J. Phys. Chem. B* **2010**, *114*, 7312.
(16) Yu, G. R.; Zhao, D. C.; Wen, L.; Yang, S. D.; Chen, X. C. Viscosity of ionic liquids: Database, observation, and quantitative structure-property relationship analysis. *Aiche J.* **2012**, *58*, 2885.
(17) Timmermans, J. Plastic Crystals: A Historical Review. *J. Phys. Chem. Solids* **1961**, *18*, 1.
(18) Pringle, J. M.; Shekibi, Y.; MacFarlane, D. R.; Forsyth, M. The influence of different nanoparticles on a range of organic ionic plastic crystals. *Electrochim. Acta* **2010**, *55*, 8847.
(19) Pringle, J. M. Recent progress in the development and use of organic ionic plastic crystal electrolytes. *Phys. Chem. Chem. Phys.* **2013**, *15*, 1339.
(20) Howlett, P. C.; Sunarso, J.; Shekibi, Y.; Wasser, E.; Jin, L. Y.; MacFarlane, D. R.; Forsyth, M. On the use of organic ionic plastic crystals in all solid-state lithium metal batteries. *Solid State Ionics* **2011**, *204*, 73.
(21) Forsyth, S. A.; Fraser, K. J.; Howlett, P. C.; MacFarlane, D. R.; Forsyth, M. N-methyl-N-alkylpyrrolidinium nonafluoro-1-butanesulfonate salts: Ionic liquid properties and plastic crystal behaviour. *Green Chemistry* **2006**, *8*, 256.
(22) Adebahr, J.; Forsyth, M.; MacFarlane, D. R. Cation dynamics in dimethyl-pyrrolidinium-based solid-state ion conductors. *Electrochim. Acta* **2005**, *50*, 3853.
(23) Adebahr, J.; Grirnsley, M.; Rocher, N. M.; MacFarlane, D. R.; Forsyth, M. Rotational and translational mobility of a highly plastic salt: Dimethylpyrrolidinium thiocyanate. *Solid State Ionics* **2008**, *178*, 1798.
(24) Adebahr, J.; Johansson, P.; Jacobsson, P.; MacFarlane, D. R.; Forsyth, M. Ab initio calculations, Raman and NMR investigation of the plastic crystal di-methyl pyrrolidinium iodide. *Electrochim. Acta* **2003**, *48*, 2283.
(25) Adebahr, J.; Seeber, A. J.; MacFarlane, D. R.; Forsyth, M. LiI-doped N,N-dimethyl-pyrrolidinium iodide, an archetypal rotator-phase ionic conductor. *J. Phys. Chem. B* **2005**, *109*, 20087.
(26) Efthimiadis, J.; Forsyth, M.; MacFarlane, D. R. A surface characterisation and microstructural study by Scanning Electron Microscopy of the N-methyl-N-alkylpyrrolidinium tetrafluoroborate organic salts. *Journal of Materials Science* **2003**, *38*, 3293.
(27) Efthimiadis, J.; Pas, S. J.; Forsyth, M.; MacFarlane, D. R. Structure and transport properties in an N,N-substituted pyrrolidinium tetrafluoroborate plastic crystal system. *Solid State Ionics* **2002**, *154*, 279.
(28) Every, H. A.; Bishop, A. G.; MacFarlane, D. R.; Oradd, G.; Forsyth, M. Room temperature fast-ion conduction in imidazolium halide salts. *J. Mater. Chem.* **2001**, *11*, 3031.

(29) Ferry, A.; Edman, L.; Forsyth, M.; MacFarlane, D. R.; Sun, J. Z. NMR and Raman studies of a novel fast-ion-conducting polymer-in-salt electrolyte based on LiCF3SO3 and PAN. *Electrochim. Acta* **2000**, *45*, 1237.
(30) Jin, L. Y.; Nairn, K. M.; Forsyth, C. M.; Seeber, A. J.; MacFarlane, D. R.; Howlett, P. C.; Forsyth, M.; Pringle, J. M. Structure and Transport Properties of a Plastic Crystal Ion Conductor: Diethyl(methyl)(isobutyl)phosphonium Hexafluorophosphate. *J. Am. Chem. Soc.* **2012**, *134*, 9688.
(31) Zhang, Z.; Madsen, L. A. Observation of separate cation and anion electrophoretic mobilities in pure ionic liquids. *J. Chem. Phys.* **2014**, *140*.
(32) Mauritz, K. A.; Moore, R. B. State of understanding of Nafion. *Chem. Rev.* **2004**, *104*, 4535.
(33) Gierke, T. D.; Munn, G. E.; Wilson, F. C. The Morphology in Nafion Perfluorinated Membrane Products, as Determined by Wide-Angle and Small-Angle X-Ray Studies. *J. Polym. Sci.* **1981**, *19*, 1687.
(34) Schmidt-Rohr, K.; Chen, Q. Parallel cylindrical water nanochannels in Nafion fuel-cell membranes. *Nat Mater* **2008**, *7*, 75.
(35) Choi, S. W.; Jo, S. M.; Lee, W. S.; Kim, Y. R. An electrospun poly(vinylidene fluoride) nanofibrous membrane and its battery applications. *Adv. Mater.* **2003**, *15*, 2027.
(36) Tarascon, J. M.; Armand, M. Issues and challenges facing rechargeable lithium batteries. *Nature* **2001**, *414*, 359.
(37) MacGlashan, G. S.; Andreev, Y. G.; Bruce, P. G. Structure of the polymer electrolyte poly(ethylene oxide)(6): LiAsF6. *Nature* **1999**, *398*, 792.
(38) *Principles and Applications of Lithium Secondary Batteries*; Wiley: Germany, 2012; Vol. 1.
(39) *Lithium Ion Rechargeable Batteries: Materials, Technology, and New Applications*; Wiley: Germany, 2009; Vol. 1.
(40) Forbey, S. J.; Divoux, G. M.; Moore, K. E.; Moore, R. B. Cross-Linked Electrospun Poly(ethylene oxide) Fiber Mats as Structured Polymer-Gel Electrolytes. *Transactions of the Electrochemical Society* **2016**, *(Submitted)*.
(41) Callaghan, P. T. *Translational Dynamics and Magnetic Resonance: Principles of Pulsed Gradient Spin Echo NMR*; Oxford University Press: New York, 2011.
(42) Callaghan, P. T.; Coy, A.; Macgowan, D.; Packer, K. J.; Zelaya, F. O. Diffraction-Like Effects in Nmr Diffusion Studies of Fluids in Porous Solids. *Nature* **1991**, *351*, 467.
(43) Mitra, P. P.; Sen, P. N.; Schwartz, L. M.; Ledoussal, P. Diffusion Propagator as a Probe of the Structure of Porous-Media. *Phys. Rev. Lett.* **1992**, *68*, 3555.
(44) Kataoka, K.; Harada, A.; Nagasaki, Y. Block copolymer micelles for drug delivery: Design, characterization and biological significance. *Adv. Drug. Deliver. Rev.* **2012**, *64*, 37.
(45) Riess, G. Micellization of block copolymers. *Prog. Polym. Sci.* **2003**, *28*, 1107.
(46) Gallou, F.; Isley, N. A.; Ganic, A.; Onken, U.; Parmentier, M. Surfactant technology applied toward an active pharmaceutical ingredient: more than a simple green chemistry advance. *Green Chemistry* **2016**, *18*, 14.
(47) McBain, J. W. *Trans. Faraday Soc.* **1913**, *9*.
(48) Jain, S.; Bates, F. S. On the origins of morphological complexity in block copolymer surfactants. *Science* **2003**, *300*, 460.
(49) Controlled Polymerization and Polymeric Structures: Flow Microreactor Polymerization, Micelles Kinetics, Polypeptide Ordering, Light Emitting Nanostructures.

Controlled Polymerization and Polymeric Structures: Flow Microreactor Polymerization, Micelles Kinetics, Polypeptide Ordering, Light Emitting Nanostructures **2013**, *259*, 1.
(50) Patist, A.; Kanicky, J. R.; Shukla, P. K.; Shah, D. O. Importance of micellar kinetics in relation to technological processes. *J. Colloid Interface Sci.* **2002**, *245*, 1.
(51) Lund, R.; Willner, L.; Pipich, V.; Grillo, I.; Lindner, P.; Colmenero, J.; Richter, D. Equilibrium Chain Exchange Kinetics of Diblock Copolymer Micelles: Effect of Morphology. *Macromolecules* **2011**, *44*, 6145.
(52) Lund, R.; Willner, L.; Richter, D.; Dormidontova, E. E. Equilibrium chain exchange kinetics of diblock copolymer micelles: Tuning and logarithmic relaxation. *Macromolecules* **2006**, *39*, 4566.
(53) Pedersen, J. S.; Hamley, I. W.; Ryu, C. Y.; Lodge, T. P. Contrast variation small-angle neutron scattering study of the structure of block copolymer micelles in a slightly selective solvent at semidilute concentrations. *Macromolecules* **2000**, *33*, 542.
(54) Pedersen, J. S.; Svaneborg, C.; Almdal, K.; Hamley, I. W.; Young, R. N. A small-angle neutron and X-ray contrast variation scattering study of the structure of block copolymer micelles: Corona shape and excluded volume interactions. *Macromolecules* **2003**, *36*, 416.
(55) Hammouda, B.; Laboratory, M. S. a. E., Ed.; National Institute of Standards and Technology: National Institute of Standards and Technology, 1995.
(56) Dill, K. A.; Bromberg, S. *Molecular Driving Forces: Statistical Thermodynamics in Chemistry and Biology*; Garland Science: New York, 2003.
(57) Einstein, A. On the Movement of Small Particles Suspended in Stationary Liquids Required by the Molecular-Kinetic Theory of Heat. *Ann. Phys.* **1905**, *17*, 549.
(58) Edward, J. T. Molecular Volumes and the Stokes-Einstein Equation. *J. Chem. Educ.* **1970**, *47*, 261.
(59) Mehrer, H. *Diffusion in Solids*, 2007; Vol. 155.
(60) Wagner, C.; Schottky, W. *Z. Physik. Chem. B* **1931**, *11*, 163.
(61) MacFarlane, D. R.; Forsyth, M. Plastic crystal electrolyte materials: New perspectives on solid state ionics. *Adv. Mater.* **2001**, *13*, 957.
(62) Baughman, R. H.; Turnbull, D. Vancancy Formation Parameters in Organic Crystals. *J. Phys. Chem. Solids* **1971**, *32*, 1375.
(63) Agmon, N. The Grotthuss Mechanism. *Chem. Phys. Lett.* **1995**, *244*, 456.
(64) Kreuer, K. D. On the development of proton conducting polymer membranes for hydrogen and methanol fuel cells. *J. Membrane Sci.* **2001**, *185*, 29.
(65) Commer, P.; Cherstvy, A. G.; Spohr, E.; Kornyshev, A. A. The effect of water content on proton transport in polymer electrolyte membranes. *Fuel Cells* **2003**, *2*, 127.
(66) Eyring, H. The Activated Complex in Chemical Reactions. *J. Chem. Phys.* **1935**, *3*, 107.
(67) de Araujo, C. C.; Kreuer, K. D.; Schuster, M.; Portale, G.; Mendil-Jakani, H.; Gebel, G.; Maier, J. Poly(p-phenylene sulfone)s with high ion exchange capacity: ionomers with unique microstructural and transport features. *Phys. Chem. Chem. Phys.* **2009**, *11*, 3305.
(68) Kreuer, K. D. Ion Conducting Membranes for Fuel Cells and other Electrochemical Devices. *Chem. Mater.* **2014**, *26*, 361.
(69) Chandler, D. *Introduction to Modern Statistical Mechanics*; Oxford University Press, Inc.: New York, New York, 1987.

Chapter 2

Nuclear Magnetic Resonance as a Versatile Tool to Study Soft Materials: Theory and Methods

2.1 Basic Nuclear Magnetic Resonance Theory

Nuclear magnetic resonance (NMR) is one of the most powerful spectroscopic tools available. Almost every element has an NMR-active isotope and is identifiable through the intrinsic property of spin.[1,2] Typical nuclei studied are ^{1}H, ^{31}P, ^{13}C, and ^{15}N, which are all spin-½ nuclei and thus are magnetically simple. NMR active nuclei are classified by their spin quantum number I, as presented in Statement 2.1:[1]

$$(2I + 1) \tag{2.1}$$

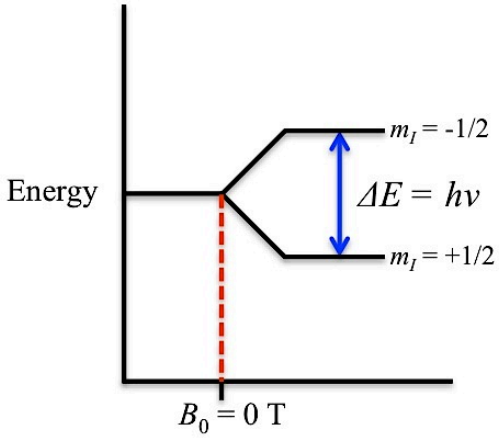

Figure 2.1. In the presence of an externally applied magnetic field, the nuclear spin states of NMR active nuclei are no longer degenerate and thus split, commonly referred to as *Zeeman splitting*. Shown is an illustration of *Zeeman splitting* for a typical spin I = ½ nucleus such as ^{1}H where there are $(2I + 1)$ spin states (i.e., two spin states), where ν is the resonance frequency.[1]

These selected nuclei are spin-½, meaning the spin states are two-fold degenerate in zero magnetic field.[2] In the presence of a magnetic field, the degeneracy is broken resulting in the nuclear spin state splitting, known as the *nuclear Zeeman effect* (*Zeeman splitting*) (Figure 2.1).[1] The magnetic moments of nuclei with a non-zero spin precess around the applied magnetic field direction (z) at the *Larmor frequency* ω_o as described by Equation 2.1, where γ is the gyromagnetic ratio and B_0 is the strength of the magnetic field.[1,2]

$$\omega_o = -\gamma B_0 \tag{2.1}$$

In the presence of B_0, random spin flips from thermal excitations (i.e., collisions between magnetic nuclei) cause a buildup of magnetization along an applied magnetic field B_0, which we define as being along the z-axis. The time constant T_1 for buildup of magnetization is called the longitudinal (or spin-lattice) relaxation time. [1,2]

T_1 is sensitive to molecular motions on the ~$1/\omega_o$ time scale (ns) [3] and is important to magnetic resonance imaging (MRI),[4] dynamics from 2D NMR methods (e.g., NOESY/EXSY, HOESY),[5] and is recently being used as a tool to understand unimer kinetics in micelle solutions (Chapter 7). T_1 quantifies the rate of energy transfer from the nuclear spin system to neighboring molecules (lattice) and depends on rotational dynamics (molecular tumbling) that are influenced by size, shape, molecular weight, and degrees of freedom within a given environment.[6-8] This rate is also influenced by interactions with paramagnetic species and electric field gradients (for quadrupolar nuclei). T_1 is commonly measured using the inversion recovery pulse-sequence (Figure 2.2a).[8]

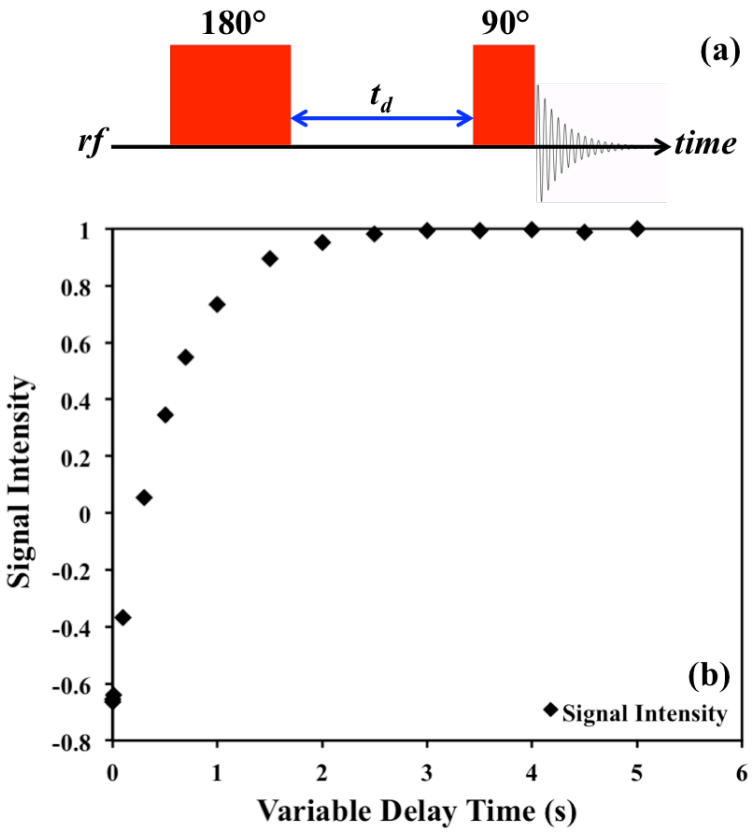

Figure 2.2. The inversion recovery pulse sequence (a) gives an exponential growth in signal intensity as a function of the variable delay time t_d (b), which is fit with Equation 2.2 to extract the T_1 time constant. In the example plot (b), t_d varies from 5 μs – 5 s.

A 180° rf excitation pulse inverts the net magnetization to the -z-axis. A variable delay time t_d (commonly 5 μs – 10 s in 8 – 32 steps) then allows spin-lattice relaxation to occur along the z-axis. Following t_d, excitation with a 90° rf pulse puts the net magnetization into the transverse plane for free induction decay (FID) acquisition. The inversion recovery method results in an exponential growth of signal intensity as a function of t_d (Figure 2.2b) and is fit with Equation 2.2 (where I_0 is the signal amplitude at $t_d = 0$) to extract the T_1 time constant.[8]

$$I(t) = I(0)(1 - 2e^{\frac{-t_d}{T_1}}) \tag{2.2}$$

Another fundamental relaxation mechanism in NMR is the spin-spin relaxation, or de-phasing, of the net magnetization in the transverse plane (xy-plane) by 37% (1/e) of the initial value, commonly characterized by the time constant T_2.[1,2,9,10] Unlike T_1, T_2 occurs due to local field inhomogeneities and/or interactions between spins (collisions).[9] Magnetic field inhomogeneity causes signal broadening as a result of small deviations in ω_o (imperfect magnetic field B_0).[11] Modern day superconducting magnets are equipped with multiple-order shim coils, which serve to manipulate the magnetic field within a given sample to produce as homogenous of a magnetic field as possible, as spectral resolution is ultimately dependent on B_0 homogeneity.[11] T_2 reports on longer time scales (μs – s) than T_1 and finds use in linewidth analysis (linewidth = $1/(\pi T_2)$),[12] quantification of species within different morphological environments (Chapter 5),[10] and gives relative information on degrees of freedom for a given nucleus. T_2 is commonly measured using the Carr-Purcell-Meiboom-Gill (CPMG) pulse sequence (Figure 2.3a).[13,14]

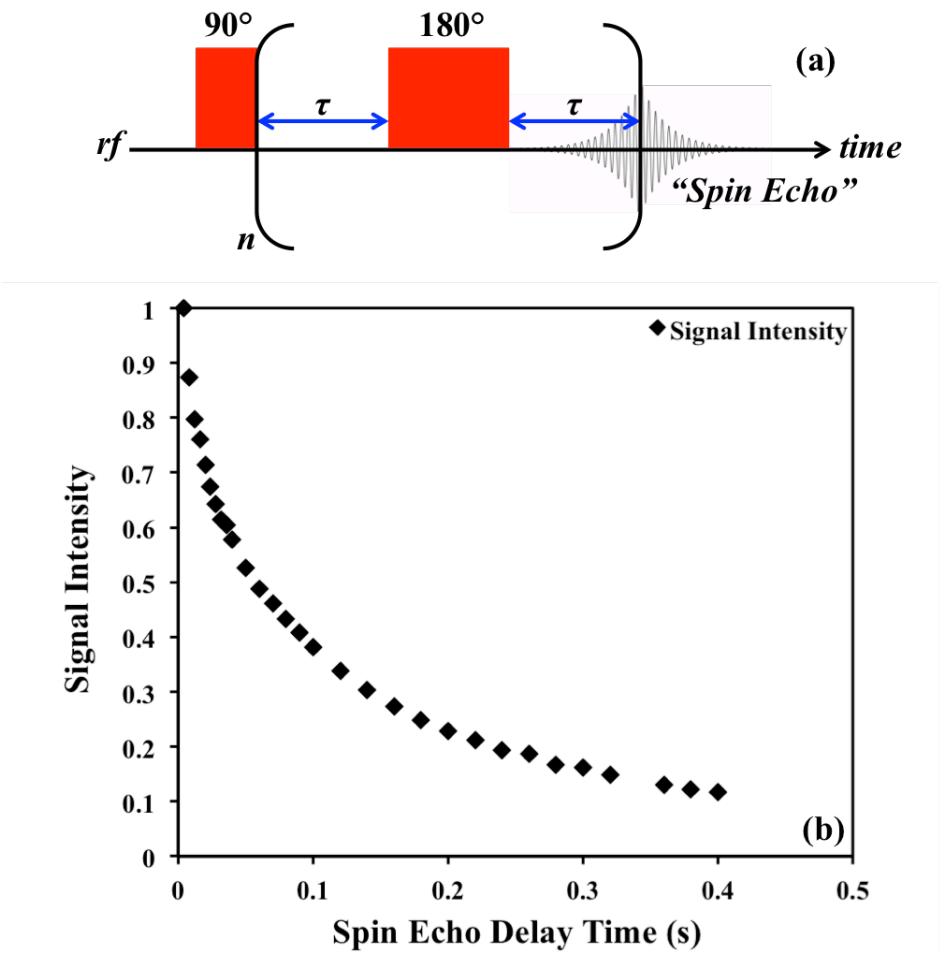

Figure 2.3. The CPMG pulse sequence (a) gives an exponential decay in signal intensity as a function of spin echo delay time $2\tau n$ (b) to achieve at least 90% attenuation, which is fit with Equation 2.3 to extract out the T_2 time constant. τ = 1 ms and n ranges from 2 – 200 in the example plot (b).

Upon excitation with a 90° rf pulse, the net magnetization de-phases ("fans out") in the transverse plane (xy-plane) due to spin-spin relaxation, thus leading to an inherent signal attenuation. After some time period τ, prior to full signal attenuation, a 180° rf pulse is applied such that the net magnetization is "flipped" and refocused, thus forming a "spin echo" (Figure 2.3a). This follows with FID acquisition at the top of the spin echo (2τ), which results in an

exponential decay in signal intensity as a function of $2\tau n$ (Figure 2.3b) and fit with Equation 2.3 to extract the T_2 time constant (where I_0 is the signal amplitude at $2\tau n = 0$).[13,14]

$$I = I_0 e^{-\frac{2\tau n}{T_2}} \tag{2.3}$$

The spin echo was first discovered by Erwin Hahn in 1950 and represents one of the most important discoveries in the evolution of modern-day NMR techniques.[9]

Commonly, $T_1 > T_2$ due to their respective relaxation mechanisms previously mentioned.[1] Knowing T_1 and T_2 is critical for optimizing many NMR experiments such as the diffusometry experiment used to obtain self-diffusion coefficients, as discussed below.

2.2 Pulsed-Field-Gradient NMR Diffusometry

As discussed in Chapter 1, the self-diffusion coefficient of a molecular species can provide insight to the molecular environment encompassing the diffusing species.[3,10,15-22] During Hahn's discovery of the spin echo (Figure 2.3a), additional contributions to signal attenuation due to the diffusion of molecules in the presence of magnetic field inhomogeneity were seen.[9] Quantification of the self-diffusion coefficient would later be proposed by Carr and Purcell[14] in 1954 and further developed by Stejskal and Tanner in 1965,[23] who ultimately innovated the use of pulsed-field gradients and finalized the mathematical relationship of the time-dependent diffusion with the observed NMR signal (discussed below).

Revisiting Equation 2.1, we showed that a spin-active nucleus has an intrinsic resonance frequency ω_0 in the presence of an externally applied magnetic field B_0. If we assume B_0 is homogenous at all locations along the z-axis, then ω_0 for each spin is the same at all locations. Adding a magnetic field gradient $\mathbf{g}$ (G cm^{-1}) (Equation 2.4), where $\mathbf{i}$, $\mathbf{j}$, and $\mathbf{k}$ are unit vectors[24]

$$\mathbf{g} = \nabla B_0 = \frac{\partial B_z}{\partial x}\mathbf{i} + \frac{\partial B_z}{\partial y}\mathbf{j} + \frac{\partial B_z}{\partial z}\mathbf{k}\,, \tag{2.4}$$

to the already existing B_0 causes ω_0 to become dependent on the overall strength of the magnetic field at varying locations, thus producing a linear variation in ω_0 along the sample (z-axis in Equation 2.5).[24]

$$\omega_0 = \gamma(B_0 + \mathrm{g}_z) = \omega_0 + \gamma \mathrm{g}_z \tag{2.5}$$

This allows us to encode spins' spatial positions into NMR (Larmor) frequencies by varying the magnetic field, usually with a linear magnetic field gradient.[24] The gradient evenly slices the sample into microscopic groups of spins along the direction of interest. A single group of spins is represented by a single magnetization vector, or "spin isochromat." Each magnetization vector is in phase upon excitation of a 90° rf pulse in the transverse plane. For example, using a z-directed field gradient, g_z, causes the magnetization vectors to wind and form a "magnetization helix" with wavelength λ (Equation 2.6):

$$\lambda = \frac{2\pi}{\gamma \mathrm{g}_z \delta}\,, \tag{2.6}$$

where δ is the time over which the gradient is applied. Figure 2.4 illustrates how the magnetization helix evolves under the influence of linear gradient pulses and a simple spin echo pulse sequence.[11,25]

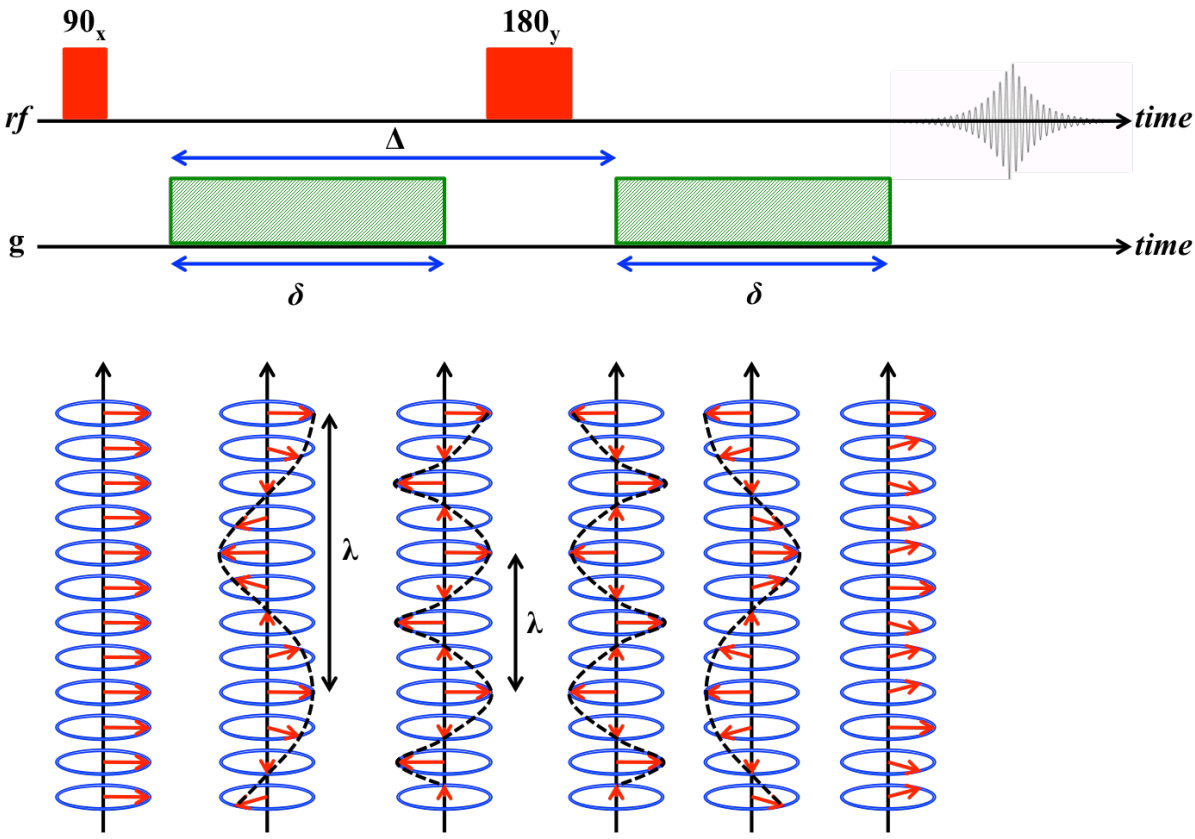

Figure 2.4. A simple spin echo pulse sequence in the presence of a pair of matched externally applied magnetic field gradients is commonly used to determine the diffusion coefficient by linearly varying the strength of the magnetic field gradient g. A 90° rf pulse causes all spin isochromats to be in phase in the transverse plane (xy-plane). Upon the application of a gradient, the magnetization vectors are wound to form a "magnetization helix" with wavelength λ, where the pitch of the helix becomes smaller during the gradient pulse. A 180° rf pulse flips the helix, then this is followed by another gradient pulse (after the diffusion time Δ), which unwinds the magnetization helix, thus forming a spin echo. The winding/unwinding are "scrambled" by diffusion (spins exchange between slices during Δ) and gives a distribution of ending magnetization vector phases, thus decreasing signal intensity. Figure adapted from Callaghan.[11]

In Figure 2.4, it can be seen that the wavelength of the helix decreases with time (during δ) as a result of the magnetization vector of each slice becoming more de-phased in the transverse plane. A 180° rf pulse makes a mirror image of the magnetization vectors, and then they are later unwound and refocused with another a matched gradient pulse, thus forming the spin echo. A phase shift φ in the refocused net magnetization occurs due to a change in spin position (if diffusion is present) along the applied gradient axis during the encoding time Δ (Equation 2.7):[11]

$$\varphi = \gamma \mathrm{g} \delta (z_1 - z_2) \, . \tag{2.7}$$

There is a linear dependence of φ on the gradient strength g, holding δ constant (γ is a fixed intrinsic property of the nucleus). Stejskal and Tanner developed a mathematical relationship to describe the signal attenuation as a function of gradient strength, which is now referred to as the Stejskal-Tanner equation (Equation 2.8):[23]

$$I = I_0 e^{-D\gamma^2 \mathrm{g}^2 \delta^2 (\Delta - \frac{\delta}{3})} \, , \tag{2.8}$$

where I is the signal intensity, γ is the gyromagnetic ratio, g is the gradient strength, δ is the effective gradient pulse length, Δ is the diffusion time, and D is the self-diffusion coefficient.[23] Choices for the effective gradient pulse length, δ, and the diffusion time, Δ, depend on the relaxation time constants T_2 and T_1, respectively. The self-diffusion coefficient is determined by linearly varying the applied magnetic field gradient across the sample, such that the signal intensity decreases as a function of gradient strength (Figure 2.5) and fit to the Stejskal-Tanner equation (Equation 2.8).

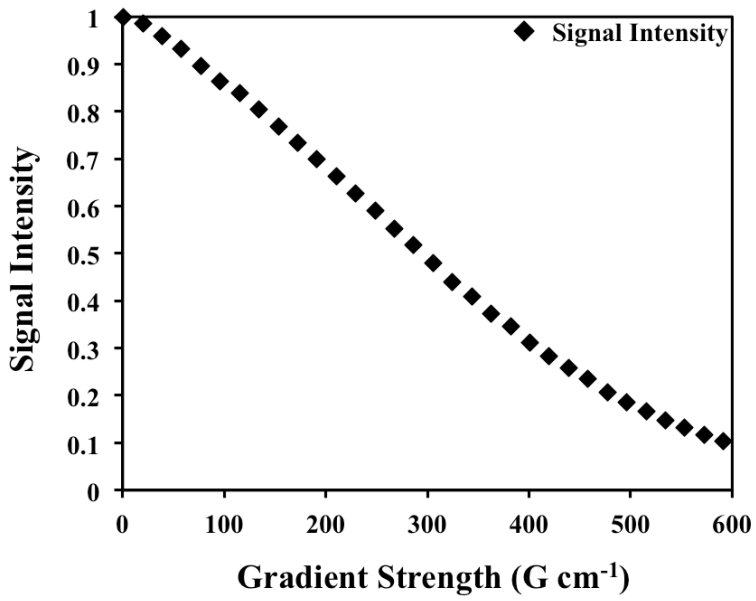

Figure 2.5. A Gaussian decay in signal intensity *I* as a function of gradient strength g is observed when carrying out the PFG NMR experiment. The self-diffusion coefficient is extracted by fitting with the Stejskal-Tanner equation (Equation 2.8).[23] In this example, γ = 42.6 MHz T^{-1} (^{1}H), δ = 2 ms, and Δ = 25 ms.

For a polycrystalline material, the crystallites are rigid and thus the nuclei are not motionally averaged. Upon rf excitation, nuclear relaxation in the transverse plane (i.e., T_2) will occur much more rapidly (ms - μs time scale) versus nuclei in a liquid. Typically, the T_2 relaxation time is the limiting factor for the PFG NMR experiment as it defines the effective gradient pulse length that can be used. The pulse sequence in Figure 2.4 is generally sufficient for use when $T_2 \geq 1$ ms. It should be noted that PFG NMR studies are "T_2-weighted." That is, signals that have short T_2's (less than about 3 ms) will not be detected and/or signals with T_2's > 3 ms will have different intensity weighting in the PFG NMR experiment (discussed in more detail below), as the spin-spin relaxation occurs during gradient encoding before acquisition of signal during the echo. T_2-weighting can also be used as a "spectral editing" feature if broad

signals prevent resolution of more narrow signals. Figure 2.6 illustrates how T_2-weighting removes immobile (broad signal in 1D spectrum) components and leaves the mobile component (narrow signal) after the PFG NMR experiment. This will be discussed in more detail in Chapter 3.

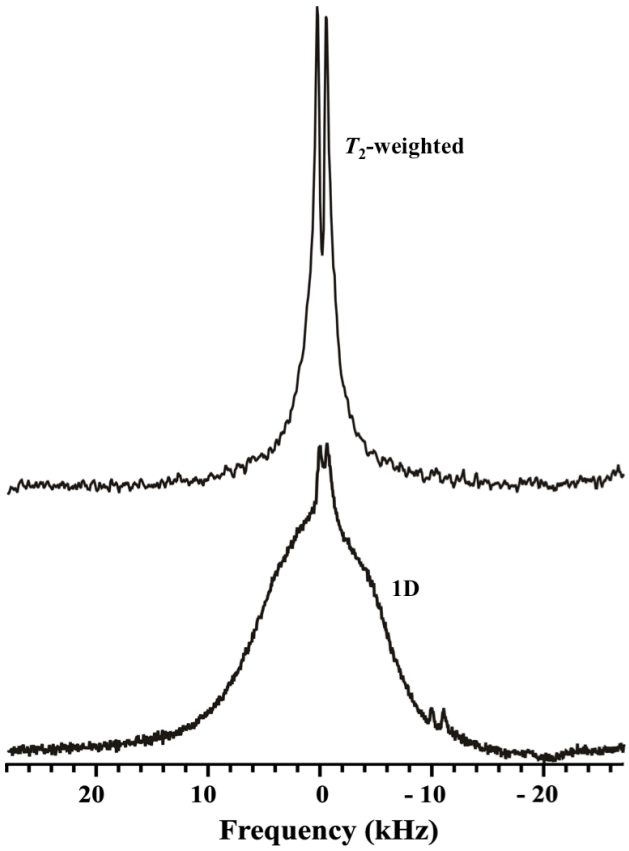

Figure 2.6. 1D and T_2-weighted spectra before (1D) and after (T_2-weighted) a PFG NMR experiment.

Described in detail by Stejskal and Tanner, PFG NMR represents a powerful tool that gives direct insight into the molecular diffusion within a system, as discussed in Chapter 1.[23] Small molecule and ion transport in soft materials can occur through multiple mechanisms and variable temperature diffusion measurements can report on individual small molecule and ion E_a

values that give insight into how morphology and transport are coupled. Discussed below and shown in subsequent chapters, NMR spectroscopy and diffusometry can be utilized to probe dynamics on multiple time and length scales.

2.3 Multi-Component Relaxation and Diffusometry to Probe Material Morphology

When analyzing a material that exhibits nm – μm length scale morphologically distinct environments, it can be advantageous to conduct each of the aforementioned NMR methods to develop a deeper understanding of how polymeric morphology, transport, and dynamics are coupled. Such methods offer the unique ability to aid material scientists in their future developments of new polymeric materials. Indeed, when investigating a new material, special care must be taken to insure each NMR experiment is designed properly. The following section serves as a guide for material scientists interested in such measurements and highlights how relaxation and diffusometry methods can be used to probe systems that have morphologically distinct environments.

2.3.1 Multi-Component Spin-Spin Relaxation

We begin by introducing how T_2 can quantify species residing within multiple environments and present common pitfalls in doing such analyses. As previously mentioned, T_2 can probe dynamics on the μs – s time scale. Thus, if nm – μm length scale morphological environments exist within a single sample, the probe molecule/ion can give a quantitative understanding of relative degrees of freedom within each environment, relative fraction within each environment, and potentially the length scale (nm – μm) over which the environment exists.[10] Indeed, such observations depend on: 1) if the probe molecule/ion resides within each

environment, 2) the exchange rate of the probe molecule/ion between environments relative to experimental time scale, and 3) the length scale traversed (diffusion coefficient) by the probe species relative to the T_2 experimental time scale. Deriving length scales from T_2 data will be discussed below. Figure 2.7 shows a representative bi-exponential T_2 intensity decay curve of a probe ion within a material that has μm-length scale morphological features that the ion experiences (discussed below and in more detail in Chapter 5). Note that the dotted lines in Figure 2.7 are not fits but instead are used to guide the eye.

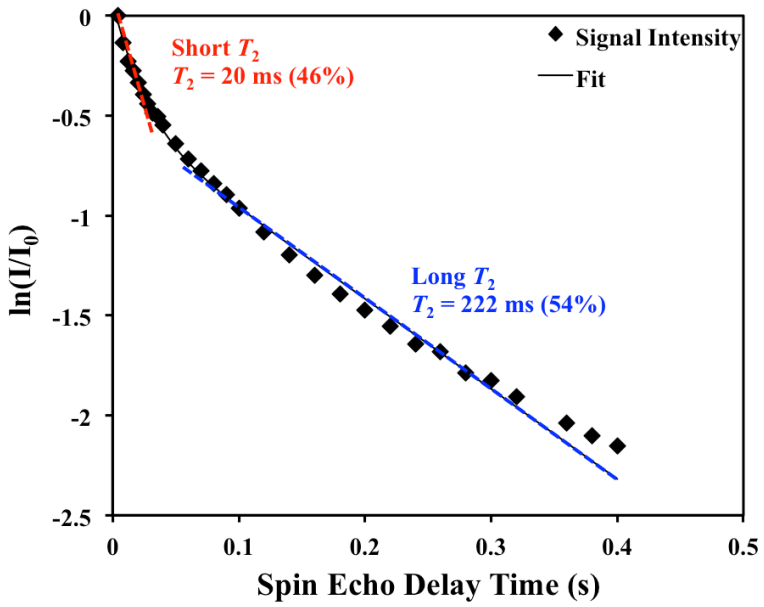

Figure 2.7. Bi-exponential T_2 intensity decay curves allow quantitative analysis of a probe ion within two distinct environments (τ = 1 ms and n ranges from 2 – 200).

We take the natural log of Equation 2.3 to observe if deviation from linearity is present (two slopes) to aid in our multi-component analysis. If only one component were present, we would observe linearity through the entire intensity decay curve. This allows direct extraction of the T_2 time constants (slopes) and relative fractions of each component. In this example, The T_2 times are different by an order of magnitude and the relative fractions are each ~50% of the total

intensity decay curve. While this is an ideal example, multi-component analysis becomes more difficult if: 1) the difference between the T_2 values is < 10% and/or 2) the short or long-T_2 components constitute <10% of the total intensity decay curve. This can be seen for polymers with a large polydispersity and polymeric materials that contain not well defined morphological regions, where a distribution in T_2 values may be seen and/or the total number of probe molecules/ions within a given region is relatively small. Indeed, one should apply Occam's razor and be hesitant to fit an intensity decay curve with more than two-components. Unlike a diffusion experiment, where the experimental time scale is defined by the diffusion time (Δ), a T_2 experiment varies in experimental time scale with the spin echo delay time $2\tau n$. Thus, when a bi-exponential decay curve is seen, the length scale over which the short-T_2 component reports on can be derived (assuming the diffusion coefficient is known) using the equation $\langle r^2 \rangle^{1/2} = (2D2\tau n)^{1/2}$.

Figure 2.7 features a few "checkpoints" to ensure accurate analysis of two-component intensity decay curves. First, in order to observe the entire short-T_2 component and acquire the most accurate relative fraction, the smallest spin echo delay time is used (5 μs in this case) and gradually incremented to allow at least 8 data points for the fit. Secondly, 90% signal attenuation allows accurate analysis of the relative fractions of both components but can be increased if the signal-to-noise ratio of the spectra at long spin echo delay times is sufficient. Lastly, at least 16 – 32 data points are necessary for multiple components within a single curve.

Diagnosing errors in multi-component T_2 experiments is key for such methods, as one can easily be fooled by incorrect data. It is imperative to observe at least 90 – 95% signal attenuation; however, care should be taken to monitor the signal-to-noise ratio of spectra. Figure

2.8 is an example of how spectral noise at long spin echo delay times can be perceived as a long-T_2 component.

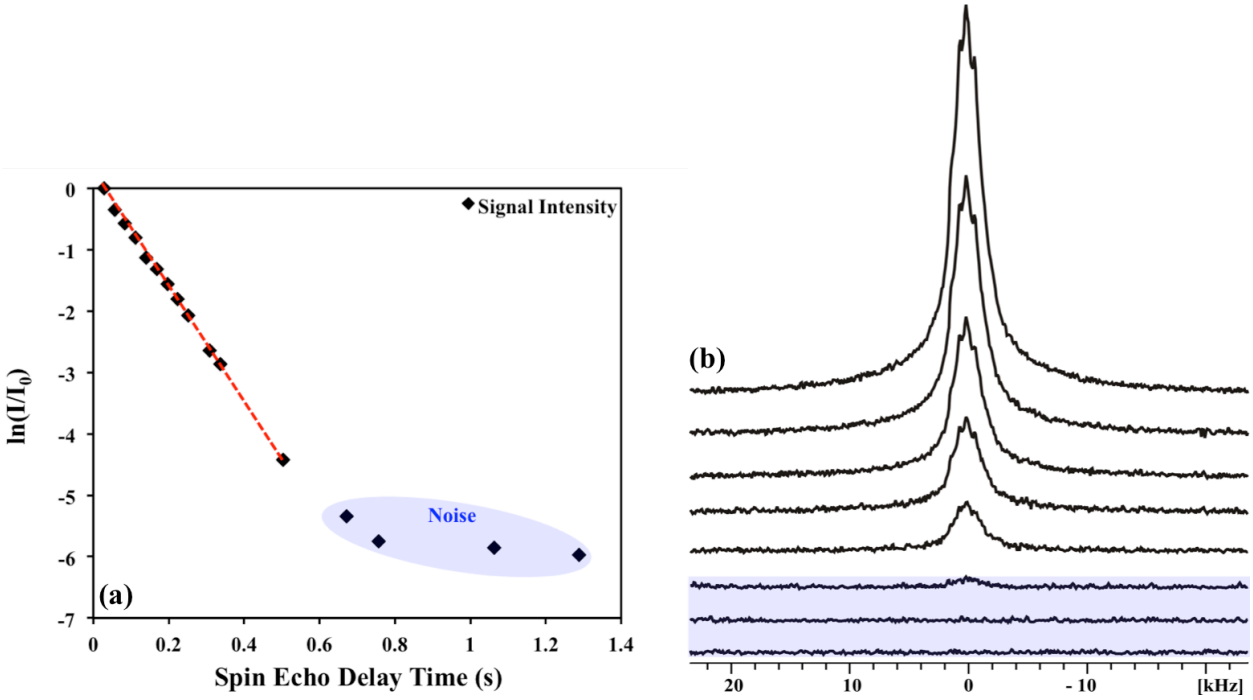

Figure 2.8. Representative T_2 intensity decay curves of an incorrect decay curve that appears to be two-component. τ = 7 ms and n ranges from 2 – 92 in the example plot (b).

Clearly, Figures 2.6 and 2.7a are identical in that two linear regressions can in principle be fit to the data. However, inspection of select 1D spectra for data points at long spin echo delay times (Figure 2.8b) reveals that the perceived long-T_2 component, as seen by a change in slope (Figure 2.8a), is indeed noise. Since noise is still being processed within the region of interest, a change in slope at long spin echo delay times is expected due to invariance in the noise intensity. Thus, judicious CPMG pulse sequence parameter optimization as well as a careful eye in data analysis can save substantial time.

2.3.2 Multi-Component Diffusometry

Analogous to multi-component T_2 experiments and analysis, multi-component diffusion curves can also arise in polymeric materials and should subject to the same scrutiny. As previously mentioned, the diffusometry experiment has a single experimental time scale (Δ) over which the probe molecule/ion reports on. Figure 2.9 shows a representative two-component diffusion intensity decay curve of a probe ion within a material that has μm-length scale morphological features that the ion experiences (discussed in more detail in Chapter 5). Note that the dotted lines in Figure 2.8 are not fits but instead are used to guide the eye.

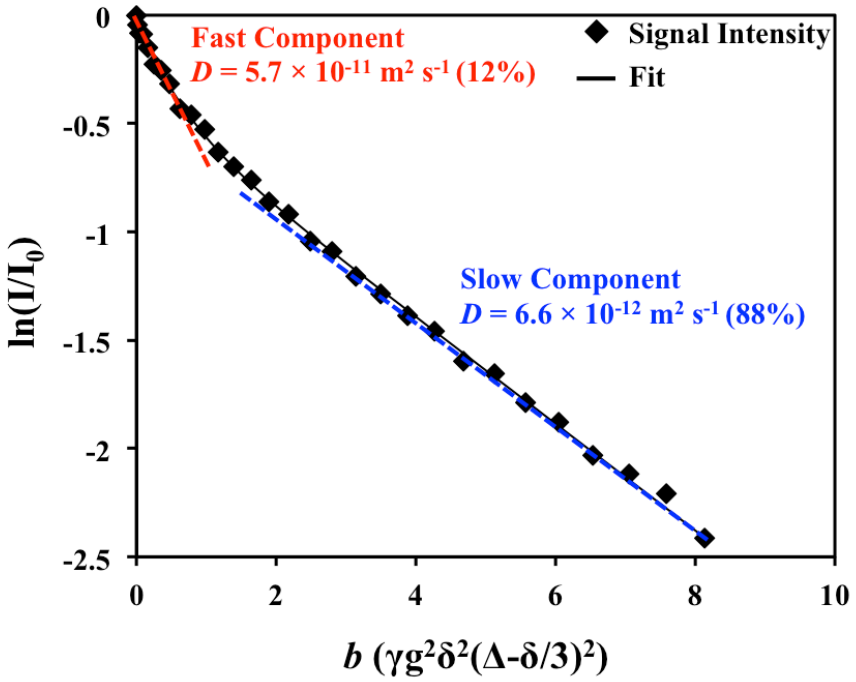

Figure 2.9. Representative Stejskal-Tanner intensity decay curve that shows two-component diffusion coefficient, where two independent slopes of the signal intensity decay curve allow extraction of diffusion coefficients are relative fractions. In this example, $\gamma = 42.6$ MHz T^{-1} (^{1}H), $\delta = 2$ ms, and $\Delta = 25$ ms.

Just like T_2 experiments, we take the natural log of Equation 2.8 to observe if deviation from linearity is present (two slopes). Immediately, one can see identical features between Figures 2.9 and 2.7, where two independent slopes are seen. As mentioned above, T_2-weighting from the gradient pulse can influence the measured signal intensity such that inaccurate relative fractions are obtained and/or the slow component is not observed (if T_2 is too short). In this example case, the T_2 values for the fast (335 ms) and slow (81 ms) component do not significantly influence accurate relative fractions with a δ = 2 ms. However, as T_2 approaches δ, issues in multi-component, and sometimes single-component, analysis may arise. The same process for error diagnosis as discussed with T_2 experiments also applies to multi-component diffusometry.

Discussed in Chapter 1, the equation $\langle r^2 \rangle^{1/2} = (2D\Delta)^{1/2}$ tells us that the diffusion coefficient of a probe molecule/ion is independent of the diffusion time within unrestrictive environments (an isotropic liquid such as bulk H_2O). However, the diffusion coefficient will be independent of the diffusion time (Δ) until the diffusion length scale is large enough to sample a domain that restricts the probe molecule/ion motion such that a reduction in the diffusion coefficient is seen at longer diffusion times.[3,10,11,18,26,27] This method is significant since long-time-limit diffusion is directly related to bulk transport in polymeric materials. Figure 2.10 illustrates a probe ion that experiences morphological restrictions and diffuses on average 1 – 10 μm during Δ = 6 – 200 ms.

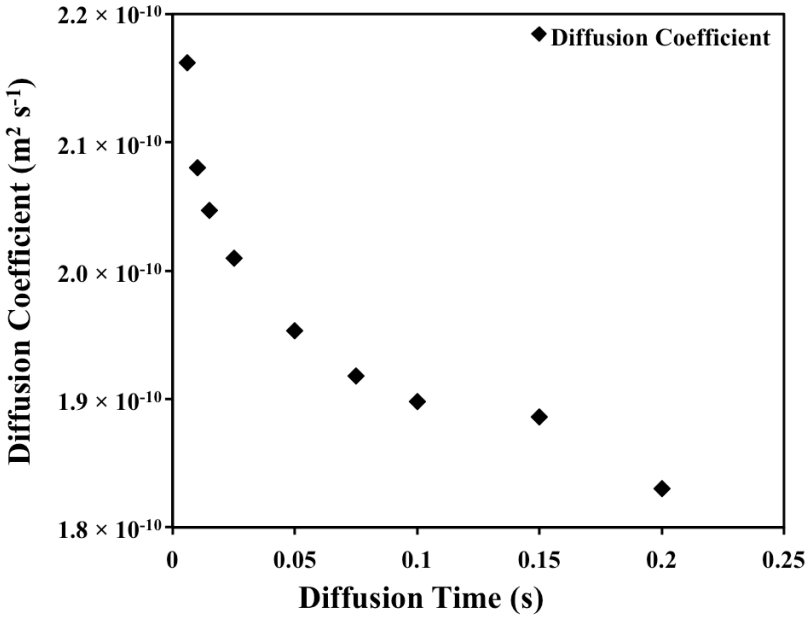

Figure 2.10. Restricted diffusion curve of an ion experiencing morphological boundaries at ~ 3 μm.

Note that in Figure 2.10 the change in diffusion coefficient is relatively small, suggestive of a "soft restriction" (swollen polymer fiber). For some systems, orders of magnitude decreases in diffusion coefficient can be seen (discussed in Chapter 3), which suggest "hard restrictions" (OIPCs). Such methods allow direct interrogation of the size of restrictive domains in which the probe species exist by: 1) measuring the diffusion coefficient as a function of diffusion probing time (Δ), 2) modulating the diffusion coefficient by changing the probe molecule size, and/or 3) modulating the diffusion coefficient by changing solvent uptake (if applicable).

Studies presented in Chapters 3, 5, 6, 7, and 8 utilize multi-component analysis to understand how polymeric material morphology influences transport and dynamics in a range of systems. As will be shown, NMR can give rich information that may otherwise be inaccessible using other techniques.

2.4 General Remarks on Solid-State NMR

Chemical shift anisotropy (CSA), quadrupole coupling (Q), and dipole-dipole coupling (DD) are the nuclear spin interactions that affect solid-state NMR signals due to their dependence on molecular orientation with respect to the applied magnetic field B_0.[28-31] Analysis of spectral lineshapes affords the study of molecular dynamics occurring in the kHz frequency range.[32] Powder samples that contain crystallites with various orientations (polycrystalline materials) can be observed with solid-state NMR. These interactions produce spectral frequencies pertaining to a distribution of specific internuclear (molecular) orientations with respect to B_0 that superimpose to make up a so-called "powder pattern",[31] which will be discussed in the following section. The systems presented in this Thesis were studied with spin I = 1/2, 1, and 3/2 nuclei thus, we will also introduce the fundamentals of quadrupolar NMR.

2.4.1 Quadrupolar NMR Theory

For a given sample, the nuclei experience magnetic and electric fields that originate from that sample.[31] Of the internal spin Hamiltonian (spin interaction energy) terms:

$$\widehat{H}_{internal} = \widehat{H}_J + \widehat{H}_{CS} + \widehat{H}_{DD} + \widehat{H}_Q, \tag{2.9}$$

where $\widehat{H}_J$ is the J-coupling, $\widehat{H}_{CS}$ is the chemical shift, $\widehat{H}_{DD}$ is the dipolar coupling, and $\widehat{H}_Q$ is the quadrupolar coupling, the quadrupolar coupling of a spin ≥ 1 within a solid or soft material will only be considered here because other interactions are small in comparison or are not studied (e.g., dipolar couplings) in the present Thesis. Quadrupolar couplings represent the electric quadrupole interactions of spin ≥ 1 nuclei with the surrounding electric field.[31] Considering a C-^{2}H (or O-^{2}H) bond, the non-spherical charge distribution of the C-^{2}H bond generates an electric field gradient (EFG) that interacts with the electric quadrupole moment, Q, of the ^{2}H nucleus. It

should be noted that a non-spherical charge distribution of the nucleus itself can also create an EFG. The quadrupolar coupling constant C_Q (Equation 2.10) defines this interaction:

$$C_Q = \frac{e^2qQ}{h}, \tag{2.10}$$

where e^2q is the EFG term and h is Planck's constant. In a typical aliphatic or aromatic molecule containing a C-^{2}H bond, C_Q for ^{2}H is ≈ 180 kHz. C_Q is commonly derived from the splitting ν_Q between the two singularities found in a powder pattern ($\nu_Q = 3C_Q/4$) (isotopically labeled polycrystalline material); also known as a *Pake pattern* (Figure 2.11a).[1,33,34]

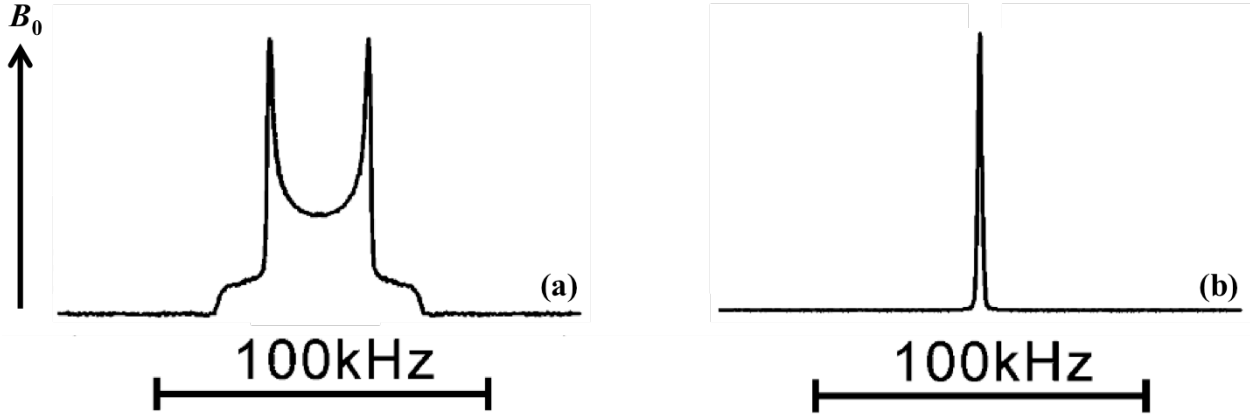

Figure 2.11. A distribution of first-order splittings produces the well known Pake powder spectrum (a); where most of the high signal intensity singularities come from the C-^{2}H bonds perpendicular, $\theta = 90°$, to the magnetic field.[1,33,34] An isotropic signal is seen if the C-^{2}H bond is rotating fast so that it is sampling all angles rapidly on the experimental time scale (b).

The common case of a uniaxial EFG tensor produces such a spectrum. The powder pattern is a superposition of every possible molecular orientation that produces its own first-order quadrupole splitting $\Delta\nu_Q$.[1] The larger signal intensity components come from the molecules whose EFG tensor principal axes are perpendicular to the magnetic field, $\theta = 90°$ (a large

number of spins contributing). The weakest signals come from the molecules whose EFG tensor principal axes are parallel to the magnetic field, θ = 0° and/or 180° (small number of spins contributing).[1] If the C-^{2}H bond is rotating fast so that it is sampling all angles rapidly on the experimental time scale, an isotropic signal is seen (Figure 2.11b). Power patterns are commonly measured using the quadrupolar spin-echo pulse sequence (Figure 2.12).[2]

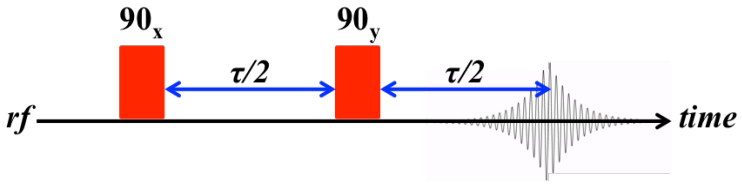

Figure 2.12. The quadrupolar spin-echo pulse sequence is commonly used in solid materials to refocus magnetization.[2]

For non-polycrystalline materials that exhibit some degree of orientational ordering (anisotropic) and phase dynamics (uniaxially drawn Nafion 117, Chapter 4), absorbing quadrupolar nuclei (probe molecule and/or ion) within the oriented matrix causes the probe species to adopt partial ordering due to pseudo-nematic interaction with the matrix.[15,19,21] Thus, partially averaged internal motions reduce the observed quadrupolar coupling and can produce a first-order quadrupole splitting $\Delta\nu_Q$:

$$\Delta\nu_Q = C_Q S P_2(cos\theta)\ , \qquad (2.11)$$

where $S = \langle P_2(\cos\chi)\rangle$ is the orientational order parameter of the probe molecule, $\langle P_2(\cos\chi)\rangle = (3\cos^2\chi - 1)/2$ is the second Legendre polynomial, χ is the angle between the O-^{2}H bond and the matrix alignment axis, θ is the angle between the matrix alignment axis and B_0. This angular dependence is described with the aid of Figure 2.13.[19]

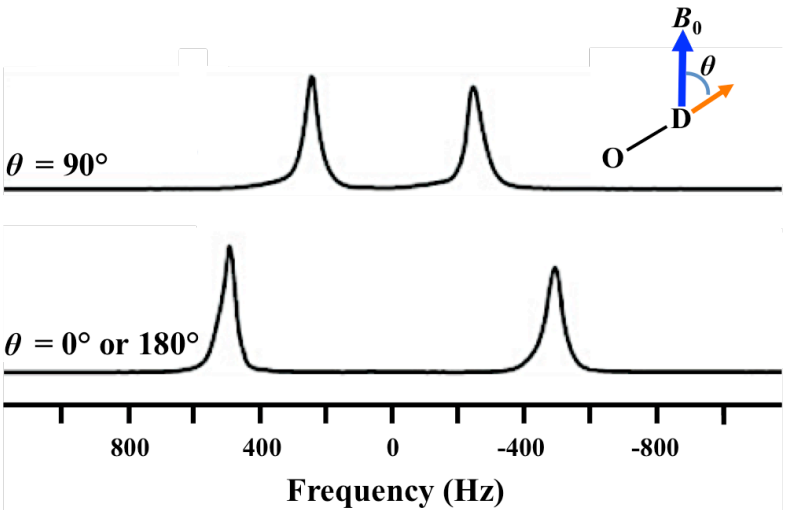

Figure 2.13. Illustration of $\Delta\nu_Q$ as a function of θ between the O-^{2}H bond axis and B_0 for an anisotropic material.[19] This angular dependence can be described by the second Legendre polynomial term in Equation 2.11. Reprinted by permission from Macmillan Publishers Ltd: [Nature Materials] (Ref 19), copyright (2011).

With the goal of understanding ion transport within the high temperature solid phases of OIPCs and channel ordering within swollen Nafion channels, we employ quadrupolar NMR methods to interrogate such morphology. As previously mentioned, line-broadening effects, such as CSA, DD, and Q couplings can make it difficult to properly understand specific molecular environments. However, isotopic labeling (i.e., replacing ^{1}H with ^{2}H) or swelling with quadrupolar nuclei ions ($^7Li^+$ and $^{23}Na^+$) allows access to very specific molecular environments. Chapters 3 and 4 will discuss how such methods can yield the degree of material alignment, channel biaxiality, phase transitions, and dynamics.

2.5 References

(1) Levitt, M. H. *Spin Dynamics*; John Wiley and Sons Ltd.: England, 2008; Vol. 2.

(2) Roberts, J. D. *ABC's of FT-NMR*, 2000.
(3) Hou, J.; Li, J.; Mountz, D.; Hull, M.; Madsen, L. A. Correlating morphology, proton conductivity, and water transport in polyelectrolyte-fluoropolymer blend membranes. *J. Membr. Sci.* **2013**, *448*, 292.
(4) Wang, X. L.; Chen, Y.; Xue, L.; Pothayee, N.; Zhang, R.; Riffle, J. S.; Reineke, T. M.; Madsen, L. A. Diffusion of Drug Delivery Nanoparticles into Biogels Using Time-Resolved MicroMRI. *J Phys Chem Lett* **2014**, *5*, 3825.
(5) Jeener, J.; Meier, B. H.; Bachmann, P.; Ernst, R. R. Investigation of Exchange Processes by 2-Dimensional Nmr-Spectroscopy. *J. Chem. Phys.* **1979**, *71*, 4546.
(6) Bloembergen, N.; Purcell, E. M.; Pound, R. V. Nuclear Magnetic Relaxation. *Nature* **1947**, *160*, 475.
(7) Bloembergen, N.; Purcell, E. M.; Pound, R. V. Relaxation Effects in Nuclear Magnetic Resonance Absorption. *Physical Review* **1948**, *73*, 679.
(8) Hahn, E. L. An Accurate Nuclear Magnetic Resonance Method for Measuring Spin-Lattice Relaxation Times. *Physical Review* **1949**, *76*, 145.
(9) Hahn, E. Spin Echoes. *Physical Review* **1950**, *80*, 580.
(10) Kidd, B. E.; Forbey, S. J.; Steuber, F. W.; Moore, R. B.; Madsen, L. A. Multiscale Lithium and Counterion Transport in an Electrospun Polymer-Gel Electrolyte. *Macromolecules* **2015**, *48*, 4481.
(11) Callaghan, P. T. *Translational Dynamics and Magnetic Resonance: Principles of Pulsed Gradient Spin Echo NMR*; Oxford University Press: New York, 2011.
(12) Adebahr, J.; Forsyth, M.; MacFarlane, D. R.; Gavelin, P.; Jacobsson, P. Li-7 NMR measurements of polymer gel electrolytes. *Solid State Ionics* **2002**, *147*, 303.
(13) Meiboom, S. Citation Classic - Modified Spin-Echo Method for Measuring Nuclear-Relaxation Times. *Cc/Eng Tech Appl Sci* **1980**, 16.
(14) Carr, H.; Purcell, E. Effects of Diffusion on Free Precession in Nuclear Magnetic Resonance Experiments. *Phys. Rev.* **1954**, *94*, 630.
(15) Hou, J.; Li, J.; Madsen, L. A. Anisotropy and Transport in Poly(arylene ether sulfone) Hydrophilic−Hydrophobic Block Copolymers. *Macromolecules* **2010**, *43*, 347.
(16) Hou, J.; Madsen, L. A. New insights for accurate chemically specific measurements of slow diffusing molecules. *J. Chem. Phys.* **2013**, *138*.
(17) Hou, J.; Zhang, Z.; Madsen, L. A. Cation/anion associations in ionic liquids modulated by hydration and ionic medium. *J. Phys. Chem. B* **2011**, *115*, 4576.
(18) Kidd, B. E.; Lingwood, M. D.; Lee, M.; Gibson, H. W.; Madsen, L. A. Cation and Anion Transport in a Dicationic Imidazolium-Based Plastic Crystal Ion Conductor. *J. Phys. Chem. B* **2014**, *118*, 2176.
(19) Li, J.; Park, J. K.; Moore, R. B.; Madsen, L. A. Linear coupling of alignment with transport in a polymer electrolyte membrane. *Nat Mater* **2011**, *10*, 507
(20) Li, J.; Wilmsmeyer, K. G.; Hou, J.; Madsen, L. A. The role of water in transport of ionic liquids in polymeric artificial muscle actuators. *Soft Matter* **2009**.
(21) Li, J.; Wilmsmeyer, K. G.; Madsen, L. A. Anisotropic Diffusion and Morphology in Perfluorosulfonate Ionomers Investigated by NMR. *Macromolecules* **2009**, *42*, 255.
(22) Lingwood, M. D.; Zhang, Z.; Kidd, B. E.; McCreary, K. B.; Hou, J.; Madsen, L. A. Unraveling the local energetics of transport in a polymer ion conductor. *Chem. Commun.* **2013**, 4283.

(23) Stejskal, E.; Tanner, J. Spin Diffusion Measurements: Spin Echoes in the Presence of a Time-Dependent Field Gradient*. *J. Chem. Phys.* **1965**, *42*.
(24) Price, W. S. Pulsed-field gradient nuclear magnetic resonance as a tool for studying translational diffusion .1. Basic theory. *Concept Magnetic Res* **1997**, *9*, 299
(25) Price, W. S. Pulsed-field gradient nuclear magnetic resonance as a tool for studying translational diffusion .1. Basic theory. *Concepts in Magnetic Resonance* **1997**, *9*, 299.
(26) Callaghan, P. T.; Coy, A.; Macgowan, D.; Packer, K. J.; Zelaya, F. O. Diffraction-Like Effects in Nmr Diffusion Studies of Fluids in Porous Solids. *Nature* **1991**, *351*, 467.
(27) Mitra, P. P.; Sen, P. N.; Schwartz, L. M.; Ledoussal, P. Diffusion Propagator as a Probe of the Structure of Porous-Media. *Phys. Rev. Lett.* **1992**, *68*, 3555.
(28) Reichert, D. *Prog. Nucl. Magn. Reson. Spectrosc.* **2005**, *47*, 137.
(29) Ashbrook, S. E.; Duer, M. J. Structural information from quadrupolar nuclei in solid state NMR. *Concepts in Magnetic Resonance Part A* **2006**, *28A*, 183.
(30) Duer, M. J. *Introduction to Solid-State NMR Spectroscopy: Principles and Applications*, 2002; Vol. 1.
(31) Duer, M. J. *Solid-State NMR Spectroscopy Principles and Applications*, 2004; Vol. 2.
(32) Dixon, W. T. *J Magn Reson* **1984**, *57*, 85.
(33) Dan, H.; Nishikiori, S.; Yamamuro, O. Tridymite-like host clathrate [K(H2O)(n)][CuZn(CN)(4)]: crystal structure, guest molecular motion and properties. *Dalton T* **2011**, *40*, 1168.
(34) Pake, G. E. Nuclear Resonance Absorption in Hydrated Crystals - Fine Structure of the Proton Line. *J. Chem. Phys.* **1948**, *16*, 327.

Chapter 3

Cation and Anion Transport in a Dicationic Imidazolium-Based Plastic Crystal Ion Conductor

Reprinted with permission from Bryce E. Kidd, Mark D. Lingwood, Minjae Lee, Harry W. Gibson, and Louis A. Madsen, Journal of Physical Chemistry B, **2014**, *118 (8)*, 2176-2185

© 2014, American Chemical Society.

Abstract

Here we investigate the organic ionic plastic crystal 1,2-bis[*N*-(*N'*-hexylimidazolium-d_2(4,5))]ethane $2PF_6^-$ in one of its solid plastic crystal phases by means of multinuclear solid-state (SS) NMR and pulsed-field-gradient NMR diffusometry. We quantify distinct cation and anion diffusion coefficients as well as the Arrhenius diffusion activation energies (E_a) in this *dicationic* imidazolium-based plastic crystal. Our studies suggest a change in transport mechanism for the cation upon varying thermal and magnetic treatment (9.4 T), evidenced by differences in cation and anion E_a. Moreover, variable temperature ^2H SSNMR lineshapes support a change in local molecular environment upon slow cooling in B_0. We quantify the percentage of mobile anions as a function of temperature with ^{19}F SSNMR, wherein two distinct spectral features are present. We also comment on the Arrhenius pre-exponential factor for diffusion (D_0), giving insight into the number of degrees of freedom for transport for both cation and anion as a function of thermal treatment. Given the breadth and depth of our measurements, we propose that bulk ion transport is dominated by anion diffusion in ionic-liquid-like domain

boundaries separating crystallites. This study elucidates fundamental properties of this plastic crystal, and allows for a more general and deeper understanding of ion transport within such materials.

3.1 Introduction

Solid-state electrolytes, such as the perfluorosulfonate ionomer Nafion®, have garnered much interest in the past decades for use in applications ranging from batteries to fuel cells.[1] Not only are new applications emerging, but new phenomena are being unveiled in these complex systems.[2] From a battery and fuel cell standpoint, a highly conductive stable matrix that allows fast charge transport from anode to cathode is required, and this conduction arises from intrinsic properties of the solid-state electrolyte. While ionic polymers such as Nafion® are exceptional solid-state electrolytes, ion conduction is highly dependent on small volatile molecules (usually water) to mediate charge transport. This dependence on a volatile small molecule results in reduction of conductivity at elevated temperatures when the small molecule evaporates out of the electrolyte matrix.[3]

In contrast, a relatively new class of solid-state electrolytes known as organic ionic plastic crystals (OIPCs) have shown competitive ionic conductivity (10^{-3} S cm^{-1}) without some of the disadvantages of polymer electrolyte conductors. Similar to ionic liquids (ILs), OIPCs are electrolytes consisting purely of cations and anions. At room temperature (25°C), an IL is a liquid salt, while an OIPC is a solid salt.[4] Unlike ILs, OIPCs exhibit efficient packing through long-range crystalline order of ions, but have short-range disorder where isotropic states (i.e., isotropic rotational mobility of the cation and/or anion about one or more axes) exist below the melting temperature (T_m).[4,5] OIPCs have generated great interest due to their high ionic

conductivity in one or more solid phases, which is attributed to joint rotational and translational motions within the crystalline lattice (i.e., rotator phase).[4,5] Many OIPCs possess multiple high enthalpy first-order solid-solid phase transitions below T_m and conductivity tends to increase in the higher temperature phases.[4-7]

It is well known that ion conduction within an ionic solid can occur through the classical "ion hopping" mechanism, whereby open vacancies within the crystalline lattice can promote diffusion.[8] If vacancies are present, charge neutrality must be conserved, so for every vacant cation there must be a vacant anion within the lattice (commonly known as Schottky disorder).[8] In conjunction with conductivity and differential scanning calorimetry (DSC),[9] positron annihilation spectroscopy (PALS) studies[10] on OIPCs have shown relationships between the size and number of vacancies as a function of temperature, as well as discontinuous changes in the free-volume of vacancies. Such behavior supports the ion hopping mechanism, as strong evidence suggests correlations between sizes of individual cations/anions, cation-anion pairs, and free-volume changes within the crystalline lattice.[10] While this holds true for OIPCs composed of small cations and/or anions, large steric or ionic potential barriers in the crystalline lattice can make ion transport difficult for more bulky cations and anions. For a system in which fast ion conduction is observed but cannot reasonably occur within the crystalline lattice, one must rethink the ion transport mechanism.

Because OIPCs are polycrystalline materials, grain boundaries on the nanometer-to-micron scale are naturally present. In general, grain boundaries form as a result of a mismatch in crystallite orientations in a polycrystalline material. Synthesis,[11] crystallite nucleation when cooling from above T_m,[12] thermal treatment,[11] and small applied forces[4] may induce and alter the size and number of grain boundaries present in a polycrystalline material. Previous work by

Dosseh *et al*.[13] showed that molecular plastic crystals, such as 1,4-dioxane (T_m = 11°C), cyclohexanol (T_m = 25°C), cyclohexane (T_m = 7°C), pivalic acid (T_m = 37°C), and succinonitrile (T_m = 58°C), melt at the grain boundary up to 10° below the bulk T_m. This is commonly known as the pre-melting phenomenon and occurs at the surface of a crystallite where gradual melting prior to T_m occurs. Through variable temperature ^{1}H SSNMR, Dosseh *et al*. observed a two-component system with a narrow signal centered on top of a broad signal. The narrow and broad signals were assigned to material in the grain boundary and crystallite, respectively. Approaching T_m caused the broad signal to diminish, accompanied by an increase in narrow signal.[13] For OIPCs, similar NMR spectral features have been reported for pure and doped forms of the materials. However, such spectral features are highly dependent on the cation-anion pair and concentration of dopant. While collections of dynamic crystalline defects (i.e., vacancies) can influence ion transport within OIPCs, grain boundaries (nm - μm in size) between abutting crystallites that contain non-crystalline ions can also contribute to ion transport. For OIPCs, such collections of defects have been regarded as heterogeneous and dynamic (i.e., amorphous domain boundaries), wherein the bulk material is composed of an amorphous and crystalline component.[14] In the context of this work, we will refer to nm - μm lengthscale amorphous phase components, whether due to abutting of crystal grains or due to dynamic defects, as 'domain boundaries.'

Diffusion through the domain boundary represents an interesting way to think about ion transport within polycrystalline materials (and other materials). Since domain boundaries do not represent the lowest free energy state, usually only a small fraction of the total number of cations and anions reside within the domain boundary, and thus the molecules in the domain boundary may give a low contribution to the overall material conductivity. The Nernst-Einstein equation[9]

$$\sigma = \frac{(D_+ c_+ + D_- c_-)q^2}{kT} \quad , \tag{3.1}$$

where σ is conductivity, $D_{+/-}$ are diffusion coefficients for cation (+) and anion (−), $c_{+/-}$ are the concentrations of each charge carrier, q is the unit charge of the carrier, and kT is the average thermal energy (k is Boltzmann's constant and T is temperature), shows us that traditionally the contribution to the conductivity from domain boundaries should be small. It can be seen that σ linearly depends on each of the quantities $D_{+/-}$ and $c_{+/-}$. However, in order to optimize OIPCs, it is imperative to fully understand $D_{+/-}$ in both the solid phases and domain boundaries of these materials. Domain boundary diffusion represents one diffusion pathway in OIPCs, and the local energetics associated with $D_{+/-}$ are not well understood. Variable temperature conductivity is commonly used to obtain translational activation energies (E_a); however, such measurements lack chemical specificity. In conjunction with chemically specific PFG-NMR diffusometry (discussed below), the Arrhenius equation

$$D = D_0 e^{\frac{-E_a}{kT}} \quad , \tag{3.2}$$

allows analysis of the T-dependent cation and anion diffusion coefficient D, thus giving insight into local energetics (i.e., activation energy E_a) on the pre-diffusion (~ 1 ps) timescale, commonly referred to as the inertial or ballistic timescale.[15,16] D_0 can be described as diffusion at infinite temperature or the "barrierless" diffusion coefficient, and kT is the average thermal energy. A deeper investigation on the pre-diffusion lengthscale allows understanding of collective interactions that govern the transport of small molecules in various environments, particularly environments where a crystalline lattice does not exist but diffusion occurs.

While DSC, conductivity, PALS, and X-ray diffraction have been used extensively to understand the OIPCs studied thus far, analyzing chemically specific transport properties, such

as D, E_a, and D_0, will bring more comprehensive understanding of ion transport and local energetics. Previously, we measured separate cation and anion diffusion coefficients for free ILs, such as [C_2mim][TfO], [C_2mim][BF_4], [C_4mim][TfO], and [C_4mim][BF_4], to better understand ion associations within the polymeric electrolyte membrane (PEM) Nafion 117 (N117) as a function of water content χ_{water} (n_{water}:n_{ILs}).[17] We showed anomalous cation diffusion (D_{cation} > D_{anion} by 30 – 50%) at low χ_{water} values as a result of anion aggregations and water-screened ionic interactions at high χ_{water} values. Thus, within pure ionic systems, such associations may influence E_a of cations, anions, and solvents. D_0 can also be used to report on the configurational degrees of freedom (i.e., entropic contributions) governing diffusion of various mobile species.[15,16,18,19]

Here we employ multinuclear pulsed-field-gradient (PFG) NMR diffusometry to report on the diffusion of cations and anions as well as their local energetics (i.e., E_a), and we use multinuclear static solid-state NMR to spectroscopically observe both crystalline and non-crystalline ions. We show that the ionic species that dominate bulk conductivity reside within the domain boundary. Strikingly, cooling in the strong spectrometer magnetic field (B_0) of 9.4 tesla (T) induces a weak alignment of crystallites such that the E_a for the cation increases from 14 to 39 kJ mol^{-1}. Additionally, we quantify the percentage of mobile anions as a function of temperature from variable temperature ^{19}F SSNMR, where two distinct spectral features are observed. We also comment on the pre-exponential factor (D_0), giving insight into the configurational degrees of freedom[15,16,18,19] and how the local environment affects E_a for both cation and anion as a function of thermal treatment.

3.2 Experimental

3.2.1 Sample preparation

The deuterated analog of bis[*N*-(*N'*-hexylimidazolium)] salt was synthesized in three steps (Scheme 3.1):

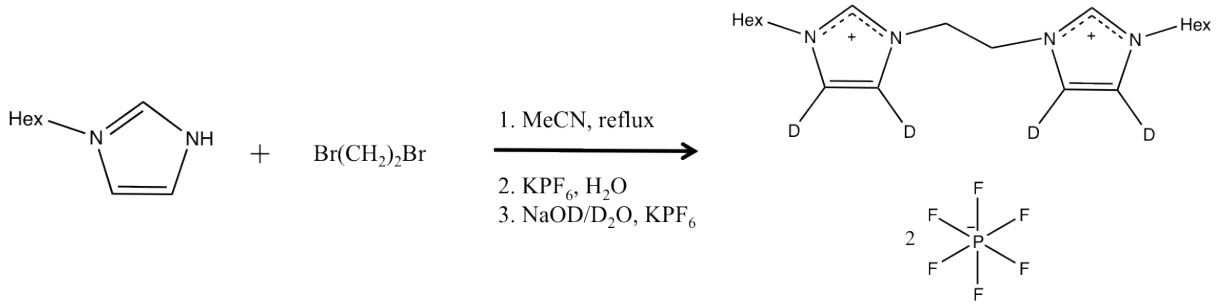

Scheme 3.1. Synthesis of 1,2-bis[*N*-(*N'*-hexylimidazolium-d_2(4,5))]ethane $2PF_6^-$.[6,7]

First, the quaternization coupling reaction of 1-hexylimidazole (2 molar equivalents) with dibromoalkane (1 molar equivalent) was carried out, followed by PF_6^- exchange in water, as previously reported.[6,7] Deuterium exchange on the 4- and 5-positions of the imidazolium was done with 10 wt % NaOD solution in D_2O. The final product was precipitated in aqueous (H_2O) saturated KPF_6 solution and was a white crystalline solid at room temperature (25°C). It should be noted that the labile 2-position had been also deuterated but reverted back to protonated form upon introduction of the saturated aqueous KPF_6 solution.[6,7] Drying in a vacuum oven for 24 hours with heat gave the colorless crystalline deuterated product with a quantitative yield. The material (~30 mg) was loaded into a 5 mm outer diameter glass bulb, heated in an oil bath under vacuum to 210°C (T_m = 196°C), and degassed under vacuum to prevent degradation. Upon cooling to room temperature (25°C) and leaving under vacuum overnight, the glass bulb was sealed with an oxygen/natural gas torch.

3.2.2 Variable temperature solid-state NMR

All $^1H/^2H/^{19}F$ variable temperature (^1H: 207 – 25°C, ^2H: 196 – 30°C, ^{19}F: 205 – 40°C) SSNMR experiments were performed using a 400 MHz Bruker Avance III WB NMR spectrometer,

equipped with a two channel HX wideline static solids probe (Bruker HP WB 73A). The sample was allowed to equilibrate at each temperature for twenty minutes prior to spectral acquisition. The quadrupolar (solid) echo pulse sequence[20] was used to acquire ^{2}H NMR spectra, and a simple pulse-acquire sequence was used to acquire ^{1}H/^{19}F NMR spectra. For this study, a series of deuterated standards, hexamethylbenzene-d_{18} (HMB-d_{18}) (T_m = ~167°C) purchased from Sigma Aldrich with > 99% purity, urea-d_4 (T_m = ~133°C) purchased from Sigma Aldrich with > 98% purity, and the liquid crystal 2,5-bis-(*p*-hydroxyphenyl)-1,3,4-oxadiazole (ODBP-Ph-C_7-*d6*) [phase map: crystal to smectic Y (148°C), smectic Y to B2 (166°C), B2 to biaxial nematic (173°C), biaxial nematic to uniaxial nematic (215°C), and uniaxial nematic to isotropic (222 °C)][21,22] were used to calibrate the probe at multiple temperatures, as each of these materials displays distinct changes in quadrupole splitting $\Delta\nu_Q$ at their respective phase transitions.

3.2.3 Variable temperature pulsed-field-gradient NMR

All variable temperature (75 – 65°C, PFG probe temperature maximum is 80°C) ^{1}H (cation diffusion) and ^{19}F (anion diffusion) PFG-NMR diffusometry experiments were performed using a 400 MHz Bruker Avance III WB NMR spectrometer, equipped with an MIC probe coupled to a Diff60 single-axis (z-axis) gradient system. In the PFG-NMR diffusometry experiment, the Stejskal-Tanner equation (Equation 3.3)[23] was fit to the measured signal amplitude I as a function of gradient strength g,

$$I = I_0 e^{-D\gamma^2 g^2 \delta^2 (\Delta - \frac{\delta}{3})}, \tag{3.3}$$

where I_0 is the signal amplitude at $g = 0$, γ is the gyromagnetic ratio, δ is the effective gradient pulse length, Δ is the diffusion time between gradient pulses, and D is the self-diffusion coefficient.[23] The simple and robust pulsed-gradient stimulated echo (PGSTE) sequence was used with $\pi/2$ pulse lengths of 7 μs and 7.1 μs for cation (^{1}H) and anion (^{19}F), respectively. A

repetition time of 1.3 s, a diffusion time of Δ = 35 ms, and acquisition times of 15 ms (cation) and 10 ms (anion), were used for cation and anion diffusion measurements. A sinusoidal gradient pulse length of δ = 3.14 ms (actual pulse length = 1.57 × 2.00 ms, where 2.00 ms is the effective pulse length as if the pulse were rectangular) and maximum gradient strength of 1850 G cm^{-1} was used to achieve 80% signal attenuation in eight steps. Sufficient signal-to-noise ratio (SNR) for each data point was achieved with 64 scans and 320 scans for cation and anion, respectively. Acquisition times of 16 ms and 8 ms were used for cation and anion, respectively. The PGSTE parameters were calibrated as previously reported.[24] Cation and anion spin-lattice relaxation times (T_1) in phase S_3 were measured using the inversion-recovery pulse sequence to be 140 ms and 630 ms, respectively. Cation and anion spin-spin relaxation times (T_2) were measured using the Carr-Purcell-Meiboom-Gill pulse sequence to be 6 ms and 48 ms, respectively.

3.3 Results and discussion

The DSC trace for the present OIPC (Figure 3.1) displays three distinct solid-solid phase transitions, where each phase has distinct ion transport behavior.[6,7] High T_m's for this class of OIPCs are due to the many hydrogen – fluorine contacts, reported from single crystal X-ray diffraction.[7] For the present study, we studied phases S_3 through I using variable temperature multinuclear NMR experiments, and studied phase S_3 only using variable temperature multinuclear PFG-NMR diffusometry experiments, due to NMR probe temperature limitations (80°C).

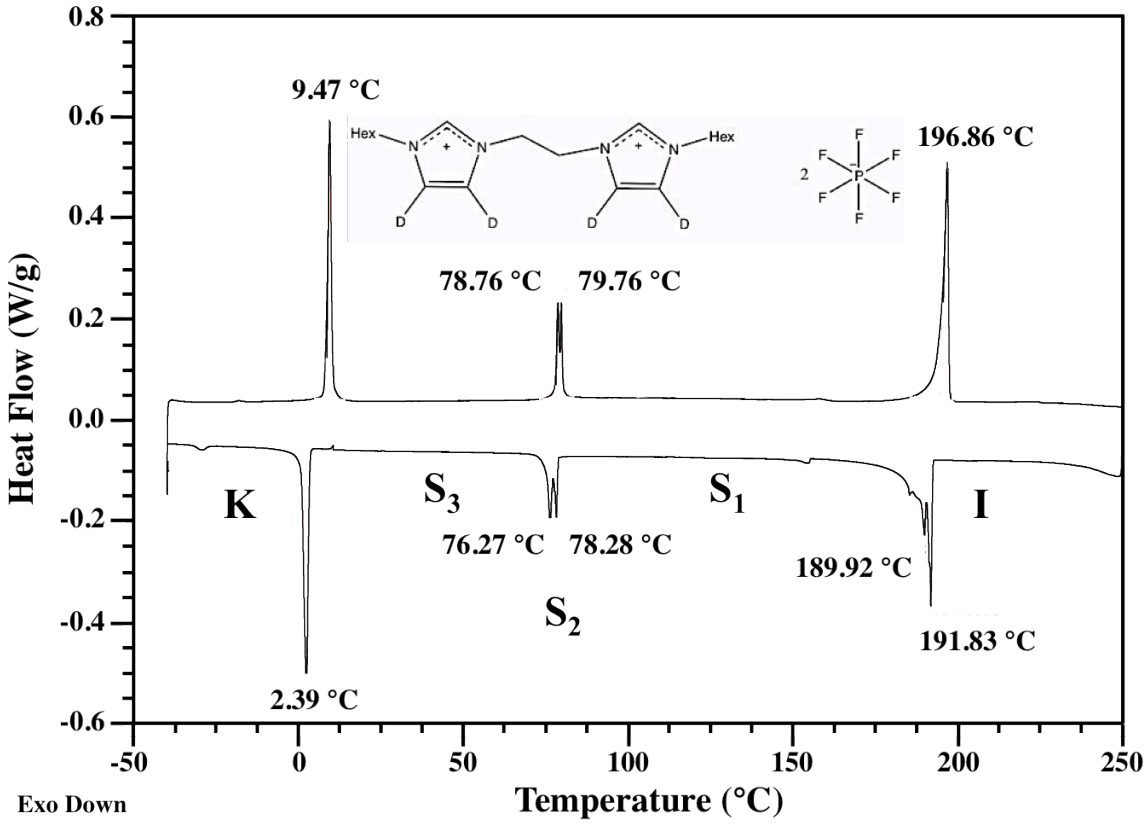

Figure 3.1. Differential scanning calorimetry (DSC) trace (heating and cooling rate 5 K min^{-1}, N_2) of the ionic compound 1,2-bis[*N*-(*N'*-hexylimidazolium-d_2(4,5))]ethane $2PF_6^-$ used in this study. K (crystal), S_3, S_2, and S_1 all represent solid phases, and I represents the isotropic melt.

3.3.1 Temperature-dependent ^{2}H NMR studies

Figure 3.2 shows a representative ^{2}H NMR spectrum obtained at room temperature (25°C, phase S_3) before heating the sample in the magnetic field, which displays an isotropic distribution of crystallite orientations with B_0, thus forming the well known Pake powder pattern.[25] Such a spectrum can be described by

$$\Delta\nu_Q(\theta_Q) = 3\pi C_Q \times \frac{1}{2}(3\cos^2\theta_Q - 1) \quad , \tag{3.4}$$

where θ is the angle of the C-^{2}H bond (^{2}H being a spin I = 1 quadrupolar nucleus) with respect to the spectrometer field B_0, C_Q is the quadrupole coupling constant, and $\Delta\nu_Q$ is the quadrupolar (spectral) splitting for a given nucleus oriented at angle θ.[26] C_Q represents the magnitude of the nuclear quadrupole moment interaction with the electric field gradient, which is sensitive to the local environment. We observe a splitting ν_Q between the two singularities (θ_Q = 90°) of 121 kHz. Since ^{2}H is spin I = 1, $\nu_Q = 3C_Q/4$,[27] thus C_Q = 161 kHz. Figure 3.2 also shows a small single peak centered at 0 Hz, which likely arises from a small (~ 1 %) population of motionally averaged mobile cations.

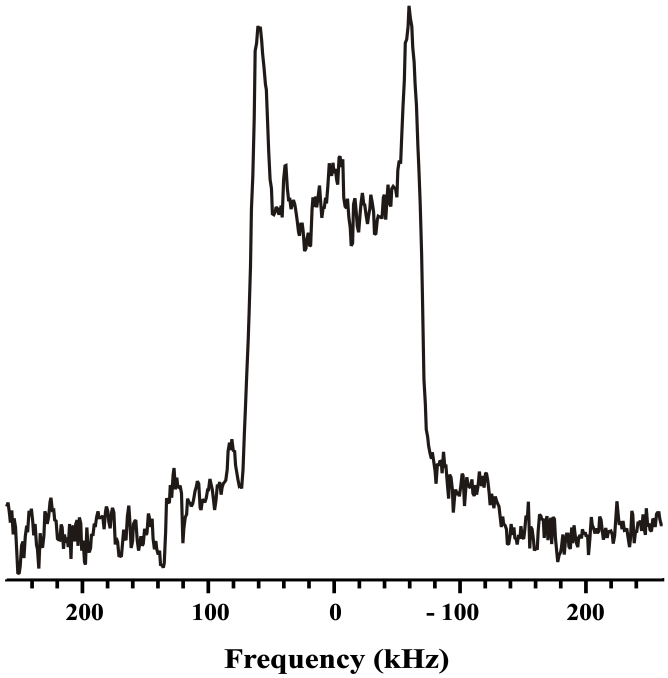

Figure 3.2. Room temperature (25°C) ^{2}H NMR measurement of OIPC powder (before heating in the magnetic field) displays the well-known Pake pattern, confirming a random orientation of crystallites with respect to B_0. We observe a ν_Q = 121 kHz, which translates to a C_Q = 161 kHz.

We use temperature-dependent ^{2}H NMR to probe the imidazolium dynamics through all solid phases and into the isotropic phase. Figure 3.3 shows ^{2}H NMR spectra as a function of temperature (steps of 5 – 20°C with 30 min equilibration for each step over the course of 16 hours), in phases I, S_1, and S_3. When the OIPC is heated above T_m (196°C), we observe a single narrow signal, indicating that the quadrupolar interactions average to zero due to rapid tumbling of molecules in the isotropic (melt) state. Upon cooling to 85°C (phase S_1) in the magnetic field, we still observe a significant fraction of the isotropic phase, suggesting that isotropic tumbling of many cations occurs, even in the solid state. Two distinct spectral features, a narrow signal residing on a broad signal, occur at 50°C (phase S_3). However, at 30°C (phase S_3) the isotropic signal diminishes dramatically along with the broad flat shoulders, leaving behind a broad doublet ($\Delta\nu_Q \approx 120$ kHz) due to an anisotropic distribution of crystallites. According to Equation 3.4, and if there is an average alignment axis present for the crystallites, $\Delta\nu_Q$ should reduce by half when the alignment axis relative to the B_0 field is rotated to $\theta = 90°$. Therefore, we tested this by manually rotating the sample 90° while still in the S_3 solid phase. The bottom trace of Figure 3.3 shows that $\Delta\nu_Q$ is approximately halved ($\Delta\nu_Q \approx 60$ kHz) when $\theta = 90°$. The lowest two spectra in Figure 3.3 are after slow cooling and multiple thermal cycles, and the central signal is reduced relative to the broad signals and relative to the spectrum 3rd from bottom, which was after initial cooling in the field. These results indicate that melting and then cooling in the magnetic field induces alignment of crystalline domains inside this material.

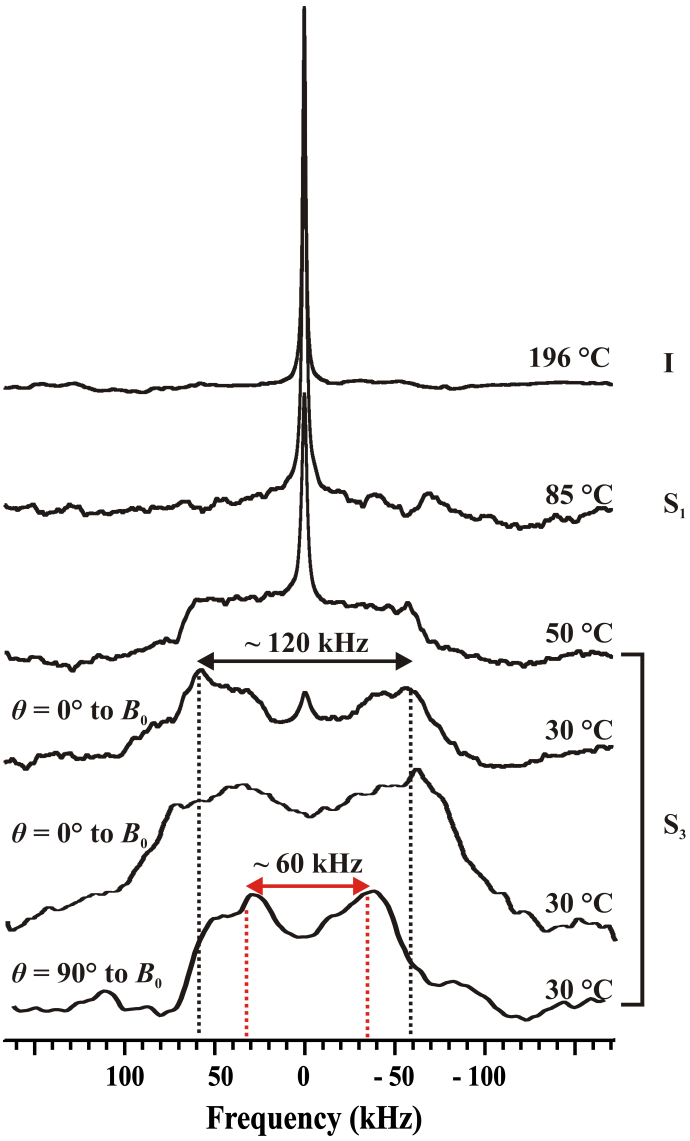

Figure 3.3. ^{2}H NMR spectra vs. temperature displaying imidazolium orientation and dynamics in phases I, S_1, and S_3. One observes weak alignment upon cooling in the magnetic field, evidenced by the broad quadrupolar doublet in phase S_3 at 30°C when $\theta = 0°$ followed by a reduction in $\Delta\nu_Q$ by approximately half when the sample is manually rotated to $\theta = 90°$. The spectrum 3rd from bottom at 30°C was after initial cooling, while the lowest two spectra were for the subsequently melted sample that was then reoriented in the solid phase.

We propose a broadly distributed but anisotropic crystallite alignment upon melting and subsequent cooling in the presence of B_0. Alignment of the long axis of a molecule (i.e., the molecule has an aspect ratio > 1) along the direction of a strong magnetic field B_0 has been observed for many liquid-crystalline (LC) systems,[28] but not so far for an OIPC. Within a magnetically aligned LC phase, the molecules collectively align to minimize magnetic free energy. We propose a related effect for OIPCs composed of anisotropic crystallites. While OIPCs and LCs are quite different, molecular susceptibility anisotropy effects may extend to OIPC *crystallites* composed of aromatic rings (i.e., imidazolium). Crystallites can have an aspect ratio associated with them and thus magnetic susceptibility anisotropy may exist. We believe that crystallite alignment with B_0 begins immediately upon solidification from T_m but is not observed until lower temperatures due to imidazolium motional averaging. Figure 3.4 gives a conceptual illustration to depict realignment of the crystallites upon cooling in B_0. These ^{2}H NMR results are the first to show crystallite alignment within an OIPC induced by a strong magnetic field, carrying implications for orientational control of plastic crystal ion conductors. As with other systems,[2] enhanced transport can result from control of morphological alignment of elongated crystallite structures.

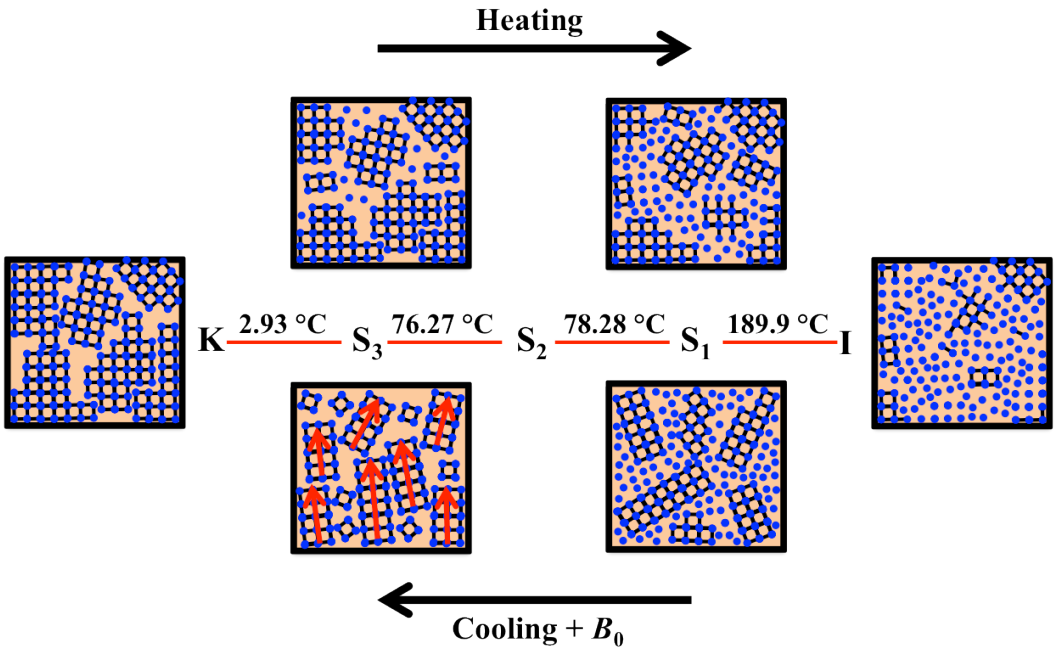

Figure 3.4. Illustration of crystallite realignment model in a magnetic field upon heating to phase I and cooling to phase S_3 (transition temperatures taken from DSC exotherm). Cooling in B_0 induces the formation of anisotropic crystallites such that the crystallite long-axes (red arrows for emphasis) become biased along B_0.

3.3.2 Temperature-dependent ^{19}F and ^{1}H NMR

To augment our variable temperature ^{2}H NMR results, we investigate how anion (^{19}F) and cation (^{1}H) dynamics change as a function of temperature in the solid phases, as this gives molecular insights into bulk material properties. Figure 3.5 shows representative ^{19}F NMR spectra as a function of temperature (205 – 40°C) in 20° increments. In the isotropic phase we clearly observe the J_{PF} scalar coupling (i.e., doublet in Figure 3.5) between phosphorous and fluorine. This coupling constant, J_{PF} = 720 Hz, is exactly that observed in a standard solution of KPF_6. We note that the small doublet at -10 kHz with a splitting of 1 kHz cannot be from PF_6^- and could be a small sample impurity. However, we do not see this doublet in our T_2-weighted PFG spectrum (discussed below), thus it could arise from some ^{19}F-containing material within

our solids probe. Cooling the sample to phase S_1 drastically decreases the intensity of the isotropic signal, and a broad signal also emerges. We might be tempted to rationalize that the isotropic averaging occurs through the rotation of PF_6^- about the fixed crystalline lattice point (a rotator phase effect). However, such spectral features are observed for other OIPCs[11,29,30] and molecular crystals,[13] whose isotropic signal is suggested to be ions diffusing between crystallites (i.e., in domain boundaries), while the broad signal is suggested to be ions in a rigid environment (i.e., in crystallites). The ratio of narrow to broad signals changes continuously and strongly over this temperature range, also suggesting that the isotropic signal is not simply PF_6^- in fixed lattice positions. Thus we assign the isotropic signal to PF_6^- within the domain boundary and the broad signal to crystalline PF_6^-.

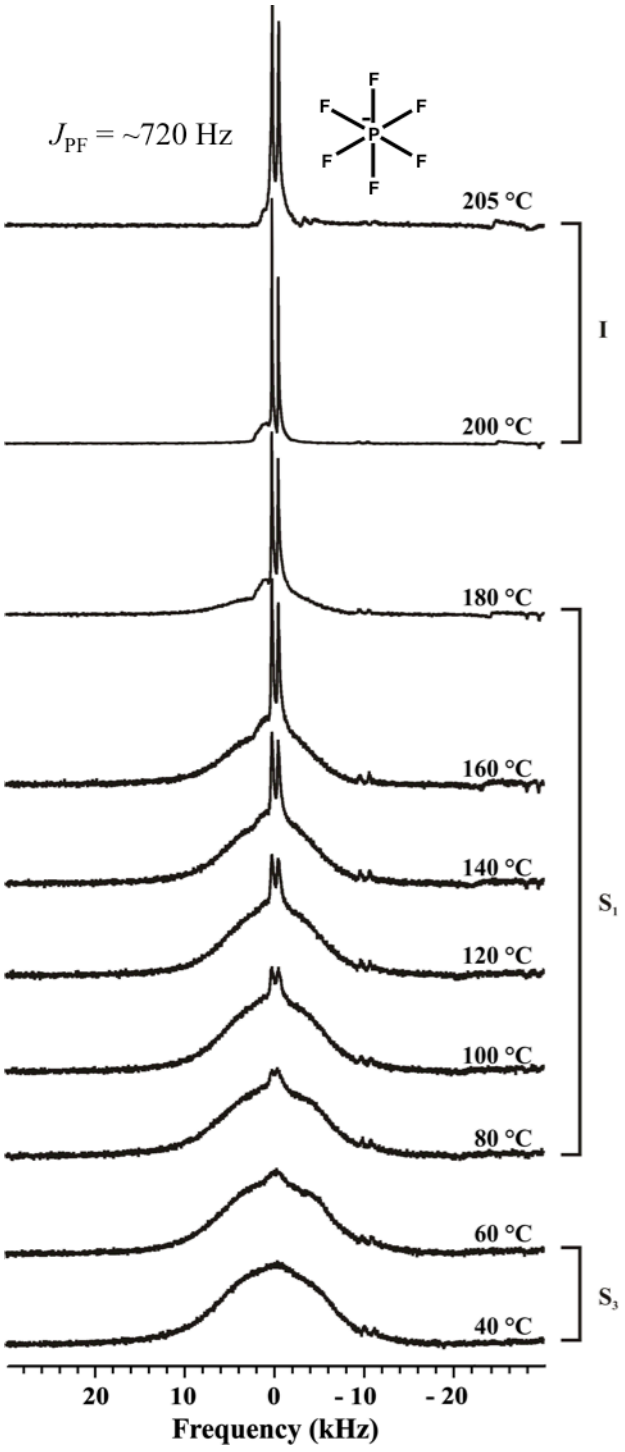

Figure 3.5. ^{19}F spectra as a function of temperature. Spectra at 205°C, 200°C, and 180°C are decreased on the vertical scale by factors of 10, 10, and 4, respectively, relative to the other spectra. We observe an isotropic signal from phase I to phase S_3 with J_{PF} = 720 Hz, consistent

with the PF_6^-. The isotropic signal indicates rapidly rotating and diffusing PF_6^- in the domain boundary, supporting ^{19}F PFG-NMR diffusometry. The broad signal corresponds to PF_6^- in crystallites.

We quantify the relative proportions of PF_6^- in the domain boundary and crystallite from Figure 3.5 through integration of the broad and narrow spectral components (Figure 3.6). To compensate for the area integrated below the isotropic signal (i.e., part of the broad signal) a reference area under the broad signal is subtracted from the isotropic region integral. At 190°C (just below phase I), 40 % of the PF_6^- anions (and by charge balance, the counter-cations) reside in the domain boundaries (narrow isotropic signal) while the remaining 60 % reside in the crystallites (broad signal). With decreasing temperature, an exponential-like decrease in isotropic PF_6^- is observed. Although ionic conductivity measurements for the OIPC used in this study have not been reported, variable temperature σ values in the range of $10^{-5} - 10^{-14}$ S cm^{-1} were reported for the related materials 1,2-bis[*N*-(*N*'-nonylimidazolium)]ethane $2PF_6^-$, 1,2-bis[*N*-(*N*'-decylimidazolium)]ethane $2PF_6^-$, and 1,2-bis[*N*-(*N*'-dodecylimidazolium)]ethane $2PF_6^-$.[6] As discussed above, the Nernst-Einstein equation (Equation 3.1) relates conductivity to the diffusion coefficients and concentrations of charge carrying species. Thus, the initially small percentage of fast tumbling PF_6^- and relatively small diffusion coefficient (discussed below) observed in the large temperature window (40 - 140°C) can explain the initially low but accelerating increase in conductivity with *T*, as reported for other OIPCs.[6] Previous work by Dosseh *et al*. reported the premelting of polycrystalline materials at the surface of domain boundaries prior to T_m.[13] Based on the present variable temperature ^{19}F NMR results, we are apparently observing gradual melting of the material at the surface of the domain boundary until ≈150°C when a more dramatic increase in "local melting" occurs as *T* approaches T_m.

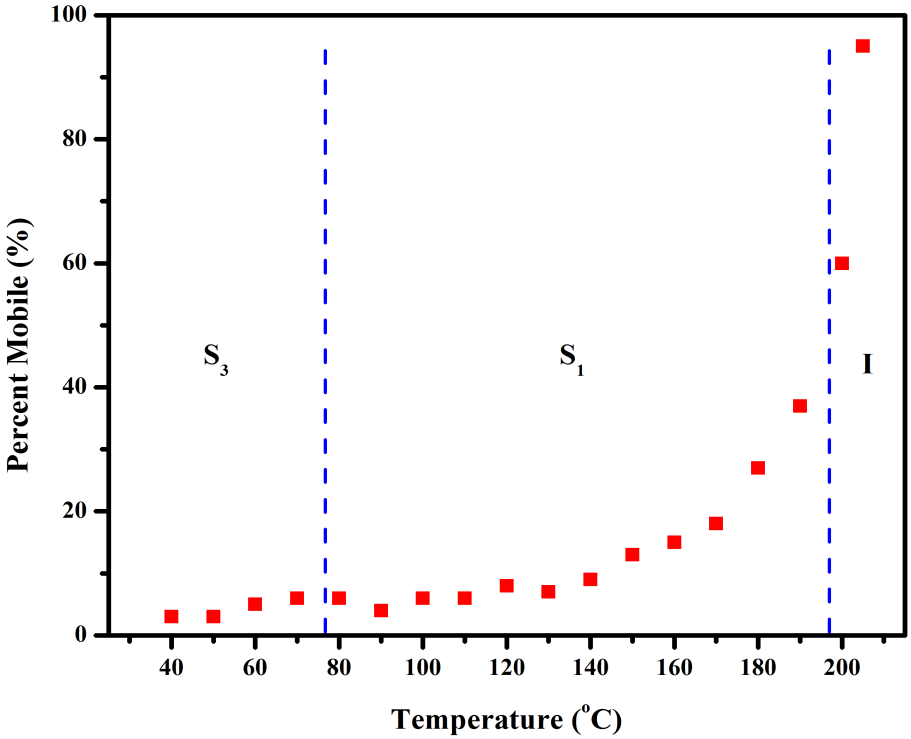

Figure 3.6. Percentage of mobile PF_6^- (i.e., in the domain boundary) as a function of temperature. We observe a gradual increase in percentage below the middle of phase S_1, and an exponential-like growth above 140°C. The dotted lines represent the transition temperatures from DSC.

Figure 3.7 shows variable temperature ^{1}H NMR. Two-component spectral features do not appear as cleanly as in our ^{19}F NMR results due to the spectral crowding and somewhat broad lines, but we observe clear spectral changes in phases S_1 and S_3. Dipolar couplings between protons contain the same orientation dependence with B_0, but we do not observe clean orientation dependence with respect to B_0 as in ^{2}H NMR, further emphasizing the advantage of isotopic labeling. Clearly isotropic mobility exists well below T_m, consistent with our variable temperature ^{2}H NMR spectra, wherein an isotropic signal is observed even down to 25°C. Note

that a residual signal from protons 2 and 3 remains after the ^{2}H exchange reaction. The proton 2 and 3 signals differ by only 0.13 ppm at 400 MHz when measured in solution (acetone-d_6),[7] and thus our lines are too broad to resolve them.

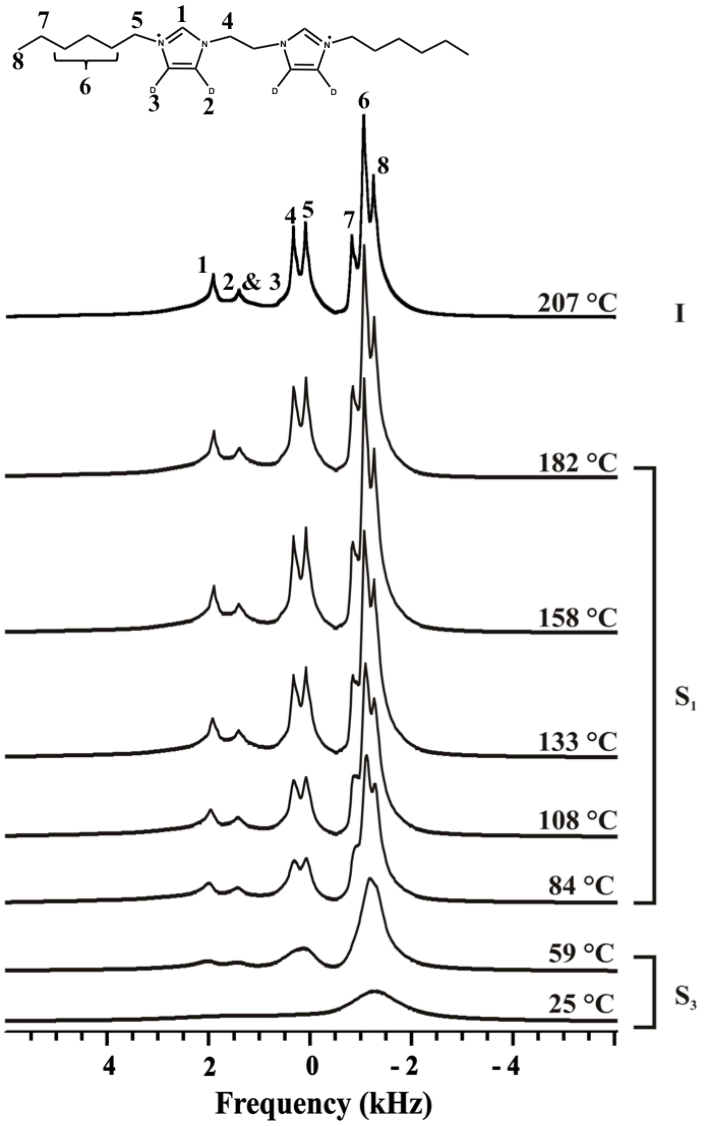

Figure 3.7. ^{1}H NMR spectra as a function of temperature. Above T_m, we clearly see all ^{1}H signals. An unresolved residual signal from protons 2 and 3 remains after the ^{2}H exchange reaction. We observe a change in spectral features when cooling in phase S_3, which is consistent with variable temperature ^{2}H NMR spectral changes in phase S_3.

3.3.3 Thermal and magnetic treatment

Previous work by Rana *et al*.[11] on the OIPC choline dihydrogen phosphate [Choline][DHP] doped with phosphoric acid [H_3PO_4], trifluoromethanesulfonic acid [TfOH], and bis-trifluoromethanesulfonyl imide [$HN(Tf)_2$] showed that the thermal history of an OIPC critically affects macroscopic and microscopic properties. Changes were reported in ^{1}H NMR spectra for the pure material "as-prepared" and annealed (both with no dopants).[11] The ^{1}H NMR spectra at 100°C for both materials displayed two distinct spectral components: a broad component (~ 35 kHz) representative of crystalline material, and a narrow component (~ 300 Hz) representative of non-crystalline material. The narrow component was suggested to be diffusing cations. Annealing the material afforded the formation of less defective crystallites (i.e., less Schottky-disorder) and/or fewer/smaller domain boundaries, as evidenced by the increase in the broad component (i.e., more crystalline material) and decrease in conductivity.[11]

To study the effect of varying magnetic and thermal history on transport, we present a systematic study of ^{1}H and ^{19}F PFG-NMR diffusometry experiments with two different thermal treatments (slowly and rapidly cooled out of B_0) in conjunction with the magnetic treatment (slowly cooled in B_0) resulting in different observations in phase S_3. The magnetic treatment involved starting in the melt state in B_0, then the temperature was decreased in steps of 5 – 20°C with 30 min equilibration between steps, all while acquiring NMR data as in the ^{1}H, ^{2}H, and ^{19}F studies described above. Due to PFG-probe temperature limitations (maximum 80°C), the B_0 aligned sample was transferred from the wideline static solids probe to the PFG probe for diffusion measurements. The second treatment was to melt the material in an oil bath, remove it, and cool it quickly in air to room temperature (sample cool to touch within 10 min), thus erasing

the crystallite alignment history outside of B_0. The third thermal treatment was to melt the material in an oil bath and allow it to cool to room temperature while held in the oil bath (≈2 hrs), resulting in a slow cooling thermal treatment outside of B_0.

3.3.4 Diffusion coefficient vs. temperature

We conducted cation (^{1}H) and anion (^{19}F) PFG-NMR diffusometry experiments on the OIPC 1,2-bis[N-(N'-hexylimidazolium-d_2(4,5))]C_2H_4 $2PF_6^-$. The accessible PFG-NMR pulse sequence parameters δ and Δ depend on the OIPC relaxation time constants T_2 and T_1, respectively. In the PFG experiment, a T_2-weighted spectrum is produced (Figure 3.8) as a result of T_2 relaxation during the gradient pulse encoding periods. Thus, we do not observe signals with relatively short T_2 as we do with simple pulse-acquire spectra. The spectral components with short T_2 correspond to the slowly rotating material components, in this case the ions in the crystallites.

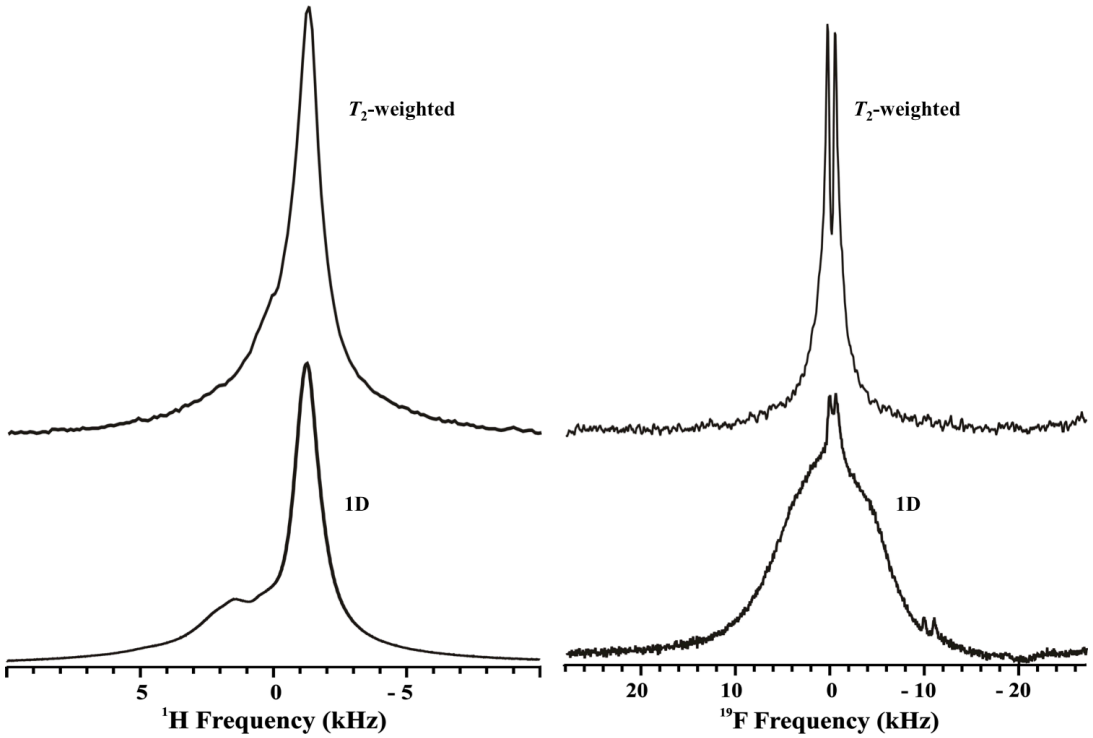

Figure 3.8. Comparison of static 1D and T_2-weighted PFG ^{1}H and ^{19}F spectra, all within phase S_3, emphasizing that PFG-NMR diffusometry measures only mobile cations and anions within this material. The T_2-weighted signals result from T_2 relaxation during the gradient pulse encoding periods. ^{1}H and ^{19}F T_2-weighted spectra were scaled vertically by factors of 137 and 52, respectively, relative to 1D spectra, to allow for easy comparison.

Figure 3.9 shows Arrhenius plots of temperature-dependent diffusion measurements between 75 and 67°C (phase S_3) in 2° increments to allow measurement of E_a for the cation and anion. Note that the high precision (error in $D \leq \pm 6\%$) of these measurements allows for E_a measurements over a relatively small T range. We extended this temperature window to 41°C for one sample to verify that our measurements exhibit Arrhenius behavior over a wider temperature range. Figure 3.9 is a compilation of all Arrhenius plots with respective E_a values for both cation and anion as a function of thermal treatment. Thermal treatment of the material is critical for the following measurements, as E_a is sensitive to thermally driven changes in D.

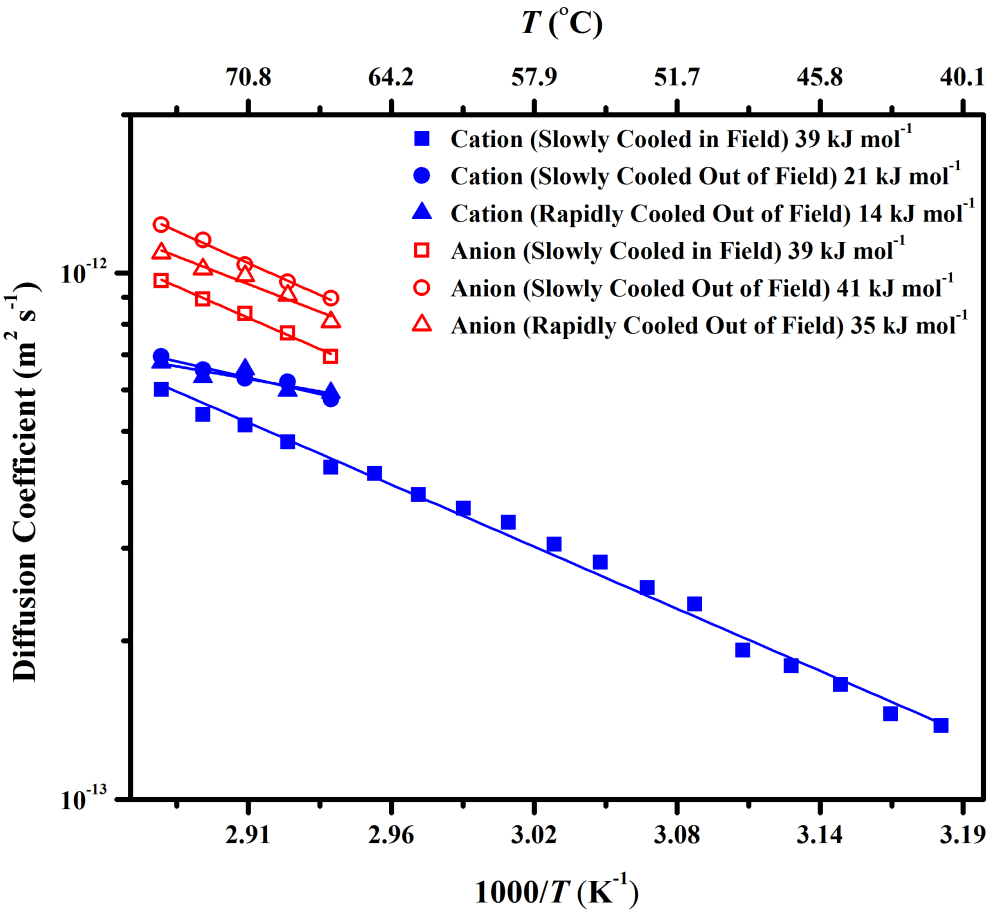

Figure 3.9. Temperature dependence of diffusion coefficient for both cation and anion as a function of thermal treatment and summary of all E_a values extracted from Arrhenius plots. Anion E_a changes fall within error as a function of thermal treatment, suggesting that the anion transport mechanism does not change significantly with respect to thermal treatment. Slow cooling in B_0 causes E_a for the cation to increase drastically to 39 kJ mol^{-1}, suggestive of a change in transport mechanism (local molecular environment). D and E_a errors are $\leq \pm$ 6% and $\pm$ 5 kJ mol^{-1} using the statistics of the linear fit.

For OIPCs, we observe that magnetically driven changes in D can strongly supplement, or even outweigh, changes due to thermal cooling rate when starting from the melt state. Interestingly, both the cation and anion have E_a values of 39 kJ mol^{-1} in phase S_3 when the

material is slowly cooled in B_0. However, when the material is slowly cooled outside of B_0, cation E_a decreases by a factor of two (39 kJ mol^{-1} to 21 kJ mol^{-1}) while anion E_a does not change, within error bars. This suggests that after cooling out of B_0, the cation local (~ 1 nm) environment is influenced such that less energy is required for ion transport, while the anion's environment remains unchanged. When the sample is rapidly cooled outside of B_0, the anion E_a is unchanged while the cation E_a appears to be lower than when slowly cooled outside of B_0, although these measurements are still within error. Rapid cooling should promote the formation of smaller or more defective crystallites (on the nm lengthscale) with more and/or larger domain boundaries (on the μm lengthscale), and this appears to manifest as a slight decrease in the activation energy for cation transport. The cation E_a change is larger when varying the magnetic cooling conditions (slow cooling in vs. out of B_0) than when varying the cooling rate (rapid vs. slow cooling out of B_0). These results indicate that the presence of a large magnetic field B_0, rather than cooling rate, dominates local energetic environment changes. This agrees with our ^2H observations and supports a crystallite orientation effect that strongly influences transport processes.

To further rationalize changes in local energetics experienced by the cation and anion within the domain boundary, we revisit the Arrhenius equation (Equation 3.2). The pre-exponential factor, D_0, contains information about the local structure (i.e., the configurational degrees of freedom, or the entropy of translation) of the system governing D for diffusing species.[15,16,18,19] For the polymer electrolyte Nafion®, experimental[15] and molecular dynamics[16] investigations have shown that D_0 depends on water content (i.e., $\lambda = mols_{H_2O}/mols_{SO_3^-}$) within the nanophase separated ion conducting channel.

We are currently working to extend the interpretation of D_0 and its quantitative significance to other materials. At the moment, we can gain at least a qualitative understanding of the relationship between E_a and D for the cation and anion by comparing their respective D_0 values. Figure 3.10 shows D_0 for the cation and anion as a function of thermal treatment. We note that our first investigation of D_0 in Nafion involved an inverted (reciprocal) error[15] and we have corrected that in these analyses.

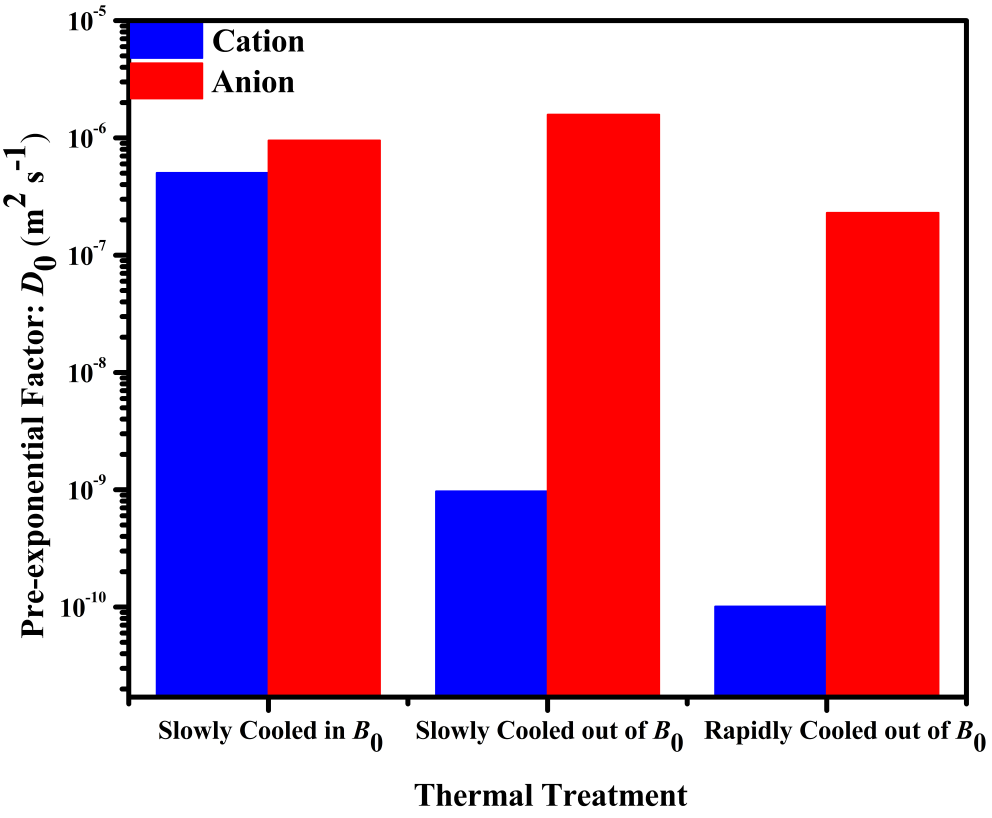

Figure 3.10. Cation and anion D_0 as a function of thermal treatment. Anion D_0 changes fall within the measurement error, suggesting that the local configurational degrees of freedom do not change with thermal treatment. The cation D_0 decreases by 3 to 4 orders of magnitude from slowly cooled in B_0 to cooled out of B_0. The D_0 error is estimated to be ± 50%.

It can be seen that the D_0 changes for the anion with respect to thermal treatment fall within measurement error, suggesting that the degrees of freedom do not change, i.e., the available anion local configurations do not change significantly with thermal treatment. Surprisingly, the cation D_0 is largest when the material is slowly cooled in B_0 (i.e., higher translational entropy, less ordered environment). Cation and anion E_a values as a function of thermal treatment might suggest D_0 to be the largest when the material is rapidly cooled out of B_0 (i.e., least restricted cation environment) and smallest when the material is slowly cooled in B_0 (i.e., most restricted cation environment). However, cation and anion D_0 values do not reflect such rationale.

When contemplating the larger cation D_0 upon slowly cooling in B_0, we can consider the alignment of crystallites (Figure 3.4) observed when the material is slowly cooled in B_0. In liquid crystals, one observes a gain in translational entropy, compared to the isotropic phase, upon alignment of anisotropic species.[31] If the anisotropic cation is aligned in anisotropic cavities formed between the crystallites (anisotropic domain boundaries), then its translational entropy may increase relative to randomly shaped (isotropic) domain boundaries. Thus, slowly cooling in B_0 may increase cation translational entropy (i.e., D_0) and decrease E_a. Aligning in B_0, however, would not influence the anion local domain boundary dynamics or translational entropy since PF_6^- is octahedral (i.e., nearly spherical). We are continuing to explore the significance of D_0 in this and other systems, and hope to provide further quantitative insight in the future.

3.3.5 Domain boundary restricted diffusion

As stated above, it has been suggested that an amorphous domain boundary can exist within these materials. We may further understand how the amorphous domain boundary influences ion transport by experimentally probing nm – μm lengthscale environments using an NMR restricted diffusion study.[17,32-34] This method has shown previous utility in probing restrictive environments

in solid-state electrolytes, where μm lengthscale morphological effects can influence small molecule/ion transport properties.[34] In the PFG-NMR diffusometry experiment, D vs. diffusion time Δ will show a flat dependence (slope = 0) if the root-mean-square displacement $\langle r^2 \rangle$ is smaller than the size of the domain containing the diffusing species. If the diffusing species samples morphological restrictions, such as crystallite walls, during Δ, a decrease in D as a function of diffusion time Δ can appear, also known as restricted diffusion. Figure 3.11 representatively shows anion D vs. Δ at 75°C (slowly cooled in B_0) in a Δ range of 10 – 200 ms, thus enabling us to probe diffusion lengths from 0.1 – 0.4 μm.

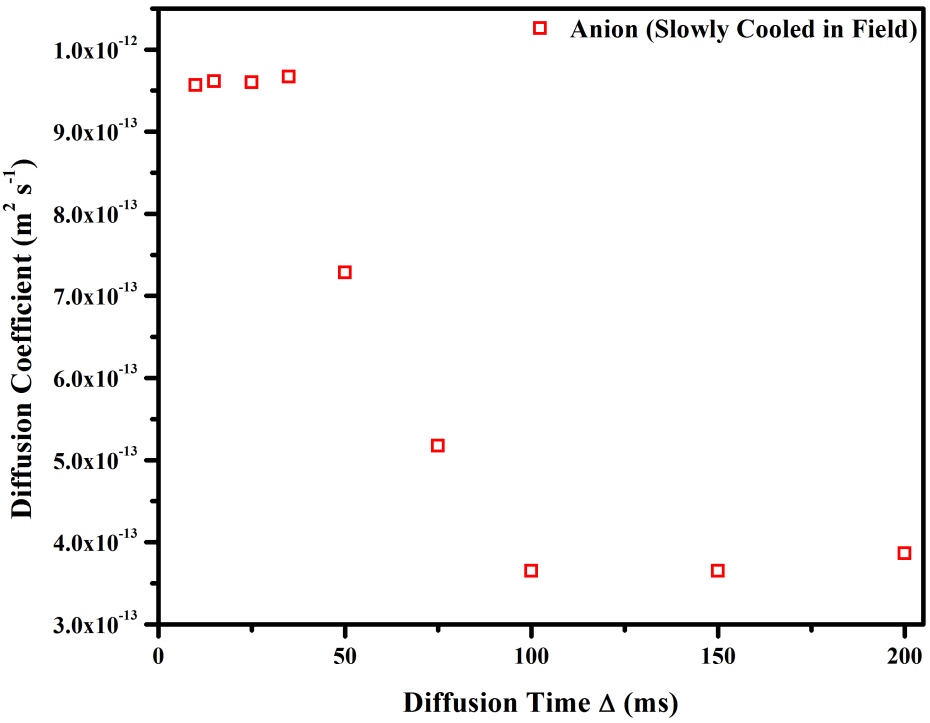

Figure 3.11. Anion D as a function of diffusion time Δ probes 0.1 – 0.4 μm lengthscales. A sharp decrease in D as a function of Δ indicates restricted diffusion when $\Delta \geq 50$ ms, giving an average domain boundary dimension of ~ 0.2 μm.

We observe a sharp decrease in D as a function of Δ to a plateau that is a factor of 3 smaller in D, indicating strong restricted diffusion. Based on the root-mean-square displacement, also known as the diffusion length $\langle r^2 \rangle^{1/2} = (2D\Delta)^{1/2}$, an average domain boundary dimension of ~ 0.2 μm is present within this OIPC. This calculated rough dimension assumes a model of spherical cavities with limited pathways between them.[32,33] Since we do not know the exact symmetry of the domains or crystallites, this will require further study (e.g., anisotropic restricted diffusion) to determine the crystallite and domain boundary geometries and dimensions. However, since we are probing D vs. Δ along the proposed alignment axis of the crystallites, it is likely that 0.2 μm represents the length of the crystallites along that axis.

Since cation and anion local interactions govern the measured diffusion coefficients, we can take the perspective that essentially an ionic liquid exists in the domain boundary, and thus use our experimentally determined D values to evaluate intrinsic properties of the ionic microphase within the domain boundary, such as viscosity η and cation/anion hydrodynamic radii r_H, using the well known Stokes-Einstein equation[35,36]

$$D = \frac{kT}{6\pi\eta r_H} , \tag{3.5}$$

wherein kT is the average thermal energy (k is Boltzmann's constant and T is temperature), η is the viscosity of the medium, and r_H is the hydrodynamic radius of the diffusing species. As previously reported, PF_6^- should have $r_H = 0.25$ nm.[37] Knowing this value allows us to calculate a local viscosity η = 4.2 Pa · s and cation r_H = 0.41 nm. This viscosity is similar to those for viscous ionic liquids with relatively large ions, as is the cation in this study.[38] Based on the Stokes-Einstein relation, the measured cation and anion diffusion coefficients in the present material result from essentially a viscous IL residing in the domain boundary.

3.4 Conclusions

We have investigated the OIPC 1,2-bis[*N*-(*N*'-hexylimidazolium-d_2(4,5))]C_2H_4 $2PF_6^-$ by means of multinuclear variable temperature SSNMR and PFG-NMR diffusometry. This study uncovers new aspects of ion associations and transport in this OIPC, and presents a rich combination of NMR techniques that promises to give further insights into these materials. We show the importance of deuterium labeling these materials by using the C-^{2}H quadrupole coupling to spectrally observe an induced crystallite alignment upon slowly cooling in a 9.4 T magnetic field. This phenomenon has not been previously reported for any OIPC. Moreover, a change in local transport mechanism (molecular energetics) for the cation occurs in phase S_3 depending on thermal and magnetic treatment, evidenced by a change in E_a (14 to 39 kJ mol^{-1}), from the rapidly cooled case to when we slowly cool the sample in B_0. Changes in E_a as a function of thermal treatment for the anion fall within measurement error, suggesting that the transport mechanism of the anion does not significantly change. From variable temperature ^{19}F SSNMR, we also propose that the ion conduction for this OIPC is dominated by anion transport via domain boundaries, and we quantify the fraction of anions in domain boundaries versus those in crystallites. Utilization of the Stokes-Einstein equation yields a cation r_H = 0.41 nm and viscosity η = 4.2 Pa · s, suggestive of a viscous IL moving through domain boundaries. Structurally similar ILs have viscosities within this range.[38] Finally, a restricted diffusion study reveals a ~ 0.2 μm dimension of restriction for ions in these domain boundaries.

Further studies on these materials are ongoing, including E_a measurements for the cation and anion within all phases, and the study of materials with different structures. While these OIPCs do not exhibit remarkable conductivities, doping with small amounts of lithium or sodium salts

could potentially enhance conductivity and bring about new electrolyte applications, as previously observed for other OIPCs.[4,5,39-43]

3.5 Acknowledgements

This work was supported by the National Science Foundation under award number CHE 1057797. Any opinions, findings and conclusions or recommendations expressed in this material are those of the author(s) and do not necessarily reflect the views of the National Science Foundation (NSF). This material is also based upon work supported in part by the U.S. Army Research Office under Grant W911NF-07-1-0452 Ionic Liquids in Electro-Active Devices (ILEAD) MURI.

3.6 References

(1) Mauritz, K. A.; Moore, R. B. State of understanding of Nafion. *Chem. Rev.* **2004**, *104*, 4535.
(2) Li, J.; Park, J. K.; Moore, R. B.; Madsen, L. A. Linear coupling of alignment with transport in a polymer electrolyte membrane. *Nat Mater* **2011**, *10*, 507
(3) Li, J.; Wilmsmeyer, K. G.; Hou, J.; Madsen, L. A. The role of water in transport of ionic liquids in polymeric artificial muscle actuators. *Soft Matter* **2009**.
(4) Pringle, J. M.; Howlett, P. C.; MacFarlane, D. R.; Forsyth, M. Organic ionic plastic crystals: recent advances. *J. Mater. Chem.* **2010**, *20*, 2056.
(5) Pringle, J. M. Recent progress in the development and use of organic ionic plastic crystal electrolytes. *PCCP* **2013**, *15*, 1339.
(6) Lee, M.; Choi, U. H.; Wi, S.; Slebodnick, C.; Colby, R. H.; Gibson, H. W. 1,2-Bis[N-(N '-alkylimidazolium)]ethane salts: a new class of organic ionic plastic crystals. *J. Mater. Chem.* **2011**, *21*, 12280.
(7) Lee, M.; Niu, Z.; Slebodnick, C.; Gibson, H. W. Structure and Properties of N,N-Alkylene Bis(N '-Alkylimidazolium) Salts. *J. Phys. Chem. B* **2010**, *114*, 7312.
(8) Mehrer, H. *Diffusion in Solids*, 2007; Vol. 155.
(9) Every, H. A.; Bishop, A. G.; MacFarlane, D. R.; Oradd, G.; Forsyth, M. Room temperature fast-ion conduction in imidazolium halide salts. *J. Mater. Chem.* **2001**, *11*, 3031.
(10) Huang, J. H.; Hill, A.; Forsyth, M.; MacFarlane, D.; Hollenkamp, A. Conduction in ionic organic plastic crystals: The role of defects. *Solid State Ionics* **2006**, *177*, 2569.

(11) Rana, U. A.; Vijayaraghavan, R.; MacFarlane, D. R.; Forsyth, M. Plastic crystal phases with high proton conductivity. *J. Mater. Chem.* **2012**, *22*, 2965.
(12) Humphreys, F. J., and Max Hatherly *Recrystallization and related annealing phenomena*; Elsevier, 1995.
(13) Dosseh, G.; Fressigne, C.; Fuchs, A. H. Premelting in Orientationally Disordered Molecular Crystals. A Re-Appraisal. *J. Phys. Chem. Solids* **1992**, *53*, 203
(14) Chen, F.; de Leeuw, S. W.; Forsyth, M. Dynamic Heterogeneity and Ionic Conduction in an Organic Ionic Plastic Crystal and the Role of Vacancies. *J Phys Chem Lett* **2013**, *4*, 4085.
(15) Lingwood, M. D.; Zhang, Z.; Kidd, B. E.; McCreary, K. B.; Hou, J.; Madsen, L. A. Unraveling the local energetics of transport in a polymer ion conductor. *Chem. Commun.* **2013**, 4283.
(16) Commer, P.; Cherstvy, A. G.; Spohr, E.; Kornyshev, A. A. The effect of water content on proton transport in polymer electrolyte membranes. *Fuel Cells* **2002**, *2*, 127.
(17) Hou, J.; Zhang, Z.; Madsen, L. A. Cation/anion associations in ionic liquids modulated by hydration and ionic medium. *J. Phys. Chem. B* **2011**, *115*, 4576.
(18) Urry, D. W. Henry Eyring (1901-1981): A 20th Century Physical Chemist and His Models. *Math Mod* **1982**, *3*, 503.
(19) Eyring, H. The Activated Complex in Chemical Reactions. *J. Chem. Phys.* **1935**, *3*, 107.
(20) Solomon, I. Multiple Echoes in Solids. *Phys Rev* **1958**, *110*, 61.
(21) Madsen, L. A.; Dingemans, T. J.; Nakata, M.; Samulski, E. T. Thermotropic biaxial nematic liquid crystals. *Phys. Rev. Lett.* **2004**, *92*.
(22) Dingemans, T. J.; Madsen, L. A.; Zafiropoulos, N. A.; Lin, W. B.; Samulski, E. T. Uniaxial and biaxial nematic liquid crystals. *Philosophical Transactions of the Royal Society a-Mathematical Physical and Engineering Sciences* **2006**, *364*, 2681.
(23) Stejskal, E.; Tanner, J. Spin Diffusion Measurements: Spin Echoes in the Presence of a Time-Dependent Field Gradient*. *J. Chem. Phys.* **1965**, *42*.
(24) Hou, J.; Madsen, L. A. New insights for accurate chemically specific measurements of slow diffusing molecules. *J. Chem. Phys.* **2013**, *138*.
(25) Ashbrook, S. E.; Duer, M. J. Structural information from quadrupolar nuclei in solid state NMR. *Concepts in Magnetic Resonance Part A* **2006**, *28A*, 183.
(26) Li, J.; Wilmsmeyer, K. G.; Madsen, L. A. Anisotropic Diffusion and Morphology in Perfluorosulfonate Ionomers Investigated by NMR. *Macromolecules* **2009**, *42*, 255.
(27) Levitt, M. H. *Spin Dynamics*; John Wiley and Sons Ltd.: England, 2008; Vol. 2.
(28) Collings, P. J. *Liquid Crystals: Nature's Delicate Phase of Matter*; 2 ed.; Princeton University Press, 2002.
(29) Jin, L. Y.; Nairn, K. M.; Forsyth, C. M.; Seeber, A. J.; MacFarlane, D. R.; Howlett, P. C.; Forsyth, M.; Pringle, J. M. Structure and Transport Properties of a Plastic Crystal Ion Conductor: Diethyl(methyl)(isobutyl)phosphonium Hexafluorophosphate. *J Amer Chem Soc* **2012**, *134*, 9688.
(30) Adebahr, J.; Forsyth, M.; MacFarlane, D. R. Cation dynamics in dimethyl-pyrrolidinium-based solid-state ion conductors. *Electrochim. Acta* **2005**, *50*, 3853.
(31) P. G. de Gennes, J. P. *The Physics of Liquid Crystals*; 2nd ed.; Oxford Science Publications, 1993.
(32) Callaghan, P. T. *Translational Dynamics and Magnetic Resonance: Principles of Pulsed Gradient Spin Echo NMR*; Oxford University Press: New York, 2011.

(33) Callaghan, P. T.; Coy, A.; Macgowan, D.; Packer, K. J.; Zelaya, F. O. Diffraction-Like Effects in Nmr Diffusion Studies of Fluids in Porous Solids. *Nature* **1991**, *351*, 467.
(34) Hou, J.; Li, J.; Mountz, D.; Hull, M.; Madsen, L. A. Correlating morphology, proton conductivity, and water transport in polyelectrolyte-fluoropolymer blend membranes. *J. Membr. Sci.* **2013**, *448*, 292.
(35) Edward, J. T. Molecular Volumes and the Stokes-Einstein Equation. *J. Chem. Educ.* **1970**, *47*, 261.
(36) Einstein, A. On the Movement of Small Particles Suspended in Stationary Liquids Required by the Molecular-Kinetic Theory of Heat. *Annalen der Physik* **1905**, *17*, 549.
(37) Chen, W. T.; Hsu, W. Y.; Lin, M. Y.; Tai, C. C.; Wang, S. P.; Sun, I. W. Isolated BMI+ Cations are More than Isolated PF6- Anions in the Room Temperature 1-Butyl-3-methylimidazolium Hexafluorophosphate (BMI-PF6) Ionic Liquid. *J. Chin. Chem. Soc.* **2010**, *57*, 1293.
(38) Yu, G. R.; Zhao, D. C.; Wen, L.; Yang, S. D.; Chen, X. C. Viscosity of ionic liquids: Database, observation, and quantitative structure-property relationship analysis. *AlChE J.* **2012**, *58*, 2885.
(39) Adebahr, J.; Seeber, A. J.; MacFarlane, D. R.; Forsyth, M. LiI-doped N,N-dimethyl-pyrrolidinium iodide, an archetypal rotator-phase ionic conductor. *J. Phys. Chem. B* **2005**, *109*, 20087.
(40) Forsyth, M.; Huang, J.; MacFarlane, D. R. Lithium doped N-methyl-N-ethylpyrrolidinium bis(trifluoromethanesulfonyl)amide fast-ion conducting plastic crystals. *J. Mater. Chem.* **2000**, *10*, 2259.
(41) Howlett, P. C.; Sunarso, J.; Shekibi, Y.; Wasser, E.; Jin, L. Y.; MacFarlane, D. R.; Forsyth, M. On the use of organic ionic plastic crystals in all solid-state lithium metal batteries. *Solid State Ionics* **2011**, *204*, 73.
(42) MacFarlane, D. R.; Forsyth, M. Plastic crystal electrolyte materials: New perspectives on solid state ionics. *Adv. Mater.* **2001**, *13*, 957.
(43) MacFarlane, D. R.; Huang, J. H.; Forsyth, M. Lithium-doped plastic crystal electrolytes exhibiting fast ion conduction for secondary batteries. *Nature* **1999**, *402*, 792.

Chapter 4

Probing Ion-Conducting Channel Geometry in a Perfluorosulfonate Ionomer

4.1 Introduction

Bridging fundamental properties that relate polymer morphology to small molecule/ion transport in ion-conducting materials is crucial to overall optimization of new material design. Nafion® (Figure 4.1) nanophase separates into hydrophilic and hydrophobic domains, wherein ion transport takes place within the SO_3^--lined hydrophilic channels (Nafion® can swell ~ 40% by volume, to ~ 20 H_2O molecules per SO_3^- group). This benchmark material has provided researchers rich information on how multi-lengthscale morphology is coupled to transport.[1-10]

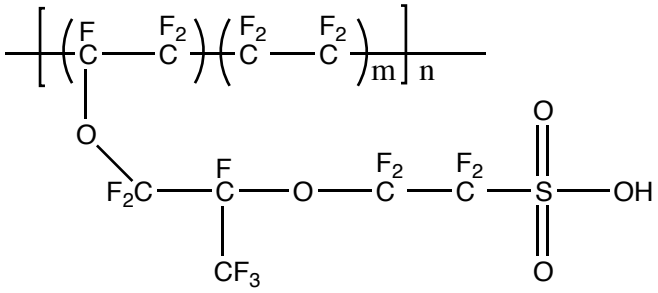

Figure 4.1. Chemical structure of Nafion®.

The size, shape, and connectivity (within a single domain and between adjacent domains) of the ion-conducting channels all directly influence ion transport. Prevalent and controversial models to describe the morphology of Nafion®, such as rod-like cylinders,[8] inverse spherical micelles, and "board-like" channels,[7] have emerged from the analysis and modeling of small-angle X-ray/neutron scattering (SAXS/SANS) profiles. However, experimental uncertainties associated with such techniques (discussed below) as well as limitations in current mathematical models

have raised many questions in defining the morphology of Nafion®. This is further compounded by analysis of various Nafion® derivatives,[9] differences in casting conditions,[1] thermal history,[9] and mechanical deformations (under dry[2] and wet[6] conditions) of the membrane.

Schimdt-Rohr and Chen modeled the nanoscale morphology of Nafion® by fitting a range of previously reported experimental SAXS patterns, including the original Gierke profile, and concluded that the parallel cylinder model best represented the morphology of Nafion®.[8,9] Schimdt-Rohr and Chen's conclusions hinge on the original Gierke data and accurate assignment of water volume fractions, as the position of the characteristic "ionomer peak" in the SAXS profile depends heavily on water content.[7] Kreuer *et al.* recently re-evaluated Schimdt-Rohr and Chen's data to show a flaw in the water volume fraction used in their analysis, thus biasing their conclusions. Kreuer *et al.* instead offered their own perspective and modeled their SAXS profiles as "flattened channels" and suggested that Nafion®'s nano-morphology was composed of nm-size "water films" that are flat in geometry, wherein H_2O chemically stabilizes the nanophase separated hydrophilic and hydrophobic domains.[7] One issue with all Nafion studies based on scattering is that thermal or casting history can strongly influence ionomer peaks and low-q scaling (slopes), and thus limited information exists in the scattering profiles.

Application of liquid crystal (LC) theory in conjunction with quadrupolar NMR to ion-conducting materials that exhibit some degree of anisotropy on μm lengthscales has yielded new advances in our understanding of how morphological properties influence transport on the nm – μm lengthscale.[2-4] Probe species that contain quadrupolar nuclei adopt the local orientation of an environment to provide sensitive measurements in quantifying various order parameters. ^{2}H quadrupolar NMR studies are of particular utility due to easy integration of ^{2}H into many

systems. The partially averaged (aka, residual) quadrupolar splitting $\Delta\nu_Q$ (Equation 4.1) is given by,

$$\Delta\nu_Q = Q_p S P_2(\cos\theta) = Q_p \rho S_{\text{matrix}} P_2(\cos\theta) \tag{4.1}$$

where Q_p is the quadrupolar coupling constant, S is the orientational order parameter of the C–^{2}H (or O–^{2}H for D_2O) bond with respect to the alignment axis of the material, which lies at an angle θ to the magnetic field, S_{matrix} is the orientational order parameter of the channel network, ρ is a scaling factor, and $P_2(\cos\theta)$ is the second-order Legendre polynomial. This spectral line splitting provides information on the nm – μm lengthscale hydrophilic channel ordering, usually by way of a deuterated "probe molecule".[2-4,10] Previous work in our group has shown a linear correlation between channel ordering (S_{matrix}) and transport (H_2O diffusion) within uniaxially drawn Nafion® 117 through ^{2}H quadrupolar NMR of ^2H_2O (D_2O).[2] As Li *et al.* discovered, uniaxially drawing Nafion® simply reorients the nm – μm-size domains to increase the orientational order parameter (S_{matrix} = 0.06 – 0.78) of the hydrophilic channels along the draw direction, thus enhancing transport along the channels.[2-4]

While a gain in transport along the draw direction occurs, higher resolution of $\Delta\nu_Q$ and retention of channel geometry upon drawing occurs as well. With an increase in $\Delta\nu_Q$ as a function of draw ratio, full analysis of the tensorial components ($\Delta\nu_Q^{xx}$, $\Delta\nu_Q^{yy}$, and $\Delta\nu_Q^{zz}$) along the main principal axes is possible. With multi-directional $\Delta\nu_Q$, more subtle order parameters beyond the uniaxial order parameter S can be probed, such as the biaxiality parameter η_Q, with value ranging from 0 – 1:

$$\Delta\nu_Q = \frac{1}{2} Q_p \rho S_{matrix} [3cos^2\theta - 1 + \eta sin^2\theta] \tag{4.2}$$

For LCs, η_Q of a probe molecule is commonly used to interrogate the biaxiality of a LC molecule within a given phase, or the biaxiality of the liquid crystal phase itself.[11-14] Similarly, η_Q of a

probe molecule within a nanoscopic hydrophilic channel may report on the biaxiality of the channel (for a non-cylindrical channel $\eta_Q \neq 0$) or the biaxiality of distributions of channels.[4,10] While D_2O usually reports on the degree of domain alignment S, so far η_Q for uniaxially drawn Nafion® 117 has only been weakly observable due to the length scale over which D_2O reports on ordering (discussed below);[2,4] thus a more sensitive probe of local ordering is desirable in order to appropriately map the nanoscale morphology of Nafion®. Interestingly, other quadrupolar nuclei, such as ^{23}Na and ^{7}Li, are not commonly used to study orientational order unless residing in a polycrystalline solid. Both of these nuclei have a spin quantum number $I = 3/2$, but have drastically different quadrupolar moments eQ (^{7}Li $eQ = -4.01 \times 10^{-28}$ m^2 and ^{23}Na $eQ = 10.4 \times 10^{-28}$ m^2). ^{23}Na and ^{7}Li are thus ideal ion-exchangeable probe species to perform such studies and can give insight into lower symmetry ordered structures, such as the channel biaxiality.[15]

The present work is an analysis of Nafion®'s nano-morphology through ^{7}Li and ^{23}Na quadrupolar NMR measurements in uniaxially drawn Nafion® 117 and this work builds on recent results by SAXS.[7] ^{7}Li and ^{23}Na residual quadrupole splittings as a function of water content show that the hydrophilic channel of Nafion is biaxial. Moreover, ^{7}Li η as a function of water content λ (where $\lambda = mol_{H2O} : mol_{SO3-}$) shows a gradual decrease ($\eta_Q = 0.26 - 0.2$) and then dramatically drops at $\lambda = 9.5$. The present work promises to guide future ion-conducting material design strategies using quadrupolar probe species to understand oriented soft materials.

4.2 Experimental

4.2.1 ^{7}Li and ^{23}Na Quadrupolar NMR Spectroscopy

A stack of 10 pieces (3mm x 3mm) of uniaxially drawn (4:1) Nafion® 117 was tightly wrapped with Teflon tape (of known weight) and vacuum dried for 24 hours to obtain a

membrane stack dry weight. Nafion® 117 is a 175 μm thick membrane with an equivalent weight of 1100 g of polymer per ionic group, and we study the same material as in previous work from our group.[2,4,16] The membrane stack was allowed to soak in a 1M aqueous salt solution (LiOH or NaOH) for at least one week prior to experimental acquisition. The membrane stack was removed from the salt solution, lightly dabbed to remove residual solution, and tightly wrapped in plastic wrap. The membrane stack was then loaded into a custom built Teflon cell as previously described and allowed to equilibrate for 30 minutes prior to data acquisition.[4,10] All ^{7}Li and ^{23}Na experiments were performed using a 400 MHz Bruker Avance III WB NMR spectrometer, equipped with a two-channel HX wideline static sample solids probe (Bruker HP WB 73A). Single RF pulse experiments with 90° pulse lengths of 7 μs (^{7}Li) and 5 μs (^{23}Na) with relaxation delay times of 1 s (^{7}Li) and 3 s (^{23}Na) were used to acquire spectra.

4.3 Results and Discussion

4.3.1 ^{7}Li and ^{23}Na Quadrupolar NMR Spectroscopy

Utilization of ^{23}Na and ^{7}Li as ion-exchangeable "probe species" allows correlations between the quadrupole splitting and morphology over length scales of ~ 50 nm – 1 μm. We choose these species due to their chemically and magnetically distinct properties, thus accessing different aspects of orientational order in these materials. We begin our analysis by presenting ^{23}Na and ^{7}Li NMR spectra in uniaxially drawn 4:1 Nafion® 117 (along the draw direction) at λ = 11.7 (Figure 4.2).

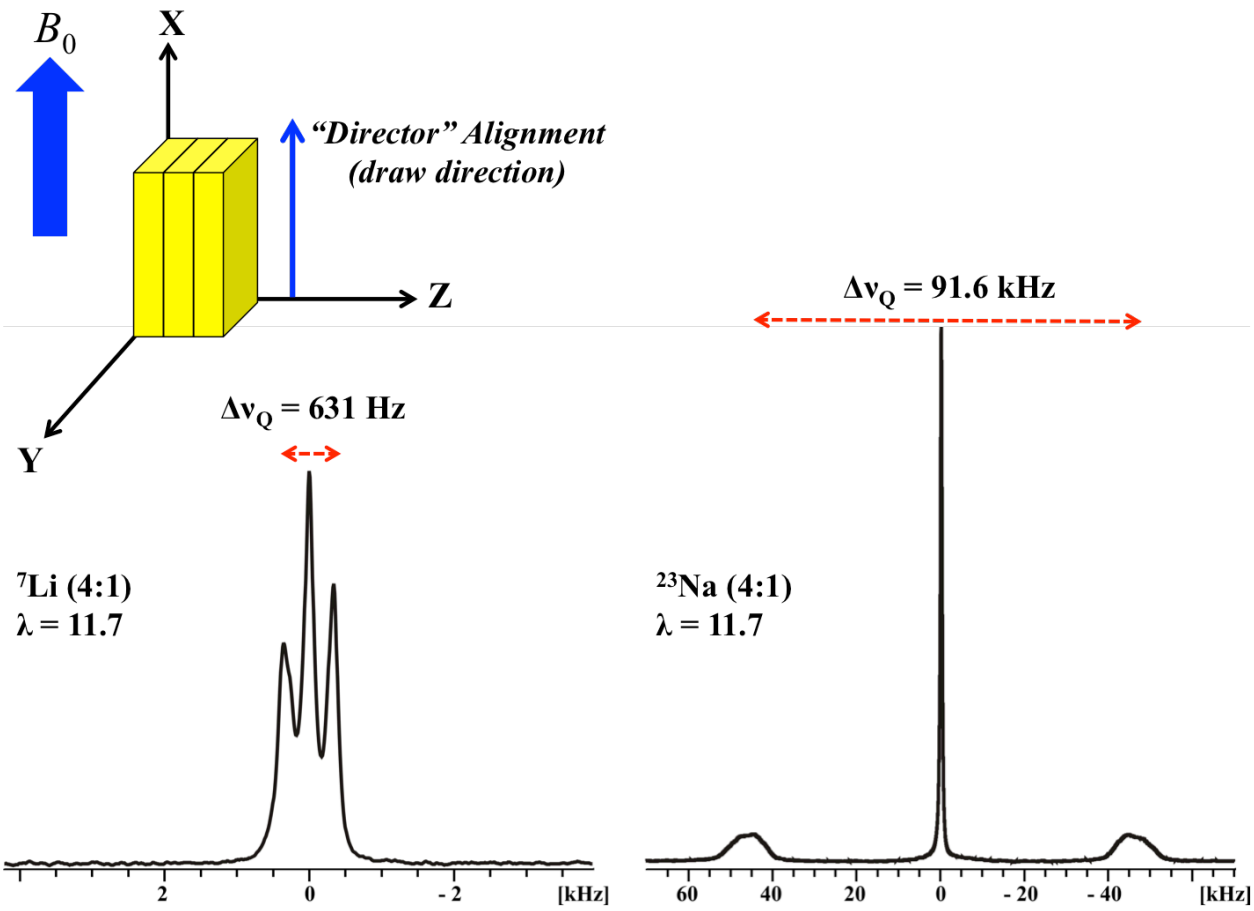

Figure 4.2. ^{7}Li and ^{23}Na spectra at λ = 11.7 show stark differences in their respective $\Delta\nu_Q$ values.

Previous work on 4:1 drawn Nafion® 117 hydrated with D_2O exhibits a ^{2}H $\Delta\nu_Q$ = 992 Hz at λ = 11.[2] As previously discussed, the probe species partially adopts or "inherits" the ordering of the hydrophilic channel due to limited degrees of freedom during rotations, collisions, and librations.[2,4,17-19] This "pseudonematic interaction"[2,4] is encoded into $\Delta\nu_Q$ and gives insight into multiscale ordering within perfluorosulfonate ionomers. While ^{7}Li and ^{23}Na experience a similar channel anisotropy from the proposed ~ 0.1 μm size rod-like semicrystalline bundles (referred to as "domains") at similar hydration levels, significant differences in their respective $\Delta\nu_Q$ originate from multiple factors, such as differences in their quadrupole coupling constants, asymmetry (or

biaxiality) parameter η of the nucleus, asymmetry of the ion orbitals as they interact with chemical groups in the channel, and length scale over which $\Delta\nu_Q$ reports. We discuss this length scale component below (see Fig 4.6 and associated text). The presence of a non-zero quadrupole splitting for ^{7}Li and ^{23}Na within the swollen hydrophilic channel demonstrates a non-zero electric field gradient (EFG) tensor, which is generated by the interaction between the local electronic environment and the asymmetric electric quadrupole moment of the nucleus.[15] Unlike Nafion® swollen with D_2O, wherein the interaction of ^{2}H with the internal molecular EFG from the O–^{2}H bond perturbs the Zeeman states to give a doublet (Zeeman + 1st-order quadrupolar interaction), solvated ^{7}Li and ^{23}Na ions within the hydrophilic channels experience an EFG in an environment external and in close proximity (< 1 nm) to the polymer-fixed -SO_3^- ion itself. That is, likely the SO_3^- groups generate an EFG that dominates interactions with the quadrupole moments of ^{7}Li and ^{23}Na ions.

The quadrupole splitting becomes more pronounced by decreasing λ within the hydrophilic channel; we observe an exponential-like increase in ^{7}Li $\Delta\nu_Q$ due to stronger orientational ordering of the ion within the channel due to Li^+-SO_3^- interactions (Figure 4.3). This dependence appears to hold for each species studied (^{2}H and ^{23}Na not shown) and also depends on Q_p and η_Q.[2,4]

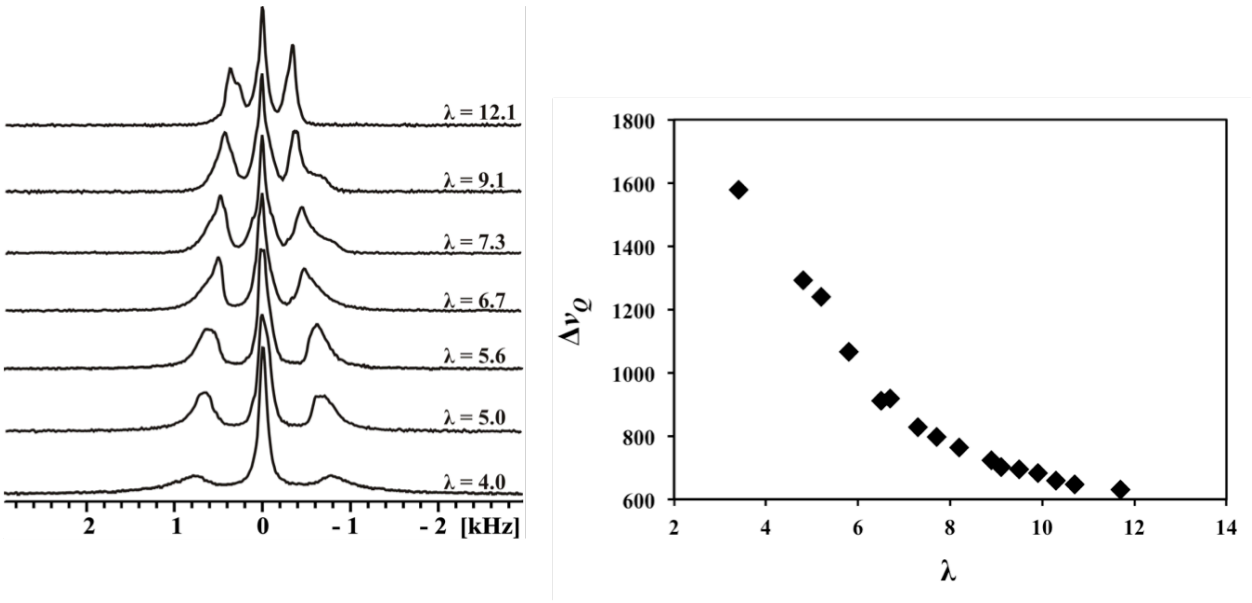

Figure 4.3. ^{7}Li quadrupole splitting ($\Delta\nu_Q$) in drawn Nafion as a function of hydration level (λ) with the membrane alignment axis along the magnetic field (θ = 0° in Equation 4.2). $\Delta\nu_Q$ is maximized at this angle due to maximized inherited alignment of ^{7}Li within the hydrophilic channel. Error in $\Delta\nu_Q$ is approximately the symbol size.

In order to probe channel biaxiality, we can observe the quadrupole splitting with different membrane alignment with respect to B_0. If biaxiality is not present, $\Delta\nu_Q$ = 0 at the magic angle θ = 54.7° (Equation 4.2). Modulating the angle of the material alignment axis with respect to the magnetic field affords direct insight into any deviation from the magic angle (Figure 4.4). Our observations agree qualitatively with Kreuer's model of a flattened channel or "water film" that potentially acts as a charge stabilizer in the ion-lined channels of Nafion®.[7]

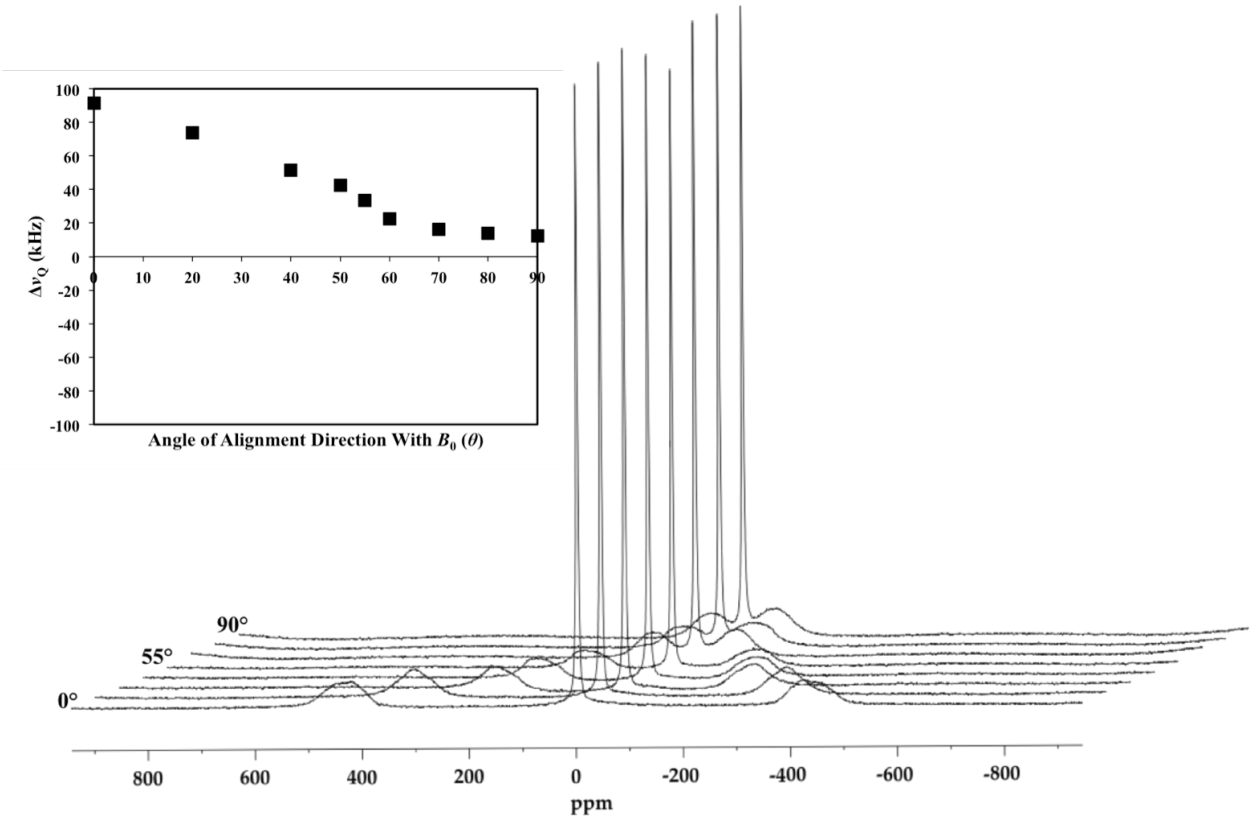

Figure 4.4. ^{23}Na $\Delta\nu_Q$ as a function of θ at λ = 11.7 shows dramatic deviation from a uniaxial environment. Recall, for uniaxial environments, $\Delta\nu_Q = 0$ at the magic angle ($\theta = 54.7°$). Here we do not see $\Delta\nu_Q$ apparently cross 0 at any angle, suggesting the ions experience a highly biaxial environment. Error in $\Delta\nu_Q$ is approximately the symbol size.

We see that the angular dependence of ^{23}Na $\Delta\nu_Q$ significantly deviates from uniaxial behavior. In fact, $\Delta\nu_Q$ does not cross 0 at any angle (or potentially there is a zero crossing at an angle near 80°), signifying a large η_Q value (~ 1) in Equation 4.2. Since the order parameter S_{matrix} is traceless, if only two of the diagonal components of $\Delta\nu_Q$ are known η_Q can be derived via

$$\eta_Q = \frac{\left|\Delta\nu_Q^y - \Delta\nu_Q^z\right|}{\Delta\nu_Q^x} \quad . \tag{4.3}$$

Figure 4.5 shows a representative set of ^{7}Li spectra about the three principal axes (at λ = 5) and the extracted η_Q as a function of λ.

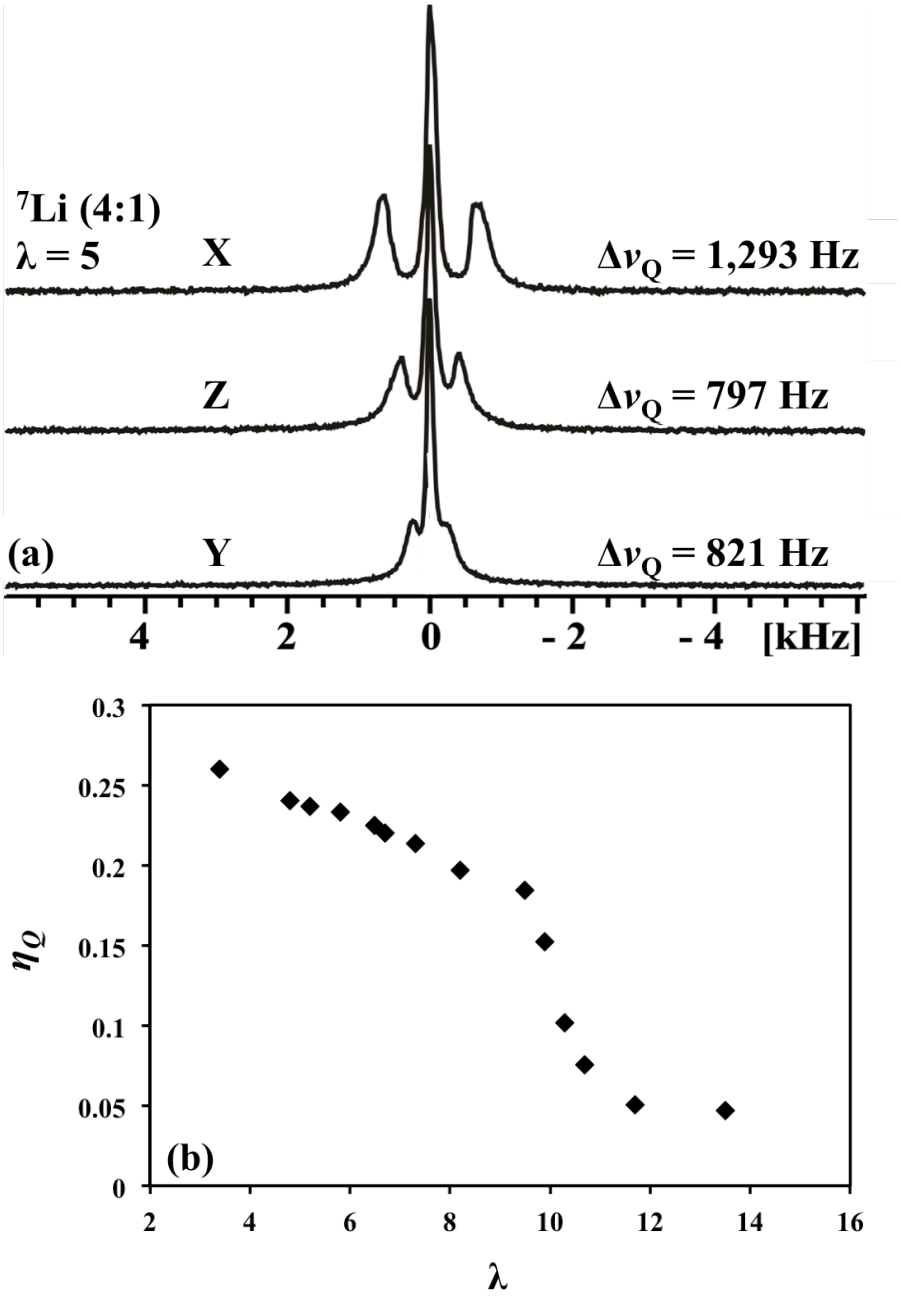

Figure 4.5. ^{7}Li spectra with membrane principal axes (*x*, *y*, and *z*) along B_0 (a) allow measurement of the biaxiality parameter η_Q (b). In the range λ = 3 to 13.5, we observe η_Q = 0.25

to 0.05, demonstrating a non-spherical (and varying) local environment for the ion. Error in η_Q is approximately +/- 0.03.

Interestingly, Figure 4.5 shows a gradual decrease in η_Q between $\lambda = 2 – 9.5$ followed by a dramatic decrease and then a plateau above $\lambda = 11$. Clearly, a release of biaxial constraint occurs around $\lambda = 10$, which must correspond to a transition to more fully averaged local ion-ion interactions (faster motions in the transverse axes of the channel). Previous work in our group has shown a sharp increase in H_2O diffusion E_a (< 1 nm length scale measurement) at $\lambda = 7$ due to preferential interactions with SO_3^- within the channel.[20] Thus, figures 4.4 and 4.5 collectively imply that the local environment surrounding the ions is biaxial and is measurable through the ^{7}Li and ^{23}Na quadrupole moments interacting with the EFG generated by asymmetrically placed SO_3^- groups. As suggested by Kreuer *et al.*, staggered SO_3^- groups reside within the locally flat channels.[7] Note that in the present system, the maximum η_Q value observed depends on the probe species quadrupole moment, as we see differences between ^{7}Li and ^{23}Na η_Q values that do not directly quantify the ion-conducting channels true η_Q.

Furthermore, we measure diffusion as a function of λ for ^{7}Li and ^{23}Na (D_2O and H_2O are previously published)[2] to better understand the length scale over which we probe η_Q. During the diffusion time Δ, the diffusing species interrogates a length scale derived from the equation $\langle r^2 \rangle = (2D\Delta)^{1/2}$.[21-23] PFG NMR diffusometry reports on the ms time scale and can probe 50 nm to 10 μm in material morphology. In systems that exhibit orientational order, $1/\Delta\nu_Q$ represents the time scale for probe motion during the ^{7}Li ($1/\Delta\nu_{Q,X}$ = 1.5 ms at $\lambda = 12.1$) and ^{23}Na ($1/\Delta\nu_{Q,X}$ = 11 μs at $\lambda = 11.7$) experiments. Thus, the equation $\langle r^2 \rangle = (2D\Delta\nu_Q^{-1})^{1/2}$ allows us to derive the length scale

over which η_Q reports as a function of λ (Figure 4.6).[2,4,19] We calculate the length scale over which η_Q reports as a function of λ (Figure 4.6).

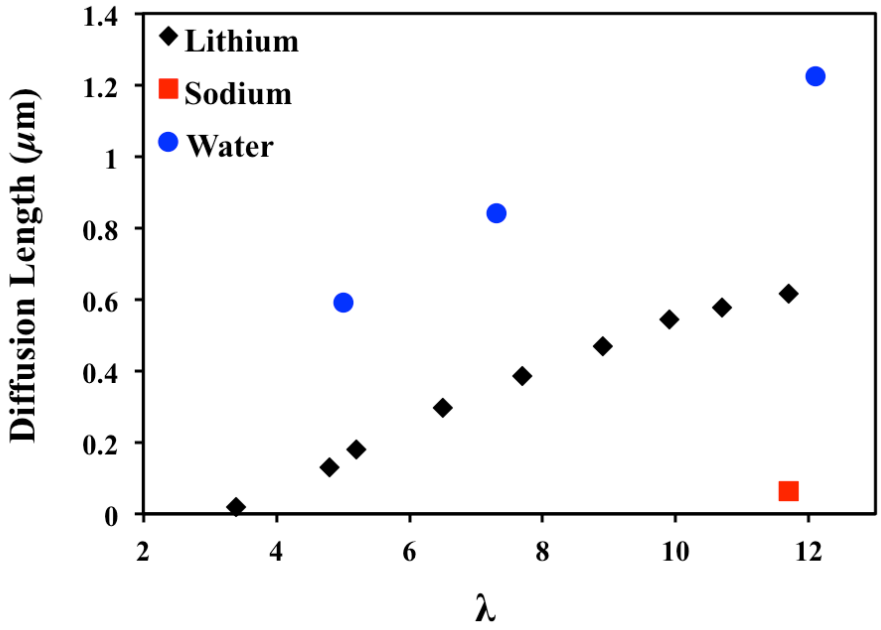

Figure 4.6. Diffusion lengths as a function of λ for ^{7}Li, ^{23}Na, and residual ^{1}H in D_2O. Error in diffusion length is ≤ ± 5%.

Here we use $\Delta\nu_Q$ and diffusion coefficients along the channel alignment axis. At the highest λ value we see that ^{23}Na $\Delta\nu_Q$ reports on the shortest distance, followed by ^{7}Li and D_2O. The length scale sampled by ^{23}Na (63 nm) falls within the size of a single domain (~ 100 nm).[2,24] In Figure 4.5, we see a dramatic decrease in η_Q at λ > 9.5 that correlates with a length scale of 0.5 μm sampled by ^{7}Li. We note that the D_2O $\Delta\nu_Q$ reports over the length 0.5 μm even at the lowest λ and gives η_Q = 0.03 at λ = 4.3,[2,4] which is within the error bar of the η_Q measurement. This suggests that the flattened (biaxial) ion-conducting channels within a single domain are well correlated. Furthermore, due to the fast averaging of water over a large number of domains, we were not previously able to observe these biaxial channels using D_2O quadrupole splittings. As

water content increases or we go to a faster diffusing probe, the probe samples the biaxial ion-conducting channels in adjacent domains and over longer length scales become gradually less correlated. Thus, we observe reduced η_Q until we are probing a length scale > 0.5 μm, at which point an average uniaxial environment is reported with $\Delta\nu_Q$. Figure 4.7 depicts a rough schematic of the interactions responsible for this biaxial channel environment.

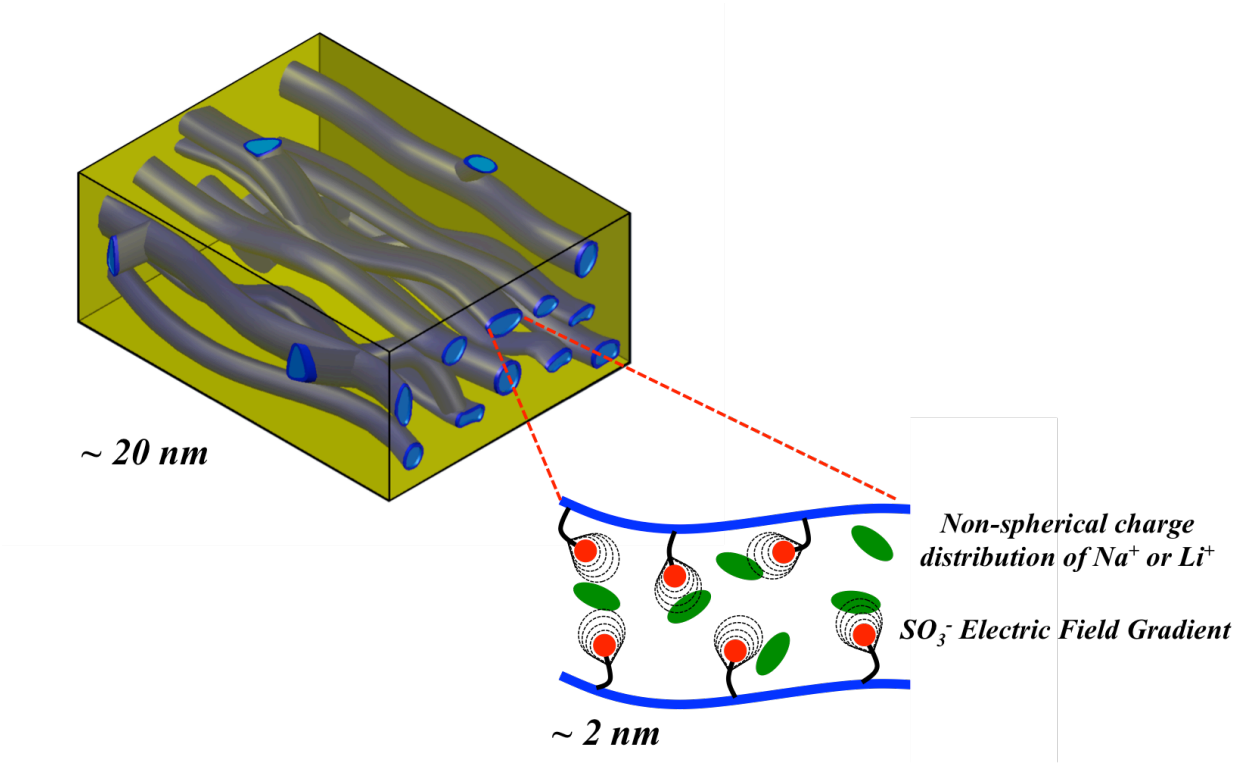

Figure 4.7. Illustration of the local channel biaxiality that ^{7}Li and ^{23}Na sense through the coupling of their quadrupole moment with the EFG generated by SO_3^- groups, which are asymmetrically (biaxially) distributed in the Nafion nanochannels.

4.4 Conclusions

Here we utilized NMR spectroscopy to probe geometrical features of a hydrophilic channel within uniaxially drawn Nafion® 117. ^{7}Li and ^{23}Na residual quadrupole splitting as a function of water content strongly indicate that the hydrophilic channel of Nafion is biaxial.

These results and conclusions agree with Kreuer's model of ribbon-like hydrophilic channels[7] and previous indications by scattering of biaxial domains in Nafion.[24] Moreover, ^{7}Li η_Q exhibits a gradual decrease (η_Q = 0.26 – 0.2) as a function of water content λ followed by a dramatic drop at λ > 9.5 to a plateau value of η_Q = 0.05. Finally, we find that channel biaxiality as measured by three different probe species, D_2O, ^{7}Li, and ^{23}Na, is sensitive to the length scale associated with the quadrupole splitting measurement; we observe a nominally uniaxial environment when the length scale exceeds 0.5 μm. We will expand these studies in the future to a more detailed analysis of aligned Nafion, as well as to the characterization of nanochannel asymmetry in other polymeric systems.

4.5 References

(1) Mauritz, K. A.; Moore, R. B. State of understanding of Nafion. *Chem. Rev.* **2004**, *104*, 4535.
(2) Li, J.; Park, J. K.; Moore, R. B.; Madsen, L. A. Linear coupling of alignment with transport in a polymer electrolyte membrane. *Nat Mater* **2011**, *10*, 507
(3) Li, J.; Wilmsmeyer, K. G.; Hou, J.; Madsen, L. A. The role of water in transport of ionic liquids in polymeric artificial muscle actuators. *Soft Matter* **2009**.
(4) Li, J.; Wilmsmeyer, K. G.; Madsen, L. A. Anisotropic Diffusion and Morphology in Perfluorosulfonate Ionomers Investigated by NMR. *Macromolecules* **2009**, *42*, 255.
(5) Kreuer, K. D. Ion Conducting Membranes for Fuel Cells and other Electrochemical Devices. *Chem. Mater.* **2014**, *26*, 361.
(6) Melchior, J. P.; Brauniger, T.; Wohlfarth, A.; Portale, G.; Kreuer, K. D. About the Interactions Controlling Nafion's Viscoelastic Properties and Morphology. *Macromolecules* **2015**, *48*, 8534.
(7) Kreuer, K. D.; Portale, G. A Critical Revision of the Nano-Morphology of Proton Conducting Ionomers and Polyelectrolytes for Fuel Cell Applications. *Adv. Funct. Mater.* **2013**, *23*, 5390.
(8) Schmidt-Rohr, K.; Chen, Q. Parallel cylindrical water nanochannels in Nafion fuel-cell membranes. *Nat Mater* **2008**, *7*, 75.
(9) Gierke, T. D.; Munn, G. E.; Wilson, F. C. The Morphology in Nafion Perfluorinated Membrane Products, as Determined by Wide-Angle and Small-Angle X-Ray Studies. *J Polym Sci Pol Phys* **1981**, *19*, 1687.
(10) Li, J.; Wilmsmeyer, K. G.; Madsen, L. A. Hydrophilic channel alignment modes in perfluorosulfonate ionomers: Implications for proton transport. *Macromolecules* **2008**, *41*, 4555.

(11) Emsley, J. W., Ed.; Reidel: Dordrecht Nulcear Magnetic Resonance of Liquid Crystals. *The Netherlands* **1983**.
(12) Madsen, L. A.; Dingemans, T. J.; Nakata, M.; Samulski, E. T. Thermotropic biaxial nematic liquid crystals. *Phys. Rev. Lett.* **2004**, *92*.
(13) Luckhurst, G. R. Liquid crystals - A missing phase found at last? *Nature* **2004**, *430*, 413.
(14) Acharya, B. R.; Primak, A.; Kumar, S. Biaxial nematic phase in bent-core thermotropic mesogens. *Phys. Rev. Lett.* **2004**, *92*.
(15) Levitt, M. H. *Spin Dynamics*; John Wiley and Sons Ltd.: England, 2008; Vol. 2.
(16) Hou, J.; Zhang, Z.; Madsen, L. A. Cation/anion associations in ionic liquids modulated by hydration and ionic medium. *J. Phys. Chem. B* **2011**, *115*, 4576.
(17) Deloche, B.; Samulski, E. T. Short-Range Nematic-Like Orientational Order in Strained Elastomers - a Deuterium Magnetic-Resonance Study. *Macromolecules* **1981**, *14*, 575.
(18) Hou, J.; Li, J.; Madsen, L. A. Anisotropy and Transport in Poly(arylene ether sulfone) Hydrophilic−Hydrophobic Block Copolymers. *Macromolecules* **2010**, *43*, 347.
(19) Chowdhury, S.; Madsen, L. A.; Frazier, C. E. Probing Alignment and Phase Behavior in Intact Wood Cell Walls Using H-2 NMR Spectroscopy. *Biomacromolecules* **2012**, *13*, 1043.
(20) Lingwood, M. D.; Zhang, Z.; Kidd, B. E.; McCreary, K. B.; Hou, J.; Madsen, L. A. Unraveling the local energetics of transport in a polymer ion conductor. *Chem. Commun.* **2013**, 4283.
(21) Stejskal, E.; Tanner, J. Spin Diffusion Measurements: Spin Echoes in the Presence of a Time-Dependent Field Gradient*. *J. Chem. Phys.* **1965**, *42*.
(22) Callaghan, P. T. *Translational Dynamics and Magnetic Resonance: Principles of Pulsed Gradient Spin Echo NMR*; Oxford University Press: New York, 2011.
(23) Tanner, J. E.; Stejskal, E. O. Restricted Self-Diffusion of Protons in Colloidal Systems by Pulsed-Gradient Spin-Echo Method. *J. Chem. Phys.* **1968**, *49*, 1768.
(24) Rubatat, L.; Rollet, A. L.; Gebel, G.; Diat, O. Evidence of elongated polymeric aggregates in Nafion. *Macromolecules* **2002**, *35*, 4050.

Chapter 5

Multiscale Lithium and Counterion Transport in an Electrospun Polymer-Gel Electrolyte

Reprinted with permission from Bryce E. Kidd, Scott J. Forbey, Friedrich W. Steuber, Robert B. Moore, and Louis A. Madsen, Macromolecules, **2015**, *48 (13)*, 4481-4490

© 2015, American Chemical Society.

Abstract:

We explore fundamental lithium ion (Li^+) and triflate counterion ($CF_3SO_3^-$) transport properties within an electrospun UV-crosslinked poly(ethylene oxide) polymer-gel electrolyte. With modulation of crosslinker (10 – 30 wt%), the fully swollen fibrous framework swells and retains between 1,700 and 1,200 wt% liquid electrolyte and exhibits room temperature ionic conductivity up to 6 mS cm^{-1}. ^7Li and ^{19}F spin-spin relaxation (T_2) measurements reveal the presence of inter- and intra-fiber lithium ions, where the long- and short-T_2 lithium ion and counterion components enable quantification of the fractions of free liquid electrolyte between fibers and liquid electrolyte within fibers. Pulsed-field-gradient NMR diffusometry shows increases in lithium and triflate diffusion coefficients with crosslinker content, suggestive of enhanced ion transport within the free liquid-electrolyte phase due to a reduction in morphological restrictions. Arrhenius fits to temperature-dependent diffusion experiments show that lithium and triflate values for the activation energy of diffusion (15 and 12 kJ mol^{-1}, respectively) are identical for ions in pure liquid solutions and for ions within the electrospun gel, showing that the framework does not influence the local energetics of ion transport. The

present study thus offers new insights into understanding ion transport properties within lithium-ion battery materials on length scales ranging from sub-nm to micron scales.

5.1 Introduction

The use of polymer-gel electrolytes (PGEs) in lithium secondary batteries has gained tremendous interest due to many attractive qualities, such as high ionic conductivity σ (2 – 15 mS cm^{-1}) over a large temperature window (-20 to 50 °C).[1-6] Current PGEs combine a polymer host, such as poly(vinylidene difluoride) (PVdF), poly(methyl methacrylate) (PMMA), poly(acrylonitrile) (PAN), or poly(ethylene oxide) (PEO), with a lithium salt solution composed of cyclic and/or linear polar solvents, such as such as ethylene carbonate (EC), propylene carbonate (PC), dimethyl carbonate (DMC), and diethyl carbonate (DEC).[4,7,8] Common lithium salts that utilize bulky charge-delocalized anions, such as tetrafluoroborate (BF_4^-), perchlorate (ClO_4^-), hexafluorophosphate (PF_6^-), bis(trifluoromethane)sulfonimide $[(CF_3SO_2)_2N]^-$, and trifluoromethanesulfonate ($CF_3SO_3^-$, also known as OTf or triflate), provide for relatively weak associations between cation and anion and thus higher conductivity.[4] The polymer host generally provides a matrix to act as a mechanical separator between battery electrodes.[9]

The Stokes-Einstein relation,[10-12]

$$D = \frac{kT}{c\eta r_H}, \tag{5.1}$$

relates the quantities D the diffusion coefficient, k Boltzmann's constant, T the temperature, c (6π to 2π) a constant that depends on the diffusing species size, interaction type, and geometry relative to surrounding molecules/ions, η the bulk viscosity, and r_H the hydrodynamic radius. Delicate tailoring of the liquid electrolyte should in principle allow minimization of short time

scale (generally ~ 1 ns) electrostatic interactions between cation and anion, i.e., the formation of neutral ion pairs, triples, quadrupoles, and higher order charged aggregates,[13,14] and thus provide for low η and high D.

Ion transport within PGEs not only depends on the salt-solvent system, but can also couple to polymer chain dynamics (e.g., segmental motion). Researchers have explored polymer-mediated ion transport phenomena within PGEs since the first studies on solid polymer electrolytes (SPEs) involving sodium and potassium salt complexes with PEO.[15] With a dielectric constant ε of 5,[16] PEO aids in shielding cation and anion electrostatic interactions through solvation of the cation by the electron donating ether oxygen atoms (commonly referred to as "coordination" or "complexation").[17,18] Electrostatic interactions coupled with polymer chain segmental motion promote a "coordination-exchange-type" transport mechanism.[17] Unfortunately, SPEs produce somewhat low ionic conductivities in the range 10^{-8} to 10^{-4} S cm^{-1} (40 – 100 °C) due to slow ion diffusion and low concentration of charge carrying species within the amorphous phase of SPEs.[4] Thus, for Li^+ batteries we desire a separator that retains a large concentration of liquid electrolyte for high conductivity but is also mechanically stable.

Electrospinning, in conjunction with UV-crosslinking, offers fine control in creating mechanically stable fibrous networks that can swell and retain large concentrations of liquid electrolyte for battery separators.[6] Typically, a polymer solution (variable concentration) is forced through a syringe and spinneret (variable diameter) where a large voltage difference between the spinneret and counter electrode fiber collector promotes rapid fiber extrusion and solvent evaporation to form a fiber mat composed completely of polymer.[6] Choi *et al.* first introduced such fibrous networks in PGEs in 2003 when they electrospun a PVdF (Kynar® 761) nanofibrous (250 nm diameter fibers) membrane.[1] Swelling this matrix with 260 wt% of 1M

$LiPF_6$ (in 1:1 wt/wt mixture of EC:DMC) yielded PGEs with conductivities as high as 1.7 mS cm^{-1} (0 °C). However, the benchmark PVdF-based PGE can only retain 400 wt% liquid electrolyte. To overcome these shortfalls, work by Forbey *et al.* has shown ionic conductivities as high as 12 mS cm^{-1} (25 °C) in electrospun fiber mats composed of UV-crosslinked PEO with the crosslinking agent pentaerythritol triacrylate (PETA).[6]

While ionic conductivity measurements provide information on the conductive properties of battery electrolyte materials, this average measurement lacks the ability to quantify separate cation and anion contributions to battery performance. As a complement, pulsed-field-gradient (PFG) nuclear magnetic resonance (NMR) diffusometry can probe the translational motions of multiple chemically distinct diffusing species and is a widely tunable technique for understanding transport phenomena over a range of length and time scales.[19-24] More recently, our group is exploring how variable temperature PFG NMR diffusometry can probe how microscopic short time scale (ps) interactions[21,25] impact macroscopic long time scale (ms) transport through the Arrhenius equation,

$$D = D_0 e^{\frac{-E_a}{kT}}, \tag{5.2}$$

where D_0 is the pre-exponential factor (also known as the "barrierless" diffusion rate or diffusion at infinite temperature) and E_a is the so-called activation energy of diffusion.[21,26-29] Typically, when comparing translational E_a values, a lower E_a is attributed to a less hindered transport process.[30] While this may be true, the current understanding of E_a and how to further utilize the Arrhenius equation in evaluating ion and neutral molecule transport within materials requires further study. Recently, Lingwood *et al.* investigated the side-chain-terminal sulfonate (SO_3^-) contribution to water D and E_a within the nanophase-separated ion conducting channels of Nafion®, and studied analogous trifluoromethanesulfonic acid (triflic acid) solutions with

equivalent water-to-sulfonate molar ratio λ (moles H_2O : moles SO_3^-).[21] Both inside Nafion® and in pure triflic acid solutions, E_a of water at high hydration approaches E_a of bulk water. However, water E_a rises sharply when the ~ 2 nm Nafion® channels constrict at lower hydration (λ < 7), indicating that E_a specifically reports on short length scale (~ 1 nm) and time scale (~ 1 ps) intermolecular interactions.[21] Thus, E_a can provide insights into how local ion and small molecule interactions influence transport within polymeric battery[31] and fuel cell[21] materials.

Herein we explore lithium ion and counterion (triflate) transport properties within an electrospun polyethylene oxide (PEO) polymer-gel electrolyte that is UV-crosslinked using varying amounts of pentaerythritol triacrylate (PETA).[6] ^{7}Li and ^{19}F NMR spin-spin relaxation (T_2) analysis reveals the dynamics and quantitative populations of ions within two chemically distinct environments. ^{7}Li and ^{19}F PFG NMR diffusometry as a function of diffusion encoding (drift) time shows restricted diffusion behavior that exposes the influence of the polymer fiber mat on transport. Arrhenius fits to temperature-dependent ^{1}H, ^{7}Li, and ^{19}F diffusion experiments provide evidence that micron-scale restricted diffusion is decoupled from the local molecular-scale energetics of lithium and triflate transport. Finally, ^{17}O NMR spectroscopy allows us to probe local molecular association effects on ion transport within the present material. This study thus brings together a novel suite of transport and dynamics measurements to provide fundamental insights into ion conduction. Such insights will be critical for informed design of new conducting materials and for advances in energy storage and conversion devices.

5.2 Experimental

5.2.1 Synthesis of Crosslinked PEO Fiber-Mats

Poly(ethylene oxide) (PEO, M_n = 300,000, Aldrich Chemical Co.) and pentaerythritol triacrylate (PETA, Aldrich Chemical Co.) were dissolved into anhydrous acetonitrile (Aldrich

Chemical Co.) at 5 wt%/vol. Relative to PEO mass, 10, 20, and 30 wt% PETA was used. The polymer solutions were loaded into a KDscientific 100 syringe pump equipped with a Spellman high voltage source (Berton 205B) and extruded from a 3 mL syringe through a non-beveled stainless steel needle tip (I.D. 0.8 mm) at 4 mL/hr. A negative biased voltage (8 – 12 kV) was applied to the needle tip, which was held at 25 cm from the collector (1 cm diameter aluminum cylinder rotating at 200 RPM). UV-initiated crosslinking of the fiber mats were carried out with a 459 W mercury vapor lamp at 25 cm distance (30 minutes per side). Gel fractions were determined gravimetrically by weighing the resulting fiber mat, ultrasonicating in a methanol bath (MeOH, Aldrich Chemical Co.) for one hour, drying in a vacuum oven (25°C) overnight, and reweighing. The final samples are referred to as PEO10, PEO20, and PEO30 herein. Uncrosslinked control PVdF fiber mats were electrospun from 20 wt%/vol solutions in 1:1 dimethyl acetamide (DMAc):acetone (both from Aldrich Chemical Co.).

5.2.2 Ionic Conductivity

The fiber mats were swollen with a 1M lithium triflate (LiOTf, Aldrich Chemical Co.) solution in a 1:1 (vol/vol) mixture of ethylene carbonate (EC, Aldrich Chemical Co.) and dimethyl carbonate (DMC, Aldrich Chemical Co.). After swelling to equilibrium over three days (1,700 – 1,200 wt% liquid electrolyte), the samples were sandwiched between two gold plated stainless steel electrodes of a Solartron 12960 sample holder. A Solartron SI 1260-impedance analyzer in conjunction with Scribner Z-Plot software was utilized to obtain standard Nyquist plots (1.7 MHz – 0.1 Hz). The high frequency intercept for the real impedance (Z') of the swollen samples was used as the electrolyte resistance (R) based upon accepted literature.[32,33] The ionic conductivity σ was determined using Equation 5.3,

$$\sigma = \frac{d}{R \cdot S}, \tag{5.3}$$

where d is the swollen fiber mat thickness (determined using a built-in micrometer), R is the resistance, and S is the swollen fiber mat surface area. An error of ± 1 mS cm^{-1} is estimated for σ.

5.2.3 NMR Analyses: Spin-Spin Relaxation, PFG Diffusion, and ^{17}O Spectroscopy

The 1M LiOTf liquid electrolyte was sealed using an oxygen/natural gas torch into a 5 mm NMR tube to eliminate changes due to volatility and water absorption. Four capillaries of 0.8 mm I.D. and 1.0 mm O.D. (Fisher Scientific) were placed axially in the NMR tube prior to sealing to minimize the contribution of convection to the measured diffusion coefficients.[23] PEO10, PEO20, PEO30, PVdF control, and glass fibers (control) were cut into 2 mm x 10 mm strips and threaded through a 3.0 mm I.D. and 4.0 mm O.D. hollow glass tube. The samples were vacuum dried (25°C) for 24 hrs and then one end of the tube was put into contact with the liquid electrolyte in a sealed vial for three days in order to wick solution into the fiber mats. Residual liquid electrolyte was blotted off and the sample-loaded glass tubes were then placed into a 5 mm NMR tube and sealed with an oxygen/natural gas torch.

All spin-spin relaxation time (T_2) measurements were conducted at 35°C using a 400 MHz Bruker Avance III WB NMR spectrometer, equipped with a MIC probe and 5.0 mm ^{7}Li or ^{19}F coils. The Carr-Purcell-Meiboom-Gill (CPMG) pulse sequence[34] ($90°_{x} - [\tau - 180°_{y} - \tau]_{n}$) with an individual echo delay time τ = 1 ms, 90° and 180° pulse lengths of 5 μs and 10 μs for ^{7}Li, and 15 μs and 30 μs for ^{19}F, afforded an exponential attenuation of signal intensity as a function of total spin echo delay time $2\tau n$ and these decays were fit using

$$I = I_0 e^{-\frac{2\tau n}{T_2}}, \tag{5.4}$$

where I_0 is the signal amplitude at $\tau = 0$ and $n = 1$.[34-36] A bi-exponential fit was used, where appropriate, to extract two-component T_2 values and intensities.

All $^{7}Li/^{19}F/^{1}H$ PFG-NMR diffusometry experiments were performed using a 400 MHz Bruker Avance III widebore NMR spectrometer, equipped with a MIC probe coupled to a Diff60 z-axis gradient. In the NMR diffusometry experiment, measured signal amplitude I as a function of gradient strength, g, was fit to the Stejskal-Tanner equation[19,23,37]

$$I = I_0 e^{-D\gamma^2 g^2 \delta^2 (\Delta - \frac{\delta}{3})}, \quad (5.5)$$

where I_0 is the signal amplitude at $g = 0$, γ is the gyromagnetic ratio, δ is the effective gradient pulse length, Δ is the diffusion time between gradient pulses, and D is the self-diffusion coefficient.[37] The simple and robust pulsed-gradient stimulated echo (PGSTE) pulse sequence was used with 90° pulse lengths of 5 μs, 15 μs, and 18 μs for ^{7}Li (Li^{+}), ^{19}F (triflate), and ^{1}H (carbonate solvents) respectively. A repetition time of 4 s, effective gradient pulse lengths of δ = 1 – 4 ms (actual pulse length = 1.57 × effective gradient pulse length for the half sinusoid gradient pulse), and diffusion times of Δ = 6 – 200 ms were used for lithium and triflate diffusion measurements. Maximum gradient strengths of 50 – 500 G cm^{-1} were used to achieve 80% signal attenuation in 16 – 32 gradient steps. Sufficient signal-to-noise ratio (SNR) for each data point was achieved with 8 – 16 scans for each nucleus. Acquisition times of 2.0 s, 1.6 s, and 3 s were used for lithium, triflate, and carbonates, respectively, for the pure liquid electrolyte studies. Acquisition times of 100 and 50 ms were used for lithium and triflate, respectively, for the swollen fiber mat studies. PGSTE parameters were calibrated as previously reported.[38] Variable temperature NMR diffusometry experiments were conducted over a relatively narrow temperature range (20 – 50 °C or 30 – 40 °C in 2° increments), to minimize the influence of convection on diffusion. Each temperature set point was allowed to equilibrate for at least 30 minutes prior to acquisition.

Natural abundance ^{17}O NMR measurements were conducted on a 600 MHz Bruker Avance III narrowbore NMR spectrometer (ν_o = 81.4 MHz), equipped with a DOTY $^{1}H/X$ 5 mm probe (DSI Model). Pulse-acquire experiments with an acquisition time of 1 ms, relaxation delay of 1 s, 90° pulse length of 15 μs, and 10,240 scans were used to collect spectra.

5.3 Results and Discussion

5.3.1 Probing the Morphology and Ion Transport of Polymer-Gel Electrolytes

Here we present a tunable fibrous framework that retains a high concentration of liquid electrolyte, is mechanically stable, and exhibits high ionic conductivity. We utilize electrospinning from PEO/PETA solutions in conjunction with UV initiated crosslinking.[6] After UV exposure (1 hour per side) and vacuum drying, a mat composed of 1 μm diameter fibers swells and retains up to 1,700 wt% of the liquid electrolyte (Figure 5.1). Dynamic mechanical analysis (DMA) shows the bulk dry fiber mats have a Young's Modulus of ~ 5 MPa (not shown), which is likely much lower than the individual fiber modulus. For battery applications, one should consider the μm-scale modulus to suppress dendritic growth at the fiber-electrode interface.[39] Such modulus studies should be the subject of further studies for the present material. Notably, as the PETA content increases, the equilibrated wt% uptake decreases to 1,200 wt%, a factor of three higher uptake in comparison to a conventional PVdF fiber mat.[6] A decrease in liquid electrolyte uptake is likely due to a reduction in polymer chain dynamics and increase in network stiffness as the crosslink density increases. With a high liquid electrolyte uptake that depends on PETA content, we aim to understand correlations between the swollen fiber mat morphology, multiscale transport properties, and ionic conductivity within the present material.

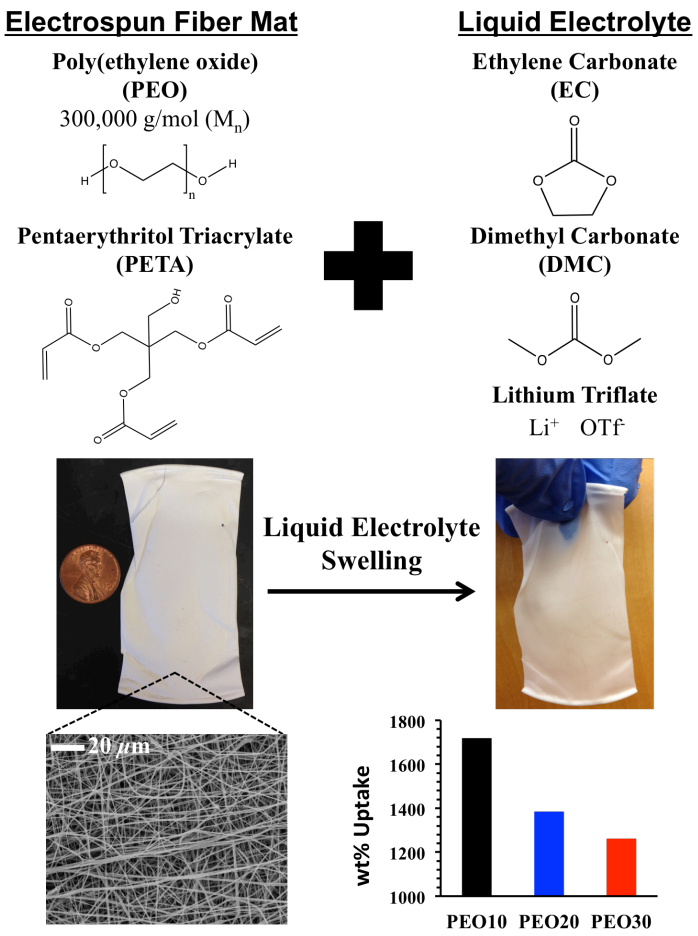

Figure 5.1. The electrospinning process affords fibers that are on average 1 μm in diameter (SEM at lower left). Equilibrium liquid electrolyte uptake varies from up to 1,700 – 1,200 wt% depending on crosslinking agent (PETA) content. Errors in fiber mat wt% uptakes are ± 5%.

We include sample 1D ^{1}H (EC and DMC), ^{7}Li (lithium), and ^{19}F (triflate) NMR spectra of the liquid electrolyte components swollen into PEO10 in supporting information (not shown), which indicate clean samples with single peaks for each of Li^{+}, OTf^{-}, EC, and DMC. ^{1}H spectra also show narrow low intensity vinyl signals from PETA that increase in area from PEO10 to PEO30 (Figure 5.2). These signals represent the presence of unreacted acrylate PETA groups with some substantial degree of molecular mobility, but which were not washed out after

crosslinking, indicating that these are not isolated uncrosslinked PETA. Thus, these signals likely come from PETA experiencing rapid rotational motion about a single or multiple bonds to PEO (or to other PETAs). A systematic NMR and sample modulation study would yield more specific information about final crosslinking properties, which we leave for the future.

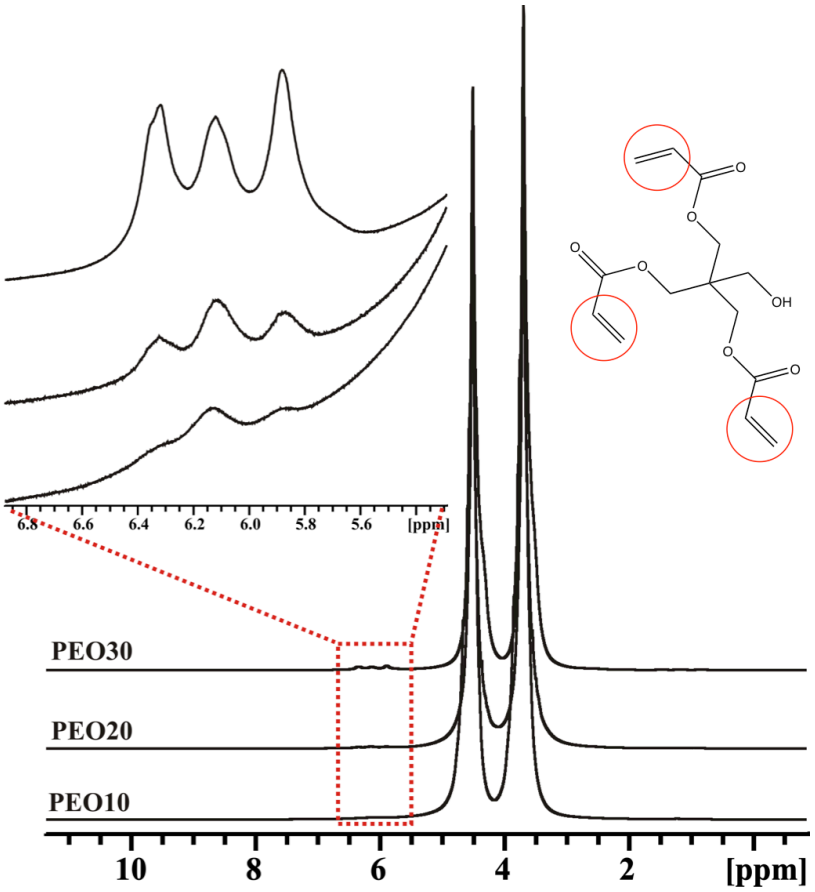

Figure 5.2. 1D ^{1}H NMR spectra of swollen fiber mat electrolytes. In addition to the large peaks due to EC and DMR, narrow signals near 6 ppm (inset) report on a mobile fraction of vinyl functionality on PETA, indicating the presence of PETA vinyl groups that are not fully reacted.

We begin by investigating the swollen fiber mat morphology through spin-spin relaxation time (T_2) measurements. T_2 probes variations in local magnetic field, and so allows us to investigate differences in chemical or physical environments that a nucleus (e.g., ^{7}Li)

experiences during the total spin echo delay time ($2\tau n$). Lithium T_2 yields bi-exponential fits for all samples (Figure 5.3). To explore whether a faster relaxing Li^+ species might be present, we decrease our spin echo delay time τ to 100 μs and see the same T_2 values and relative intensities (not shown). Moreover, we compare the 1D pulse-acquire spectrum to the shortest spin echo delay time ($2\tau n$ = 400 μs) spectrum and see similar lineshape and signal intensity, verifying that a "tightly bound" (faster relaxing) lithium component is not present (not shown). The short-T_2 and long-T_2 fit components differ by an order of magnitude (not shown), enabling clean three parameter fits (including intensities for each T_2 component, normalized for total population). As a function of wt% PETA, we see an increase (26% to 79%) in the relative intensity of the long-T_2 component and a decrease (74% to 21%) in the short-T_2 component, which indicates a change in relative population of lithium within two different environments. We see similar T_2 component intensity variations for triflate (not shown).

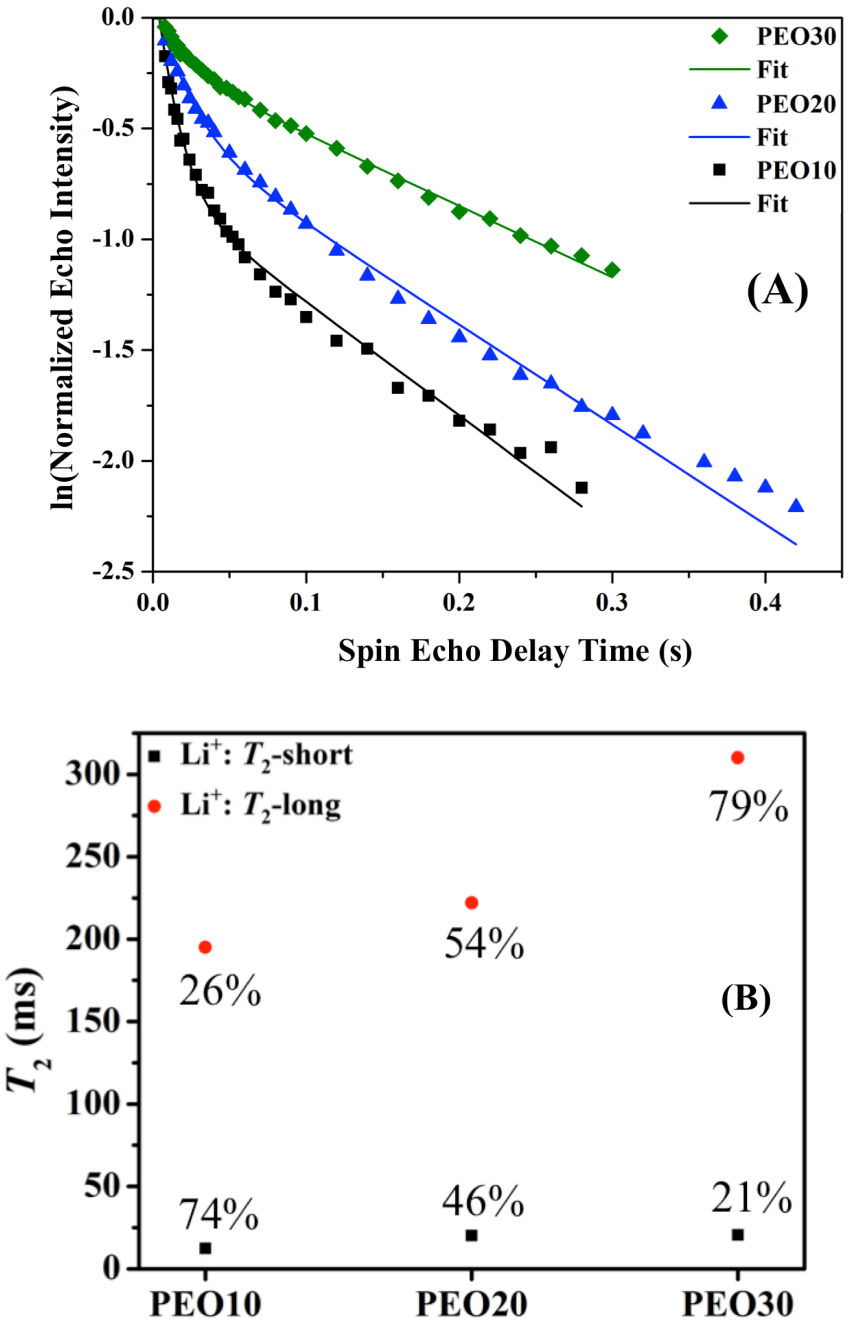

Figure 5.3. ^{7}Li spin-spin (T_2) relaxation time measurements (A) yield two-component decay curves (35°C). The relative intensities (%) of the long-T_2 and short-T_2 components increase and decrease (B), respectively, as a function of wt% PETA, delineating an increase in the mobile lithium component (long-T_2) with increasing PETA. Errors in T_2 values are approximately ± 3%, and for relative component fractions are ± 6%. Both components increase in T_2 values with

PETA crosslinker content, indicating increasing average Li^+ mobility. We assign the short- and long-T_2 components to ions within and between the fibers, respectively.

When contemplating the bi-exponential T_2, we consider the time scale and length scale T_2 reports on. From our measured T_2 data, we define a length scale over which magnetization decoherence occurs during the total spin echo delay $2\tau n$. We choose the maximum $2\tau n$ delay time for the short-T_2 component (i.e., before changing slope to the long-T_2 component), thus providing a time scale to calculate the average maximum length scale the short-T_2 reports on. In conjunction with our experimentally measured diffusion coefficients (discussed below) and the equation $\langle r^2 \rangle^{1/2} = (2D2\tau n)^{1/2}$, where $\langle r^2 \rangle^{1/2}$ is the root-mean-square displacement during the time $2\tau n$,[19,20] we calculate an average length scale of 3 μm. This suggests the lithium associated with the short-T_2 component resides within an environment that is smaller than 3 μm, and the relative fraction of lithium within that environment decreases with wt% PETA. Thus, we conclude that the long- and short-T_2 components represent ions between and within the fibers, respectively. Triflate and Li^+ must conserve charge neutrality within the different liquid and fiber environments, thus giving rise to the agreement in population fractions for the two ions across all samples. Note that the pure liquid, control electrospun PVdF, and control glass fiber electrolytes all show *single component* lithium T_2 values of 1.6 s, 213 ms, and 585 ms, respectively (not shown), consistent with zero absorption of electrolyte into the control fibers. While this T_2 study does not provide direct information on how changes in morphology influence transport, the following PFG NMR diffusometry experiments can aid in such correlations.

In order to understand the myriad material features that drive transport in these electrolytes, and reach beyond the information available using conventional ionic conductivity

measurements, we employ ^{7}Li and ^{19}F PFG NMR diffusometry as a function of diffusion time and temperature. A method for mapping multi-length scale morphology of porous systems is through so-called restricted diffusion studies.[19,22,40] By measuring D with increasing diffusion encoding (drift) time Δ in the PGSTE sequence and/or by changing the observed diffusing species size, these experiments can probe transport over a range 50 nm to 10 μm in length scale.[19,20,22,25,40] If morphological boundaries or restrictions (i.e., structural heterogeneities) exist on such length scales, a decrease in D vs. Δ signifies restricted diffusion,[19,22,40] which allows assessment of the material heterogeneity features that directly affect transport.

Figure 5.4 shows a compilation of lithium and triflate D vs. diffusion time Δ for PEO10, PEO20, and PEO30. Strikingly, lithium and triflate exhibit a reduction in D with Δ for PEO10 and PEO20, while for PEO30 D is independent of Δ. Based on the root-mean-square displacement equation $\langle r^2 \rangle^{1/2} = (2D\Delta)^{1/2}$, lithium and triflate diffuse on average 1 – 10 μm during Δ = 6 – 200 ms.[19,40] Thus, lithium and triflate sample a region within the swollen fiber mat that contains restrictions on the few μm length scale, as evidenced by a factor of 1.3 decrease in D. Note that we do not see two-component diffusion at short Δ times. We show ^{7}Li and ^{19}F Stejskal-Tanner plots for PEO10 at Δ = 6 ms (not shown) and δ = 1 ms (not shown) to show that single-component diffusion exists for these samples. T_1-filtering effects might also be expected to appear in lineshape differences when sampling a large range of diffusion times, however, we see no such differences (not shown). Moreover, we employ a T_2-filter (100 ms total δ window time in the PGSTE experiment) to remove the short-T_2 component, however, we see no increase in D value to within error bars (not shown). This strongly indicates that the diffusion coefficients of the two T_2 components (assigned to Li^+ within the highly swollen fibers and outside the fibers) are very nearly the same. We conclude that the Li^+ ions within the fibers are experiencing

significantly shorter T_2 due to sub-micron magnetic variations, but the Li^+ transport is not significantly affected by the relatively spatially dilute (relative to individual ion size) polymer chains in the swollen fibers. In other words, magnetic interactions arising from the polymer chains and fiber structure that shorten T_2 in the fibers may not correlate with electric and steric interactions that modify transport, and the electric and steric interactions should be very similar between PEO fibers and carbonate solvent molecules.

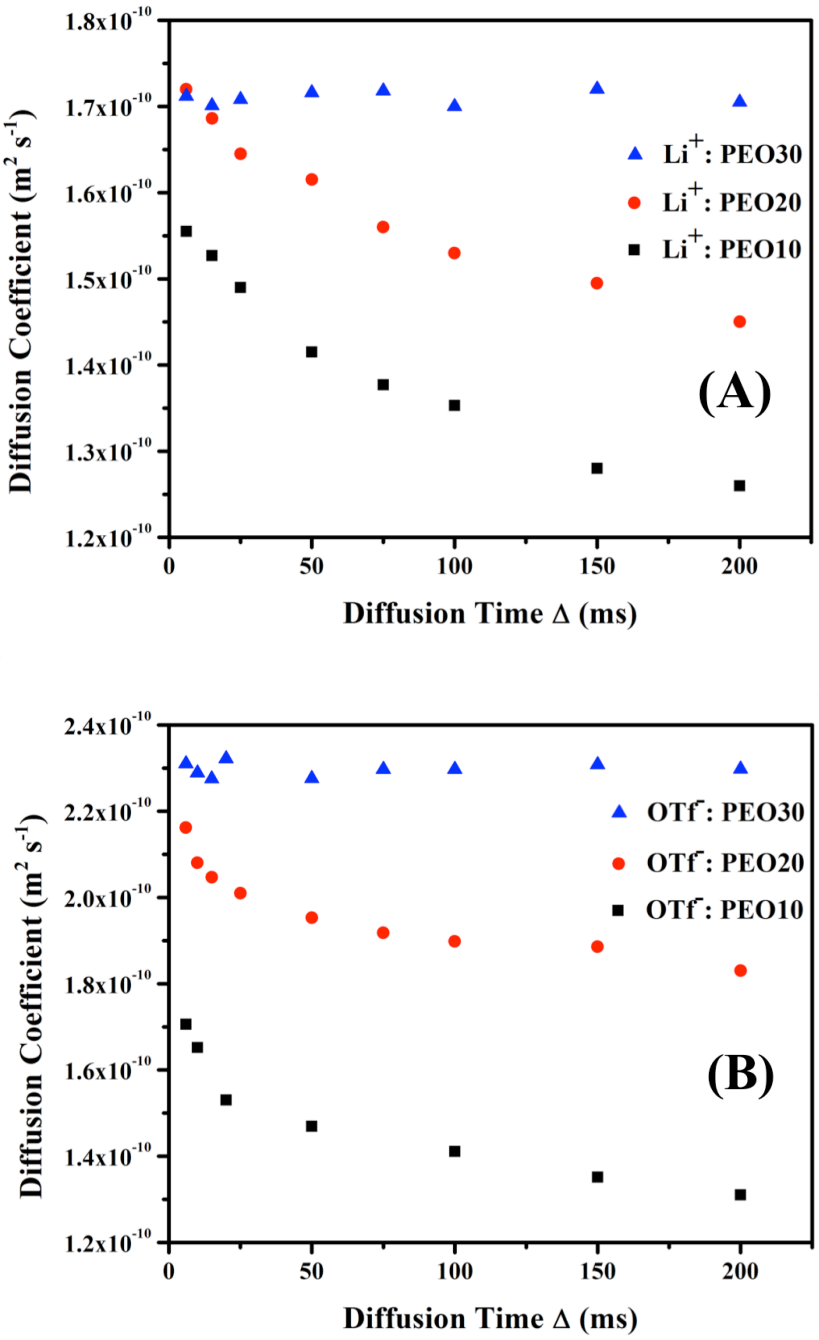

Figure 5.4. Lithium (A) and triflate (B) diffusion coefficients as a function of diffusion encoding (drift) time Δ show decreasing *D* for PEO10 and PEO20, while PEO30 shows a flat dependence. A decrease in *D* shows that lithium and triflate experience significant morphological restrictions.

Our bi-exponential T_2 results (Figure 5.3) suggest that the short-T_2 lithium component represents lithium within an environment ≤ 3 μm in size, which equals the swollen fiber diameter. Moreover, the T_2 data indicates that the relative fraction of lithium and triflate within a more mobile environment (long-T_2) increases with wt% PETA. Our time-dependent diffusion data (Figure 5.4) shows restricted motion for PEO10 and PEO20, while PEO30 D is independent of Δ. Thus, ion transport becomes increasingly dominated by "free" liquid electrolyte between fibers as PETA content increases. Assuming the short-T_2 lithium component represents the fraction of liquid electrolyte within the fiber and taking into account the drop from 1700 wt% to 1200 wt% equilibrium swelling with increasing PETA, we calculate an increase in free liquid electrolyte in the space between fibers by a factor of 2 and a decrease in liquid electrolyte within the fibers by a factor of 6 from PEO10 – PEO30. Figure 5.5 illustrates key features of the three electrolyte samples.

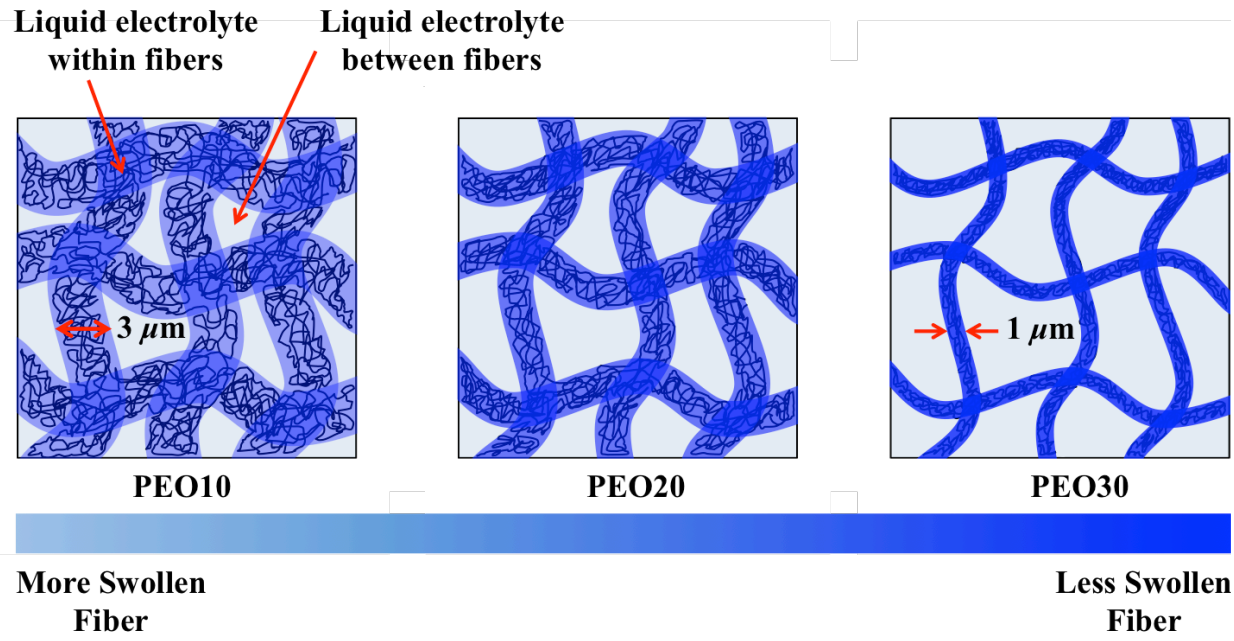

Figure 5.5. Fiber mat morphology and electrolyte population changes with crosslinker (PETA) content, as evidenced by T_2, restricted diffusion, and equilibrium liquid uptake results. Fibers swell less with ions and solvent with increasing PETA for the PEO10, PEO20, and PEO30 samples. An increase in salt solution content (26% to 79%) within the inter-fiber phase is seen from T_2 measurements due to a decrease in liquid electrolyte penetration into the fiber, thus PEO30 shows no restricted diffusion.

Next we investigate these electrolytes using ionic conductivity measurements. Previous conductivity measurements by Forbey *et al.* on 400 wt% uptake of 1M $LiClO_4$ (same EC/DMC solvent system) into the PEO-based crosslinked fiber mat show $\sigma \cong$ 6 mS cm^{-1}.[6] Using our new experimental procedures for electrospinning and equilibrium swelling (1,700 – 1,200 wt%) with 1M LiOTf, Figure 5.6 shows representative ionic conductivity values for the pure liquid electrolyte as well as PEO10, PEO20, and PEO30 at room temperature (25 °C). When compared with the previous 1M $LiClO_4$ data,[6] we observe similar ionic conductivities. None of the

measurements in this paper, including conductivity, will depend on changes in the dielectric permittivity of PEO, as there is no crystallinity present in any of the swollen membranes.[6] We note that a range of lithium salts and polar electrolyte solvents could be imbibed into this fibrous network to form highly conductive and mechanically robust gel electrolytes.

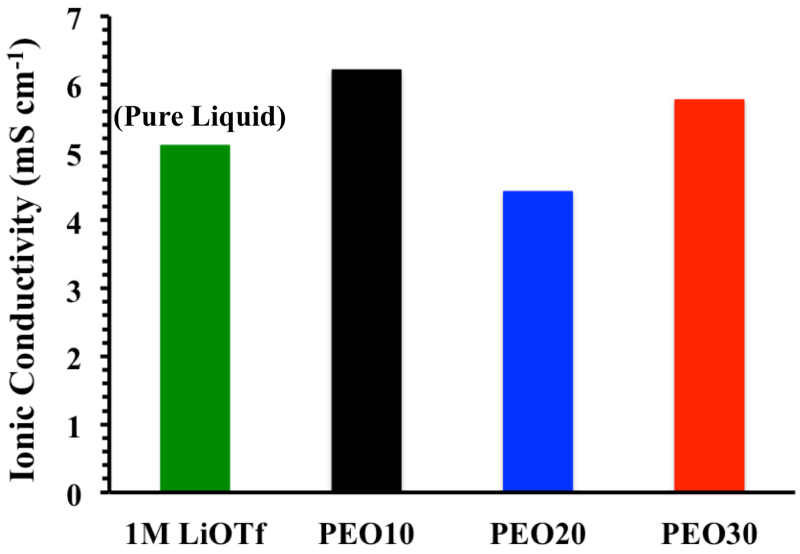

Figure 5.6. Ionic conductivity of pure liquid electrolyte (1M LiOTf in 50:50 (v/v) EC:DMC) and electrospun gel electrolytes. All conductivities are calculated from the resistance at $v_{touchdown}$ (~ 100 Hz) and are within error (± 1 mS cm^{-1}) of each other.

To understand correlations between the T_2, restricted diffusion, and ionic conductivity data presented thus far, we consider the fundamental interpretation of alternating current (AC) impedance spectroscopy measurements. In the presence of an AC electric field, ions move according to electrophoretic motion with a mobility μ over a distance that depends on the chosen frequency. The inverse of the high frequency intercept for the real impedance (Z') defines a time scale Δ_σ during which ions are driven. Thus, the length scale AC impedance probes should be considered in order to properly correlate changes in σ values to changes in material morphology. We can estimate (or predict) the electrophoretic mobility μ_{pred} using[13,41]

$$\mu_{pred} = \frac{D_{meas} Z F}{R T} \quad , \tag{5.6}$$

where D_{meas} is the measured diffusion coefficient, Z is the number of unit charges per ion, F is Faraday's constant, and R is the universal gas constant. For this system, we calculate μ_{pred} values of ~ 6 × 10^{-9} m^2 s^{-1} V^{-1} for lithium and triflate ions. In calculating μ_{pred}, we use measured diffusion coefficients that represent ms time scale transport. During a PFG NMR diffusometry experiment, diffusing species experience short time scale (~ 1 ns) intermolecular exchanges among locally associated solvent molecules and ions during Δ_σ.[14] Since D_{meas} depends on the ensemble average of charged and uncharged species, μ_{pred} is an overestimation (by typically a factor of 2) in comparison to electrophoretic NMR (ENMR) measurements of μ, which measure the average motion of only charge-carrying species.[13] Direct measurements of μ for this and other ion-containing systems are ongoing efforts and will be the focus in future publications. Given the ionic conductivity measurement applies a potential difference ΔV over a distance m (i.e., $E = \Delta V/m$) and during a time period Δ_σ, we can estimate the distance traveled d for the ion,

$$d = \mu E \Delta_\sigma . \tag{5.7}$$

From our impedance spectroscopy experiments, the Nyquist touchdown frequency $\nu_{touchdown}$ ~ 100 Hz and so the inverse Δ_σ ~ 0.01 s is the time scale used to obtain the conductivity, ΔV ~ 0.01 V, and m = 150 μm (i.e., swollen fiber mat thickness). Thus, using our μ_{pred} values, we calculate ion displacement distances of ~ 5 nm during the conductivity measurement, much smaller than the length scale probed in our restricted diffusion measurements. That is, *during the ionic conductivity measurement, moving ions only travel ~ 5 nm and thus report only weakly on morphological properties within the present material.* We emphasize that this length scale for σ

measurements should be considered when interpreting and comparing ionic conductivity results across other systems.

5.3.2 Understanding Material Factors That Influence Ion Transport

In polymeric systems ion transport is influenced by a variety of material features, from local intermolecular interactions to micron-scale morphological structures. Our group seeks to deepen the current understanding of how local intermolecular energetics drive ion transport within ion-dense systems (e.g., lithium liquid electrolytes, ionic liquids, and ion conducting membranes). A key technique for probing chemically specific transport phenomena is variable temperature PFG NMR diffusometry in conjunction with the Arrhenius equation (Equation 5.2), to yield an activation energy E_a.[21,25] Note that transport in polymeric media over large temperature ranges can often exhibit Vogel-Fulcher-Tammann (VFT) dependence,[42] however in the present case Arrhenius analysis yields excellent fits and allows simpler physical interpretation.

Figure 5.7 compiles Arrhenius plots for all individual components of the liquid electrolyte (i.e., EC (^{1}H), DMC (^{1}H), lithium (^{7}Li), and triflate (^{19}F)). The high precision of our variable temperature diffusion measurements gives errors in E_a of $\leq \pm 1$ kJ mol^{-1}.

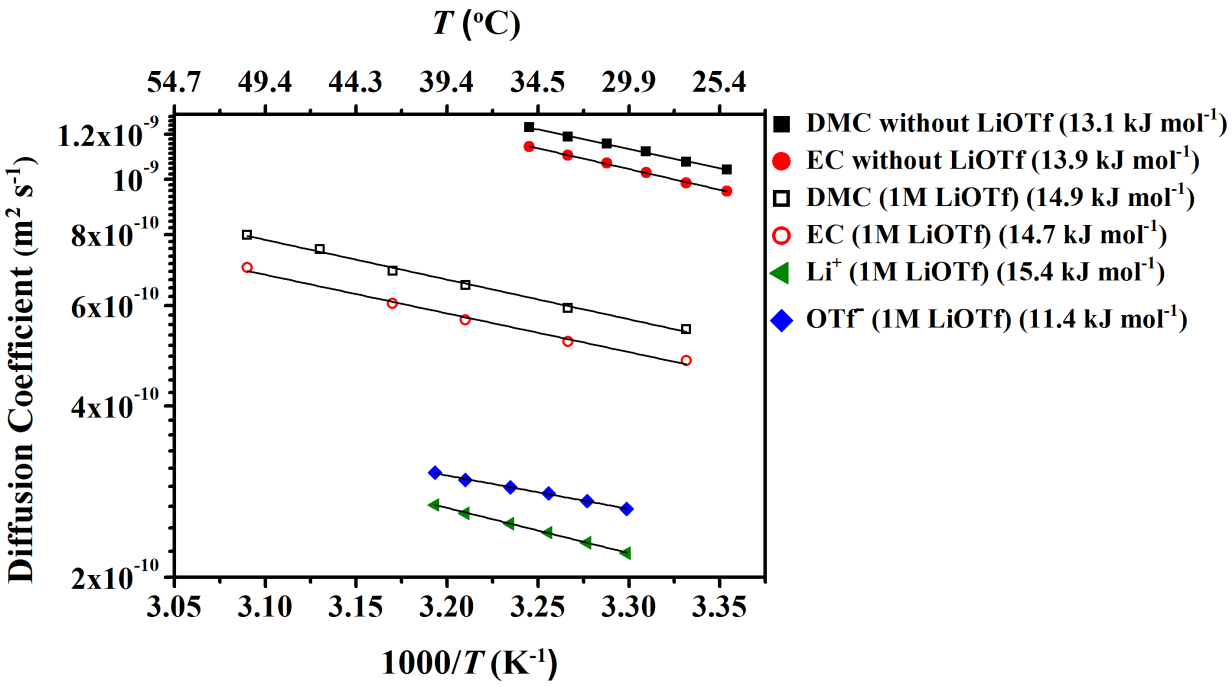

Figure 5.7. Arrhenius plots of lithium (^{7}Li) triflate (^{19}F) ions and EC (^{1}H), and DMC (^{1}H) solvents (with and without LiOTf) give insight into local intermolecular interactions for the pure liquid electrolyte. D and E_a values for the solvents decrease and increase, respectively, with addition of LiOTf due to the introduction of ion-dipole associations. Lithium D and E_a are slower and larger than triflate, suggestive of stronger ion-dipole interactions for lithium, creating a larger solvation shell. Estimated error in D is $\leq \pm 5\%$ and E_a is $\leq \pm 1$ kJ mol^{-1}.

We see that the diffusion coefficients and E_a for EC and DMC are very similar to each other without LiOTf, suggestive of a homogenous mixture of the two carbonate molecules with similar local energetics. Furthermore, lithium and triflate D are a factor of 3 slower than the carbonates. Despite the smaller van der Waals radius of lithium ion (Li^+ = 0.073 nm and OTf^- = 0.27 nm) in vacuum, a slower diffusion coefficient and larger E_a (by 4 kJ mol^{-1}) than triflate suggests stronger intermolecular interactions that influence D via the effective solvated r_H.

We now discuss how the electrospun fiber mat influences E_a of absorbed lithium and triflate ions. Figure 5.8 shows lithium (a) and triflate (b) Arrhenius plots for PEO10, PEO20, and PEO30. Note that D values in Figure 5.8 are acquired with diffusion time Δ = 25 ms.

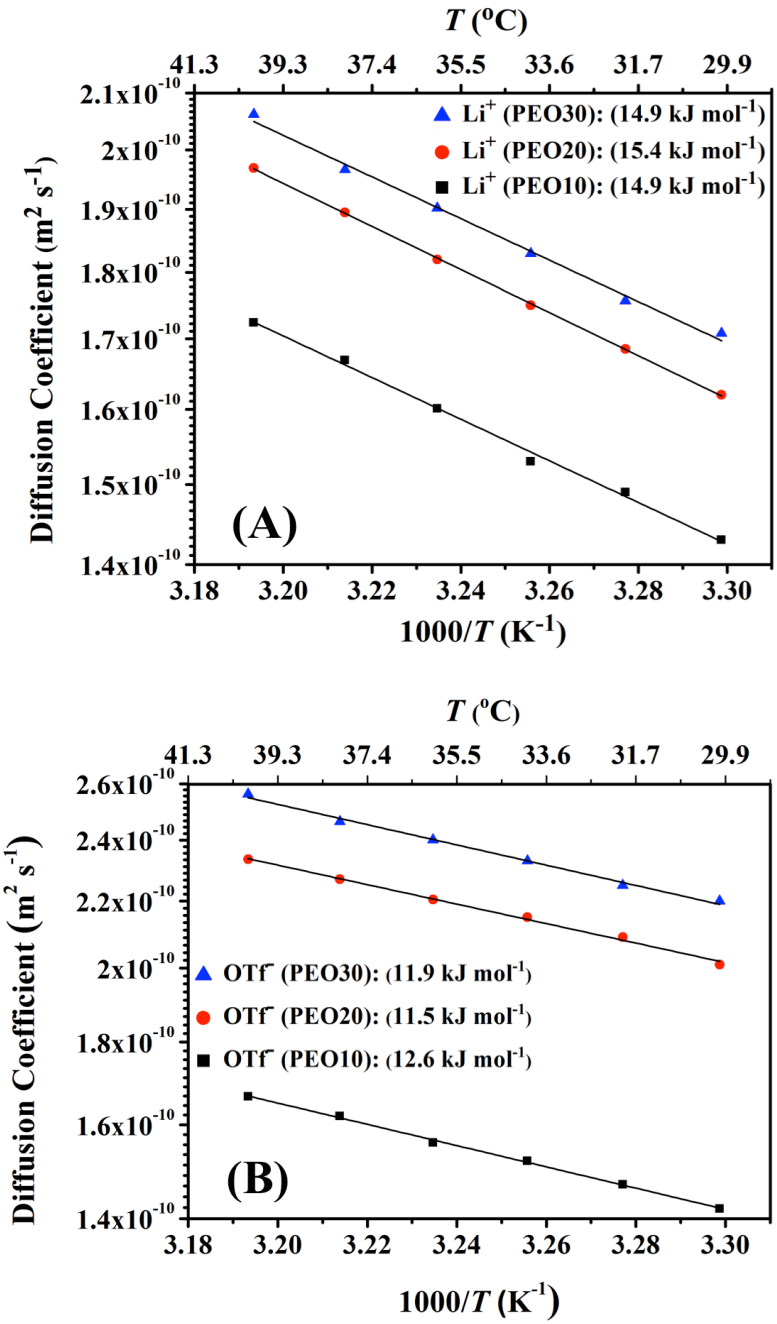

Figure 5.8. Lithium (A) and triflate (B) Arrhenius plots as a function of wt% crosslinker (PETA) allows understanding of how the fiber mat influences macro- and microscopic transport

properties. Lithium and triflate diffusion rates vary significantly across PEO10, PEO20, and PEO30 samples, while E_a is independent of wt% crosslinker for both ions with average E_a = 15.1 for Li^+ and E_a = 12.0 kJ mol^{-1} for OTf^-. Estimated error in D is $\leq \pm 5\%$ and E_a is $\leq \pm 1$ kJ mol^{-1}.

Consistent with T_2 measurements (Figure 5.3) showing faster dynamics at higher crosslinker content, lithium and triflate diffusion coefficients increase with wt% PETA. The small but significant changes in D also correlate with little change in σ (Figure 5.6). Comparing with our control electrospun PVdF and glass fiber mats (not shown), lithium D is 1.6×10^{-10} m^2 s^{-1} and 1.9×10^{-10} m^2 s^{-1} at 30 °C for PVdF and glass fibers, respectively. Moreover, lithium E_a is 15.4 kJ mol^{-1} and 14.8 kJ mol^{-1} for PVdF and glass fibers, respectively, both within error of our PEO-based materials.

Strikingly, there is no change in lithium and triflate E_a when swollen into the electrospun mats and control materials when compared to the pure liquid electrolyte. Therefore we raise a question: Will lithium and triflate E_a show any dependence on the length scale of the D measurement (morphology effects)? From Figure 5.8, lithium and triflate E_a show no dependence on PETA content; however, our D measurements show restricted diffusion (D vs. diffusion time Δ) behavior (Figure 5.4). To explore this idea, we evaluate lithium (A) and triflate (B) Arrhenius behavior at short-Δ (6 ms) and long-Δ (200 ms) (Figure 5.9) for PEO20. Clearly, E_a does not depend on the μm length scale morphological features, indicating that D and E_a are, in this case, separable quantities and report on structuring and dynamics at different length scales. We draw parallels from previous studies of H_2O E_a in Nafion® and trifluoromethanesulfonic acid (CF_3SO_3H) solutions, wherein E_a becomes invariant at high water-

to-sulfonate molar ratio λ (*mols*H_2O : *mols*SO_3^-).[21] In Nafion®, there is little influence from the SO_3^- groups to measurably change E_a for λ > 8, which aligns well H_2O E_a in solutions. We see no change of E_a in the present material due to a similar effect as in highly hydrated Nafion®,[21] where the carbonate (EC and DMC):lithium molar ratio is ~ 13 in/out of the fiber, the (EC and DMC):PEO oxygen atom ratio is ~ 16, and the (PEO oxygen atom):lithium molar ratio is ~ 2 (much more dilute). Note a clear dependence of the pre-exponential factor D_0 on Δ (line slopes are the same, lines are parallel and offset vertically). Morphological information such as tortuosity must be encoded into D_0 when observing such a D dependence with Δ. With invariance in the local diffusion process (i.e., no change in E_a) between liquid electrolyte and swollen fiber mats, we see a reduction in D_0 dominated by the micron-scale morphological restrictions that decrease the ensemble average diffusion coefficient. In liquids, any changes in D_0 must only arise from local entropy changes on the nm scale,[21] but this would produce no dependence of D_0 with Δ due to the absence of morphological boundaries on the diffusion scale of $(2D\Delta)^{1/2} \sim 1$ μm.

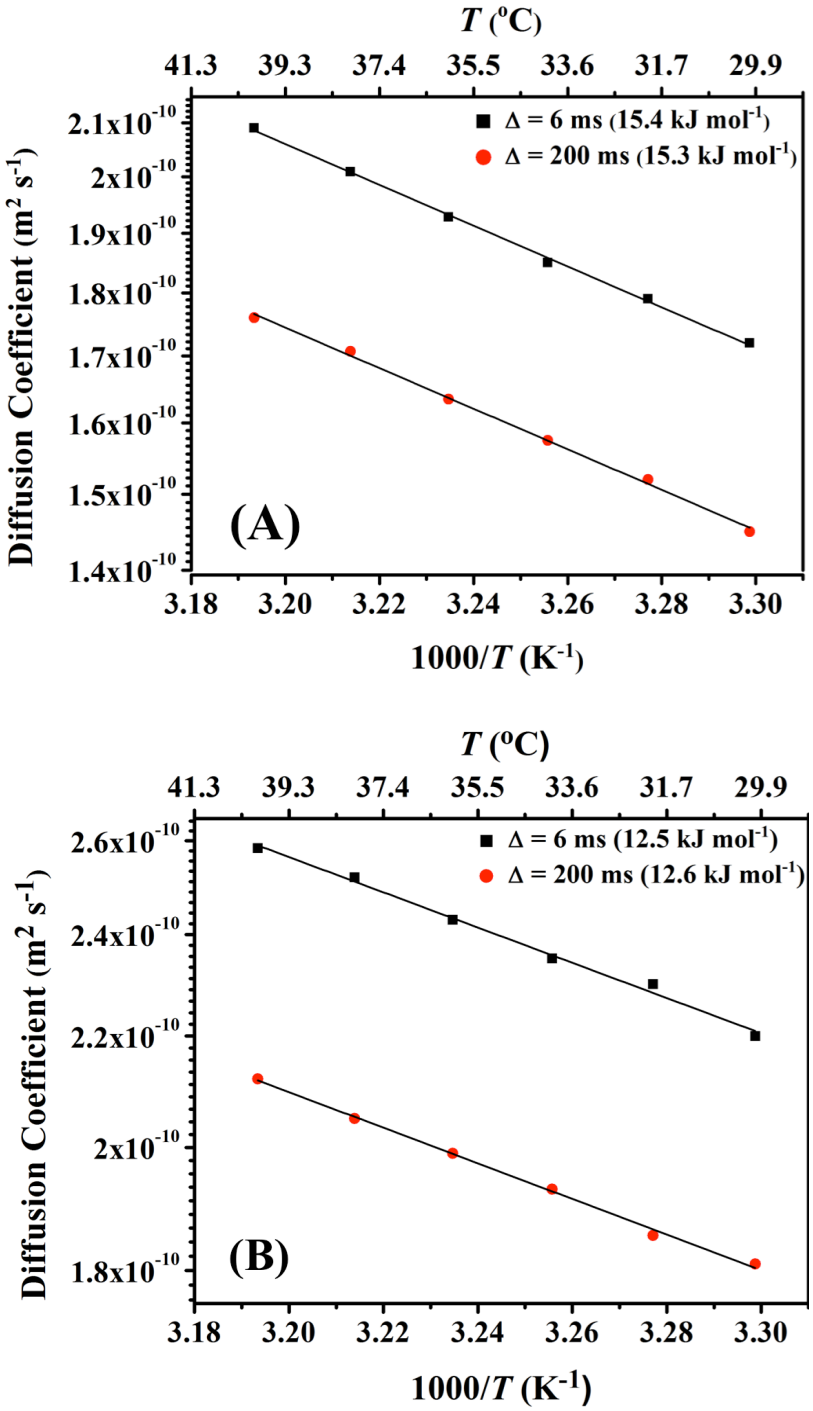

Figure 5.9. Lithium (A) and triflate (B) Arrhenius plots at short (Δ = 6 ms) and long (Δ = 200 ms) diffusion time shows that E_a does not depend on morphology while D does, further suggesting that the two parameters report on different length scales and E_a can provide distinct local information.

Recently, Alam *et al.* investigated the influence of backbone and side chain dynamics on H_2O and methanol (MeOH) diffusion and E_a in a series of anion exchange membranes (AEM).[43] Interestingly, the authors are able to resolve two-component E_a values. The exchange rate between "free H_2O" and "polymer membrane-associated H_2O" and "free MeOH" and "polymer membrane-associated MeOH" are 53 s^{-1} and 373 s^{-1}, respectively, and affords spectral resolution of both signals to yield two diffusion coefficients and calculation of two E_a values. Based on our current understanding of E_a, the resolution of more than one E_a value in systems where chemically different environments exist will depend on: 1) How chemically different the local solvation shell is, 2) If diffusing species sample different morphological or chemical environments, and 3) If they do, the exchange rate between the environments relative to the diffusion measurement timescale Δ. In the case of Alam *et al.*, their H_2O and MeOH environments must be in slow exchange relative to the Δ timescale.

To further understand molecular-scale interactions in the present material, we conduct natural abundance (0.037%) ^{17}O NMR on EC/DMC mixture, pure liquid electrolyte (EC/DMC – 1M LiOTf), and the swollen PEO10, PEO20, and PEO30 mats (Figure 5.10).

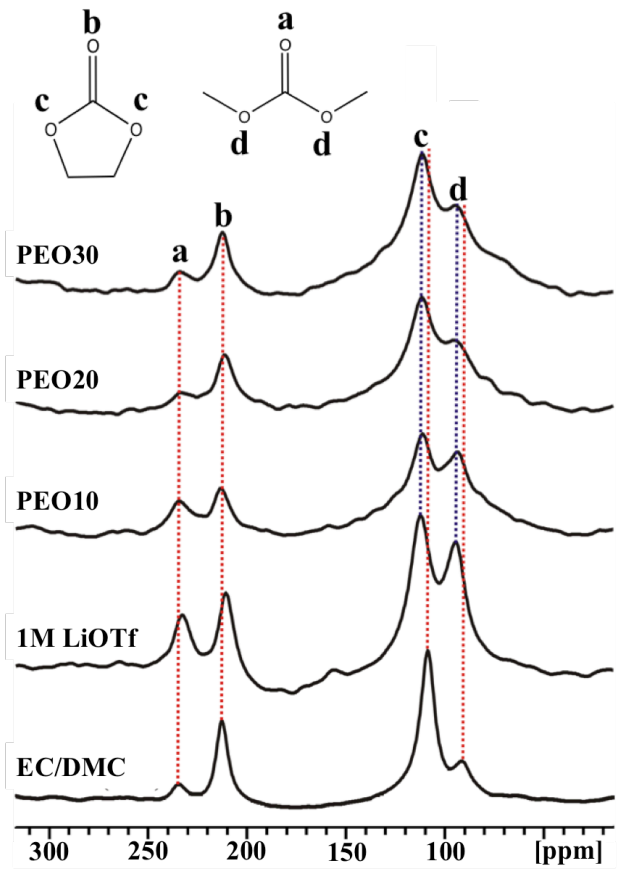

Figure 5.10. Natural abundance ^{17}O NMR on carbonate solvent molecules. We observe a change in chemical shift with addition of LiOTf to the EC/DMC liquid due to the introduction of ion-dipole interactions, thus perturbing the electron density of the oxygen atoms. However, no change in chemical shift arises when the liquid electrolyte is swollen into the fiber mat, suggesting that the fibers cause no significant change to solvation associations.

The resonance frequency (chemical shift) of the carbonate oxygen's depend on small perturbations in local electron density, and thus report on changes to the ion solvation shell (i.e., ensemble average change to intermolecular interactions).[44] With the addition of LiOTf to the EC/DMC solvent mixture, we see a small but evident deshielding of the EC and DMC ether oxygen atoms, as shown by Bogle *et al.* in their study of $LiPF_6$, wherein a change in chemical

shift of nearly 10 ppm can be seen as the amount of EC in solution increases.[44] We note that there is no observable change in the local ion solvation structure due to the presence of or variations in the fiber mat. Notably, we do not see the shielding effect of the carbonyl oxygen atoms with addition of 1M salt as observed by Bogle *et al.* This indicates a difference in ion-solvent and/or ion-ion associations between solutions of these two anions (PF_6^- and OTf^-). Finally, we see little change in chemical shift and linewidth for the ether oxygen atoms in PEO10, PEO20, and PEO30 (not shown) when compared to the pure 1M LiOTf solution ^{17}O spectrum, further supporting no change to molecular-scale interactions when the liquid electrolyte is swollen into the fiber mat. We note that signal intensities vary slightly due to noise variations across the spectra due to the relatively low signal-to-noise ratio.

To provide a conceptual overview of our findings, Figure 5.11 illustrates the information from these measurements over multiple length scales. This includes separate information gleaned from D and E_a and the difference in the length scales probed by each quantity. Note that we do not imply that morphological properties cannot in some cases influence E_a. For example, if there is enough change within the sphere of influence that E_a probes, such as a change in diameter or symmetry of a channel lined with charged groups (i.e., SO_3^-), a change in E_a will arise when compared to the pure liquid E_a.[21] We will expand on these concepts in future publications.

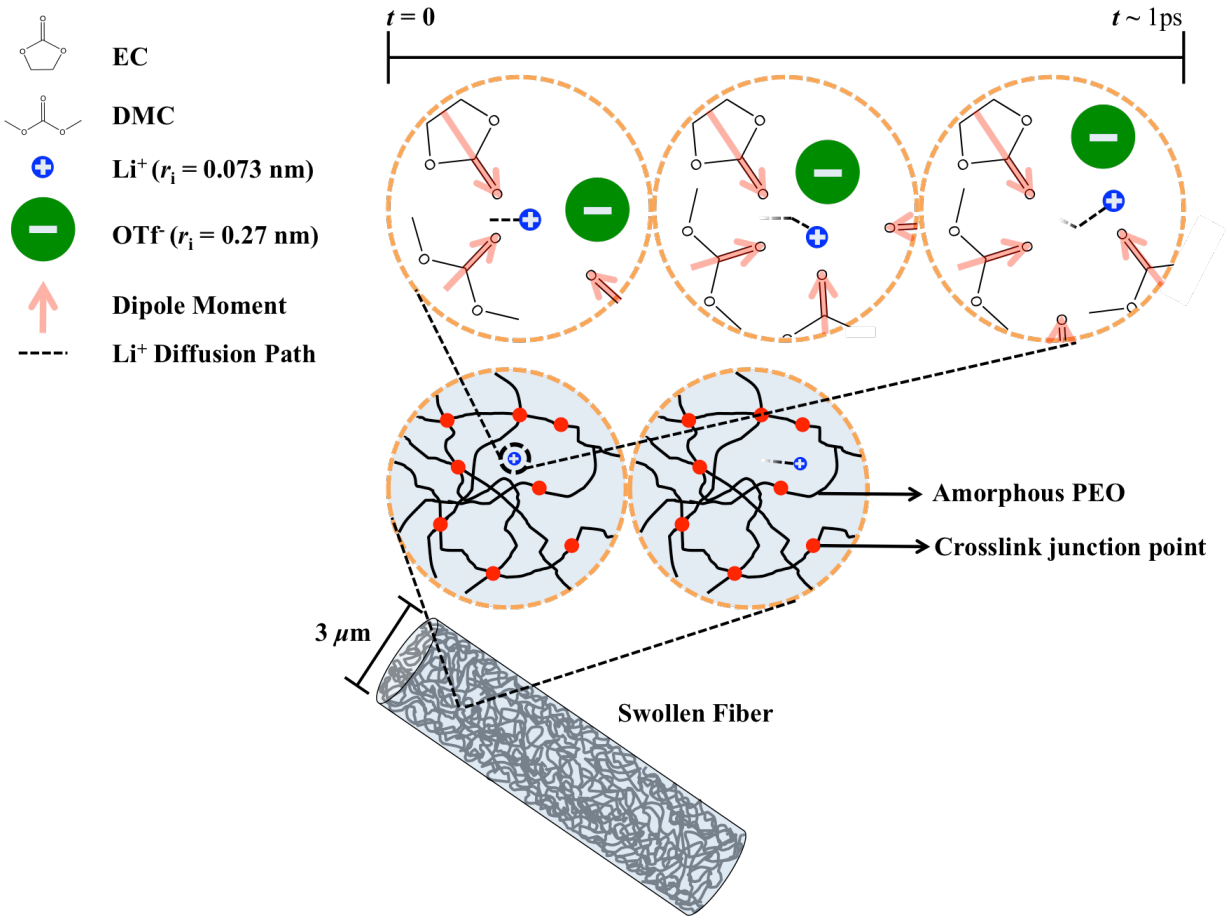

Figure 5.11. A depiction of the information obtained on this polymer-gel electrolyte system. Measured E_a and D values for lithium on the local molecular correlation time scale ($t \sim 1$ ps)[21] and the diffusion time scale (t = 6 – 200 ms), respectively, interrogate different transport phenomena. Experimentally measured D values represent an ensemble average of all lithium species on long time scales and thus derive from both local interactions as well as morphological effects, such as restricted transport due to the swollen fibers. Extracted E_a values reflect an ensemble average of all lithium species on the $t \leq \tau_c$ time scale, due primarily to ~ 1 nm local interactions, such as ion-dipole and ion-ion.

From the liquid electrolyte analysis and our previously reported studies on E_a,[21,25] lithium E_a for the present material represents the ensemble average of intermolecular interactions (e.g., ion-dipole and ion-ion) within a ~ 1 nm sphere of influence on the inertial or ballistic motion time scale (~ 1 ps).[21] Our results show that lithium transport within the present material is not intimately related to polymer chain segmental motion, but rather is dominated by the liquid electrolyte dynamics in combination with the μm-scale morphological restrictions to transport due to the polymer fibers.

5.4 Conclusions

We have investigated a new PEO-based crosslinked fibrous network that swells and retains up to 1,700 wt% of 1M LiOTf liquid electrolyte. Electrospinning and UV crosslinking enable design of a robust fibrous polymer-gel electrolyte for lithium-ion batteries. Multi-modal NMR and ionic conductivity studies provide fundamental understanding of small molecule and ion transport properties within this electrolyte system. We use NMR T_2 spin-spin relaxation to quantify fractions of ions residing within and between fibers. Restricted diffusion studies show a decrease in ion diffusion coefficient with diffusion encoding time (Δ = 6 – 200 ms), and reveal the effects of crosslinker content on morphology-influenced transport. Finally, an Arrhenius analysis of diffusion and ^{17}O NMR spectroscopy show that lithium and triflate local intermolecular interactions are independent of modulations to the fibrous network morphology. Such studies are critical for understanding how morphology and intermolecular forces can separately influence ion transport in polymeric systems for Li^+ battery applications. Indeed, this work breathes fresh air into how combined analyses using NMR spectroscopy, diffusometry (D and E_a), and spin relaxation can be used generally to probe multi-scale transport effects in polymeric materials.

5.5 Acknowledgements

This work was supported by the National Science Foundation under Awards CHE 1057797, DMR 0844933, and DMR 1507764. Any opinions, findings and conclusions or recommendations expressed in this material are those of the author(s) and do not necessarily reflect the views of the National Science Foundation (NSF).

5.6 References

(1) Choi, S. W.; Jo, S. M.; Lee, W. S.; Kim, Y. R. An electrospun poly(vinylidene fluoride) nanofibrous membrane and its battery applications. *Adv. Mater.* **2003**, *15*, 2027.
(2) Tarascon, J. M.; Armand, M. Issues and challenges facing rechargeable lithium batteries. *Nature* **2001**, *414*, 359.
(3) MacGlashan, G. S.; Andreev, Y. G.; Bruce, P. G. Structure of the polymer electrolyte poly(ethylene oxide)(6): LiAsF6. *Nature* **1999**, *398*, 792.
(4) *Principles and Applications of Lithium Secondary Batteries*; Wiley: Germany, 2012; Vol. 1.
(5) *Lithium Ion Rechargeable Batteries: Materials, Technology, and New Applications*; Wiley: Germany, 2009; Vol. 1.
(6) Forbey, S. J.; Divoux, G. M.; Moore, K. E.; Moore, R. B. Cross-Linked Electrospun Poly(ethylene oxide) Fiber Mats as Structured Polymer-Gel Electrolytes. *Transactions of the Electrochemical Society* **2015**, *(Submitted)*.
(7) Hayamizu, K.; Aihara, Y.; Arai, S.; Martinez, C. G. Pulse-gradient spin-echo H-1, Li-7, and F-19 NMR diffusion and ionic conductivity measurements of 14 organic electrolytes containing LiN(SO2CF3)(2). *J. Phys. Chem. B* **1999**, *103*, 519.
(8) Hayamizu, K.; Aihara, Y.; Price, W. S. Correlating the NMR self-diffusion and relaxation measurements with ionic conductivity in polymer electrolytes composed of cross-linked poly(ethylene oxide-propylene oxide) doped with LiN(SO2CF3)(2). *J. Chem. Phys.* **2000**, *113*, 4785.
(9) Arora, P.; Zhang, Z. M. Battery separators. *Chem. Rev.* **2004**, *104*, 4419.
(10) Edward, J. T. Molecular Volumes and the Stokes-Einstein Equation. *J. Chem. Educ.* **1970**, *47*, 261.
(11) Einstein, A. On the Movement of Small Particles Suspended in Stationary Liquids Required by the Molecular-Kinetic Theory of Heat. *Annalen der Physik* **1905**, *17*, 549.
(12) Edward, J. T. Citation-Classic - Molecular Volumes and the Stokes-Einstein Equation. *Current Contents/Physical Chemical & Earth Sciences* **1986**, 14.
(13) Zhang, Z.; Madsen, L. A. Observation of separate cation and anion electrophoretic mobilities in pure ionic liquids. *J. Chem. Phys.* **2014**, *140*.

(14) Hou, J.; Zhang, Z.; Madsen, L. A. Cation/anion associations in ionic liquids modulated by hydration and ionic medium. *J. Phys. Chem. B* **2011**, *115*, 4576.
(15) Fenton, D. E.; Parker, J. M.; Wright, P. V. Complexes of Alkali Metal Ions with Poly(ethylene oxide). *Polymer* **1973**, *14*, 589.
(16) Kumar, M.; Sekhon, S. S. Role of plasticizer's dielectric constant on conductivity modification of PEO-NH4F polymer electrolytes. *Eur. Polym. J.* **2002**, *38*, 1297.
(17) Bruce, P. G. Coordination chemistry in the solid state. *Philosophical Transactions of the Royal Society a-Mathematical Physical and Engineering Sciences* **1996**, *354*, 415.
(18) Berthier, C.; Gorecki, W.; Minier, M.; Armand, M. B.; Chabagno, J. M.; Rigaud, P. Microscopic Investigation of Ionic-Conductivity in Alkali-Metal Salts Poly(Ethylene Oxide) Adducts. *Solid State Ionics* **1983**, *11*, 91.
(19) Callaghan, P. T. *Translational Dynamics and Magnetic Resonance: Principles of Pulsed Gradient Spin Echo NMR*; Oxford University Press: New York, 2011.
(20) Hou, J.; Li, J.; Mountz, D.; Hull, M.; Madsen, L. A. Correlating morphology, proton conductivity, and water transport in polyelectrolyte-fluoropolymer blend membranes. *J. Membr. Sci.* **2013**, *448*, 292.
(21) Lingwood, M. D.; Zhang, Z.; Kidd, B. E.; McCreary, K. B.; Hou, J.; Madsen, L. A. Unraveling the local energetics of transport in a polymer ion conductor. *Chem. Commun.* **2013**, 4283.
(22) Mitra, P. P.; Sen, P. N.; Schwartz, L. M.; Ledoussal, P. Diffusion Propagator as a Probe of the Structure of Porous-Media. *Phys. Rev. Lett.* **1992**, *68*, 3555.
(23) Price, W. S. Pulsed-field gradient nuclear magnetic resonance as a tool for studying translational diffusion .1. Basic theory. *Concept Magnetic Res* **1997**, *9*, 299
(24) Woessner, D. E. N.M.R. Spin-Echo Self-Diffusion Measurements on Fluids Undergoing Restricted Diffusion. *J. Phys. Chem.* **1963**, *67*, 1365.
(25) Kidd, B. E.; Lingwood, M. D.; Lee, M.; Gibson, H. W.; Madsen, L. A. Cation and Anion Transport in a Dicationic Imidazolium-Based Plastic Crystal Ion Conductor. *Journal of Physical Chemistry B* **2014**, *118*, 2176.
(26) Commer, P.; Cherstvy, A. G.; Spohr, E.; Kornyshev, A. A. The effect of water content on proton transport in polymer electrolyte membranes. *Fuel Cells* **2003**, *2*, 127.
(27) Eyring, H. The Activated Complex in Chemical Reactions. *J. Chem. Phys.* **1935**, *3*, 107.
(28) de Araujo, C. C.; Kreuer, K. D.; Schuster, M.; Portale, G.; Mendil-Jakani, H.; Gebel, G.; Maier, J. Poly(p-phenylene sulfone)s with high ion exchange capacity: ionomers with unique microstructural and transport features. *PCCP* **2009**, *11*, 3305.
(29) Kreuer, K. D. Ion Conducting Membranes for Fuel Cells and other Electrochemical Devices. *Chem. Mater.* **2014**, *26*, 361.
(30) Dill, K. A.; Bromberg, S. *Molecular Driving Forces: Statistical Thermodynamics in Chemistry and Biology*; Garland Science: New York, 2003.
(31) Gouverneur, M.; Jeremias, S.; Schönhoff, M. 7Li nuclear magnetic resonance studies of dynamics in a ternary gel polymer electrolyte based on polymeric ionic liquids. *Electrochim. Acta* **2015**, *(Accepted)*.
(32) Du Pasquier, A.; Warren, P. C.; Culver, D.; Gozdz, A. S.; Amatucci, G. G.; Tarascon, J. M. Plastic PVDF-HFP electrolyte laminates prepared by a phase-inversion process. *Solid State Ionics* **2000**, *135*, 249.

(33) Shi, Q.; Yu, M. X.; Zhou, X.; Yan, Y. S.; Wan, C. R. Structure and performance of porous polymer electrolytes based on P(VDF-HFP) for lithium ion batteries. *J. Power Sources* **2002**, *103*, 286.
(34) Meiboom, S. Citation Classic - Modified Spin-Echo Method for Measuring Nuclear-Relaxation Times. *Cc/Eng Tech Appl Sci* **1980**, 16.
(35) Carr, H.; Purcell, E. Effects of Diffusion on Free Precession in Nuclear Magnetic Resonance Experiments. *Phys. Rev.* **1954**, *94*, 630.
(36) Levitt, M. H. *Spin Dynamics*; John Wiley and Sons Ltd.: England, 2008; Vol. 2.
(37) Stejskal, E.; Tanner, J. Spin Diffusion Measurements: Spin Echoes in the Presence of a Time-Dependent Field Gradient*. *J. Chem. Phys.* **1965**, *42*.
(38) Hou, J.; Madsen, L. A. New insights for accurate chemically specific measurements of slow diffusing molecules. *J. Chem. Phys.* **2013**, *138*.
(39) Schauser, N. S.; Harry, K. J.; Parkinson, D. Y.; Watanabe, H.; Balsara, N. P. Lithium Dendrite Growth in Glassy and Rubbery Nanostructured Block Copolymer Electrolytes. *J. Electrochem. Soc.* **2015**, *162*, A398.
(40) Callaghan, P. T.; Coy, A.; Macgowan, D.; Packer, K. J.; Zelaya, F. O. Diffraction-Like Effects in Nmr Diffusion Studies of Fluids in Porous Solids. *Nature* **1991**, *351*, 467.
(41) Holz, M.; Muller, C. Direct Measurement of Single Ionic Drift Velocities in Electrolyte-Solutions - an Nmr Method. *Ber. Bun. Phys. Chem.* **1982**, *86*, 141.
(42) Fulcher, G. S. Analysis of Recent Measurements of the Viscosity of Glasses *J. Am. Ceram. Soc.* **1925**, *8*, 339.
(43) Alam, T. M.; Hibbs, M. R. Characterization of Heterogeneous Solvent Diffusion Environments in Anion Exchange Membranes. *Macromolecules* **2014**, *47*, 1073.
(44) Bogle, X.; Vazquez, R.; Greenbaum, S.; Cresce, A. V.; Xu, K. Understanding Li+-Solvent Interaction in Nonaqueous Carbonate Electrolytes with O-17 NMR. *J. Phys. Chem. Lett.* **2013**, *4*, 1664.

Chapter 6

Tuning Self-Assembly and Diffusion of Block Copolymer Micelles Via Co-Solvent Addition

Abstract:

Optimization of drug delivery vehicles can be achieved through fundamental understanding of block copolymer micelle structure and dynamics. Herein, we present a comprehensive study of PEO-PCL block copolymer spherical micelles that self-assemble at 1% wt/vol in D_2O. Varying composition by adding the co-solvent THF_{d8}, which preferentially imbibes into the micelle (PCL) core, allows sensitive study of how small molecule additives influence micelle structure and dynamics. We conduct NMR spectroscopy and diffusometry on two block-copolymer micelle systems (PEO_{2k}-PCL_{3k} and PEO_{5k}-PCL_{8k}) that show substantially different behavior. Coexistence of unimers and micelles is present from 10 – 60 vol% THF_{d8} for the 2k-series and only exists at 60 vol% THF_{d8} for the 5k-series. At ≥ 60 vol % THF_{d8} the micelle disassembles into free unimers for both systems. We see a slight decrease in micelle diffusion coefficients before the coexistence region (10 – 50 vol% THF_{d8}) for the 5k-series largely due to a decrease in $\eta_{solution}$ and invariance in micelle radius $r_H^{micelle}$ (14 – 16 nm). Both solutions show a gradual decrease in unimer radius r_H^{unimer} (5 – 1 nm) from the start of the coexistence region to pure unimers region. By understanding solvent environment effects and partitioning of small molecules into the micelle core, this study shows promise for enabling fine control over block copolymer self-assembly as well as cargo (*e.g.*, drug) carrying or release properties.

6.1 Introduction

Self-assembly of block copolymers into functional nm-length scale structures are of interest for drug-delivery applications, especially for hydrophobic drugs with poor bioavailability and also find applications as nanoreactors to replace solvent-intensive organic synthesis.[1,2] Wormlike micelles, lamellae, spherical micelles, and vesicles represent an array of possible morphologies that are obtainable through careful unimer and solvent system design.[3] Polymer molecular weight, chain composition, concentration of polymer, and solvent-polymer intermolecular interactions govern unimer dynamics and ultimately micelle self-assembly.[4,5] Typically, design of drug-carrying copolymer micelles begins with hydrophobic and hydrophilic blocks that result in self-assembly of the hydrophobic block to form a core-shell nanostructure that is highly stable in H_2O.[1] The core size and specific molecular interactions determine drug-loading capacity in the core "micro-reservoir". Moreover, for cancer treatment the micelle should be no larger than ~ 50 nm to enable microfiltration sterilization and penetration through a solid tumor vessel wall.[1] Upon introduction into the human body (typically intravenous injection), non-specific elimination of drug-carrying micelles becomes an issue, such as enzymatic and non-enzymatic degradation prior to reaching the target site followed by excretion through the kidneys. Assuming the micelle survives a myriad of biological roadblocks, controlled delivery to tumor cells is possible. Thus, the unique ability to tune self-assembly and drug-loading capacity of micelles holds powerful potential in developing next generation drug delivery vehicles. Understanding unimer and micelle dynamics as well as drug cargo carrying and delivery properties will aid in judicious design of block copolymer micelles.

Most block copolymer micelles for drug delivery use poly(ethyleneoxide) (PEO) as the hydrophilic block due to weak cellular adhesion of the PEO corona onto cells, which minimizes

protein adsorption into the core and protects the hydrophobic core from enzymatic degradation.[6] Biodegradable and hydrophobic polycaprolactone (PCL) has shown promise in forming the core of block copolymer micelle systems. Increasing the PCL block length allows one to increase the core volume to optimize drug capacity. Since PCL is more hydrophobic than commonly used polypropylene oxide, one may expect higher drug capacity for hydrophobic drugs when using PCL. Drug release kinetics can also be tuned by adjusting block sizes, which in turn changes unimer chain dynamics and exchange rates in solution.[7-9]

Unimer exchange phenomena, such as fusion/fission and aggregation,[8,9] depend strongly on block chemistry, solvent type, and other molecules in solution, thus we seek to understand and quantify such properties. Dynamic light scattering (DLS) and small angle neutron scattering (SANS) are commonly used to characterize block copolymer micelles.[10] DLS can give information on micelle size and shape but lacks chemically specific information. SANS can yield core and corona size as well as unimer exchange dynamics through time-resolved contrast-matching experiments.[11,12] Here we complement and expand on these techniques with NMR, which can probe equilibrium and non-equilibrium dynamics with chemical specificity across a range of time scales within these systems and thus provide a larger breadth of information.

In addition to NMR spectroscopy providing chemical structure information and core/corona dynamics, NMR diffusometry affords fundamental translational dynamics properties of small molecules and ions in these micellar systems. Resolution of free unimer and micelle dynamics is possible through the Stokes-Einstein equation,[13]

$$D = \frac{kT}{c\eta r_H}, \tag{6.1}$$

where D is diffusion coefficient, kT is average thermal energy at temperature T, η is viscosity of the diffusing medium, r_H is hydrodynamic radius, and c ($6\pi - 2\pi$) is a constant that depends on the size, shape, and specific medium-particle interactions. Information such as unimer exchange rate, micelle size, and how such properties depend on solvent system and drug loading, can be accessed through careful experimental design. Thus, NMR offers the ability to probe such properties and can expand beyond common micelle characterization techniques.

Here we present a study that showcases DLS, SANS, and NMR spectroscopy and diffusometry results on two block-copolymer (2k-series: PEO_{2k}-PCL_{3k} and 5k-series: PEO_{5k}-PCL_{8k}) spherical micelles that self-assemble at 1% wt/vol in D_2O with $r_H^{micelle} \approx 14$ nm for both 2k- and 5k-series. We observe drastic differences in micelle and unimer dynamics between the two series as a function of THF_{d8} co-solvent content. Coexistence of unimers and micelles is present from 10 – 60 vol% THF_{d8} for the 2k-series (with a 12 – 45 % increase in unimer content) and only exists at 60 vol% THF_{d8} for the 5k-series. Interestingly, we see that as THF_{d8} content increases, simultaneous expansion and contraction of the core and corona, respectively, causes invariance in $r_H^{micelle}$ from 10 – 50 vol% THF_{d8} for the 5k-series. At ≥ 60 vol % THF_{d8} the micelle disassembles into free unimers for both systems. Both sets of data also show a decrease and increase (at 50 vol% THF_{d8}) in diffusion coefficient for the solvents and polymer chains vol% THF_{d8} that correlate well with changes in $\eta_{solution}$. These results show promise in fine-tuning micelle uptake and unimer dynamics across a broad range of solvent environments, thus guiding future studies and design of block copolymer micelles.

6.2 Experimental

6.2.1 Diblock Copolymer Synthesis and Characterization

Monomethoxy-polyethylene oxide (PEO) was purchased from Polymer Source and used as received. ε-Caprolactone (ε-CL, 97%) and benzene (ACS grade, ≥99%) were purified through distillation (twice) over calcium hydride (CaH_2, ACS reagent, ≥95%). The catalyst 1,5,7-triazabicyclo[4.4.0]dec-5-ene (TBD, 98%), was used as received and stored in an inert environment to prevent deactivation.

Poly(ethylene oxide-*b*-ε-caprolactone) (PEO-PCL) diblock copolymers were synthesized using monomethoxy-PEO as a macroinitiator for the ring-opening polymerization of ε-CL (Scheme 1), following literature procedures.[14,15] ε-CL was added to a solution of PEO in benzene (ε-CL concentration was 0.24 g/mL and PEO concentration was determined by the targeted block copolymer block ratio assuming a monomer conversion of 0.60). A stock solution of TBD in benzene was added to the ε-CL/PEO solution (0.0072295 g catalyst per g ε-CL) to initiate the reaction. After sufficient time, the reaction was quenched with benzoic acid (≥99.5%). The resultant polymer was then dissolved in tetrahydrofuran (THF, chromatography grade, ≥99.5%, inhibitor free) and precipitated in hexanes (ACS grade, >99%) 5 times. The polymer was dried under vacuum at room temperature overnight, and then dried under vacuum at 60°C for 8 h.

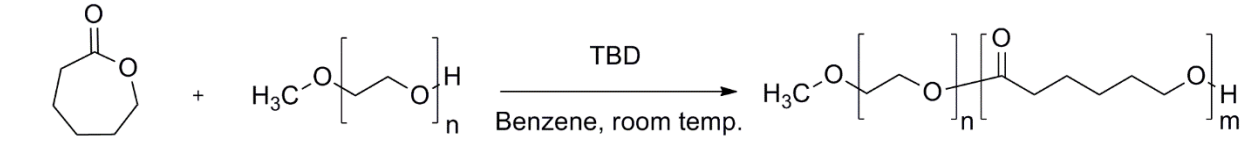

Scheme 6.1: PEO-PCL diblock copolymer synthesis

Proton nuclear magnetic resonance (^{1}H-NMR) experiments were performed on JEOL ECA-500 and ECX-400P instruments using deuterated chloroform (99.8 atom% D) as the solvent, for the determination of weight fractions of the PEO and PCL blocks, as well as the number-average molecular weight (M_n). The molecular weight distribution (including the

dispersity, *Đ*) was characterized by a Viscotek gel permeation chromatography (GPC) GPCmax instrument containing Agilent ResiPore columns using THF (OmniSolv, HPLC grade) as the mobile phase at 30°C. The flow rate was 1 mL/min and the injection volume was 100 µL. Universal analysis, using the refractometer and viscometer, was employed for the characterization of *Đ* (the low light scattering signal precluded light scattering analysis). The PEO precursors purchased from Polymer Source had the following characteristics: 1) M_n = 1.9 kg/mol and *Đ* = 1.05 and 2) M_n = 5.0 kg/mol and *Đ* = 1.06, as determined by GPC using universal analysis and ^{1}H NMR. The PEO-PCL block copolymer characteristics are listed in Table 6.1.

	M_n PEO (kg mol^{-1})	**M_n PCL (kg mol^{-1})**	***Đ***	**PCL wt%**
PEO_{2k}-PCL_{3k}	1.9	2.9	1.13	60
PEO_{5k}-PCL_{8k}	5.0	7.5	1.18	60

Table 6.1: Characteristics of the PEO-PCL block copolymers.

6.2.2 Pulsed-Field-Gradient NMR Diffusometry

1% wt/vol block copolymer solutions were transferred to a 5 mm NMR tube and sonicated in a H_2O bath (Bransonic M1800, 90W) for 30 minutes prior to NMR data acquisition. Sonication was performed to minimize micelle aggregation.

All ^{1}H PFG NMR diffusometry experiments were performed using a 400 MHz Bruker Avance III WB NMR spectrometer, equipped with a MIC probe coupled to a Diff60 single-axis (z-axis) gradient system. In the PFG NMR experiment, measured signal amplitude *I* as a function of gradient strength, *g*, was fit to the Stejskal-Tanner equation,[16-18]

$$I = I_0 e^{-D\gamma^2 g^2 \delta^2 (\Delta - \frac{\delta}{3})}, \quad (6.2)$$

where I_0 the signal amplitude at $g = 0$, γ the gyromagnetic ratio, δ the effective gradient pulse length, Δ the diffusion time between gradient pulses, and D the self-diffusion coefficient. The simple and robust pulsed-gradient stimulated echo (PGSTE) sequence was used with a 90° pulse length of 4.5 μs. A half sinusoid gradient pulse length of δ = 3.14 ms (effective rectangular pulse length = 2.00 ms), and a diffusion time Δ = 25 ms were used for ^{1}H diffusion measurements. Maximum gradient strengths were adjusted in the range 5 – 600 G cm^{-1} to achieve ≥ 90 – 95% signal attenuation in 16 – 32 steps. Sufficient signal-to-noise ratio (SNR) for each data point was achieved with 4 – 8 scans and acquisition times of 0.5 s (polymer signals) and 1.0 s (solvent signals) with 1 Hz linebroadening. Relaxation delay times of 2.0 s were used for both polymer and solvent signals. Repetition times of 2.5 s (polymer signals) and 3.0 s (solvent signals) were used. Spin-lattice relaxation time (T_1) measurements using the same RF pulse lengths as above and the inversion-recovery sequence yielded T_1 values in the range of 0.4 to 4.0 s for all resonances.

6.3 Results and Discussion

6.3.1 Probing the Effect of Small Molecule Additives on Micelle and Unimer Dynamics

To aid our understanding of how small molecule additives affect equilibrium and non-equilibrium dynamics of block copolymer micelles, we choose THF_{d8} as a co-solvent that partitions selectively into the core (Figure 6.1).

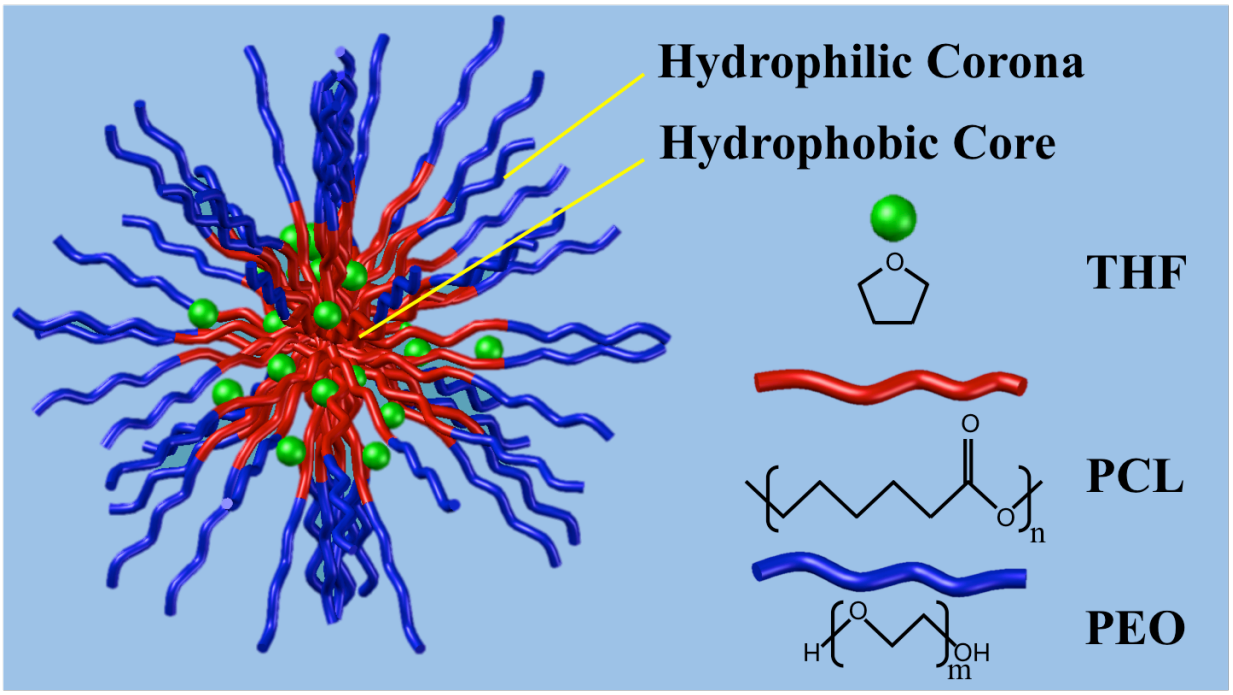

Figure 6.1. At 1% wt/vol block-copolymer in D_2O, unimers self-assemble into spherical micelles where PEO and PCL reside in the corona and core, respectively. Loading THF_{d8} into the core serves as a model co-solvent probe to aid in our understanding of fundamental unimer, micelle, and small molecule cargo dynamics.

We sample a range of solvent volume ratios for our binary solvent mixture starting with 10:90 vol/vol% THF_{d8}:D_2O and increasing in steps of 10 vol% up to 100 vol% THF_{d8}, all at constant polymer concentration (1% wt/vol). By changing the solvent volume ratio, we gain insight into how micelle self-assembly depends on solvent environment. Use of deuterated solvents allows for clean resolution of polymer signals (Figure 6.2) in NMR spectra.

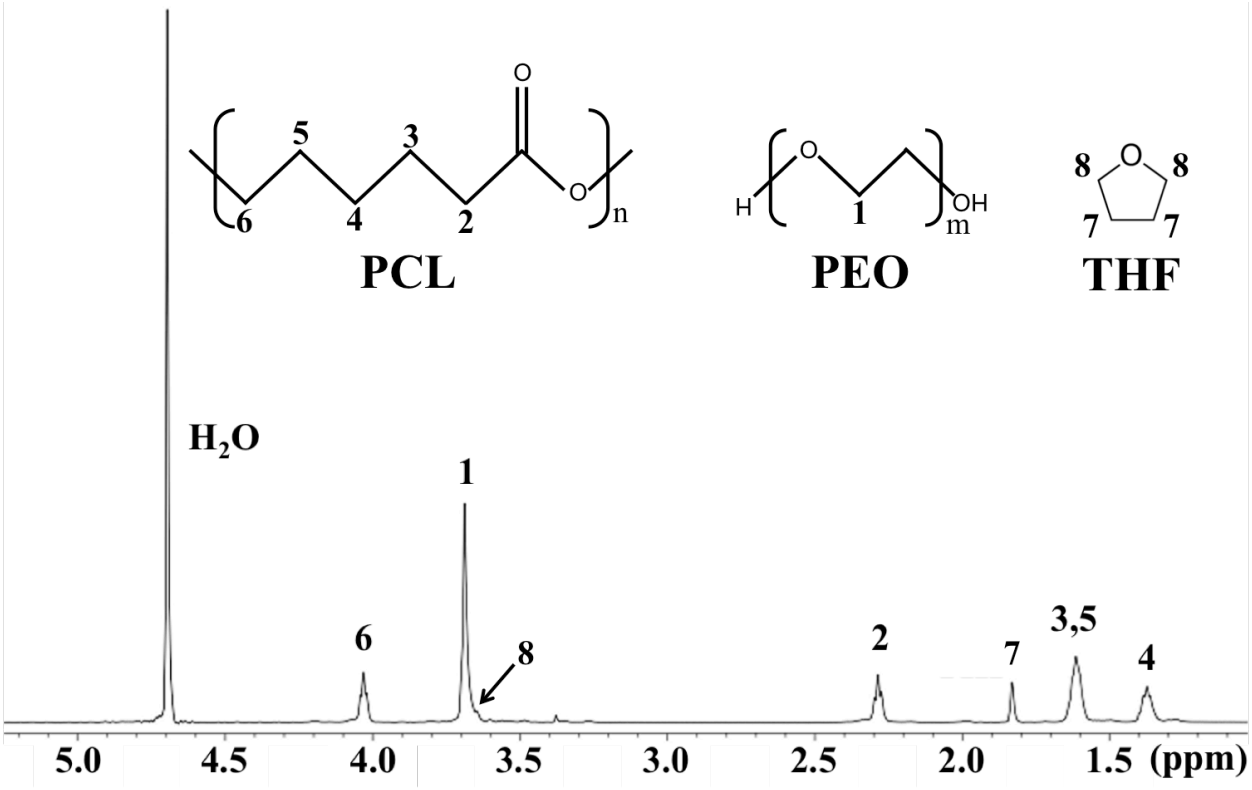

Figure 6.2. ^{1}H NMR spectrum of the PEO_{2k}-PCL_{3k} micelle solution at 10:90 vol/vol% THF_{d8}:D_2O. We do not see the second THF signal at ~3.7 ppm due to spectral overlap with PEO.

Figure 6.2 shows that the polymer signal linewidths are broader (by a factor of >20) than the solvent signals (residual ^{1}H). This is related to the shorter spin-spin relaxation time (T_2), which is the relaxation of net magnetization in the transverse (xy) plane,[19,20] as the full-width-half-max (FWHM) = $1/\pi T_2$.[21] Relative T_2 gives information on how "rigid" or "mobile" the molecular environment is for a given nuclear site. That is, for the polymer signals, a shorter T_2 value relative to the solvent signals indicates that the polymer chain environment is more rigid (slower tumbling) than the solvent molecules since the chains reside in the core and corona. Note that PCL signals (core) are also substantially broader (30Hz) than PEO signals (corona) (10Hz), demonstrating that PCL chain dynamics is significantly slower than for PEO. Compared to the

solvent signals linewidth (< 1Hz), a simple 1D ^{1}H spectrum strongly suggests that the polymer chains are aggregated. Figure 6.3a shows how the 2k-series PCL T_2 evolves as a function of vol% THF_{d8}.

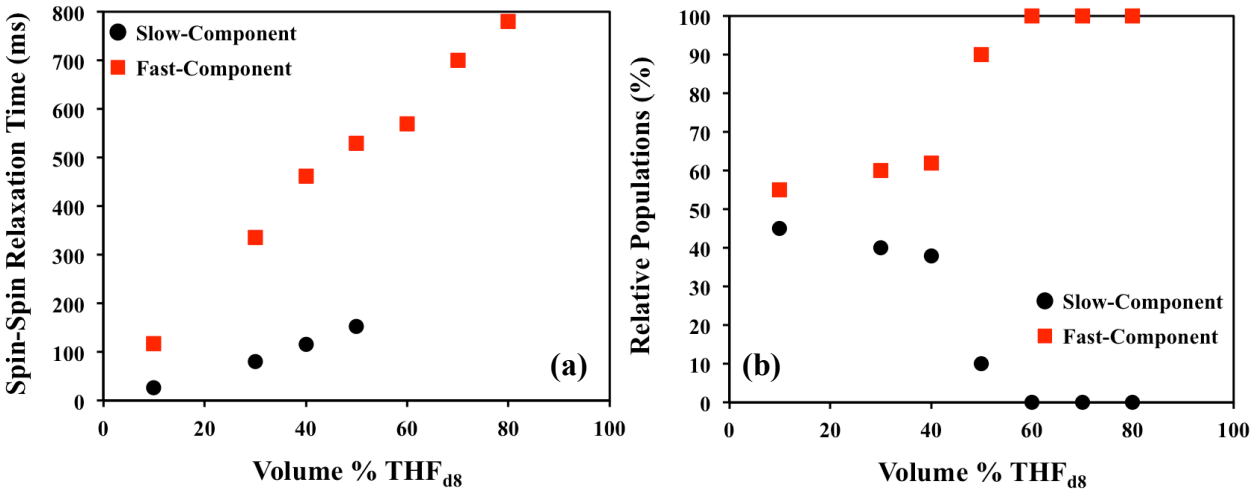

Figure 6.3. 2k-series T_2 values (a) and relative populations from T_2 (b) shows the polymer chains exist in two chemically distinct environments within 10 – 50 vol% THF_{d8}.

Interestingly, we see two-component T_2 values for PCL within 10 – 50 vol% THF_{d8}. This reflects that the polymer chains exist in two chemically distinct environments within 10 – 50 vol% THF_{d8}. Two-component T_2 analysis allows us to extract relative populations of the fast- and slow-T_2 components across the range of THF_{d8} content. We see that the populations begin roughly equal and the fast-component begins to dominate the signal beyond 10 vol% THF_{d8}. It should be noted that T_2 experiments do not contain a fixed measurement time-scale, unlike NMR diffusometry (discussed below). Thus, as the T_2 experiment proceeds, we are not accounting for unimer exchange dynamics across the T_2 experimental time scales.

In order to simultaneously probe translational dynamics of the solvent molecules, unimers, and whole micelles, we employ pulsed-field-gradient (PFG) NMR diffusometry. Figure

6.4 shows THF (residual ^{1}H), H_2O (residual ^{1}H), and PCL diffusion coefficients as a function of THF_{d8} vol% for the 2k-series (a) and 5k-series (b).

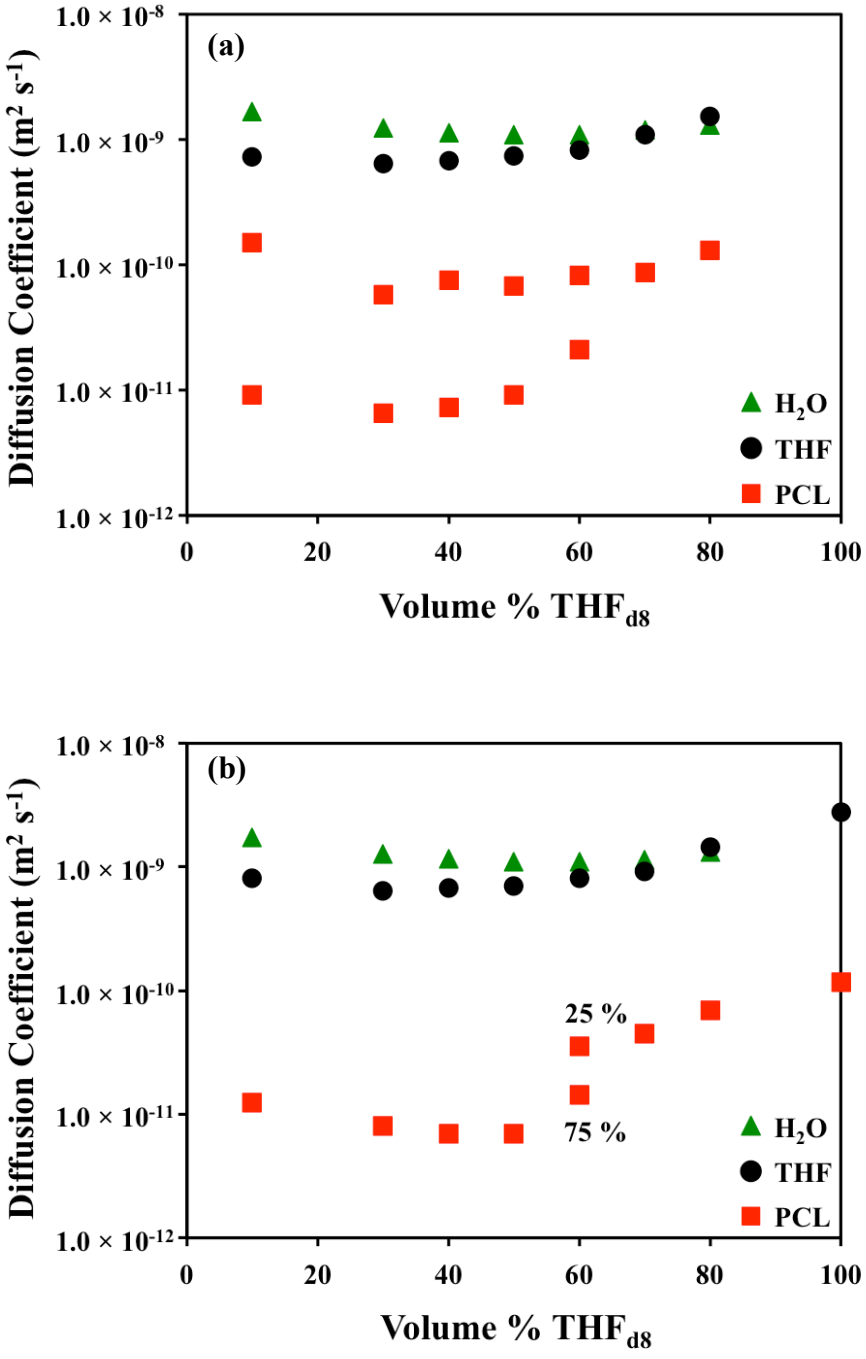

Figure 6.4. ^{1}H NMR diffusometry of the 2k-series (a) and 5k-series (b) block copolymer chains and residual ^{1}H-solvents. We observe drastic differences between the 2k- and 5k-series. The 2k-

series shows two-component diffusion coefficients between 10 – 60 vol% THF_{d8} while 5k-series only shows two-component diffusion at 60 vol% THF_{d8}. Error bars for each measurement are ≤ ±5%.

The 2k- and 5k-series polymer chain diffusion coefficients show drastically different dependencies with vol% THF_{d8}. For the 2k-series, two-component diffusion is present in the range of 10 – 60 vol% THF_{d8}, where the relative fraction of the fast component increases as a function of vol% THF_{d8} (Figure 6.4a). However, we only see two-component diffusion at 60 vol% THF_{d8} for the 5k-series (Figure 6.4b). Note that we detect no diffusing homopolymer component, indicating that block-copolymer samples are of high purity. If a significant amount of homopolymer were present (or smaller block-copolymer fragments) in solution, one would see multi-component or distorted diffusion curves across the entire vol% range of THF_{d8}. Figure 6.5 shows representative 2k-series Stejskal-Tanner plots highlighting the evolution of the diffusion decay curves (a) and relative populations of slow- and fast-components (b).

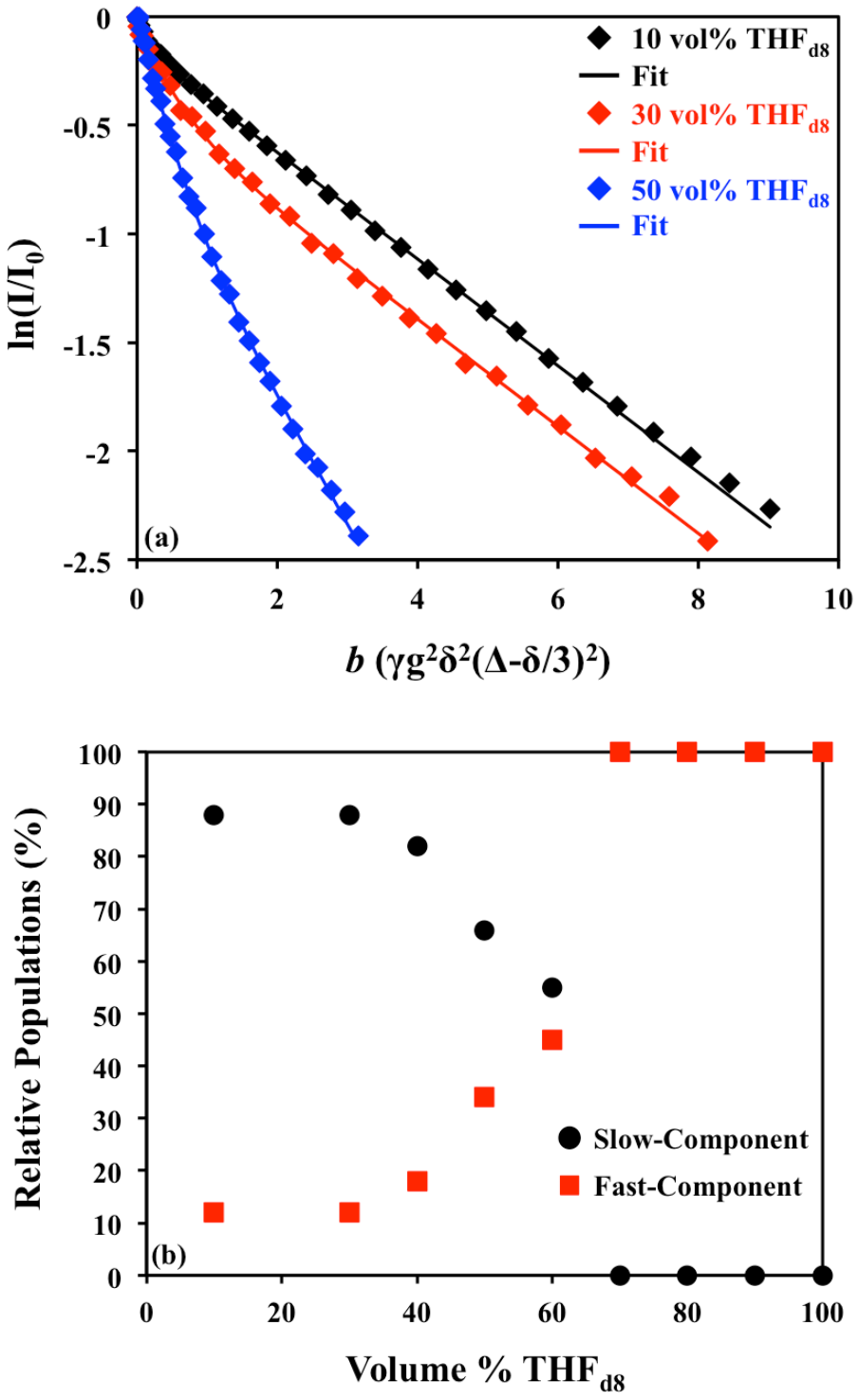

Figure 6.5. Stejskal-Tanner plots (a) and relative population % (b) as a function of vol% THF_{d8} shows an increase in the relative amount of fast-component. Error bars for each population measurement are ≤ ±10%.

Two-component diffusion coefficients can be seen for diffusion of soft materials if the species of interest resides within two distinct environments that are not exchanging rapidly on the diffusion time scale Δ (typically ~ 10 ms), such as polymer chain populations residing both in micelles and in bulk solution.[22-24] By taking the natural log of I/I_0 in a Stejskal-Tanner intensity decay curve, diagnosis of multi-component fits is less cumbersome. A single linear regression is seen for a single component fit (slope $m = D$). Any deviation from linearity (i.e., two independent slopes) suggests more than one diffusion coefficient for a given chemical moeity (associated with a distinct NMR peak). That is, the fast diffusion coefficient (polymer chains in bulk solution) decays more rapidly at lower gradient strengths followed by a change in slope to the slow diffusion coefficient (polymer chains in micelles), which decays at a slower rate at higher gradient strengths.

To aid material scientists in acquiring and evaluating multi-component diffusion experiments, we briefly address common practices useful for obtaining accurate data. First, in order to observe the entire slow diffusion component and acquire true relative population fractions, a much shorter gradient pulse length in comparison to the T_2 value of the signal of interest is used to minimize T_2-weighting effects. That is, T_2-weighting occurs due to spin-spin relaxation during the gradient pulse, thus resulting in different intensity weightings of the fast- and slow-diffusing components. Here we use a δ = 2 ms for the fast- (T_2 = 117 – 780 ms) and slow-components (T_2 = 30 – 152 ms). Second, using gradient parameters sufficient for 90 – 99% signal attenuation at the end of the experiment (largest gradient) provides for proper analysis of the relative fraction for both components. Careful attention should be given to monitoring the spectra at higher gradient strengths, as complete attenuation to spectral noise in a single

component system can sometimes be perceived as a second component. Lastly, at least 16 – 32 data points (individual spectra) are desirable for multi-component fits to a single curve. In general, errors in multi-component analysis can arise if 1) the difference between the diffusion coefficients is less than about a factor of 2 and/or 2) either the fast or slow component constitutes < 10% of the total intensity decay curve. This can be seen for polymers with a large polydispersity and polymeric materials that contain morphological regions that are not well defined, where a distribution in diffusion coefficients may be seen and/or the total number of probe molecules/ions within a given region is relatively small.[22-24]

Figure 6.4 reflects that unimers exist within two distinct environments, which we assign to free unimers (fast component) and micelles (slow component), on the 25 ms time scale of the NMR diffusometry experiments (additional discussion below). To aid our understanding in the solvent, unimer, and micelle diffusion trends between the two series, we also compare the solvent diffusion coefficients in micelle solutions to the pure binary solvent system, therefore gauging how $\eta_{solution}$ contributes to these differences (Figure 6.6).

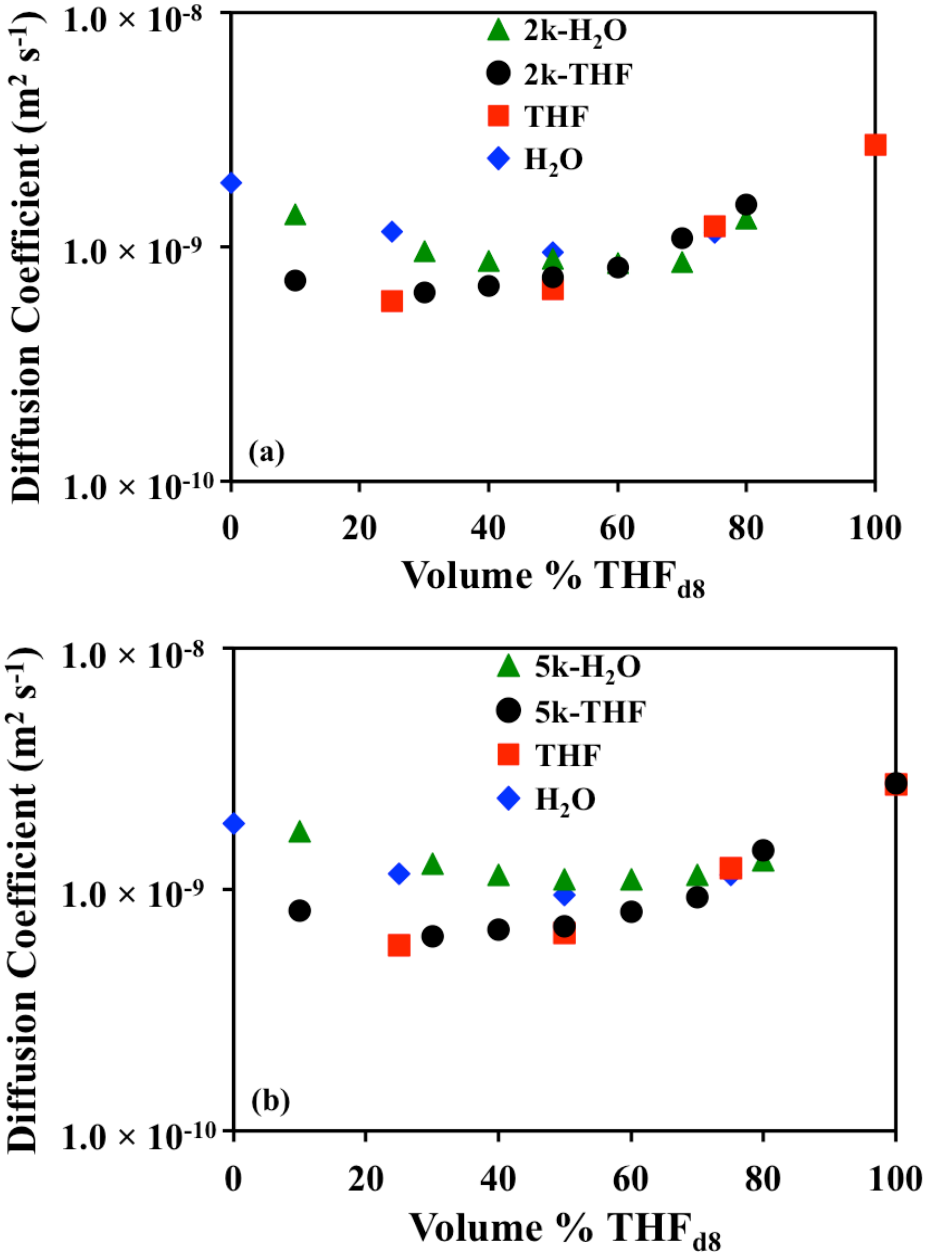

Figure 6.6. Diffusion coefficients for residual H_2O and THF in the 2k-series (a) and 5k-series (b) micelle solutions and in pure binary mixture solutions. We see that the solvent diffusion coefficients in micelle solutions overlay well with the solvents in the pure solvent mixture. We note that our diffusion measurements are not sensitive to solvents within the micelles, meaning that the solvent molecules are exchanging in and out of the micelles fast compared to the

diffusometry experiment timescale (25 ms) and the amount of solvent within the micelle is relatively small compared to the total solvent signal. Error bars for each measurement are ≤ ±5%.

Interestingly, we see a slight decrease and then increase in diffusion coefficients with increasing THF content for the micelle solution solvents, and this overlays well with the solvent diffusion coefficients in the pure binary solvent system. This diffusion minimum with concentration reflects specific molecular interactions between THF and water that must cause stronger complexation behavior that in turn slows diffusion in the mixed solution. Exploration of such effects is outside the scope of this paper. Moreover, we note that at 1% wt/vol polymer our NMR diffusometry measurements are not sensitive to solvents within the micelle and the amount of solvent within the micelle is relatively small compared to the total solvent signal. Thus, two factors can contribute to the observable decrease in micelle diffusion coefficients for the 5k-series (up to 60 vol% THF_{d8}): 1) As the THF_{d8} vol% increases, a decrease in $\eta_{solution}$ is seen, as shown by the agreement in diffusion coefficients between solvents in the micelle solutions and in the pure solvent binary mixture solutions, and 2) gradual swelling of solvents into the micelle as THF_{d8} vol% increases leads to a volume expansion (larger r_H) and results in a gradual decrease in micelle diffusion coefficient. Beyond 60 vol% THF_{d8}, we see a gradual increase in unimer diffusion coefficient.

The observable decrease in unimer and micelle diffusion coefficients for the 2k-series also correlates well with the decrease in $\eta_{solution}$ (up to 30 vol% THF_{d8}). Since $\eta_{solution}$ decreases from 10 – 50 vol% THF_{d8}, we expect to see a similar trend in the 2k-series as in the 5k-series if the micelle diffusion coefficient is largely influenced by $\eta_{solution}$. Unlike the 5k-series, the 2k-series shows both unimers and micelles in solution from 10 – 60 vol% THF_{d8}, where the micelle

diffusion coefficient increases between 30 – 60 vol% THF_{d8}. This interesting result correlates well with the rapid increase in the 2k-series unimer population between 30 – 60 vol% THF_{d8} (Figure 6.5b) and reflects that the micelle diffusion coefficient is more sensitive to the dynamic change in r_H and weighted less by $\eta_{solution}$. That is, the rate of change for the micelle r_H is faster than the rate of change in $\eta_{solution}$. The unimer diffusion coefficients, however, are more sensitive to changes in $\eta_{solution}$ due to the observed decrease and then increase in diffusion coefficients that are in good agreement with the solvent system behavior. That is, unimers not interacting with micelles on the diffusion time scale are not subject to substantial changes in r_H and are thus governed by changes in $\eta_{solution}$.

We further utilize the Stokes-Einstein equation (Equation 1) to gain insight into how continuous loading of THF_{d8} influences the relative size of the micelle. In deriving the most accurate $r_H^{micelle/unimer}$ (Equation 3) of a large particle immersed in a solvent bath of much smaller molecules, one should consider appropriate values for η, $c\pi$, and D.

$$r_H^{micelle/unimer} = \frac{kT}{c\pi\eta_{solution}D_{micelle/unimer}} \tag{6.3}$$

Here, $D_{micelle/unimer}$ is experimentally measured and the constant $c = 6$, which holds true for large particles in a bath of relatively small particles (no slip boundary condition). We derive $\eta_{solution}$ for every solution (Table SI-1) from the solvent molecule diffusion in the polymer solutions (Figure 5) as follows,

$$\eta_{solution} = \frac{kT}{c\pi r_H^{H_2O\ in\ solution}D_{H_2O}^{solution}} \tag{6.4}$$

where $\overline{D_{H_2O}^{solution}}$ is experimentally measured and $r_H^{H_2O\ in\ solution}$ is the hydrodynamic radius of residual H_2O in solution (discussed below). Recall that $\overline{D_{H_2O}^{solution}}$ is the same in both polymer solution and pure binary solvent system (Figure 5). We derive $r_H^{H_2O\ in\ solution}$ as follows,

$$r_H^{H_2O\ in\ solution} = \frac{kT}{c\pi\eta_{reference}D_{H_2O\ in\ pure\ D_2O}} \tag{6.5}$$

where $\eta_{reference}$ (1.096 cP) is an external reference for pure D_2O solvent viscosity to "correct" and derive a more accurate $\eta_{solution}$ and $D_{H_2O\ in\ pure\ D_2O}$ (2.0×10^{-9} m^2 s^{-1}) at 25°C is experimentally measured. Our key assumption in deriving $r_H^{micelle/unimer}$ is that $r_H^{H_2O\ in\ solution}$ $r_H^{H_2O}$ only weakly varies over the range of THF_{d8} vol% and thus we hold it constant. In other words, we are not considering changes in $\eta_{solution}$ due to changes in THF_{d8}:D_2O vol ratio when deriving $r_H^{H_2O}$ since $D_{micelle/unimer}$ and $\overline{D_{H_2O}^{solution}}$ already contain information about $\eta_{solution}$. Figure 6 is a compilation of $r_H^{micelle/unimer}$ vs. THF_{d8} vol%.

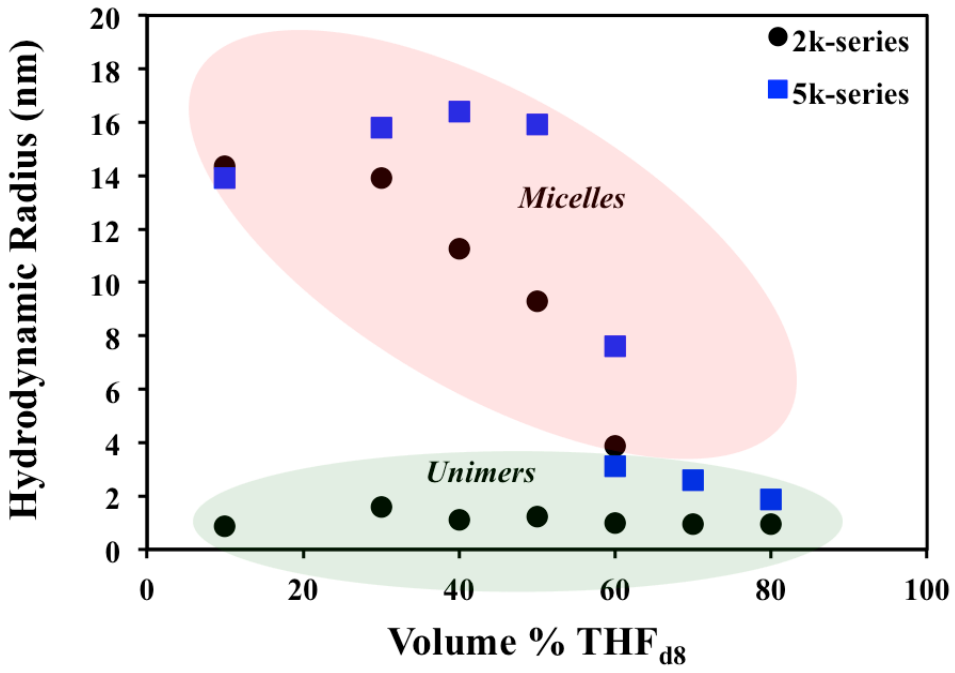

Figure 6.7. Average block copolymer r_H as a function of THF_{d8} vol% for the 2k-series and 5k-series micelles and unimers. The 5k-series r_H remains constant until 60 vol% THF_{d8} while the 2k-series shows a significant decrease in r_H with THF_{d8} vol%. Only free unimers in solution exist above 60 vol% THF_{d8} in both systems. Error bars for each measurement are approximately ≤ ±10%.

Within the 10 – 50 vol% THF_{d8} range for the 5k-series, we see that $r_H^{micelle}$ (14 – 16 nm) is essentially invariant, further suggesting that the slight decrease in diffusion coefficient (Figure 6.4b) is dominated by an initial decrease in $\eta_{solution}$ as the THF_{d8} content increases (Figure 6.6b). These results are in good agreement with our SANS results (not shown), which also show no change in $r_H^{micelle}$ (15 – 14 nm) from 10 – 50 vol% THF_{d8}. From SANS, we see that the invariance in the 5k-series $r_H^{micelle}$ is due to continuous swelling of THF_{d8} into the PCL-core (8 – 11 nm), which is also accompanied by a decrease in the PEO-corona width (7 – 2 nm). As the

vol% THF_{d8} increases, polymer-solvent interactions for PCL and for PEO become more favorable and less favorable, respectively, relative to polymer-polymer interactions, thus causing a simultaneous expansion of the core and contraction of the corona. The transition to two-component diffusion at 60 vol% THF_{d8} signifies a coexistence region, where both micelle (8 nm) and unimers (3 nm) are present. Above 60 vol% THF_{d8} the 5k-series unimers are larger than the 2k-series unimers, which we expect for higher molecular weight polymer chains.

Interestingly, the 2k-series $r_H^{micelle}$ values are nearly equivalent to the 5k-series at 10 and 30 vol% THF_{d8}, followed by a gradual decrease in $r_H^{micelle}$ to 4 nm within a coexistence region that spans 10 – 60 vol% THF_{d8}. Above 20 vol% THF_{d8}, we see that the 2k-series micelles are smaller than the 5k-series, which is also in agreement with our SANS results. However, SANS does not show as dramatic of a decrease (12 – 10 nm) in the 2k-series $r_H^{micelle}$ that we observe from NMR diffusometry. Closer inspection of the 2k-series aggregation number (N_{agg}, which represents the average number of unimers per micelle) from SANS (not shown) between 10 – 60 vol% THF_{d8} reveals a decrease from 210 – 85 (a factor of ~1.5 decrease in $r_H^{micelle}$), which correlates with the increase in unimer population from NMR diffusometry (Figure 6.5b) and subsequent decrease in $r_H^{micelle}$. However, SANS suggests the 2k-series $r_H^{micelle}$ remains relatively unchanged. This apparent disagreement might be resolved by analyzing the solvent volume fractions between these two systems (not shown). Even though N_{agg} for the 2k-series decreases between 10 – 60 vol% THF_{d8}, the solvent volume fraction increases (and nearly overlaps the 5k-series dependence) with vol% THF_{d8}. Unlike SANS, which relies on average neutron density and thus micelle size in a static sense, diffusometry is sensitive to drag of the solution on the micelle as it diffuses through the solvent medium. That is, the NMR diffusometry experiment reports a larger "effective $r_H^{micelle}$" and may account for unimers and solvents that

are hydrodynamically dragged along with the micelle but are too low in density to appear as significant SANS scattering intensity. Note also that the SANS measurements are not sensitive to free unimers in solution and thus do not report beyond 60 vol% THF_{d8}. Above 60 vol% THF_{d8}, we only see free unimers in solution for the 2k-series.

Clearly the dynamics between the 2k and 5k systems is quite different and both PFG NMR diffusometry and SANS reporting on different aspects of these micelle systems. We summarize our results in a multi-panel illustration of how micelle morphology depends on THF solvent content (Figure 6.8).

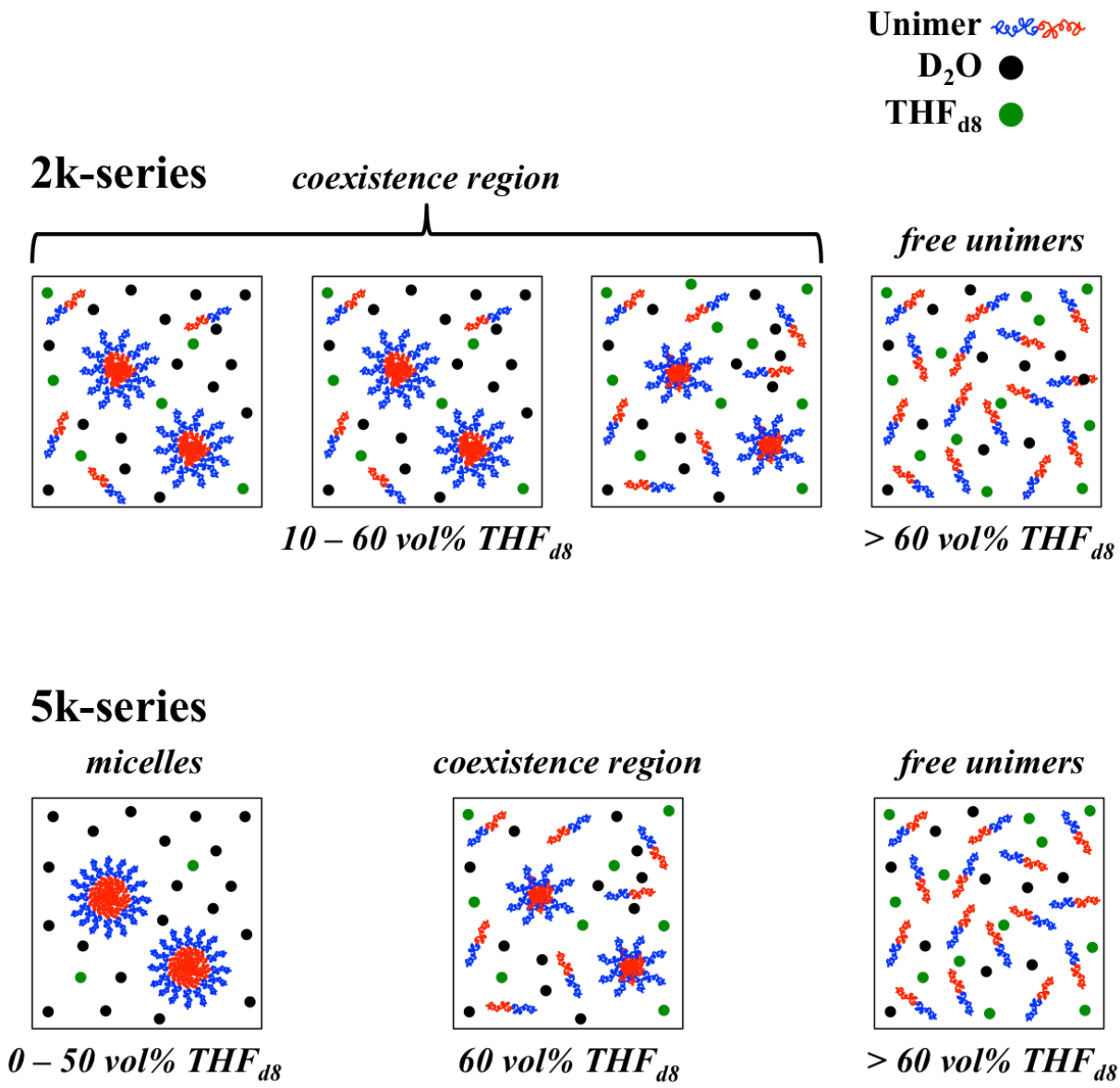

Figure 6.8. Multi-panel illustration of how the 2k- and 5k-series block-copolymer micelle morphology changes with THF_{d8} content. We see three distinct behavior regions for the 5k-series: 1) Micelles strongly dominate the solution below 60 vol% THF_{d8}, 2) micelles and unimers coexist at 60 vol% THF_{d8}, and 3) only free unimers exist above 60 vol% THF_{d8}. The 2k-series displays a coexistence region between the wide range 10 – 60 vol% THF_{d8}, and at > 60 vol% THF_{d8}, we see only free unimers in solution.

6.4 Conclusions

We have presented a detailed analysis of PEO_{2k}-PCL_{3k} and PEO_{5k}-PCL_{8k} block copolymer micelles, quantifying dynamics and structure on multiple time and length scales using NMR spectroscopy and diffusometry to complement SANS measurements. Micelles self-assemble at 1% wt/vol in D_2O with $r_H^{micelle} \approx 14$ nm for both 2k- and 5k-series. We vary the THF_{d8}:D_2O volume ratio to inform on unimer and micelle structure dependence. Specifically, we see that as THF_{d8} content increases, simultaneous expansion and contraction of the core and corona, respectively, causes invariance in $r_H^{micelle}$ from 10 – 50 vol% THF_{d8} for the 5k-series. Moreover, we observe coexistence of micelles and free unimers ($r_H^{unimer} \approx 3$ nm) at 60 vol% THF_{d8} followed by break down of the micelle into free unimers for the 5k-series. In contrast to the 5k-series, the 2k-series exhibits a coexistence region from 10 – 60 vol% THF_{d8}, wherein an increase in unimer content (12 – 45 %) is seen before break down of the micelle into free unimers. Collectively, these results show that we can fine-tune micelle self-assembly, which is critical for drug delivery applications. Ongoing efforts are exploring NMR as a candidate to probe unimer exchange dynamics, which will complement time-resolved (TR) SANS experiments, and potentially provide a new method for probing unimer exchange that can be conducted in any NMR facility at a fraction of the cost.

6.5 Acknowledgments

This work was supported by the National Science Foundation (NSF) under award number CBET 1437831/1437767. Any opinions, findings and conclusions or recommendations expressed in this material are those of the author(s) and do not necessarily reflect the views of the NSF.

6.6 References

(1) Kataoka, K.; Harada, A.; Nagasaki, Y. Block copolymer micelles for drug delivery: Design, characterization and biological significance. *Adv Drug Deliver Rev* **2012**, *64*, 37.
(2) Riess, G. Micellization of block copolymers. *Prog. Polym. Sci.* **2003**, *28*, 1107.
(3) McBain, J. W. *Trans. Faraday Soc.* **1913**, *9*.
(4) Jain, S.; Bates, F. S. On the origins of morphological complexity in block copolymer surfactants. *Science* **2003**, *300*, 460.
(5) Controlled Polymerization and Polymeric Structures: Flow Microreactor Polymerization, Micelles Kinetics, Polypeptide Ordering, Light Emitting Nanostructures. *Controlled Polymerization and Polymeric Structures: Flow Microreactor Polymerization, Micelles Kinetics, Polypeptide Ordering, Light Emitting Nanostructures* **2013**, *259*, 1.
(6) Ma, Z. S.; Haddadi, A.; Molavi, O.; Lavasanifar, A.; Lai, R.; Samuel, J. Micelles of poly(ethylene oxide)-b-poly(epsilon-caprolactone) as vehicles for the solubilization, stabilization, and controlled delivery of curcumin. *J Biomed Mater Res A* **2008**, *86A*, 300.
(7) Patist, A.; Kanicky, J. R.; Shukla, P. K.; Shah, D. O. Importance of micellar kinetics in relation to technological processes. *J. Colloid Interface Sci.* **2002**, *245*, 1.
(8) Lund, R.; Willner, L.; Pipich, V.; Grillo, I.; Lindner, P.; Colmenero, J.; Richter, D. Equilibrium Chain Exchange Kinetics of Diblock Copolymer Micelles: Effect of Morphology. *Macromolecules* **2011**, *44*, 6145.
(9) Lund, R.; Willner, L.; Richter, D.; Dormidontova, E. E. Equilibrium chain exchange kinetics of diblock copolymer micelles: Tuning and logarithmic relaxation. *Macromolecules* **2006**, *39*, 4566.
(10) Chen, S. H. Small-Angle Neutron-Scattering Studies of the Structure and Interaction in Micellar and Microemulsion Systems. *Annu. Rev. Phys. Chem.* **1986**, *37*, 351.
(11) Pedersen, J. S.; Hamley, I. W.; Ryu, C. Y.; Lodge, T. P. Contrast variation small-angle neutron scattering study of the structure of block copolymer micelles in a slightly selective solvent at semidilute concentrations. *Macromolecules* **2000**, *33*, 542.
(12) Pedersen, J. S.; Svaneborg, C.; Almdal, K.; Hamley, I. W.; Young, R. N. A small-angle neutron and X-ray contrast variation scattering study of the structure of block copolymer micelles: Corona shape and excluded volume interactions. *Macromolecules* **2003**, *36*, 416.
(13) Einstein, A. On the Movement of Small Particles Suspended in Stationary Liquids Required by the Molecular-Kinetic Theory of Heat. *Annalen der Physik* **1905**, *17*, 549.
(14) Lohmeijer, B. G. G.; Pratt, R. C.; Leibfarth, F.; Logan, J. W.; Long, D. A.; Dove, A. P.; Nederberg, F.; Choi, J.; Wade, C.; Waymouth, R. M.; Hedrick, J. L. Guanidine and amidine organocatalysts for ring-opening polymerization of cyclic esters. *Macromolecules* **2006**, *39*, 8574.
(15) Pratt, R. C.; Lohmeijer, B. G. G.; Long, D. A.; Waymouth, R. M.; Hedrick, J. L. Triazabicyclodecene: A simple bifunctional organocatalyst for acyl transfer and ring-opening polymerization of cyclic esters. *J. Am. Chem. Soc.* **2006**, *128*, 4556.
(16) Stejskal, E.; Tanner, J. Spin Diffusion Measurements: Spin Echoes in the Presence of a Time-Dependent Field Gradient*. *J. Chem. Phys.* **1965**, *42*.
(17) Callaghan, P. T. *Translational Dynamics and Magnetic Resonance: Principles of Pulsed Gradient Spin Echo NMR*; Oxford University Press: New York, 2011.

(18) Price, W. S. Pulsed-field gradient nuclear magnetic resonance as a tool for studying translational diffusion .1. Basic theory. *Concepts in Magnetic Resonance* **1997**, *9*, 299.
(19) Meiboom, S. Citation Classic - Modified Spin-Echo Method for Measuring Nuclear-Relaxation Times. *Cc/Eng Tech Appl Sci* **1980**, 16.
(20) Carr, H.; Purcell, E. Effects of Diffusion on Free Precession in Nuclear Magnetic Resonance Experiments. *Phys. Rev.* **1954**, *94*, 630.
(21) Levitt, M. H. *Spin Dynamics*; John Wiley and Sons Ltd.: England, 2008; Vol. 2.
(22) Bryskhe, K.; Jansson, J.; Topgaard, D.; Schillen, K.; Olsson, U. Spontaneous vesicle formation in a block copolymer system. *J. Phys. Chem. B* **2004**, *108*, 9710.
(23) Nilsson, M.; Hakansson, B.; Soderman, O.; Topgaard, D. Influence of polydispersity on the micellization of triblock copolymers investigated by pulsed field gradient nuclear magnetic resonance. *Macromolecules* **2007**, *40*, 8250.
(24) Walderhaug, H.; Soderman, O.; Topgaard, D. Self-diffusion in polymer systems studied by magnetic field-gradient spin-echo NMR methods. *Prog. Nucl. Magn. Reson. Spectrosc.* **2010**, *56*, 406.

Chapter 7

Unimer Exchange Dynamics in Block Copolymer Micelles Using Time-Resolved NMR

Abstract: Here we present a new method to investigate the exchange of unimers between diblock copolymer micelles. This method involves time-dependent NMR spin-relaxation time constants (T_1) measurements made after combining a micelle solution (PEO_{5k}-PCL_{8k}) containing ^{1}H-cores and a micelle solution containing ^{2}H-cores. Each ^{1}H and ^{2}H environment gives a different ^{1}H T_1 that is influenced by intermolecular dipole-dipole interactions and the smaller magnetic moment of ^{2}H. The smaller magnetic moment of ^{2}H increases the T_1 of the ^{1}H-sites as the unimers exchange and the protonated micelles become dilute with ^{2}H-unimers. The weighted average rate constant for unimer exchange at 60°C is 20.8 ± 0.8 min^{-1} and is in good agreement with time-resolved neutron scattering results, which is the only other known method of measuring this type of molecular exchange. Furthermore, variable temperature NMR diffusometry measurements show single-component diffusion until 40°C, where a second faster diffusion coefficient appears. This method can in principle work on any solution NMR spectrometer and is thus vastly simpler and cheaper than the previous neutron scattering technique.

7.1 Introduction

Polymeric micelles are self-assembled aggregates generated from amphiphilic block copolymer chains (unimers).[1] Through careful polymer design, segregation of hydrophobic and hydrophilic blocks to form a spherical core-corona morphology (Figure 7.1) affords a unique architecture to tailor for drug-delivery applications.[2]

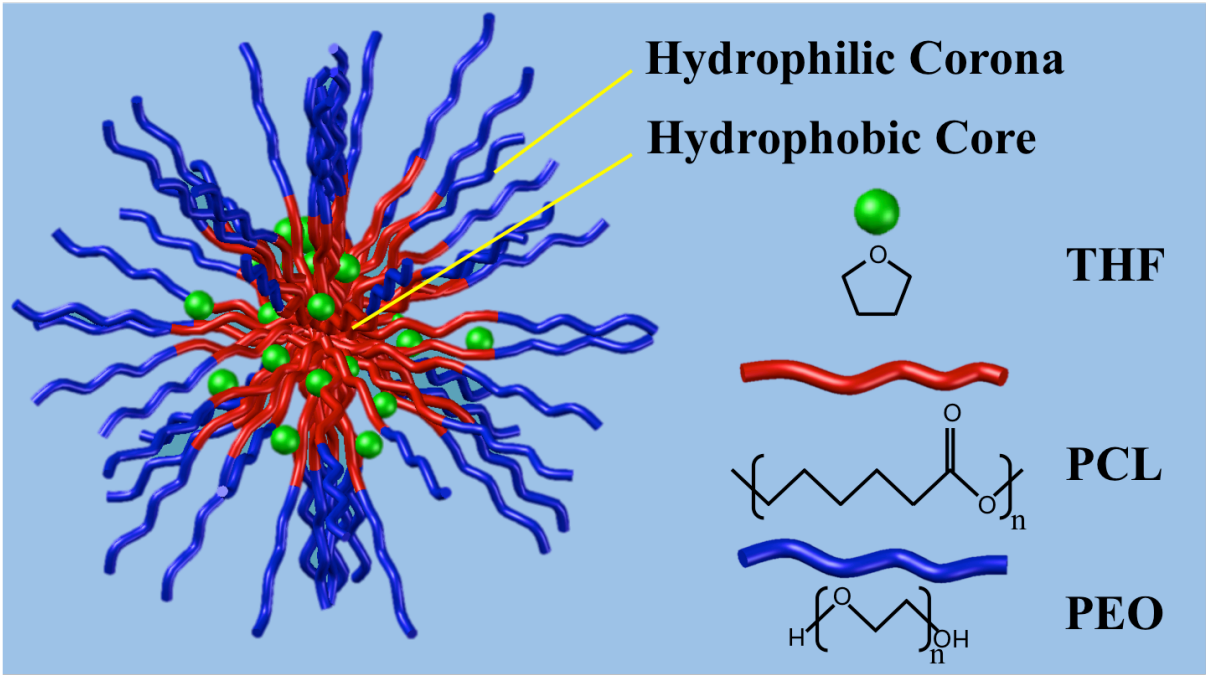

Figure 7.1. Illustration of a PEO-PCL spherical micelle that self-assembles at 1% wt/vol in D_2O. Loading THF_{d8} into the PCL core allows understanding of solvent environmental effects on micelles as well as the encapsulation of drug molecules.

Micelle morphology is sensitive to environmental changes, solvent concentration and composition, temperature, and/or pH.[3] Harnessing this sensitivity allows controllable encapsulation and release of drugs for targeted delivery.[4] Drug encapsulation in a polymeric micelle can provide an environment for hydrophobic drug compounds that demonstrate limited biocompatibility, as well as providing a physical barrier between the drug and surrounding

environment, limiting non-specific toxicity.[4] The hydrophilic nature and steric stability of poly(ethylene oxide) (PEO) combined with the biodegradability of poly(caprolactone) (PCL) make PEO-*b*-PCL diblock copolymers ideal building-blocks for drug-delivery vehicles.[5] The PEO corona is able to resist protein adsorption and cellular adhesion, which protects the encapsulated drug not only from hydrolysis and enzymatic degradation, but also from elimination by the immune system.[5]

Understanding unimer dynamics is necessary to properly design next generation drug delivery vehicles and nano-reactors.[6,7] A common technique to characterize micelle structure and dynamics is small angle neutron scattering (SANS).[8] Harnessing differences in scattering length density between elemental isotopes,[9] SANS allows detailed analysis of micelle dynamics by ^{1}H and ^{2}H contrast-matching experiments. However, SANS instrumentation comes at a high-cost (~ $1 billion), limited user time (usually biannually), and presents cumbersome data analysis.

Alternatively, nuclear magnetic resonance (NMR) offers chemical specificity and the ability to study dynamics on multiple time and length scales.[10] Measuring chemical exchange using NMR generally involves the observation of controlled changes in two chemically distinct pieces of NMR information. Key examples include irradiation of one chemically distinct nuclear signal and observing changes to a second distinct nuclear signal as in chemical exchange saturation transfer (CEST),[11,12] or the observation of various encoding-time-dependent cross peaks as in chemical exchange spectroscopy (EXSY).[13,14] How do we measure the exchange of molecules from one chemical environment, through another medium, and into an environment identical to the original one?

NMR spin-lattice relaxation (T_1) reports on Larmor frequency time scale ($1/\omega_0$) rotational dynamics and is sensitive to changes in the local nuclear environment.[15-17] The net observed T_1 time constant comes from contributions of inter- and intramolecular effects (Equation 7.1),[17]

$$\frac{1}{T_1} = \frac{1}{T_1(inter)} + \frac{1}{T_1(intra)} \tag{7.1}$$

Intramolecular dipole-dipole interactions between nuclei in a given sample are generally stronger than intermolecular dipole-dipole interactions due to the r^{-3} distance dependence. However, the dipole-dipole interaction also depends on the relative magnetic moments of interacting nuclei (^{2}H gyromagnetic ratio $\gamma_{2H} = 0.15 \times \gamma_{1H}$). Thus, when a micelle composed of 100% ^{1}H-unimers is diluted with ^{2}H-unimers (chemically similar but isotopically different), a corresponding increase in T_1 for the ^{1}H-sites is expected due to less efficient relaxation caused by intermolecular ^{2}H-^{1}H interactions.[18] Analogous to contrast-matching mixing experiments with time-resolved (TR)-SANS,[19,20] one can start with two separate micelle solutions, with one composed of 100% ^{1}H-unimers and the other composed of 100% ^{2}H-unimers. When the two solutions are combined and unimer exchange occurs between micelles, we can expect T_1 of the ^{1}H-unimers to increase as a function of time. Theoretically, the ^{1}H T_1 values should be initially low and increase as the ^{2}H-unimers dilute the ^{1}H-micelles through exchange. This is achievable with a time resolution of ~ 1 minute for a single T_1 experiment, whereas a single SANS experiment is several minutes.

In summary, here we present a simple method to measure unimer exchange between block-copolymer micelles. By taking advantage of differences in magnetic interactions between ^{1}H and ^{2}H-sites on unimers, we combine two separate samples and measure changes in T_1 as a function of time to extract rate constants for unimer exchange between micelles. We also employ variable temperature NMR diffusometry, which shows a transition to a micelle and unimer

coexistence region above 40°C, thus suggesting the dominant unimer exchange mechanism is through insertion/expulsion. This use of T_1 and NMR diffusometry to characterize micelle and unimer dynamics in solution offers a cheaper and more convenient alternative to SANS methods, thus enabling the expansion and acceleration of polymeric micelle characterizations.

7.2 Experimental

7.2.1 Diblock Copolymer Synthesis and Characterization

See Chapter 6 (section 6.2.1) for diblock copolymer synthesis and characterization.

7.2.2 Spin-Lattice Relaxation and NMR Diffusometry

Micelle solutions were sealed with an oxygen/natural gas torch in a 5mm NMR tube to eliminate changes over time due to solvent evaporation. Each sample tube contained 4 axial capillaries of 0.8 mm I.D. and 1.0 mm O.D. (Fisher Scientific) to minimize convection artifacts in NMR diffusometry and unimer exchange (T_1) experiments.

All spin-lattice relaxation time (T_1) measurements were conducted at 25°C and 60°C using a 400 MHz Bruker Avance III WB NMR spectrometer, equipped with a MIC probe and 5 mm ^{1}H RF coil. The inversion-recovery pulse sequence ($180°_x - t_d - 90°_y$) with 90° and 180° pulse lengths of 4.5 μs and 9 μs, respectively, allowed measurement of signal intensity S as a function of relaxation delay time (t_d) in 16-steps and these data were fit with Equation 7.2,[15]

$$S = S_0(1 - 2e^{-\frac{t_d}{T_1}}) \tag{7.2}$$

wherein S_0 is the initial intensity at $t = 0$ and t_d is the relaxation delay time.

All variable temperature ^{1}H PFG NMR experiments were performed using a 400 MHz Bruker Avance III WB NMR spectrometer, equipped with a MIC probe coupled to a Diff60 single-axis (*z*-axis) gradient system and 5 mm ^{1}H RF coil. In the PFG NMR experiment, measured signal amplitude I as a function of gradient strength, g, was fit using the Stejskal-Tanner equation,[21-23]

$$I = I_0 e^{-D\gamma^2 g^2 \delta^2 (\Delta - \frac{\delta}{3})}, \quad (7.3)$$

wherein I_0 is the signal amplitude at $g = 0$, γ is the gyromagnetic ratio, δ is the effective gradient pulse, Δ is the diffusion time between gradient pulses, and D is the self-diffusion coefficient. The simple and robust pulsed-gradient stimulated echo (PGSTE) sequence was used with a 90° pulse length of 4.6 μs. A repetition time of 3 s, effective gradient pulse length of δ = 2 ms (actual pulse length = 1.57 × effective gradient pulse length for the half sinusoid gradient pulse), and a diffusion time of Δ = 25 ms were used for polymer and solvent diffusion measurements. Maximum gradient strengths of 30 – 520 G cm^{-1} were used to achieve 90 – 95% signal attenuation in 16 – 32 steps. Sufficient signal-to-noise ratio (SNR) for each data point was achieved with 8 – 16 scans. Acquisition times of 5 s were used for the micelle solutions. All PGSTE parameters were calibrated as previously reported.[24]

7.3 Results and Discussion

The PEO-*b*-PCL block copolymer self-assembles into spherical micelles at 1% wt/vol in D_2O. Here we use 90:10 (vol:vol) D_2O:THF_{d8} to incorporate a small molecule additive (THF_{d8}) to investigate effects of mixed solvents on micelle dynamics, and to mimic hydrophobic drug-loading conditions within the PCL core. Previous work has shown the present micelle is stable

up to 50 vol% THF_{d8} before completely breaking apart into free unimers (Chapter 6). Use of deuterated solvents is desired to increase the prominence of the polymeric signals (Figure 7.2) in the spectrum and minimize the number of scans required for time-resolved T_1 measurements (discussed below).

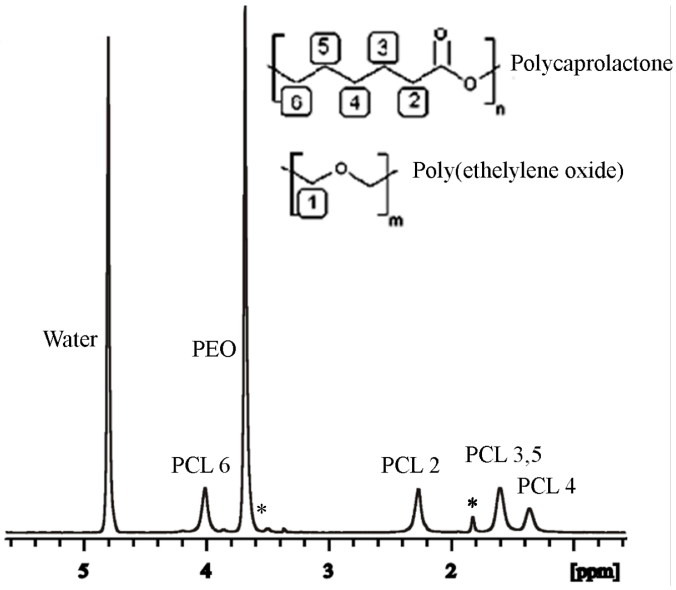

Figure 7.2. ^{1}H NMR spectrum of the PCL_{5k}-PEO_{8k} micelle solution at 10:90 vol/vol% THF_{d8}:D_2O. Residual ^{1}H-THF is indicated with an asterisk (*). See also Section 6.3 for a deeper discussion of this spectrum.

With the goal of tracking unimer exchange between micelles using T_1 relaxation times, we begin by evaluating the T_1 times for the ^{1}H-sites of PCL in two samples: 1) micelles composed of 100% ^{1}H-PCL (labeled TC-7-1) and 2) micelles composed of 90% ^{2}H(3,4,5)-PCL/10% ^{1}H-PCL (labeled TC-6b-1) at 25°C and 60°C (Table 7.1). We conduct T_1 experiments at 60°C to complement collaborative TR-SANS work (not shown).

	TC-7-1 T_1 at 25 °C (ms)	TC-7-1 T_1 at 60 °C (ms)	TC-6b-1 T_1 at 25 °C (ms)	TC-6b-1 T_1 at 60 °C (ms)
PCL-6	389	616	526	787
PCL-2	412	658	552	842
PCL-3,5	--	593	--	645
PCL-4	367	615	446	683

Table 7.1. T_1 relaxation time constants for the ^{1}H-sites on PCL for micelles composed of 100% ^{1}H-unimers (TC-7-1) and micelles composed of 10:90 ^{1}H:^{2}H-unimers (TC-6b-1). The error in measured T_1 is < 1%.

For micelles composed of 100% ^{1}H-PCL (TC-7-1) at 25°C, we see that T_1 does not vary drastically among the different PCL positions due to similar inter- and intramolecular interactions. Subtle differences likely arise from intramolecular dipolar coupling differences along the chain, along with THF_{d8} interactions (and possibly D_2O) with the individual ^{1}H-sites within the micelle core. Micelles composed of 90% ^{2}H(3,4,5)-PCL/10% ^{1}H-PCL (TC-6b-1) show a significant increase in PCL ^{1}H T_1 times in comparison to micelles composed of 100% ^{1}H-PCL. As previously discussed, an increase in ^{1}H T_1 directly results from intermolecular interactions between the ^{1}H- and ^{2}H-PCL chains (Figure 7.3). Thus, when these two samples are mixed together, we can expect to see an increase in T_1 with time after mixing as the protonated and deuterated unimers begin exchanging between micelles.

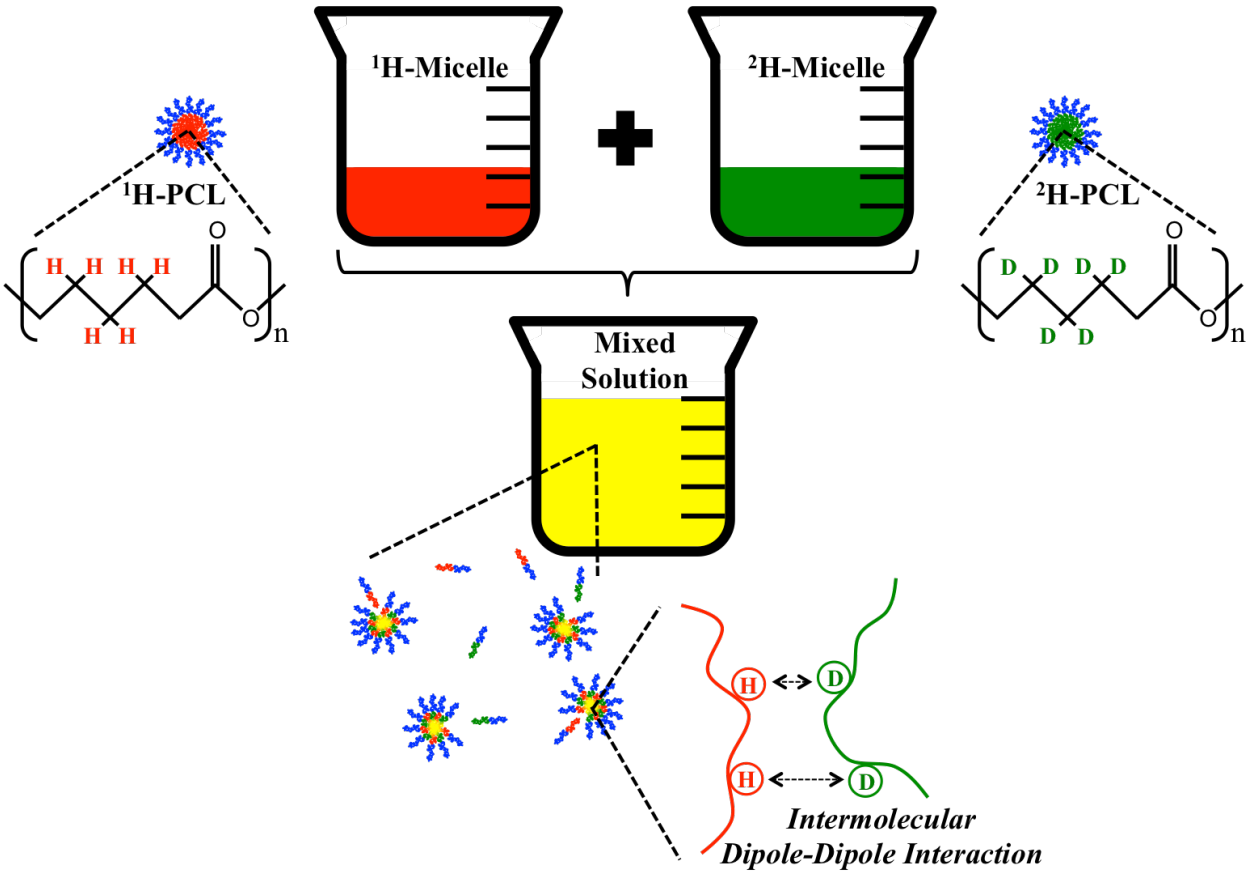

Figure 7.3. Illustration of experimental protocol for measuring time-resolved T_1 to track unimer exchange between micelles. We mix samples of protonated and deuterated micelles and measure the NMR T_1 relaxation time as a function of time after mixing. Intermolecular dipolar couplings between ^{1}H- and ^{2}H-PCL chains increase the ^{1}H T_1 with time.

For each sample, an increase in T_1 is seen with temperature, suggesting that micelles are in the "fast motion limit" and have a short rotational correlation time (~ ns time scale) for the micelle, as described by the Bloembergen-Purcell-Pound (BPP) theory.[17]

We combine the two micelle solutions (Figure 7.3) and measure T_1 as a function of time for all PCL signals at 60°C for varying volume ratios of ^{1}H:^{2}H micelle solutions (Figure 7.4). Varying the volume ratios of ^{1}H:^{2}H micelle solutions allows us to assess how sensitive this

method is to small amounts of ^{2}H-micelle, which is relevant for polymer scientists who may be limited by available ^{2}H-micelle.

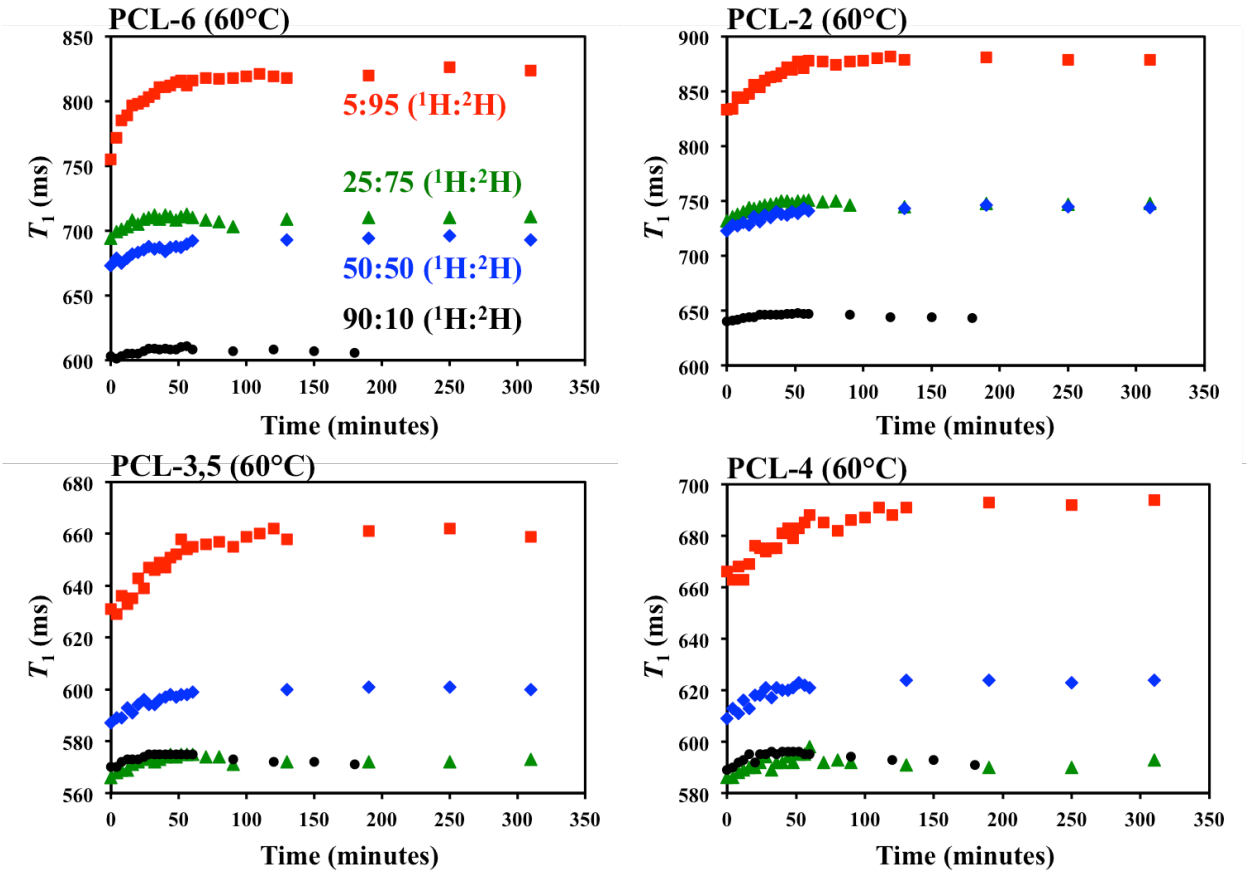

Figure 7.4. T_1 as a function of time after mixing protonated and deuterated micelle samples, where the legend labels (upper left plot) give volume percent composition of ^{1}H PCL micelle solutions relative to ^{2}H micelle solutions. A larger percentage of ^{2}H micelles produces a larger change in T_1 from time $t = 0$ to equilibrium.

Analogous to T_1 trends in Table 7.1, we see an overall increase in each individual PCL signal T_1 at $t = 0$ min as the ^{1}H:^{2}H micelle solution volume ratio decreases. This means that as the ^{1}H:^{2}H micelle solution volume ratio decreases, ^{1}H nuclei are surrounded by a larger fraction of ^{2}H

nuclei. Measuring T_1 as a function of time at 60°C shows a clear increase in T_1 for each of PCL signal. We emphasize the precision of our measurements, as the errors in individual T_1 times are < 1%. As the ^{1}H:^{2}H micelle solution volume ratio changes from 90:10 to 5:95, the average T_1 at equilibrium (time > 5 hrs) changes from 0.4 to 6 %. This is due to the significant effect of intermolecular interactions between ^{2}H- and ^{1}H-unimers on the net T_1 (Equation 7.1). Thus implying that the increase in T_1 times shown in Figure 7.4 results from individual ^{1}H- and ^{2}H-unimer exchange between micelles as the micelles establish equilibrium. To be confident that the change in T_1 as a function of time is not due to temperature equilibration, we investigate the ^{1}H-sites on PEO within the corona, which do not show any change in T_1 vs. t (not shown). This is expected, as the inter- and intramolecular interactions between the ^{1}H-sites on PEO are equivalent in the ^{1}H- and ^{2}H-micelles.

In order to extract unimer exchange rate constants k_{exch} from data in Figure 7.4, we assume that the relaxation rate ($1/T_1$) is proportional to ^{1}H-PCL chain concentration in a single micelle. Such a proportionality is consistent with the linear relation between relaxivity ($1/T_1$) and concentration of MRI contrast agents.[22,25] We fit our $1/T_1$ data using a simple exponential,

$$\frac{1}{T_1}(t) = \frac{1}{T_1^{final}} + \frac{1}{\Delta T_1} e^{-kt} \tag{7.4}$$

where ΔT_1 is the difference in experimentally measured $T_1(t) - T_1^{final}$ and t is time after mixing (Figure 7.5 and Table 7.2).

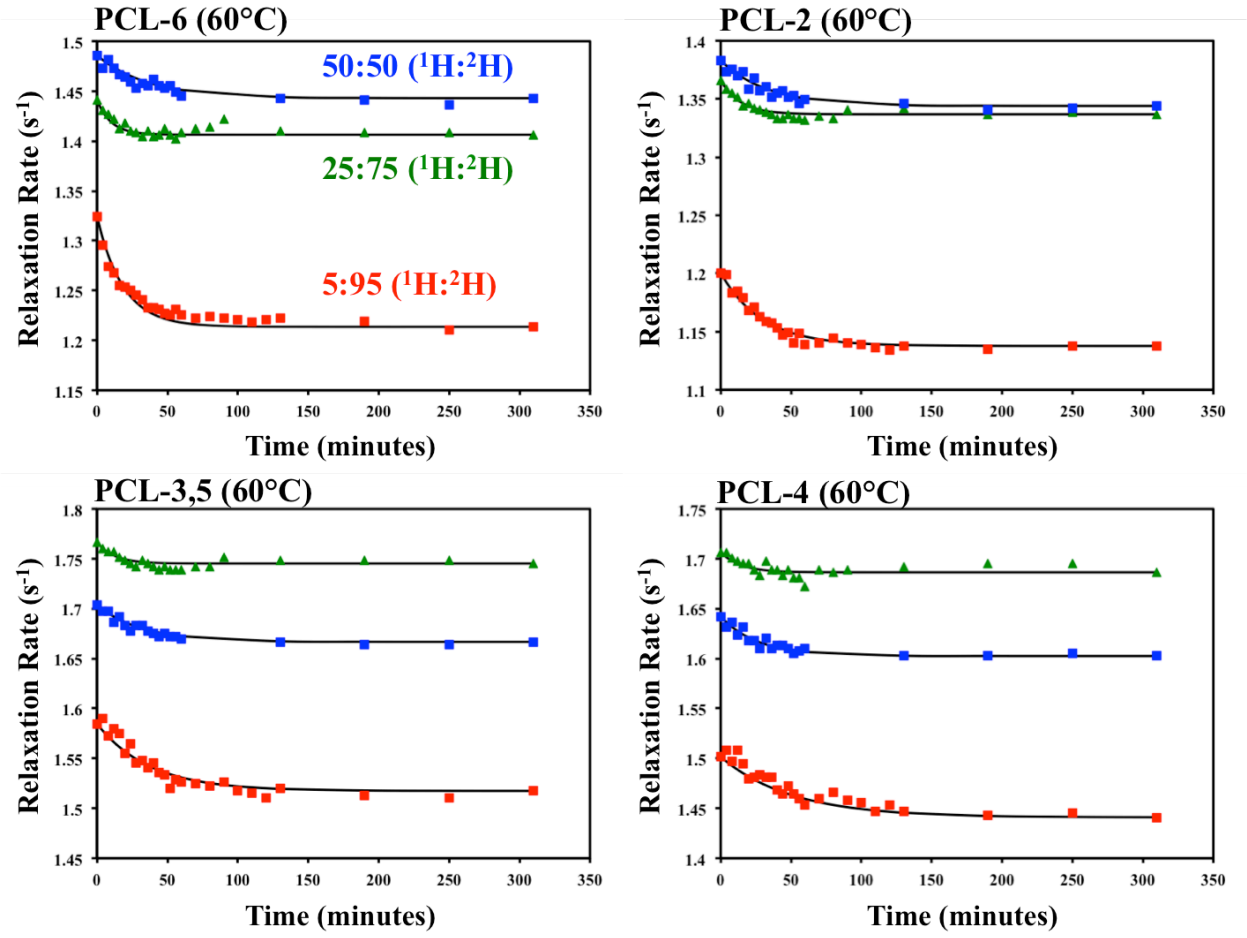

Figure 7.5. Fitting the relaxation rate ($1/T_1$) as a function of time t for each signal affords a weighted average rate constant for unimer exchange of $k_{exch} = 20.8 \pm 0.8$ min^{-1}.

	k_{exch} (min^{-1}) 5:95 (^{1}H:^{2}H)	k_{exch} (min^{-1}) 25:75 (^{1}H:^{2}H)	k_{exch} (min^{-1}) 50:50 (^{1}H:^{2}H)
PCL-6	18.4 ± 1.3	10.1 ± 2.5	36.5 ± 5.5
PCL-2	29.3 ± 2.2	13.9 ± 2.2	33.3 ± 4.8
PCL-3,5	37.2 ± 4.2	12.2 ± 3.3	31.8 ± 3.6
PCL-4	50.6 ± 7.4	14.1 ± 6.1	26.2 ± 4.4

Table 7.2. The unimer exchange rate constants (k_{exch}) and standard deviations (σ) at 60°C obtained for each position at different volume ratios of ^{1}H-micelle:^{2}H-micelle with Equation 7.4.

Table 7.2 shows variation in k_{exch} for the various ^{1}H positions. Recall, the average change in T_1 over 5 hrs increases from 0.4 to 6 % (90:10 to 5:95, ^{1}H:^{2}H). That is, as the amount of ^{2}H-unimer content increases, we expect to see a greater change in T_1 with time of the ^{1}H positions. This suggests that the measurement precision increases with ^{2}H-unimer content, which is also reflected in Table 7.2 with the most precise measurements being from the 5:95 (^{1}H:^{2}H) sample. Thus, in order to acquire an averaged k_{exch} value, the k_{exch} for each signal i across all ^{1}H:^{2}H contents is weighted (w_i) by its respective standard deviation (σ_i, wherein $w_i = 1/\sigma_i^2$) to minimize the influence of less precise measurements to obtain a weighted average k_{exch} and standard deviation,

$$k_{exch} = \frac{\sum T_1^i w_i}{\sum w_i} \tag{7.5}$$

$$\sigma_{k_{exch}} = \frac{1}{\sqrt{\sum w_i}} \tag{7.6}$$

We thus obtain a weighted average rate constant for unimer exchange k_{exch} = 20.8 ± 0.8 min^{-1}.

Previous to the above experiments, we attempted to measure mixing at 25°C (not shown), but we were not able to see any immediate (~3 hrs) change in T_1 after mixing. Clearly, unimer exchange is much slower at 25°C. Note that even with the use of low ^{2}H-micelle content mixing samples, we still see a measureable change in T_1, thus allowing implementation of this method if ^{2}H-chain resources are limited. This simple NMR technique thus offers a new and unique method to characterize unimer exchange dynamics for polymeric micelles, and opens up the possibility of routine measurements by any research lab with access to a solution NMR spectrometer.

We can then ask a deeper question: What is the unimer exchange mechanism? Currently, there are two dominant theories: fusion/fission of whole micelles, whereby free unimer concentration would be very low, and expulsion/insertion of unimers from/to micelles, with some significant free unimer concentration in solution at all times.[3,4,26,27] Variable temperature NMR diffusometry allows us to correlate changes in the unimer and/or micelle diffusion coefficients D with the hydrodynamic radius r_H of the diffusing species through rearrangement of the Stokes-Einstein equation that accounts for changes in viscosity (see also Section 6.3),

$$r_H^{micelle} = r_H^{H_2O}\left(\frac{D_{H_2O}}{D_{micelle}}\right) \tag{7.4}$$

r_H gives us insight into the size of diffusing species, such as micelles and free unimers.[28-33] Thus, if free unimers and micelles are separate populations that are not exchanging faster than the diffusion time scale (~ 10 ms), we can expect to see two D components in our data, and can relate these components to their respective r_H. Figure 7.6 shows variable temperature diffusion coefficients and corresponding hydrodynamic radii, measured from 21 – 60°C.

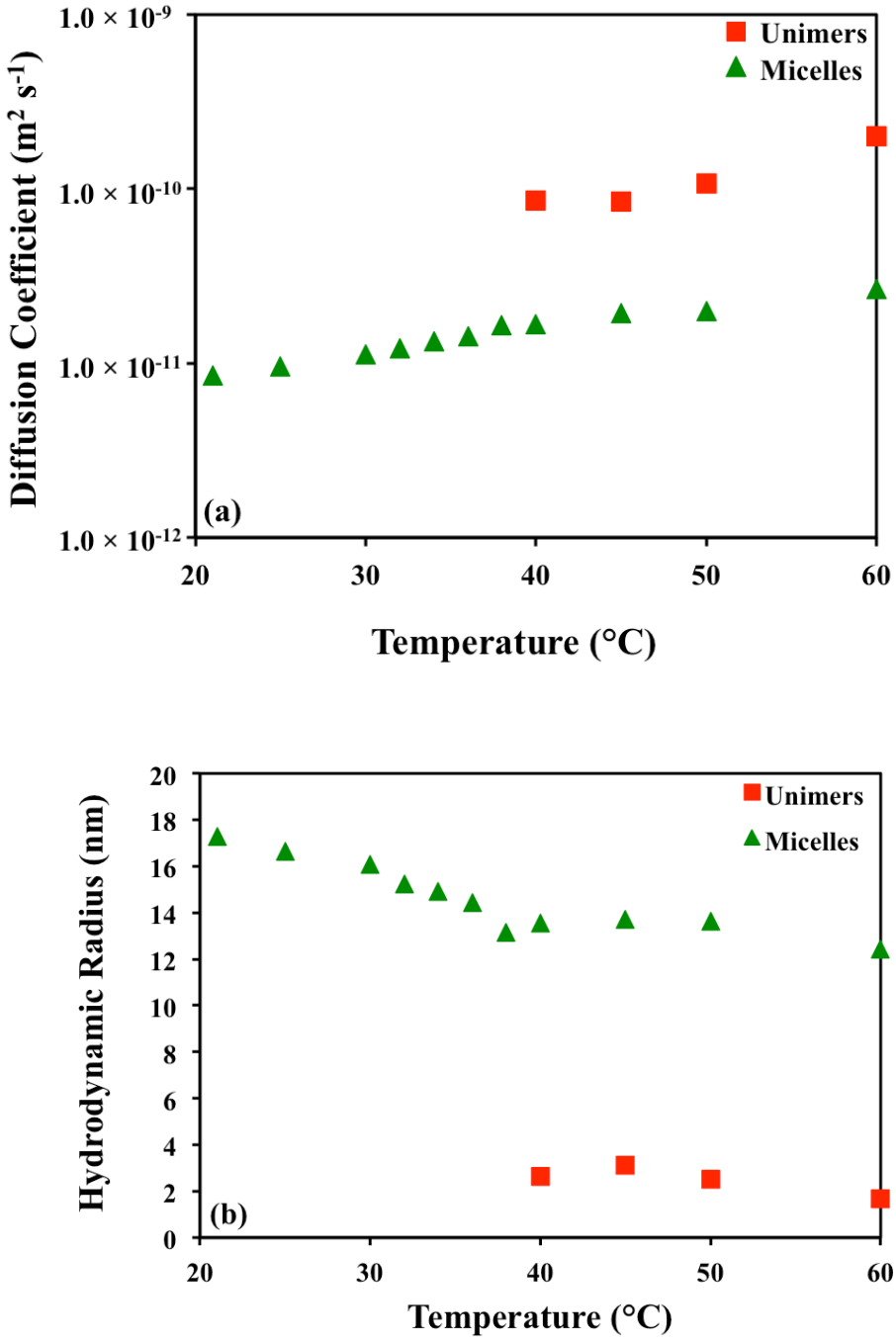

Figure 7.6. Variable temperature (21 – 60°C) diffusion coefficients (a) and hydrodynamic radii (b) show single component diffusion below 40°C, above which a second faster component (small r_H) evolves. Below 40°C, only micelles exist in solution while ≥ 40°C coexistence of free unimers and micelles exist.

We see one-component diffusion below 40°C (Figure 7.6a), which is in agreement with results shown in Chapter 6. Interestingly, we see the appearance of a second, significantly faster, diffusion coefficient at 40°C. Analogous to the onset of a coexistence over a range of THF_{d8} vol% (Chapter 6.3), these results also demonstrate that micelle and unimer coexistence depend on temperature as well. Using the above results, we can now determine that the dominant unimer exchange mechanism is insertion-expulsion. If the fusion/fission mechanism dominates, a second diffusion component will be slower at 60°C. We see that the second *D* component is significantly faster, strongly indicating the presence of free unimers in solution on the NMR diffusometry time scale (Δ = 25 ms in this case). To amplify this conclusion, we show r_H values obtained using Stokes-Einstein (Equation 7.4) as a function of temperature and see a decrease in micelle r_H from 17 – 12 nm and a much smaller r_H of 3 nm (Figure 7.6b), which must be free unimers. Our previous study on the same series of micelles showed two-component diffusion at 50 vol% THF_{d8} content at 25°C (Chapter 6.3). Our group is proceeding to further map a phase diagram for the existence of micelles and/or unimers as a function of temperature and THF_{d8} vol%, thus allowing enhanced insights into micelle dynamics, and informing design of future drug-delivery systems. Combining the concepts of micelle insertion-expulsion, ^1H-^2H spin interactions, and time-resolved T_1 measurements, we summarize the overall concept of our micelle exchange dynamics experiments in Figure 7.7.

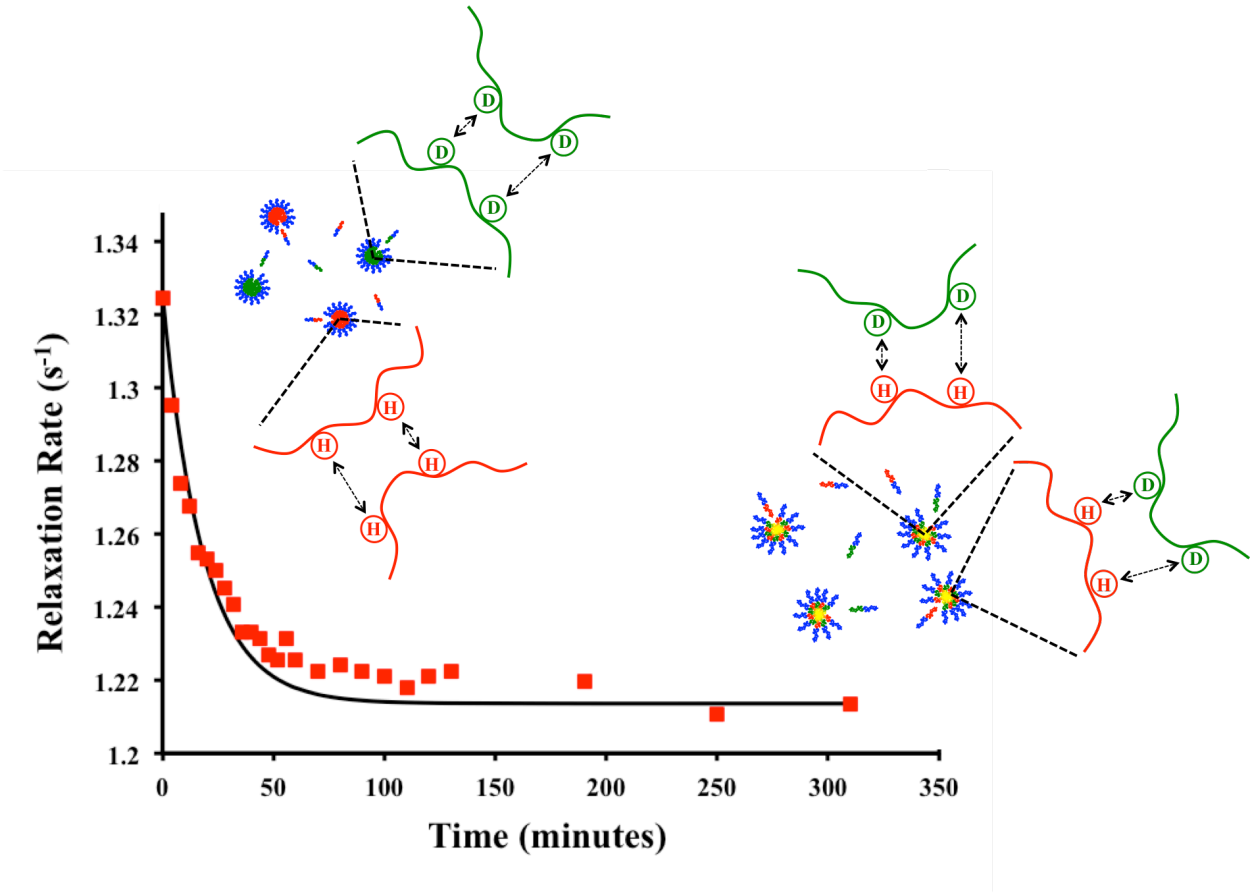

Figure 7.7. Micelle solutions composed of ^{1}H-unimer chains (red) and ^{2}H-unimer chains (green) are mixed and then exchange unimers to establish equilibrium, producing micelles with both ^{1}H- and ^{2}H-PCL cores (yellow). This exchange phenomenon is measurable through simple time-resolved NMR T_1 measurements.

7.4 Conclusions

We have presented a new method using NMR to report on unimer dynamics of a PEO-PCL block copolymer micelle. Taking advantage of differences in magnetic moments between ^{1}H- and ^{2}H-sites on otherwise chemically identical unimers, we measure time-resolved T_1 to report on unimer exchange rate constants. At 60°C, we calculate a weighted average rate constant for unimer exchange of k_{exch} = 20.8 ± 0.8 min^{-1}. In conjunction with our T_1 measurements, we

conduct variable temperature NMR diffusometry to discern the dominant unimer exchange mechanism. We see single-component diffusion until 40°C, where a second, significantly faster, diffusion coefficient appears. In conjunction with the Stokes-Einstein relation, we determine hydrodynamic radii (r_H) of ~ 13 nm and ~ 2 nm at ≥ 40°C, signifying coexistence of micelles and unimers. These results strongly indicate that the dominant unimer exchange mechanism is the insertion-expulsion of unimers to and from micelles. As an alternative to TR-SANS in this application, NMR is a much more accessible and cost effective method of analysis. Indeed, essentially any NMR spectrometer and operator can accomplish these experiments, opening up a simple method for materials developers to conveniently characterize new micelle systems. We also believe that NMR spectroscopy and diffusometry will prove to be powerful techniques for more general characterization of micelle structure dynamics.

7.5 Acknowledgements

This work was supported by the National Science Foundation (NSF) under award numbers CBET 1437767 and 1437831. Any opinions, findings and conclusions or recommendations expressed in this material are those of the author(s) and do not necessarily reflect the views of the NSF.

7.6 References

(1) McBain, J. W. *Trans. Faraday Soc.* **1913**, *9*.
(2) *Controlled Polymerization and Polymeric Structures: Flow Microreactor Polymerization, Micelles Kinetics, Polypeptide Ordering, Light Emitting Nanostructures* **2013**, *259*, 1.
(3) Jain, S.; Bates, F. S. *Science* **2003**, *300*, 460.
(4) Kataoka, K.; Harada, A.; Nagasaki, Y. *Adv Drug Deliver Rev* **2012**, *64*, 37.

(5) Ma, Z. S.; Haddadi, A.; Molavi, O.; Lavasanifar, A.; Lai, R.; Samuel, J. *J Biomed Mater Res A* **2008**, *86A*, 300.
(6) Gallou, F.; Isley, N. A.; Ganic, A.; Onken, U.; Parmentier, M. *Green Chemistry* **2016**, *18*, 14.
(7) La Sorella, G.; Strukul, G.; Scarso, A. *Green Chemistry* **2015**, *17*, 644.
(8) Chen, S. H. *Annu. Rev. Phys. Chem.* **1986**, *37*, 351.
(9) Kotlarchyk, M.; Chen, S. H. *J. Chem. Phys.* **1983**, *79*, 2461.
(10) Levitt, M. H. *Spin Dynamics*; John Wiley and Sons Ltd.: England, 2008; Vol. 2.
(11) Ward, K. M.; Aletras, A. H.; Balaban, R. S. *J Magn Reson* **2000**, *143*, 79.
(12) van Zijl, P. C. M.; Yadav, N. N. *Magn Reson Med* **2011**, *65*, 927.
(13) Meier, B. H.; Ernst, R. R. *J. Am. Chem. Soc.* **1979**, *101*, 6441.
(14) Jeener, J.; Meier, B. H.; Bachmann, P.; Ernst, R. R. *J. Chem. Phys.* **1979**, *71*, 4546.
(15) Hahn, E. L. *Physical Review* **1949**, *76*, 145.
(16) Bloembergen, N.; Purcell, E. M.; Pound, R. V. *Nature* **1947**, *160*, 475.
(17) Bloembergen, N.; Purcell, E. M.; Pound, R. V. *Physical Review* **1948**, *73*, 679.
(18) Anderson, W. A.; Arnold, J. T. *Physical Review* **1956**, *101*, 511.
(19) Pedersen, J. S.; Hamley, I. W.; Ryu, C. Y.; Lodge, T. P. *Macromolecules* **2000**, *33*, 542.
(20) Pedersen, J. S.; Svaneborg, C.; Almdal, K.; Hamley, I. W.; Young, R. N. *Macromolecules* **2003**, *36*, 416.
(21) Stejskal, E.; Tanner, J. *J. Chem. Phys.* **1965**, *42*.
(22) Callaghan, P. T. *Translational Dynamics and Magnetic Resonance: Principles of Pulsed Gradient Spin Echo NMR*; Oxford University Press: New York, 2011.
(23) Price, W. S. *Concepts in Magnetic Resonance* **1997**, *9*, 299.
(24) Hou, J.; Madsen, L. A. *J. Chem. Phys.* **2013**, *138*.
(25) Wang, X. L.; Chen, Y.; Xue, L.; Pothayee, N.; Zhang, R.; Riffle, J. S.; Reineke, T. M.; Madsen, L. A. *J Phys Chem Lett* **2014**, *5*, 3825.
(26) Lund, R.; Willner, L.; Pipich, V.; Grillo, I.; Lindner, P.; Colmenero, J.; Richter, D. *Macromolecules* **2011**, *44*, 6145.
(27) Lund, R.; Willner, L.; Richter, D.; Dormidontova, E. E. *Macromolecules* **2006**, *39*, 4566.
(28) Edward, J. T. *J. Chem. Educ.* **1970**, *47*, 261.
(29) Einstein, A. *Annalen der Physik* **1905**, *17*, 549.
(30) Hou, J.; Zhang, Z.; Madsen, L. A. *J. Phys. Chem. B* **2011**, *115*, 4576.
(31) Bryskhe, K.; Jansson, J.; Topgaard, D.; Schillen, K.; Olsson, U. *J. Phys. Chem. B* **2004**, *108*, 9710.
(32) Nilsson, M.; Hakansson, B.; Soderman, O.; Topgaard, D. *Macromolecules* **2007**, *40*, 8250.
(33) Walderhaug, H.; Soderman, O.; Topgaard, D. *Prog. Nucl. Magn. Reson. Spectrosc.* **2010**, *56*, 406.

Chapter 8

Summary and Future Work

8.1 Summary and General Material Design Guidelines

The present thesis presents multiple studies that highlight NMR spectroscopy, relaxation, and diffusometry methods to study morphology-dependent transport and dynamics within soft materials relevant to energy storage and conversion technologies, and block-copolymer micelles relevant to drug-delivery vehicles. The present thesis also aims to inform materials scientists how to use such methods in their efforts to expand research capabilities. General characterization and design strategies can be utilized to achieve highly conductive materials for battery/fuel cell applications as well as develop block copolymers for drug-delivery and nanoreactors applications. Herein, I summarize Chapters 3, 4, 5, 6, and 7 and highlight how they can help guide future research directions within these respective areas of materials science.

Chapter 3

Chapter 3 presents an investigation of the organic ionic plastic crystal 1,2-bis[*N*-(*N'*-hexylimidazolium-d_2(4,5))]ethane $2PF_6^-$ in one of its solid plastic crystal phases by means of multinuclear solid-state (SS) NMR and NMR diffusometry. We quantify distinct cation and anion diffusion coefficients as well as the Arrhenius diffusion activation energies (E_a) in this *dicationic* imidazolium-based plastic crystal. Our studies suggest a change in transport mechanism for the cation upon varying thermal and magnetic treatment (9.4 T), evidenced by differences in cation and anion E_a. Moreover, variable temperature ^2H SSNMR lineshapes support a change in local molecular environment upon slow cooling in B_0. We quantify the

percentage of mobile anions as a function of temperature with ^{19}F SSNMR, wherein two distinct spectral features are present. We also comment on the Arrhenius pre-exponential factor for diffusion (D_0), giving insight into the number of degrees of freedom for transport for both cation and anion as a function of thermal treatment. We propose that bulk ion transport is dominated by anion diffusion in ionic-liquid-like domain boundaries separating crystallites. This study elucidates fundamental properties of this plastic crystal and allows for a more general and deeper understanding of ion transport within such materials.

Dovetailing work in Chapter 3, independent MRI-based studies on a different class of OIPCs have shown magnetic field-induced orientation of crystallites. Future research directions on OIPCs should focus on further characterizing and optimizing orientational ordering within such materials, as ion-transport can be enhanced along the alignment direction and ultimately impacts material performance. Future work should also focus on better understanding how the incorporation of impurities, such as lithium salts, into OIPCs impacts transport within the liquid-like domain boundary at elevated temperatures. If ionic conductivity is dominated by a liquid-like domain boundary, it may be advantageous to correlate crystallite sizes with bulk transport, as restricted diffusion behavior can substantially reduce long-time scale diffusion. Such properties also determine how "soft" the OIPC is, thus potentially impacting the electrolyte/electrode interface. Furthermore, incorporation of "liquid nucleating" additives, such as thin fibers, sheets, or particles, to promote a larger fraction of liquid-like domain boundaries should increase ionic conductivity.

Chapter 4

Chapter 4 describes the utilization of NMR spectroscopy to probe geometric features of a hydrophilic channel within uniaxially drawn Nafion® 117. ^{7}Li and ^{23}Na residual quadrupole

splittings as a function of water content strongly indicate that the hydrophilic channel of Nafion is biaxial. These results and conclusions agree with a ribbon-like model of hydrophilic channels. Moreover, ^{7}Li biaxiality parameter (η_Q) shows a gradual decrease (η_Q = 0.26 – 0.20) as a function of water content λ followed by a dramatic drop at λ > 9.5 to a plateau value of η_Q = 0.05. Finally, we show that channel biaxiality as measured by three different probe species, D_2O, ^{7}Li, and ^{23}Na, is sensitive to the length scale associated with the quadrupole splitting measurement, where we observe a nominally uniaxial environment when the length scale exceeds 0.5 μm.

In order to advance design of ion-conducting materials like Nafion, a complete understanding of nm – μm scale morphology is necessary. This is possible by choosing select probe molecules to "map" what factors (polymer-fixed charge groups or nm – μm scale domains) influence transport across such length scales. In conjunction with the rich literature on Nafion, future research efforts should focus on modeling how the electric field gradient from sulfonate lining the ion-conducting channels of Nafion impacts the observed quadrupole splitting as a function of water content. This may give new insight into the domain size, structure, and connectivity.

Chapter 5

Chapter 5 explores fundamental lithium ion (Li^+) and triflate counterion ($CF_3SO_3^-$) transport properties within an electrospun UV-crosslinked poly(ethylene oxide) polymer-gel electrolyte. With modulation of crosslinker (10 – 30 wt%), the fully swollen fibrous framework swells and retains between 1,700 and 1,200 wt% liquid electrolyte and exhibits room temperature ionic conductivity up to 6 mS cm^{-1}. ^{7}Li and ^{19}F spin-spin relaxation (T_2) measurements reveal the presence of inter- and intra-fiber lithium ions, where the long- and

short-T_2 lithium ion and counterion components enable quantification of the fractions of free liquid electrolyte between fibers and liquid electrolyte within fibers. NMR diffusometry shows increases in lithium and triflate diffusion coefficients with crosslinker content, suggestive of enhanced ion transport within the free liquid-electrolyte phase due to a reduction in morphological restrictions. Arrhenius fits to temperature-dependent diffusion experiments show that lithium and triflate values for the activation energy of diffusion (15 and 12 kJ mol^{-1}, respectively) are identical for ions in pure liquid solutions and for ions within the electrospun gel, showing that the framework does not influence the local energetics of ion transport.

Research on UV-crosslinked fiber mats for lithium-ion battery applications should focus on modulating the chemical structure of the crosslinker, amount of crosslinker, and testing UV exposure methods/times (e.g., UV-crosslink during or after electrospinning). For lithium-ion battery applications, increasing the polymer fiber modulus can reduce dendritic growth of Li metal through the crosslinked network during battery charging. This can potentially be investigated through magic-angle-spinning ^{13}C NMR studies, which may give information on crosslink distributions and how to tailor the crosslinker structure to achieve a desired modulus. Indeed, increasing the fiber modulus will likely decrease the uptake of liquid electrolyte (impacts ionic conductivity), thus necessitating a delicate balance between the two. Moreover, our group's electrophoretic NMR method is an excellent candidate to unveil fundamental transport properties within such materials.

Chapters 6 and 7

Chapter 6 presents a comprehensive study of PEO-PCL block copolymer spherical micelles that self-assemble at 1% wt/vol in D_2O. Varying composition by adding the co-solvent THF_{d8}, which preferentially imbibes into the micelle (PCL) core, allows sensitive study of how

small molecule additives influence micelle structure and dynamics. We conduct NMR spectroscopy and diffusometry on two block-copolymer micelle systems (PEO_{2k}-PCL_{3k} and PEO_{5k}-PCL_{8k}) that show substantially different behavior. Coexistence of unimers and micelles is present from 10 – 60 vol% THF_{d8} for the 2k-series and only exists at 60 vol% THF_{d8} for the 5k-series. At ≥ 60 vol % THF_{d8}, the micelle disassembles into free unimers for both systems. We see a slight decrease in micelle diffusion coefficients before the coexistence region (10 – 50 vol% THF_{d8}) for the 5k-series largely due to a decrease in $\eta_{solution}$ and invariance in micelle radius $r_H^{micelle}$ (14 – 16 nm). Both solutions show a gradual decrease in unimer radius r_H^{unimer} (5 – 1 nm) from the start of the coexistence region to pure unimers region. By understanding solvent environment effects and partitioning of small molecules into the micelle core, this study shows promise for enabling fine control over block copolymer self-assembly as well as cargo (*e.g.*, drug) carrying or release properties.

Chapter 7 presents a new method to investigate diblock copolymer micelle unimer exchange using NMR. We utilize varying intermolecular dipole-dipole interactions between ^{1}H-bearing and ^{2}H-bearing sites on unimers exchanging between micelles that are initially spatially separated. Differences in T_1 times of ^{1}H- and ^{2}H-sites on poly(caprolactone) within the core of a poly(ethylene oxide)-*b*-poly(caprolactone) micelle that self-assembles at 1% wt/vol in D_2O affords time-resolved T_1 measurements during mixing. The smaller magnetic moment of ^{2}H increases the spin-lattice relaxation time constants (T_1) of the ^{1}H-sites as the unimers exchange and the protonated micelles become dilute with ^{2}H-unimers. The weighted average rate constant for unimer exchange at 60°C is 20.8 ± 0.8 min^{-1}, which is in good agreement with TR-SANS results. Furthermore, variable temperature NMR diffusometry measurements show single-component diffusion below 40°C, above which a second, faster diffusion coefficient appears. In

conjunction with the Stokes-Einstein relation, we calculate $r_H^{micelle}$ of ~ 15 nm and r_H^{unimer} of ~ 3 nm (at 60°C), signifying coexistence of micelles and unimers at ≥ 40°C. These results suggest the dominant unimer exchange mechanism is through insertion/expulsion between micelles.

Block copolymer micelles have the potential to revolutionize how large hydrophobic drugs are delivered and solvent-exhaustive syntheses are conducted. For drug-delivery applications, kinetically frozen micelles (minimal unimer exchange dynamics) that remain stable upon intravenous injection (significant dilution effects) should be of interest. Temperature and pH effects should also be studied when designing new block copolymer micelles for drug-delivery. For nanoreactor applications, careful choice of block structure and molecular weight should be considered depending on the specific reaction of interest. How both of these tunable properties influence reaction kinetics heavily depends on the solvent system, temperature, size of reactants/products, and number of reactants/products.

8.2 Future Work

New directions within the group are focusing on molecular dynamics simulations to better understand how long time scale diffusion measurements, extracted E_a values, and the pre-exponential factor D_0 are coupled. This will provide new insight into deconvolving these quantities by use of the Arrhenius equation and correlating them to material properties. Evaluation of such parameters across multiple materials that exhibit drastically different properties for each parameter will aid in development of fundamental equations to use as a "ruler" to tailor material performance.

Current efforts within the group are focusing on mapping micelle-dominant, micelle-unimer coexistence, and unimer-dominant regions for the PEO-PCL-based micelles. These results will directly influence future method development of time-resolved relaxation methods to study unimer exchange kinetics as well as guide incorporation of clinical drugs into the hydrophobic PCL core.

Together, this Thesis aims to guide new research areas and supplement existing ones. NMR on materials offers unprecedented insights into fundamental properties that govern transport and self-assembly across multiple time and length scales. If used properly, NMR is an extremely powerful option to discern such properties and should continue to grow to become a more routine technique for material scientists.